Target Normal Sheath Acceleration for Laser-Driven Ion Generation: Advances in Theoretical Modeling

Claudio Perego

Dipartimento Di Fisica G.Occhialini

Università degli Studi Milano-Bicocca

Directors: Dimitri Batani, Matteo Passoni

A thesis submitted for the degree of

PhilosophiæDoctor (PhD)

21st January 2013

Abstract

Recently, ultra-intense laser-driven ion acceleration has turned out to be an extremely interesting phenomenon, capable to produce ion beams which could potentially be suitable for applications as hadron therapy or dense matter diagnostics.

The present PhD thesis is addressed to the study of Target Normal Sheath Acceleration (TNSA), namely the laser-based ion acceleration mechanism which dominates the presently accessible experimental conditions. The work is focused in particular on the theoretical modeling of TNSA, motivated by the need for an effective description which, by adopting proper approximations that can limit the required computational efforts, is capable to provide reliable predictions on the resulting ion beam features, given an initial laser-target configuration. Indeed, the development of a robust TNSA theoretical model would mean a deeper comprehension of the key physical factors governing the process, allowing at the same time to draw guidelines for potential experiments in the next future.

In this dissertation, in order to achieve a significant advancement in the TNSA modeling field, the results of two original works are reported, the first is focused on a critical, quantitative analysis of existing descriptions, and the second, starting from the conclusions of such an analysis, is dedicated to the extension of a specific model, aiming at the inclusion of further, crucial, TNSA aspects.

The quantitative analysis consists in the comparison of six well-known published descriptions, relying on their capability in estimating the maximum ion energy, which is tested over an extensive database of published TNSA experimental results, covering a wide range of laser-target conditions. Such a comparative study, despite the technical issues to be faced in order to reduce the arbitrariness of the results, allows to draw some interesting conclusions about the effectiveness of the six models considered and about TNSA effective modeling in general. According to the results, the quasi-static model proposed by M. Passoni and M. Lontano turns out to be the most reliable in predicting the ion cut-off energy, at the same time achieving such estimates through a self-consistent treatment of the accelerating potential.

This work highlights also the limits of such a TNSA model, and of the main approximations usually adopted to obtain the different maximum ion

energy estimates. Thus, starting from such considerations, an extension of this Passoni-Lontano model is proposed, including new crucial elements of TNSA physics within the description. In particular, further insights of the hot electron population dynamics are implemented, leading to a refined maximum energy prediction, which exhibits more solid theoretical bases, and which broadens the predicting capability of the original model to a larger range of system parameters. The resulting estimates are validated by means of literature experimental data and numerical simulations, demonstrating a remarkable agreement in most of the cases. The achieved model turns out to be particularly suitable in reproducing the maximum ion energy dependence on the target thickness, while some promising insights are obtained in the Mass Limited Targets (MLT) case. Nonetheless, further theoretical work is still required to attain a quantitative agreement with recently published experimental results on MLTs.

Contents

1

Introduction

1.1 Introduction to Laser-Based Ion Acceleration

The present thesis work is collocated in the extremely active field of laser-plasma interaction based particle acceleration, aiming at the theoretical modeling of the so-called Target Normal Sheath Acceleration (TNSA), which is the dominant mechanism for energetic ion generation achievable with current laser technology.

The idea of an accelerator exploiting the coherent motion of charged particles in plasmas, and the subsequent accelerating field dynamics, is already older than fifty years [1], a lifetime during which the concept of plasma particles "coherent acceleration" has collected several remarkable results, both in electron and ion generation. In fact, this idea has been initially exploited for electron acceleration solely, stimulating a wide range of important works, and reaching great progress in few decades of study [2]. Present work is instead focused on the alternative possibility of laser-based ion acceleration, which was first noticed in laboratory as a lateral result of electron acceleration campaigns, before a whole dedicated research field has been developed in the following years. Indeed, as it will be clearly stressed in the following, ion beam generation is triggered by the electron collective dynamics following laser-matter interaction.

Already in the 1960's, theoretical studies of the classic problem of a plasma expanding into vacuum showed that the electron thermal motion can determine collective acceleration of the plasma ionic component by means of self-consistent electro-static fields [3]. A proper way to provide such a thermal agitation became clear in the 1980's, when ultra-high peak power and ultra-short laser pulses were made available with the invention of the Chirped Pulse Amplification (CPA) technique [4]. Such electro-magnetic pulses are indeed able to excite electrons to relativistic temperatures on a fs timescale and, in principle, to determine collective acceleration of ions as well. High intensity laser matter interaction experiments provided ions up to energies of few MeVs already before the 2000s (see for example [5, 6]), but the low brilliance and broad divergence features of such particles were not attractive for specific applications. It was only in the 2000 that laser driven ion acceleration has gained considerable attention, thanks to the results achieved by three independent experiments on laser-generated electron

beams [7, 8, 9], which have recorded intense emission of multi-MeV protons by focusing the laser light to intensities higher than $10^{18}\,\mathrm{W/cm^2}$ on micro-metric thick solid foils. The resulting ion beams were detected in the forward direction with respect to the laser propagation, characterized by a relatively low, energy-dependent divergence, a short duration ($\sim$ ps), a high ion-per-bunch number (up to 10^{13}), a thermal spectrum showing a multi-MeV energetic cut-off and an impressive laminarity ($\sim 10^{-3}\,\mathrm{mm\,mrad}$ emittance). Such features attest the laser-based ion accelerators as a valid and promising alternative to the conventional technology, since they might provide a more compact and economical source for a number of potential applications, as for example sources for hadron therapy [10, 11, 12], Positron Emission Tomography (PET) isotopes production [13, 14], energy drivers for fast ignition inertial confinement fusion [15, 16, 17] and proton radiography of dense matter or fast transient fields [18, 19].

From the achievements of 2000s the scientific community began a massive experimental and theoretical effort to develop laser driven ion acceleration both for fundamental understanding and as a reliable technology for the foreseen applications. While some of the beam parameters already meet the requirements, a number of challenges still need to be faced in order to improve and control the other key ion features, as maximum energy or monochromaticity. For example, if hadron therapy is considered, the proton energy required for deep tumors treatment is $\sim 250\,\mathrm{MeV}$ [20], and of about $400\,\mathrm{MeV/nucleon}$ for carbon therapy [21], while at the moment the highest energies reached are $120\,\mathrm{MeV}$ for protons and $80\,\mathrm{MeV/nucleon}$ for carbon ions (recently communicated by B. Hegelich). Furthermore, the detected ion spectra are mainly broad exponentials, while a quasi-mono-energetic beam ($\Delta E \sim 1\%$) would be required. Laser stability and repetition rate need to be critically improved as well, in order to compete with the established radio-frequency-wave ion acceleration technology. These challenges naturally led to a strong experimental effort aimed at optimizing the resulting beam features, to comply with each of the different requirements for potential applications [22, 23, 24].

Nonetheless, also a deep theoretical understanding of the physical processes underlying the phenomenon, which is essential to reach a satisfactory control and efficiency of the acceleration, still needs to be achieved. From the first experimental evidences a lot of work has been done in this direction, trying to understand what kind of collective physics generates the detected ions. The interpretation of the majority of published results is consistent with the TNSA scheme [23, 24, 25], in which the relativistic hot electron population, heated up by laser-target interaction, expands through the bulk of the former and sets up, at its boundaries, huge electro-static fields perpendicular to the solid-vacuum interfaces. The magnitude of these fields is of the order of TV/m, which is enough to accelerate surface and bulk ions up to multi-MeV energies. In this framework, the most efficiently accelerated ions are protons coming from the superficial impurity layer of the target, but also heavier ions, again from the impurity layer or from the bulk, can reach relevant energies.

In these years the TNSA scheme has exhibited intrinsic drawbacks as broadness of the energetic spectrum, or low laser-to-ion conversion efficiency. To overcome such

drawbacks, and thus to substantially optimize the ion beam features, alternative acceleration schemes have been proposed and supported with experimental and theoretical studies, as for example Radiation Pressure Acceleration (RPA), Break-Out After-burner (BOA) and Collisionless Shock Acceleration (CSA) [23, 24]. However, the laser-target constraints required to achieve the regimes dominated by such alternative schemes are extremely demanding, and the investigation of them still requires both satisfactory theoretical understanding and proof-of-principle experiments. Thus, despite the attractions of these mechanisms, more than ten years of combined experimental, numerical and theoretical activities have clarified how "robust" and "natural" TNSA is, as far as the super-intense laser/thin solid foil system is concerned. This is also demonstrated by the most recent research programs for the development of laser-driven ion sources for possible applications, which presently rely, to a large extent, on proper exploitation, handling and optimization of the TNSA ions [26].

Therefore, within the TNSA scheme domain, a lot of work has been directed towards a better control of the process and different paths to improve the accelerated beam features have been pointed out. On the one hand, one can of course act on the laser pulse parameters, namely the energy, the intensity, the duration and the focal spot area. The dependences of TNSA acceleration on such parameters is a question of prime importance, which only a profound knowledge of the physical process can make evident. Several studies, aimed at clarifying such dependencies, have been published and plenty of information is now available but, nevertheless, no definite scenario has been outlined yet [23, 24]. The issue is made even more intricate by the strong complexity of laser-matter interaction at the ultra-high intensity regime, in which different absorption mechanisms come into play, and high nonlinearities prevent a straightforward interpretation [27, 28]. Moreover, laser absorption is strongly influenced by the pre-pulse, that is the light preceding the main ultra-intense pulse, which can alter the interaction conditions determining the expansion of a pre-plasma from the target surface, or even destroying the former before the arrival of the ultra-intense laser spike. For this reason the tuning of pre-pulse duration and laser contrast (the pre/main pulse intensity rate) can critically affect TNSA efficiency [29, 30, 31].

On the other hand, it has been demonstrated that the target features can be optimized to improve the ion beam features as well. Target thickness and, more generally, target geometrical properties directly influence the strength and features of the accelerating fields, defining two of the most popular paths to TNSA optimization, namely the exploitation of thin or reduced volume targets [32, 33, 34, 35]. Besides that, also the foil composition can determine a strong effect on laser absorption, hot electron transport and charge separation establishment, suggesting further possibilities to achieve a more effective acceleration [36, 37, 38, 39].

1.2 Motivation and Purposes of the Thesis

In the outlined framework it is thus clear that, in order to reach sufficient control of TNSA, and to guide ion beam optimization for future experiments, the formulation of

a proper theory is essential. Such a theoretical description should take into account the main traits of the physical process, to be capable to provide reliable predictions on the resulting ion beam features, given an initial laser-target configuration. Due to the intrinsic complexity of the physical system, in which huge electro-magnetic forces can trigger strongly nonlinear processes and different kinds of instabilities, the most natural tools to model TNSA are the numerical simulations, which rely on the basic laws of relativistic plasma physics: Maxwell and Vlasov equations. An effective method capable to reproduce the dynamics of Maxwell-Vlasov system, as the popular Particle-In-Cell (PIC) algorithm [40], can in fact accurately describe the most important TNSA physical aspects. That is why PIC simulations have been widely exploited to study this kind of physics (see for example Ref. [41]). Unfortunately, nowadays, the numerical test of a laser/target realistic parameter set is still extremely expensive in term of computation time and resources, since the space and time-scales relevant for TNSA impose strict requirements on the resolution and the initial conditions. The use of reduced dimensionality computations, lower density targets, or shorter windows of evolution time are some of the techniques which guarantee a reasonable computational effort, although making such numerical predictions not completely reliable [41, 42, 43].

As an alternative and complementary path to PIC simulations many theoretical simplified models have been proposed [44, 45, 46, 47, 48, 49, 50, 51, 52], each of them aiming at predicting some of the ion beam properties, for given experimental conditions, without involving expensive numerical computations. To achieve this, the use of strong approximations on TNSA physics is mandatory and several effects have to be neglected, trying to catch, at the same time, the essential features of the system which determine the ion behavior. If successful, this approach leads to a deeper theoretical comprehension of the physical process and of the interplay among different factors responsible for the ion acceleration. Besides that, the advantage of easier quantitative predictions with respect to numerical simulations, turns out to be relevant to direct the efforts of the experimental work. Indeed, in the near future, a new generation of laser facilities will be available, and it will be possible to investigate a wider range of parameters. For this reason, the predicting capability of theoretical models is crucial, in order to extrapolate guidelines for the future experiments. Despite more than ten years of intensive research however, theoretical knowledge of TNSA is still limited, and none of the presented models has been widely accepted by the community. This is due to the complexity of the physics involved in the phenomenon, which hampers the formulation of a simple theoretical description, capable to explain and reliably predict all the different properties of TNSA ions at the same time. Moreover, the energy optimization scalings are still not completely reproduced by the existing theoretical predictions, so that the effort to improve TNSA efficiency cannot be theoretically guided toward the most convenient directions.

This discussion naturally leads to the purposes of present thesis, which is aimed at achieving a substantial progress in TNSA theoretical understanding and modeling, towards the formulation of a reliable and consistent description, capable to implement the fundamental traits of the phenomenon and to provide a convenient technique for

ion beam features prediction. In this framework, the present work is addressed towards two main purposes: the first is that of providing an extended investigation on the main TNSA theoretical modeling approaches available in the literature. This is done by means of a comparative analysis which strongly relies on experimental evidences, testing the reliability of different models in TNSA ions maximum energy prediction. Such kind of study is exploited to draw some conclusions about the most convenient modeling approaches and the possible paths to improve TNSA modeling effectiveness. The second purpose, which directly follows the outcomes of the first analysis, is that of extending an existing model by introducing further physical elements. This progress aims at proper reproduction of ion maximum energy scaling with target geometrical features as the thickness or the transverse size, so that this route to TNSA optimization can be understood and controlled.

1.3 Structure of the Thesis

The present thesis is organized as follows:

in Chapter 2, the most important experimental achievements related to the TNSA mechanism are presented, discussing in particular the main ion beam optimization techniques established in more than ten years of research, and the open problems pointed out by such an experimental picture. Being strictly correlated with the issue of ion beam tailoring and improvement, a brief introduction to the alternative acceleration mechanisms is also provided, in order to outline the domain in which ion acceleration is dominated by TNSA.

In Chapter 3, the variegated physics involved in the TNSA scenario is presented, outlining the actual theoretical knowledge in ultra-intense laser-matter interaction, relativistic plasma dynamics and collective ion acceleration. After providing such a theoretical background, the issue of TNSA modeling is tackled, with a general introduction on both PIC and simplified effective approaches.

Effective modeling is then deeply explored in Chapter 4, dedicated to the first aim of present dissertation. Here, the different approaches and approximations which lead to the formulation of known models are introduced, presenting in particular six published descriptions. These ones are then involved in the predicting capability analysis mentioned before, in which the ion cut-off energy theoretical estimates obtained by the six models are compared over an extensive database of published experimental results.

Starting from the conclusions of Chapter 4, Chapter 5 is addressed to the second purpose of the thesis, which is the extension of the description proposed by M. Passoni and M. Lontano [50]. Implementing further physical aspects within this model, it is enriched and its predicting capabilities are broadened to include some TNSA crucial effects as the ion cut-off energy dependence on target thickness. Such a theoretical development is then validated on different grounds and further improvements are proposed and tested, leading to some conclusions and perspectives, which are eventually pointed out in Chapter 6.

2

Ultra-Intense Laser-driven Ion Acceleration: State-of-the-art

In this chapter, the main laser-driven ion acceleration experiments which contributed to the present knowledge on TNSA are outlined, in order to provide the reader with the experimental background of the theoretical study developed in the remaining of the thesis. First of all, in Sec. 2.1, the typical TNSA experimental configuration is introduced, to make the reader familiar with the common traits of the experiments described afterwards. Then, in Sec. 2.2, the attention is devoted to the proof-of-principle experiments, that have confirmed the TNSA scenario as the dominant accelerating process, characterizing the typical ion beam features. After that, in Sec. 2.3, the main techniques proposed to optimize the beam properties are reviewed, before introducing the progress reached by the alternative acceleration schemes (in Sec. 2.4). Although this work is not devoted to such alternative mechanisms, a brief outline of the results obtained in these areas is useful to complete the state-of-the-art and to underline the key role of TNSA in laser-driven ion acceleration. At the end of the chapter (in Sec. 2.5) a summary of the main open problems arising from the experimental picture of the TNSA mechanism is provided, in order to motivate the theoretical study of subsequent chapters. Further details on the achieved experimental knowledge can be found in a number of overviews, some of which of recent publication [22, 23, 24, 53, 54].

2.1 The Typical TNSA Experiment

As a first step, the typical configuration of a TNSA experiment, as represented in Fig. 2.1, is described. The CPA laser system delivers an energy ranging from hundreds of mJ up to the kJ order, transported by a single pulse of fs/ps length, thus reaching a peak power of several TW, up to the PW scale. Two kinds of solid-state lasers have mainly been exploited to achieve such power regimes: the high energy, low repetition rate Nd:glass systems, providing a bandwidth which allows for $0.3 - 1\,\mathrm{ps}$ pulses, and the table-top high-repetition rate Ti:sapphire systems, generating ultra-short pulses, of $30 - 300\,\mathrm{fs}$. Other active mediums (as laser diodes or CO_2), are not commonly

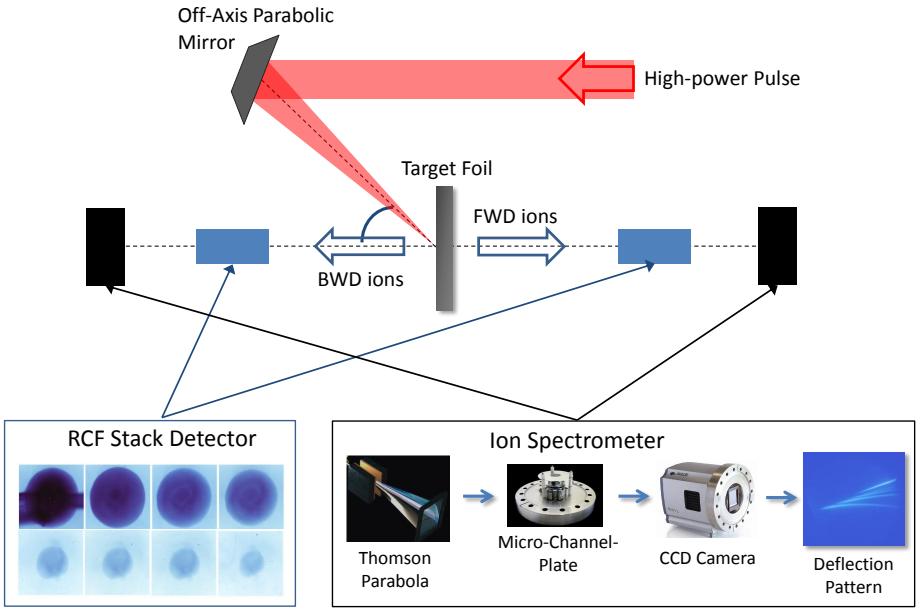

Figure 2.1: - Typical TNSA experimental configuration. Two kind of diagnostic are represented, RCF stack detectors and ion spectrometer, which can be used in combination, provided that a hole in the center of the stack allows the partial transit of the ions to the spectrometer.

used in TNSA study (they are nonetheless suitable for different interaction regimes, see [55, 56]). The high-power laser pulse, having a transverse diameter of several cm, is then focused using an off-axis parabolic mirror down to a micro-metric focal-spot (typically of $5 - 10\,\mu$m of Full Width Half Maximum (FWHM)), in which intensities from 10^{18} to $10^{21}\,\mathrm{W/cm^2}$ are reached. The target, in most of the cases a solid planar foil, is positioned with micro-metric precision in this focal spot, to exploit the highest available intensity in the interaction. Up to now, a wide variety of targets have been illuminated, with a large preference on planar metal or insulator foils, having thicknesses from a few up to hundreds of μms. Without specific treatments, the target surfaces are always covered by a thin contamination layer (few tens of nm thick), containing mainly water and hydrocarbons. For this reason the ions which are accelerated most efficiently by TNSA are protons sitting in this impurity layer, thanks to the highest charge-to-mass ratio and to their position close to the accelerating field peak.

It has to be mentioned that, as introduced in Chapter 1, ultra-intense laser pulses are always preceded by the so-called pre-pulse, a radiation determined by Amplified Spontaneous Emission (ASE) of the active mediums or by leakages and high order dispersion in the CPA chain. In Fig. 2.2, a typical temporal structure of an ultra-intense

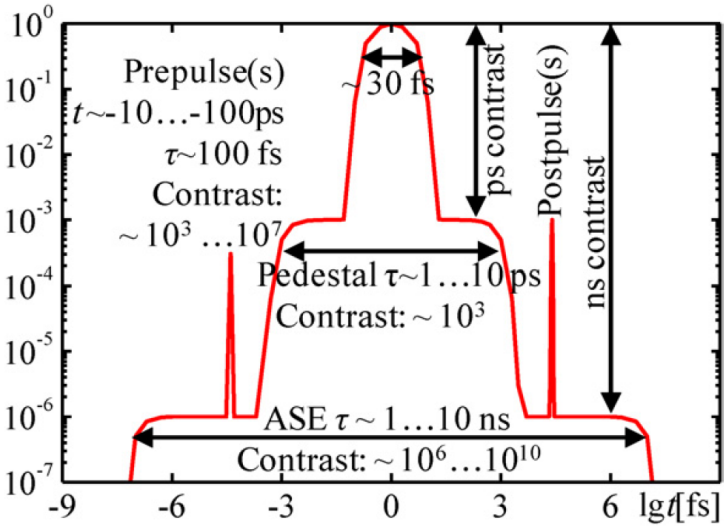

Figure 2.2: - Typical temporal structure of a Ti:Sapphire 30 fs laser pulse (figure reprinted from Ref. [23]).

pulse is represented. If the laser pre-pulse is intense enough, it can have profound effects in a TNSA experiment, for example creating a pre-plasma, that is a low-density plasma corona in front of the target surface, which may influence the main pulse interaction with matter. As anticipated in the introduction, the pre/main pulse intensity ratio is named Contrast Ratio or, more simply, contrast, and it is usually of the order of 10^{-6}, over a few ns timescale. Several techniques to "clean" the ultra-intense spike from the pre-pulse have been developed and Ultra-High-Contrast (UHC) pulses, reaching a ratio of 10^{-10}, are presently available (see e.g. Ref. [57] and references therein).

According to the TNSA scheme, the ion beams are directed along the normal, outward direction of both front and rear foil surfaces, irrespective of the laser incidence angle. Therefore, ion diagnostics are typically positioned along these two emission directions, as depicted in Fig. 2.1. The backward ion emission is usually less efficient, due to the surface perturbation determined by pre-pulse interaction; that is why most of the relevant TNSA results are relative to forward accelerated ions. Several techniques for the accelerated particles detection are available: Radio-chromic Films (RCF), CR-39 plastic track detectors, nuclear activation detectors, scintillators, Image Plates (IP), Micro-Channel Plates (MCP) and so on. The most popular diagnostic configurations used to retrieve the energetic spectra of the ion beams are: RCF or CR-39 arranged in stack detectors, exploiting the peculiar features of ion energy deposition in matter (Bragg peak), and Thomson Parabola spectrometers coupled with IP or MCPs, capable to separate ions in deflection patterns depending on their charge-to-mass ratio and energy (as represented in Fig. 2.1). Alternative techniques, as Time-of-Flight (TOF) spectrometers, have been developed as well. For a detailed and up-to-date description of ion diagnostics the reader should refer to Ref. [23].

2.2 Main Experimental Achievements

In more than ten years, a large number of experimental campaigns, mostly based on the typical setup described in Sec. 2.1, have been carried out, clarifying several aspects of the TNSA mechanism and, at the same time, highlighting a complex and variegated picture. Already the 2000s pioneering works were able to catch the key features of TNSA, as shown by the results published in Ref. [9] (see also Ref. [58]). In this experiment, performed on the Lawrence Livermore National Laboratory (LLNL) PW-class laser system, planar and wedge-shaped targets have been irradiated at intensities higher than $10^{20}\,\mathrm{W/cm^2}$. The resulting ion emission, in particular from the wedge case (shown in Fig. 2.3), has given evidence that the forward accelerated protons are mainly originating from the rear surface of the target, along its normal direction. Moreover, thanks to the use of a magnetic spectrometer, the particle spectra have also been measured, demonstrating an exponential profile with a multi-MeV cut-off, a fundamental trait of TNSA ions. The 58 MeV cut-off, detected in this circumstance using a 100 μm thick CH polymer foil, has been the highest laser driven proton energy achieved for many years. The results of this experiment have shown high brightness (more than 10^{13} protons beyond the 10 MeV, corresponding to $\sim$ 10% of the laser energy) and collimation of the beams as well.

In the following years, further investigations supported the TNSA scheme as the dominant acceleration mechanism for the available laser technology. In 2001, Mack-

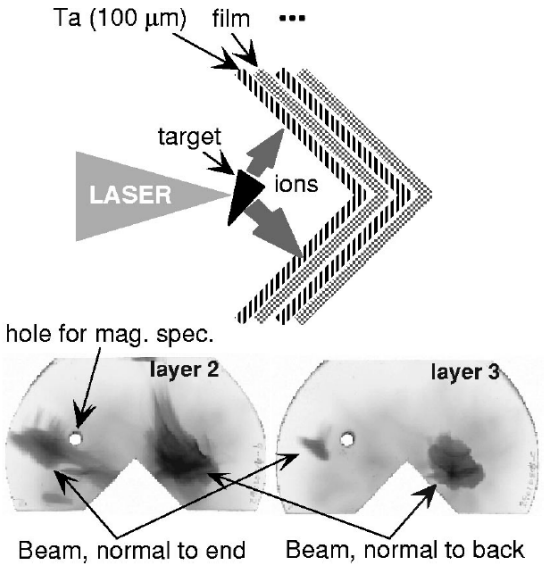

Figure 2.3: - Scheme of wedge targets irradiation. The RCF detected ion beams are directed perpendicularly from the wedge surfaces, the particle flux depending on the area of the source face (figure from Ref. [58]).

innon et al. [59] have studied the influence of the rear surface plasma density scale

length on the ion emission, by using a probe beam to control the plasma profile. The so-obtained proton energy spectra appeared to be strongly dependent on the rear side density profile, in agreement with the TNSA mechanism in which longer density scale lengths reduce the ion source efficiency (a more recent demonstration can be found in Ref. [60]).

A further, robust confirmation to the TNSA scheme has been obtained at the Laboratoire pour L'Utilisation des Lasers Intenses (LULI) 100 TW system, where the acceleration of carbon and fluorine ions has been achieved [61]. In this experiment the targets, aluminum and tungsten foils coated on the rear surface with C and CaF_2 layers, have been subject to resistive heating in order to remove CH contaminant layer (see Ref. [62] for an alternative technique of surface clearing). As Fig. 2.4 shows, the irradiation of such foils led to massive detection of C and F ions, demonstrating the onset of a rear-surface acceleration.

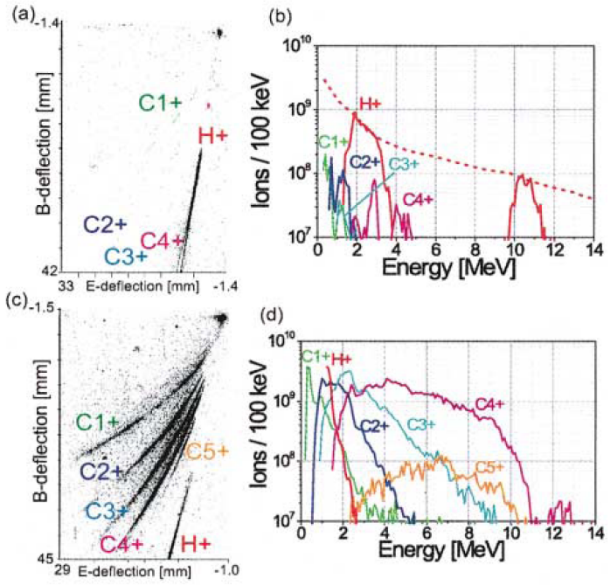

Figure 2.4: - Deflection patterns and corresponding energy spectra obtained in presence of contaminant hydrocarbon layer ((a) and (b)) and after its removal ((c) and (d)) (figure from Ref. [61]).

In the same experimental campaign (see Refs. [63, 64]), interesting results about spatial and angular ion beam features have been retrieved as well. First of all, a different ion yield and distribution has been obtained with metal targets, if compared to plastic ones (as already pointed out in Ref. [58]). In the first case the emission was more uniform, while the plastic targets, although their composition could provide a considerably higher proton yield, determined a non-homogeneous acceleration. Such a behavior has been attributed to the fact that the hot electron transport through the material is hampered by the low conductivity of plastic, thus leading to hot electron beam filamen-

tation and to the formation of non-1D structures in the accelerating field [36]. Another interesting result has been obtained after irradiation of gold wire-shaped targets. In this case, the cylindrical rear surface has provided de-collimated ions, fostering the scheme of TNSA and suggesting the possibility to focus the ion beam by proper bending of the target rear surface. Furthermore, still in this experiment, the study of the obtained ion traces allowed an estimate on the acceleration time duration, of the ps order, resulting in an extremely low longitudinal emittance of the beam ($\sim 10^{-4} - 10^{-5}$ eV s, whereas it is ~ 0.5 eV s on a typical synchrotron accelerator). Moreover, a strong dependence of the distribution on the rear surface homogeneity has been demonstrated, together with an estimate of the proton beam transverse emittance. The latter, obtained by imaging of target edges at different distances, has turned out to be quite low ($\sim 0.2\pi$ mm mrad), leading to a measurement of the real emission source size (few hundreds of μm) [64] and supporting the idea that TNSA provides ideal sources for proton radiography of fast transient phenomenons [19, 65].

The TNSA features revealed by this campaign at LULI led to the experiment presented by Cowan et al. in Ref. [66], in which the results of illuminating foils with a nano-metric grid of shallow grooves carved on the rear surface are published. The obtained ion emission has shown that the grid imprint had been transferred on the ion detectors as a modulation of the particle flux (see Fig. 2.5). This has provided another verification to the rear-side acceleration hypothesis, also allowing a measurement of spatial and angular ion beam features. The accelerated particles exhibited high collimation ($< 10^{\circ}$ divergence above 10 MeV, inversely proportional to the energy) and surprisingly low transverse emittance (< 0.004 mm mrad, while on conventional accelerators is of the order of 1 mm mrad) and longitudinal emittance (10^{-7} eV s estimated with PIC simulations). An analogous investigation of proton beam emittance and spatial properties is given in Ref. [67], in which the excellent beam quality have been again confirmed. In subsequent studies the beam diagnostic techniques have been refined and the indications of the previous experiments on the accelerated ion beam spatial and temporal features have been supported and further consolidated (see for example Refs. [68, 69, 70, 71]).

2.3 Beam Optimization

Due to the intrinsic properties of the TNSA mechanism, like the Debye sheath spatial and dynamical features, laser-accelerated ion bunches present a surprising laminarity as well as an ultra-short temporal duration. Nonetheless, other properties of the ion beam need to be substantially optimized in order to make the acceleration mechanism suitable for the proposed applications. Maximum ion energy and conversion efficiency for example, are still far from the requirements for hadron-therapy sources or fast-ignition energy drivers. For this reason, a common goal of past, present and future laser driven ion acceleration experiments is that of pointing out convenient paths to ion beam optimization. In this sense a deep understanding of the beam dependences on the experimental configuration parameters is required, in order to increase ion acceleration

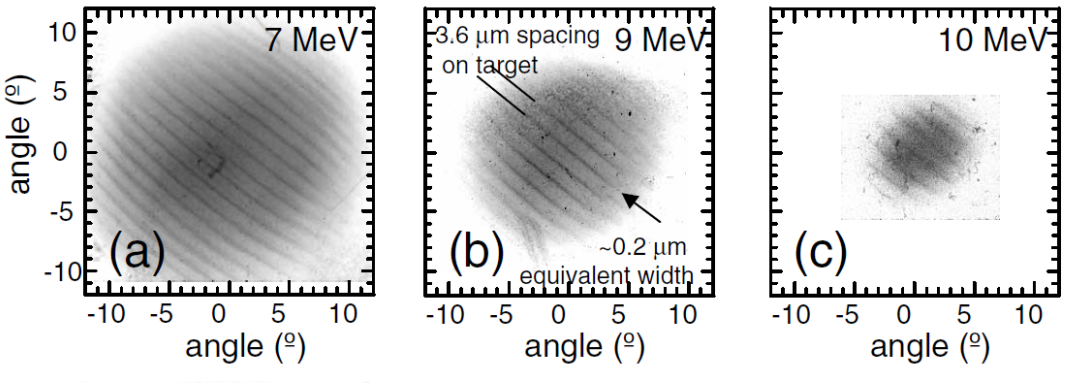

Figure 2.5: - Rear surface shallow-groove imprint on three RCFs corresponding to different proton energies (figure from Ref. [66]).

efficiency. This is still an open problem in TNSA research and it is also one of the main motivations of present dissertation. By the way, several works have been addressed at such a goal in the last years, obtaining extremely relevant results and paving the way for theoretical understanding of the TNSA mechanism.

A first, necessary step to beam optimization is the determination of TNSA dependences on laser features as energy, intensity, duration and focal spot of the pulse. Such four parameters are related by the following equation:

$$I = \frac{E_{\mathrm{p}}}{\tau_{\mathrm{p}} A_{\mathrm{fs}}}\,, \tag{2.1}$$

in which I is the electro-magnetic field intensity averaged along the temporal profile of the pulse and over its focal spot, E_{p} is the energy, τ_{p} the duration and A_{fs} the focal spot area. It is usually convenient to consider an effective focal spot, for example delimited by the FWHM diameter, not containing the whole pulse energy but inside which ultra-high intensities are reached with better uniformity, in order to restrict to the interaction regime which is relevant for ion acceleration. The same holds for the temporal profile, which presents ns and ps pedestal of much lower intensity (see Fig. 2.2). Eq. (2.1) indicates that independent parametric studies are needed to isolate and enlighten the different dependencies of TNSA features on the laser parameters. A systematic study of these dependencies has been published in Ref. [33], as a result of an experimental campaign held both on the Nd:glass 100 TW system at LULI and on the ATLAS Ti:Sapphire laser at the Garching Max-Planck Institut für Quantenoptik. Manipulating the pulse energies from 1 to 10 J, and the durations from 30 fs to 10 ps, the authors have tried to elucidate the behavior of proton cut-off energy and conversion efficiency, two key parameters for laser-ion acceleration main potential applications. The maximum ion energy has been shown to depend more sensibly on the intensity (varying together with the energy according to Eq. (2.1)) than on the pulse duration (see Fig.2.6), while the conversion efficiency is similarly affected by both parameters. The

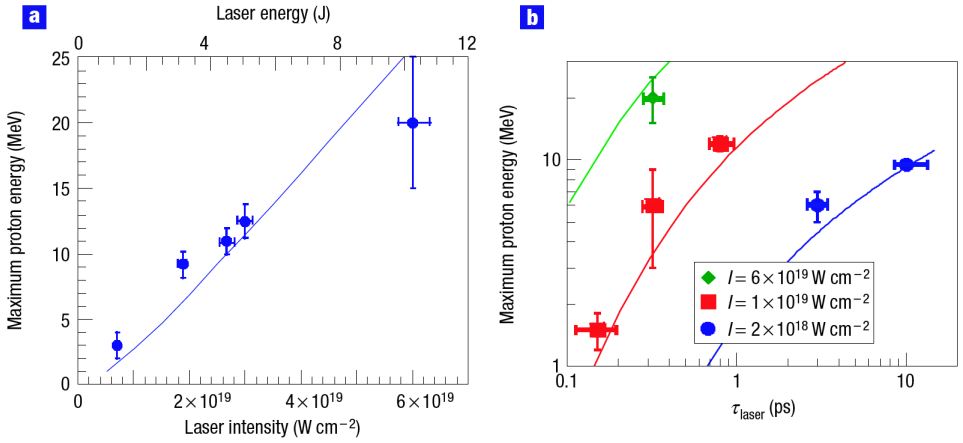

Figure 2.6: - (a) Maximum energy of the proton beam results presented by Ref. [33], as a function of laser intensity (bottom axis) and laser energy in the focal spot (top axis). (b) Maximum proton energies from the same experiment as a function of pulse duration at three different laser intensities (see legend). The lines in both figures are evaluated through an effective model, which is discussed in Ch. 4 (figure reprinted from Ref. [33]).

resulting behavior can be satisfactorily explained by a fluid plasma model [44], which is discussed in Ch. 4. Again in Ref. [33], an attempt to generalize the retrieved scalings, gathering published experimental results from different laser systems, is provided. In a subsequent high impact factor publication [49], the results of an experiment exploiting VULCAN PW system, at Rutherford Appleton Laboratory, extended the energy range of before-mentioned scalings up to 400 J, reaching intensities of 6×10^{20} W/cm^2. The retrieved proton cut-off energy behavior suggested a slower growth with laser intensity with respect to Ref. [33] predictions, attesting a $\sqrt{I}$ trend, in agreement with previous parametric studies [73, 74], while a linear scaling of the conversion efficiency with the laser pulse energy has been demonstrated. To interpret such data, the relevance of the three dimensional effects and of the hot electron cooling at longer timescales have been considered. A similar systematic study, exploring a lower energy regime ($40 - 250$ mJ), has been presented in Ref. [75], where the results obtained with a Ti:Al_2O_3 table-top, high-repetition system have been published. In this investigation a quasi-linear scaling of the maximum energy with intensity has been retrieved, while its dependence on laser pulse duration has been measured at fixed pulse energy and intensity. As a result, the role of pulse duration has been proved to be a key factor, together with intensity and energy, in TNSA acceleration. Here, the use of table-top high-repetition lasers for ion acceleration (first proposed in Ref. [76]), suggested a different behavior of TNSA, reaching lower peak energies but achieving steeper optimization scalings. The attractiveness of such a regime has been further explored, thanks to the development of Ti:Sapphire 100 TW class systems. For example, in Ref. [72], the TNSA protons which have been obtained with the ultra-short pulse 150 TW laser system Draco, installed at Dresden–Rossendorf research center, are analyzed. The proton energy cut-off depen-

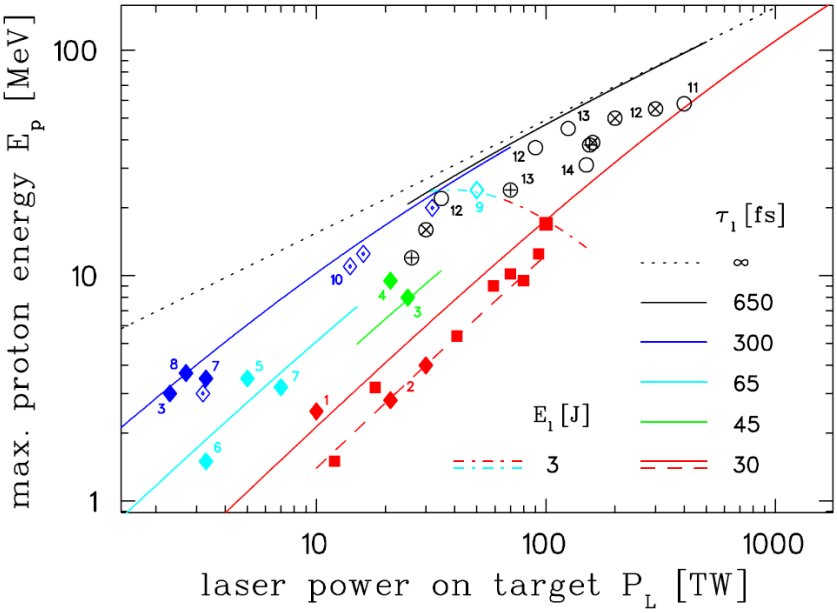

Figure 2.7: - Comparison of maximum proton energy dependence on laser power, as measured on several laser systems. Different colors indicate different pulse duration regimes, as showed by the legend. Red squares correspond to the energies measured on the Draco ultra-short laser system, plain diamonds indicate the measurements on various Ti:Sapphire lasers, with energy $\sim 1\,\mathrm{J}$ (filled) or $\sim 5\,\mathrm{J}$ (open), while the dotted diamonds have been detected at LULI Nd:glass laser [33]. The circles correspond to high-energy, single shot lasers systems, in particular the crossed-circles correspond to Ref. [49] results. The trend lines are evaluated by means of the analytical model proposed by Ref. [46] and introduced in Ch. 4 of present thesis (figure taken from Ref. [72], where the experimental data references can be found).

dence on laser power has been here studied varying the pulse energy from 0.3 to 3 J at fixed duration (30 fs) and focal spot, retrieving cut-off energies up to 18 MeV, and a quasi-linear trend in agreement with the intensity dependence indicated by Ref. [75]. Such results have been then compared to different sets of published experimental data, confirming the more promising behavior of ultra-short high-repetition systems with respect to high-energy, single-shot lasers. The resulting plot is reprinted here in Fig. 2.7, displaying also the cut-off energy scalings published in Refs. [33, 49] and discussed previously.

Thus, summarizing the large number of experiments, a general behavior of maximum ion energy, as a function of laser intensity (or, equivalently, energy/power) at fixed duration and focal spot can be identified. The spectra obtained with ps-order duration, multi-J energy pulses extend to a cut-off which increases as the square root of the laser intensity, typically with conversion efficiency of the $1 - 10\,\%$. Instead, the energy cut-off of ions produced by means of ultra-short, high-repetition lasers, scales quasi-linearly with laser intensity, while the conversion efficiency of the process remains

below the 1 %. Fig. 2.8 represents a collection of published experimental energies as a function of laser irradiance[1] which is in substantial agreement with this picture.

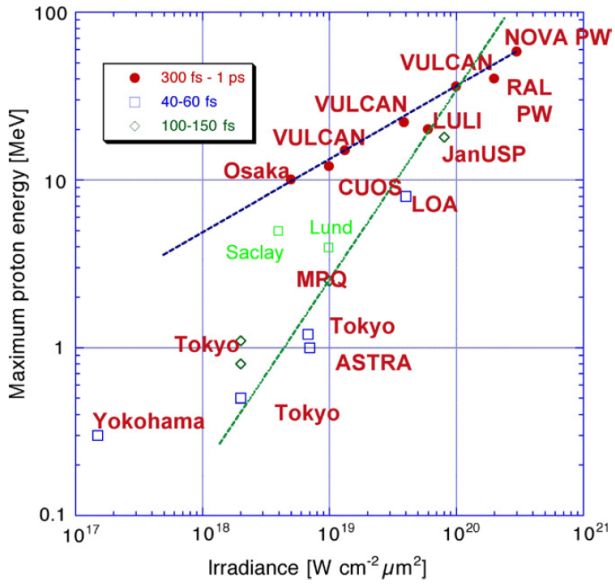

Figure 2.8: - Collection of maximum ion energies from different laser facilities, displayed as a function of laser irradiance. Square-root (dark blue) and linear (green) trends are displayed (The figure is re-printed from Ref. [78], single references can be found in [22, 78]).

Anyway, such a generalization, neglects several aspects of TNSA experimental achievements, which are of key importance in order to understand the physical process and the path to its optimization. The recent collection of ion energy cut-offs presented in [23] and displayed in Fig. 2.9, as a function of pulse energy and intensity, gives an idea of the strong deviations exhibited by many measurements with respect to the outlined general behavior. A first aspect which has not been considered up to now is the laser focal spot size, which closes the relation between laser energy and intensity, that is Eq. (2.1). The experiments are usually performed at fixed focal spot, with a typical FWHM diameter ranging from 5 to 10 μm, but the different spot dimensions among the published experiments can surely affect TNSA efficiency (see for example [79] for a study about de-focusing effects on TNSA). Dimensions and focal spot appearance might indeed determine a different spatial behavior of the hot electron generation and dynamics, or affect the laser-matter interaction regime. Different interaction conditions can in fact explain important deviations of TNSA behavior, as those of Fig. 2.9, affecting laser energy absorption and thus hot electron population features. As far as the interaction is concerned, laser incidence angle is another crucial parameter [28],

[1]The laser irradiance is defined as $I\lambda^2$ where I is the laser intensity and λ the wavelength. The latter in fact plays a key role in laser-matter interaction and, as a consequence, in laser-driven ion acceleration as well [73, 77]. In TNSA experiments however, the considered laser wavelengths are just 0.8 μm for Ti:Sapphire systems and 1.06 μm for Nd:Glass systems, resulting in a relatively weak influence on measured energies.

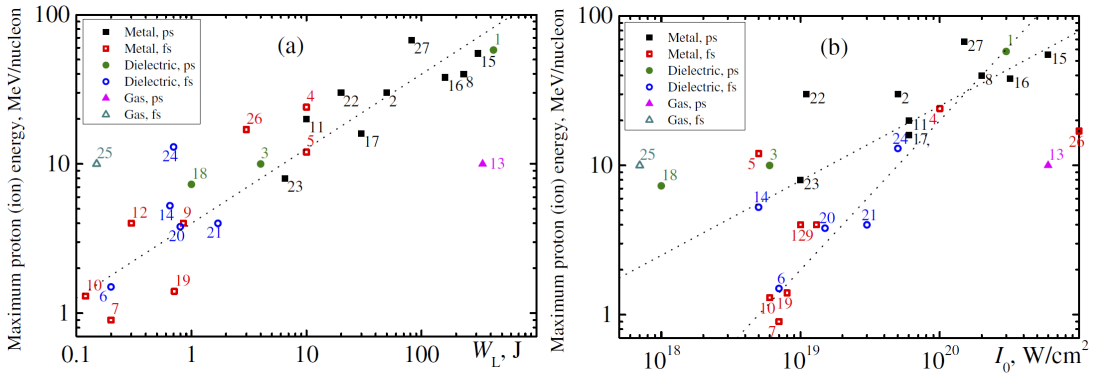

Figure 2.9: - Collection of maximum ion energies displayed in function of pulse energy (a) and intensity (b). The figure is taken from Ref. [23], where the single references can be found. The dotted trend lines grow as (a) the square root of pulse energy and (b) the square root of the intensity and the intensity itself.

which has not been considered in generalizing TNSA scaling laws. The reason for that can be supported by Ref. [33], that demonstrates a weak dependence of TNSA ion features on the incidence angle. On the contrary, the results of Refs. [31, 80, 81] show that incidence and polarization of the laser, determining the angle between the optical field and the target surface, can have a sensible influence on TNSA. This incompatibility is interpreted as an effect of the pre-formed plasma: in fact, in the case of Ref. [33], the formation of an extended pre-plasma has probably altered the interaction conditions partially ruling out the optical field orientation influence. In the other cases instead, the pre-pulse intensity is very low, letting the main pulse interact with a steep density profile [31, 80, 81]. Recently, high peak proton energies of 67.5 MeV have been obtained by illuminating special flat-top cone targets consisting in a metal cone structure with a flat foil at the tip [82, 83]. The laser is focused inside the cone from the open basis and strikes the inner cone tip surface, being absorbed at grazing incidence. The higher energies obtained, also relative to the classic foil targets results, can be partially explained as an effect of this oblique interaction angle, showing once again the influence of incidence in TNSA acceleration.

The pre-pulse/pre-plasma argument leads to other considerations of main relevance on TNSA experimental evidences. First, the presence of a pre-plasma has been shown to increase laser absorption efficiency, determining more efficient heating of target electronic population, but also laser self-focusing and filamentation instabilities. This has been studied directly on a spontaneously created pre-plasma [84] and by using a probe beam to generate a controlled density profile [85, 86, 87]. The results stimulated researches also on target manufacturing, with the proposition of a foam front surface layer, able to favor laser absorption efficiency [39]. Moreover, the pre-plasma corona emits X-rays which may preheat the target bulk, affecting the rear surface density profile as well, and spoiling forward ion emission. However, this is important only for very thin targets of relatively high-Z materials (larger hard X-ray generation) at relatively

high laser irradiances.

Apart from the formation of a pre-plasma, pre-pulse interaction with the target can also launch a shock wave throughout the latter, which can destroy it or spoil rear surface density profile [29] and orientation [88], affecting forward TNSA ions. Of course, for such detrimental effects to occur, pre-pulse duration and foil thickness should allow the shock break-out on the rear surface before TNSA ion bunch is emitted. As an example, in the experiment presented by Ref. [29] the pre-pulse duration has been controlled on a nanosecond scale using an ultra-fast Pockels cell, as different target thicknesses have been tested. Under such conditions, as displayed in Fig. 2.10, the detected proton cut-off energy has exhibited a maximum at a target thickness which has been shown to depend linearly on the pre-pulse duration. Below the optimum thickness the foil was thin enough that the pre-pulse perturbation had the time to reach and spoil the rear surface before the most energetic ions could be accelerated, determining the energy cut-off drop.

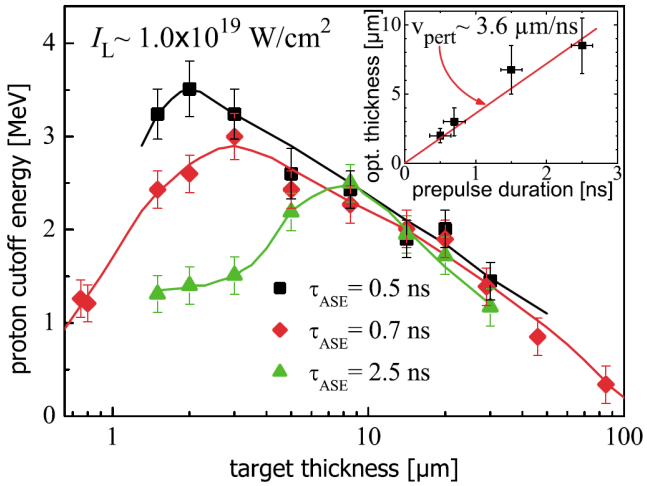

Figure 2.10: - Proton cut-off energies detected in function of the foil thickness, for three different pre-pulse duration τ_{ASE} at constant pulse intensity I_{L}. The inset represents the linear dependence of optimum target thickness on pre-pulse duration, allowing an estimate of shock velocity through the target ($v_{\mathrm{pert}} \sim 3.6\,\mu$m/ns) (image reprinted from Ref. [29]).

The results represented in Fig. 2.10 have enlightened also another key feature of the TNSA process, that is the dependence on target thicknesses above the optimum, which has attracted much attention and has been investigated in various published works [7, 29, 32, 33, 76, 89, 90]. For foils thicker than the optimum, the value of which is related to pre-pulse interaction with target, the ion energy cut-off decreases as the foil thickness increases, testifying a strong inverse dependence of TNSA efficiency on this parameter. This is due to the fact that the TV/m electro-static fields, setting up at the target-vacuum interfaces, confine most of the laser generated hot electron population inside the foil boundaries, which are set by the slower dynamics of the ion population. The majority of relativistic electrons is thus constrained to recirculate back and forth

through the foil bulk, as described in Refs. [32, 42, 91]. Due to this confinement, a reduction of the target thickness can, in principle, provide a higher concentration of hot electrons in the sheath, determining a stronger accelerating field. Thus, once the pre-pulse effect is removed, the use of thinner targets represents a possibility to optimize the energy of TNSA ions. To exploit this, a considerable improvement of laser contrast has been developed, allowing the illumination of sub-μm thin foils without the appearance of pre-pulse effects, as demonstrated for example on the UHC Ti:Sapphire system at Saclay Laser Interaction Center Facility, exploiting a Double Plasma Mirror (DPM) set up to reach a 10^{10} contrast ratio [31, 57]. In this experiment also a strong symmetry between backward and forward emitted ion beams is obtained, predicted by TNSA picture but still not observed experimentally. The achievement of this symmetry is indeed not possible on normal contrast systems because, as already mentioned, the pre-formed plasma hampers front surface TNSA.

It has been proved that the laser-heated electrons expand through the target bulk also in the transversal direction and not just longitudinally, as testified by the typical transverse dimensions of the ion source (hundreds of μm [64]), or by MeV-ion emission from the target lateral edges [92]. For this reason, it is believed that a reduction of the target transversal dimensions can provide further confinement of the hot-electron cloud and thus improve the efficiency of ion acceleration. That is the motivation why, in the last few years, Mass Limited Targets (MLT) such as planar foils or spheres, with transversal dimensions limited to a few μms, have been tested. As a result, several works [93, 94, 95, 96, 97] numerically demonstrated that TNSA conversion efficiency and peak energy can be improved noticeably by irradiating MLTs. These numerical predictions have also been confirmed on experimental grounds, using ultra-short pulses on plastic spherical targets [34], medium/short duration pulses on planar gold targets [35, 98] (showed in Fig. 2.11), and long pulses on square, triangular and circular aluminum foils [99].

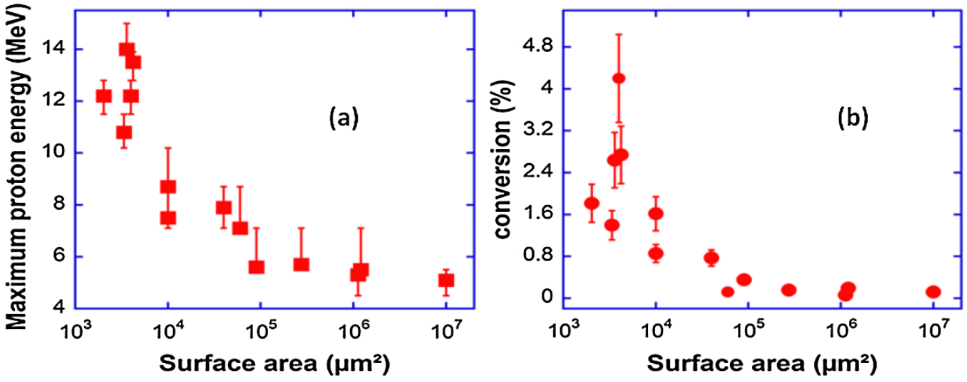

Figure 2.11: - Proton cut-off energy (a) and conversion (b) measured for 2 μm thick gold foils of variable surface areas (figure from Ref. [35]).

Up to now only the optimization of maximum ion energy and conversion efficiency has been considered, while for applications as hadron therapy, also the spectra of the

accelerated particle is a key factor. The typical TNSA spectrum is exponentially decreasing with a sharp cut-off, a broad energy distribution which is not convenient for precise cancer treatment. Post-processing of this TNSA multi-chromatic bunch is possible and different techniques to achieve a narrow spectrum have been published [23, 24]; nonetheless, spectra optimization during the acceleration phase is possible and represents an extremely attractive objective of laser-based ion acceleration research. In the framework of TNSA, the structuring of targets represents a convenient path to energy spectrum manipulation, as demonstrated on the Trident LANL facility by means of Palladium foils coated with an ultra-thin graphite layer on the back surface[1]. The ultra-thin carbon structure, of a few mono-atomic-layers (sub-nm scale), has determined acceleration of C^{5+} ions with reduced energy spread of 17%. The charge-to-mass ratio of C^{5+} is almost twice the ratio of Pd^{22+} ions, so that they are accelerated before substrate expansion. Since all the carbon atoms were situated in a sub-nm layer they were feeling the same acceleration field, at least longitudinally, providing a narrow spectrum. An alternative approach to ion spectrum manipulation by target structuring is presented in Ref. [100], in which the results of titanium foil with Polymethyl Methacrylate (PMMA) micro-dots on the back side irradiation are shown. The micro-dots are 0.5 μm thick surface limited ($20 \times 20\,\mu$m) coating layers, so that the efficiently accelerated protons are sitting in a small spot, thus experiencing a similar accelerating field. This method, which is analogous to the previous one, except for being based also on limited transversal dimensions of the ion source, has provided an energy spread of the 25%, which is narrower with respect to "ordinary" TNSA spectra. Anyway, the spectra monochromatization required for hadron therapy, of the order of 1% is still well beyond the present experimental achievements, while the TNSA scheme itself naturally provides broad thermal energy distributions, for this reason the development of alternative acceleration schemes can be a fruitful strategy to reduce the gap and meet the requirements for foreseen applications.

2.4 Alternative Acceleration Schemes

In this section the main alternative acceleration mechanisms are briefly introduced, underlining the key experimental achievements which, deviating from the typical TNSA features, testify the establishment of a different mechanism.

As seen in the previous section, a convenient way to improve the TNSA ion energy yield is to decrease the target thickness, provided that the laser contrast is sufficiently large to prevent pre-pulse effects. This path eventually leads to the possibility that the target thickness becomes comparable to the laser penetration depth. In this case, the pulse is supposed to propagate through the target determining first a highly efficient volumic heating of the electrons, and then to a relativistic Buneman instability that should enhance the electron-ion coupling. This scheme, described and studied numerically in Refs. [101, 102], is named Break-Out Afterburner (BOA) and it is in principle

[1] The hydrocarbon impurity layer here has been again removed with resistive heating, as explained in previously mentioned Ref. [61].

capable to produce higher energies with respect to TNSA and mono-chromatic spectral features. In Ref. [103] acceleration of high energy C^6 ions is achieved by irradiating Diamond-Like-Carbon (DLC) ultra-thin foils (10, 30 and 50 nm thick) with an UHC 100 TW laser, focused at $7 \times 10^{19}\,\mathrm{W/cm^2}$. At this order of intensity the relativistic effects of interaction predict a penetration of the laser radiation for tens of nanometers, providing the before-mentioned efficient heating. The unprecedented energetic peak of 185 MeV (15 MeV/u) is interpreted as a sign of a partial BOA regime, while the TNSA-like spectra show that the predicted scheme has not been completely proved.

Another acceleration mechanism, which has gained much popularity in laser driven ion acceleration research, is the so-called Radiation Pressure Dominated Acceleration (RPDA or simply RPA), based on the direct, collective thrust of particles, taking place at the front target surface, by means of the laser ponderomotive force. If the irradiating light is intense enough, the radiation pressure can in fact provide a collective push of the electrons inside the target, as the pulse penetrates into matter by a process called Hole-Boring [77, 104]. The electron displacement gives rise to a strong charge separation which pulls an ion bunch along the laser propagation direction. This double electron-ion density peak structure, called "laser piston", travels through the target as the laser penetrates, driving the electro-static peak and reflecting the ions at rest at twice the velocity of hole boring. Such a process, called Hole Boring RPA regime, has been widely studied and confirmed with numerical simulations, and reliable simple models have been proposed (see for example [105, 106]), promising higher energies and narrower spectra with respect to TNSA.

Hole Boring RPA holds as long as the laser piston penetrates through the target. If the latter is thin enough to allow the piston breakout on the rear-side, before the laser pulse has been completely reflected, then the accelerated bunch of ions can experience a further, highly efficient acceleration by the radiation pressure, as a "sail carried by the wind". Such regime is indeed called Light Sail RPA, and can be described by a "relativistic mirror" model, obtaining extremely promising conversion efficiency and ion features [107]. Establishment of light-sail regime has been proved with numerical simulation [108], confirming the attractiveness of such mechanism.

The experimental proof-of-principle of RPA is however extremely difficult, since, at the presently available intensities ($\lesssim 10^{21}\,\mathrm{W/cm^2}$), strong suppression of the natural electron heating is necessary in order to prevent detrimental instabilities and TNSA establishment. This can be partially achieved with UHC lasers and circular polarization, as showed in the study of Ref. [109], in which the detected carbon ion spectrum presents a peak emerging from the TNSA thermal structure. Circular polarization can in fact suppress the oscillation of the laser ponderomotive force, according to laser-plasma interaction models [27, 28], strongly reducing electron heating. In another experiment, a circularly polarized, low intensity ($\sim 6 \times 10^{15}\,\mathrm{W/cm^2}$), long wavelength ($CO_2$ laser) pulse, irradiating a low density target (few critical densities obtained with a gas jet) has provided protons with a narrow energy distribution ascribable in some sense to RPA process [55]. Simulations have demonstrated that RPA should become comparable to TNSA for intensities of the order of $10^{21} - 10^{22}\,\mathrm{W/cm^2}$, while for more than $10^{23}\mathrm{W/cm^2}$

it should set as the dominant acceleration regime [41, 108].

Another mechanism which deserves to be mentioned is the so-called Collision-less Shock Acceleration (CSA) [104, 110]. In this scheme the laser pressure gives rise to a piston but, due to sufficiently low target density (or high intensity), an electrostatic, collision-less shock is launched and propagates through the plasma independent from the laser piston, reflecting bunches of ions. Similarly to hole-boring RPA this mechanism predicts high energies and narrow spectra. Recently, CSA received a strong experimental support, the results of which are published in Ref. [56]. In this experiment, the irradiation of a gas jet target with a CO_2 laser has led to highly monochromatic proton emission (1% energy spread centered on 22 MeV), which have been attributed to CSA on the basis of related numerical studies. Despite the highly promising energy and spectra features, CSA seems to lack in energy conversion, which has been measured to be about 10^{-8}.

Further ion acceleration mechanisms have been proposed, based on under-dense laser plasma interaction and magnetic field generation [111, 112], provided also with experimental support [113, 114], but the argument goes beyond the present dissertation interests. Thus, concluding this brief overview it should be said that, despite the highly attractive ion features demonstrated by numerical simulations and the reaching of first experimental achievements, acceleration schemes alternative to TNSA are still extremely difficult to attain with the presently available laser technology, and TNSA remains the most naturally accessible mechanism. However, a better understanding and control of the latter, can also suggest new ways to overcome such difficulties and exploit the alternative schemes. This can represent a further motivation for the theoretical study of TNSA.

2.5 TNSA Open Problems

It is now useful to summarize the key open problems in the understanding and control of the TNSA process, as far as published experimental results are concerned. These issues are mainly referred to the optimization of ion cut-off energy and conversion efficiency, achievable through the complete comprehension of TNSA ions dependences on the ultra-intense laser pulse parameters, on the pre-pulse effects and on the target features. Besides that, also the spectral and space-time beam properties have to be controlled, in order to obtain a properly tailored particle beam, starting from the ordinary TNSA source.

First of all, a deeper knowledge on how the accelerated ion features depend on the main pulse parameters is required, so that the most convenient approaches to optimization are highlighted. In particular, the ion cut-off energy and conversion efficiency dependences on pulse intensity, energy, duration and focal spot are still not clear. This is mainly determined by the impossibility to vary such parameters independently, so that the specific scaling laws can be studied separately. Moreover, ultra-intense laser systems still do not guarantee highly reproducible results, and therefore exhaustive experimental parametric studies are very complex to achieve. Provided that the laser

technology is in continuous development, and that higher power regimes will be available in the next future, it would be extremely useful to master such scalings in order to design next experiments. Besides that, also the effect of different light polarization or incidence angle requires further studies, since the available data do not reveal at the moment any specific trend.

In the study of TNSA dependence on laser parameters another critical aspect to be clarified is the role of the pre-formed plasma, which is also related, and in some sense hides, the polarization and incidence angle influence. It is in fact generally accepted that the presence of a pre-plasma can enhance laser energy absorption by the target, and thus potentially affect the acceleration process. It has also been demonstrated that a long plasma scale-length in the front side of the foil prevents backward TNSA ions to be efficiently generated. Anyway, a lot of further progress is required so that pre-plasma effects on TNSA can be controlled and possibly exploited for optimization.

The pre-plasma can be created in controlled conditions by mild intensity probe pulses, but it can be also spontaneously present because of the laser pre-pulse. The understanding and control of pre-pulse effects has indeed turned out to be one of the key open issues of TNSA research. As seen in Sec. 2.3, apart from the pre-plasma creation, which affects laser-matter interaction and backward TNSA, the pre-pulse can also preheat the target and launch intense shock waves through it. These effects can spoil the foil rear surface, before the main ultra-intense laser peak interacts with the target, being detrimental for forward TNSA. For this reason pre-pulse cleaning is generally accepted as a convenient path to improve ion acceleration.

This leads to another important group of open issues, regarding the TNSA dependence on target features. The removal of laser pre-pulse has indeed demonstrated favorable, because it allows the use of sub-μm foils, which determine an increase in energy and conversion efficiency. Nonetheless the understanding of how TNSA effectiveness is improved by the reduction of target thickness is presently an open problem, since the physics which underlies this behavior is not completely understood. It is in fact believed that the confinement of hot electrons inside the target bulk is responsible for this improvement, but the knowledge on this dynamics is still superficial. Besides that, the techniques which determine contrast enhancement presume a substantial loss in pulse energy, in a trade-off that needs to be studied so that the use of ultra-thin targets in TNSA domain can reveal its convenience. The problem of understanding hot electron confinement dynamics is even more crucial whether MLTs are involved, and further knowledge is required also to explore the possibilities opened by reduced mass targets.

Finally, the aspects of proper ion beam tailoring still need a deeper study, so that the TNSA mechanism can be exploited for the potential applications of laser-based ion acceleration. In particular, structured target manufacturing has revealed as a convenient path to increase the level of monochromaticity accessible in the domain of TNSA, but the spectral requirements for applications are still far away from present achievements.

Of course such issues are extremely complex and surely the experimental picture needs to be extended with a large number of studies. Anyway, starting from the

available data, a lot of theoretical work can be made and some progress towards the solution of these open problems is possible. The theoretical study presented in this dissertation moves towards such a direction: after an introduction on the theoretical background related to the TNSA process, given in Chapter 3, the problem of finding a reliable model to reproduce the dependencies of the accelerated ion features on the laser and target parameters is addressed. For this reason, in Chapter 4 the present state-of-art in TNSA modeling is discussed and investigated by means of a quantitative comparison of different theoretical descriptions. This work is in fact useful to point out the most convenient approaches to the prediction of ion cut-off energy, but also the main limits of general TNSA theory, in the light of the open problems discussed here. Finally, in Chapter 5, an advancement in TNSA modeling, starting from a well-known theoretical approach, is proposed, towards the purpose of explaining and reproducing the ion cut-off energy dependence on different system parameters, as for example on laser pulse energy and target thickness.

3

TNSA Theoretical Background

In the present chapter the topic of TNSA theoretical modeling is discussed. A reliable description, capable to give quantitative predictions on the accelerated ion beam, starting from realistic laser-target configurations, is indeed extremely useful to draw guidelines for future experiments, given that a new generation of high-power lasers will be soon available. Moreover, a careful control of ion parameters, which is essential for each of the foreseen applications, can be achieved only with a solid theoretical knowledge of the physics involved in the particle acceleration.

As seen in Ch. 2 the experimental progress has outlined in these years a very complex picture, in which plenty of variable factors contribute, providing both advantages and drawbacks. Moreover, TNSA itself is intrinsically complex, due to the highly nonlinear physics involved in ultra-intense laser-matter interaction and relativistic electron transport, making the purpose of theoretical modeling really though to attain. Nonetheless, since the 2000s, different paths to find a reliable theoretical description have been pointed out and undertaken, in some cases with promising results. In the present chapter, the TNSA mechanism is described in detail, in order to underline the physics involved in the different phases of the process and to identify the possible approaches to theoretical modeling.

The first part of the chapter, namely Sec. 3.1, is dedicated to survey the physical system involved in TNSA, in order to enlighten its complexity, and the main problems that a reliable theoretical model has to deal with. Here several aspects of both ultra-intense laser and plasma physics are introduced, completing the experimental picture provided in Chapter 2 with the proper theoretical background. After that, in Sec. 3.2, the possible paths to TNSA modeling are described: first the Particle-In-Cell (PIC) method, the main numerical approach exploited for laser-driven ion acceleration, is presented, then the basic features of effective TNSA models are introduced, laying the foundations for the rest of the thesis, devoted to the study and extension of TNSA modeling.

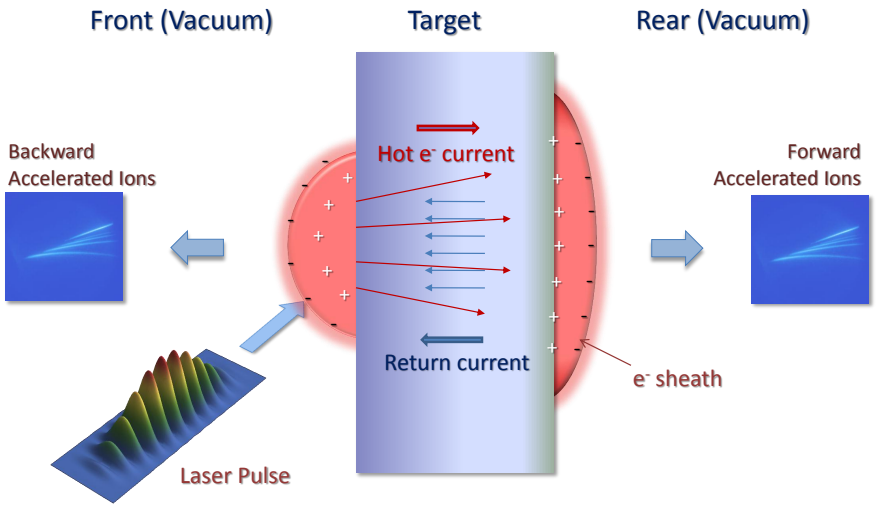

Figure 3.1: - Schematic representation of the TNSA mechanism with planar target.

3.1 The Physical System

As pointed out in the preamble of the present chapter, the TNSA scenario involves an extremely varied physical landscape, in which different fields of research are involved. Here the process is described in detail, to underline the main aspects that need to be considered in the formulation of a theory. TNSA, which is schematically represented in Fig. 3.1, has been first defined in Ref. [25], in order to provide an explanation for the accelerated protons detected in the experiments of Ref. [9], where by the way the idea of acceleration occurring in the "Debye Sheath" at the back side of the target had already been introduced. The few words used by Wilks et al. in the concluding paragraph of the paper summarize exhaustively the main features of a mechanism which have intensively been studied during the following 10 years:

> [...] the prepulse creates large plasma in front of a solid target. Once the main pulse hits the target, a cloud of energetic electrons (1–10 MeV in effective temperature) is generated, which extends past the ions on both the front and back of the target. Since the protons on the back are in a sharp, flat density gradient, they are accelerated quickly (in the first few mm off the target) to high energies in the forward direction (since the surface, locally, everywhere is flat). On the front, the outermost ions are in a sphere, in a long scale length plasma (due to prepulse) and therefore are accelerated to lower energies, and are spread out into 2π steradians.

The mechanism described by such few lines appears then as a collective acceleration process, triggered by thermal energy acquired by electron as a result of laser-matter interaction. To understand why TNSA has immediately attracted much attention as the plausible responsible for the multi-MeV ion beams obtained in the pioneering experiments it is useful to estimate the order of magnitude of the accelerating fields resulting from such a collective dynamics [25, 58]. To this purpose, a one-dimensional, step-like plasma profile composed by cold ions (of charge-to-mass ratio equal to Z/m_i) and hot electronic population at temperature T_h (of MeV order) is considered. Due to the thermal pressure the electrons tend to spontaneously expand into vacuum, while the ion population, because of its larger inertia, collectively reacts to electron expansion over ps timescales, that is to say $t \gg \omega_\mathrm{pi}^{-1}$, where $\omega_\mathrm{pi} = (4\pi n_\mathrm{i} Z e^2/m_\mathrm{i})^{1/2}$ is the ionic plasma frequency (where n_i represents the density of the ion plasma component). Such a reaction means that the charge separation is compensated and the plasma expands preserving the quasi-neutrality condition, that is $Zn_\mathrm{i} = n_\mathrm{h}$ (where n_h is the hot electron density). If the temperature is kept constant during the quasi-neutral plasma expansion, the dynamics can be easily solved by means of fluid equations [3, 115]. The self-consistent field, driving the ion population expansion, is given by:

$$\mathcal{E}_\mathrm{ss} = \frac{k_\mathrm{B} T_\mathrm{h}}{e c_\mathrm{s} t}\,, \tag{3.1}$$

in which k_B is the Boltzmann constant and $c_\mathrm{s} = (Z k_\mathrm{B} T_\mathrm{h}/m_\mathrm{i})^{1/2}$ is the ion-acoustic velocity. This means that the electric field accelerating the ions is proportional to T_h and inversely proportional to the local plasma scale-length $L_\mathrm{s} = c_\mathrm{s} t$. Now, if the expansion is described considering faster timescales, quasi-neutrality is locally broken at the boundary of the plasma fluid, where TNSA sheath is formed. Here the field can be estimated by:

$$\mathcal{E}_\mathrm{sh} = \frac{k_\mathrm{B} T_\mathrm{h}}{e \lambda_\mathrm{Dh}}\,, \tag{3.2}$$

where the hot electron Debye length, given by

$$\lambda_\mathrm{Dh} = \sqrt{\frac{k_\mathrm{B} T_\mathrm{h}}{4\pi n_\mathrm{h} e^2}}\,, \tag{3.3}$$

has substituted the plasma density scale length. The $\mathcal{E}_\mathrm{sh}$ provided by Eq. (3.2) backholds the electron cloud expanding with temperature T_h and accelerates the ions sitting on the boundary of the plasma. If, for example, a temperature of 500 keV and a density of $10^{21}\,\mathrm{cm}^{-3}$ are chosen, Eq. (3.2) gives a field of $3\,\mathrm{MV}/\mu\mathrm{m}$, capable to accelerate protons to MeV energies within a micro-metric distance. Moreover, it should be underlined that this field is directed perpendicularly from the target surfaces, determining ion bunch direction and low divergence.

A part from such a simple estimate, the words used by Wilks et al. to describe TNSA already suggest how complex and articulated the phenomenon is. For a schematic treatment TNSA can be organized in three main phases:

- the ultra-intense laser-matter interaction, influenced by the pre-pulse action, during which matter is ionized and part of the electrons is heated up to relativistic energies,
- the expansion of hot electrons through and outside the target, with the establishment of huge currents in the material and intense electro-static fields at the boundaries,
- the ion acceleration dynamics following the field rise, occurring at a slower timescale with respect to the electrons and influenced by the steepness of the plasma density gradient.

Such a division is indeed a mere conceptual partition, since the three phases are two-way correlated, without neat separations along the process time-line. For example the hot electron dynamics can in turn affect laser-matter interaction, or else, if pulse duration is large enough, ion acceleration can take place already during laser illumination. Nonetheless, for convenience reasons, this organization is exploited in the next pages to provide a complete overview of the considered physical system.

3.1.1 Laser-Matter Interaction

Ultra-intense laser-matter interaction is an extremely tough topic, which has been explored systematically for just twenty years until now, since CPA invention. Moreover, during these years, the laser intensities achievable have grown of several orders of magnitude, unlocking new regimes which were not attainable at the beginning. The experimental study is complicated by the ultra-fast timescales involved, that make diagnostic of interaction features extremely challenging, while the relatively low stability of the high power laser systems hampers the reproducibility of the results and imposes large statistics of data. Here the main physical aspects of such a subject are described, focusing on the purposes of the dissertation, and thus on the relevant interaction features in the TNSA framework. For more complete surveys, recent books and reviews deal with the topic providing precise and exhaustive descriptions [27, 28, 116].

3.1.1.1 Ionization of Matter

The first step in order to understand what happens, when an intense laser pulse impinges on a solid target, concerns ionization of matter. The relation between the electric field magnitude[1] E of an electro-magnetic wave and its intensity is the following:

$$I\left[\frac{\mathrm{W}}{\mathrm{cm}^2}\right] = c\frac{E^2}{8\pi} \simeq 1.33 \times 10^{-3}\left(E\left[\frac{\mathrm{V}}{\mathrm{cm}}\right]\right)^2 \tag{3.4}$$

[1] Within the limits of present subsection, in order to comply with usual literature notation, the electric field magnitude is indicated as E, while in the rest of the text the same character is used for the energy.

where c is the speed of light. Eq. 3.4 indicates that, already at intensities of $10^{16}\,\mathrm{W/cm^2}$, the electric field carried by the laser pulse is comparable with the atomic binding field of electrons, which is of the order of $10^9\,\mathrm{V/m}$. Since in the framework of TNSA the intensity range of interest goes from about 10^{18} up to more than $10^{21}\,\mathrm{W/cm^2}$, this means that, before the peak intensity is reached, matter is strongly ionized and a plasma is created. Actually, ionization physics is more subtle and, thanks to the nonlinear processes occurring in the high-intensity regime, there is no need to apply a field comparable to the atomic one in order to ionize the material. In fact, the large photon density of the electro-magnetic wave makes it possible for a bound electron to absorb more than one photon at a time and to gain enough energy to escape the atomic potential well [117]. This mechanism, called Multi-Photon ionization, is already active at intensities of $10^{10}\,\mathrm{W/cm^2}$. Moreover, the ponderomotive potential of the laser can distort the Coulomb potential well so that the electrons are likely to escape the latter via tunnel effect or, if the field is strong enough, even spontaneously. The intensity required for a spontaneous ionization can be easily evaluated by a classical model, obtaining values of the order of $10^{14}\,\mathrm{W/cm^2}$ for the hydrogen, while estimates for the tunnel effect require quantum mechanics calculations [118]. This means that the pre-pulse is already intense enough to ionize the matter before the arrival of the laser peak, so that this one always interacts with a plasma.

3.1.1.2 Relativistic Regime

When the oscillating optical field interacts with the plasma the electrons react over faster timescales with respect to the ions, because of the higher charge-to-mass ratio. The relevant scale for electron collective reaction is of the order of fs, while ions require a time of the order of ps. For this reason, since in the TNSA process sub-ps laser pulses are usually exploited, in the study of such an interaction regime the ions can be considered at rest, while electrons are accelerated by the laser field.

In a classical treatment the free electron subject to an incident plane wave, which can be represented by the vector potential

$$\mathbf{A}(\mathbf{r},t) = \mathcal{R}\mathrm{e}\left\{\mathbf{A}_0 \mathrm{e}^{i\psi}\right\}, \tag{3.5}$$

oscillates along the equilibrium position due to Lorentz force, reaching a quiver velocity:

$$v_\mathrm{q} = \frac{eA_0}{m_\mathrm{e}c} = \frac{eE_0}{m_\mathrm{e}\omega}, \tag{3.6}$$

here indicated both as a function of the amplitude of potential A_0 and electric field E_0. m_e is the electron mass and ω the radiation frequency. The definition of the dimensionless laser amplitude

$$a_0 \equiv \frac{eA_0}{m_\mathrm{e}c^2} = \frac{v_\mathrm{q}}{c}, \tag{3.7}$$

provides then a quantity which explicits the incidence of relativistic effects in the electron dynamics ($a_0 = 1$ the quiver velocity is of the order of c. Of course in this case the expression (3.6) is not correct anymore and a relativistic treatment is required).

Now, the peak intensity I_0 of the plane wave defined by Eq. 3.5 is given by the Poynting vector $\mathbf{S}$ magnitude:

$$I_0 = |\mathbf{S}| = \frac{\omega k}{8\pi} A_0^2 \times \begin{cases} (1 - \cos 2\psi) & \text{LP} \\ 2 & \text{CP} \end{cases}, \tag{3.8}$$

where k is the wave vector amplitude, "LP" stands for linear polarization and "CP" for circular polarization. If the intensity is averaged on a laser cycle, Eq. 3.8 leads to a relation among mean laser irradiance and adimensional amplitude:

$$I\lambda^2 = 1.37 \times 10^{18}\, a_0^2 \left[\frac{\mathrm{W}\mu\mathrm{m}^2}{\mathrm{cm}^2}\right] \times \begin{cases} 1 & \text{LP} \\ 2 & \text{CP} \end{cases}. \tag{3.9}$$

This means that, at the intensities of interest in TNSA, the electric field is strong enough to accelerate electrons to relativistic velocities in a single or few laser cycles, suggesting that the relativistic interaction regime is of central relevance for this topic.

The free electron dynamics under the action of a plane electro-magnetic wave already shows new interesting features of the relativistic framework (see for example Ref. [27]). The resulting motion is not just oscillating along the transverse field, but it acquires a drift velocity v_d, drawing an helicoidal trajectory. The drift depends on the dimensionless amplitude according to:

$$v_\mathrm{d} = \frac{a_0^2}{a_0^2 + 2}\, c\,. \tag{3.10}$$

Eq. (3.10) shows that the motion is essentially transversal for low wave amplitudes, while the drift reaches relativistic velocities for $a_0 \sim 1$. In the reference frame moving at the drift velocity the particle follows a characteristic 8-shaped figure in which, for small a_0, the motion degenerates to a transversal oscillation, while for large a_0 a limit trajectory is approached. If the plane wave is shaped by an envelope, in order to approximate a laser pulse, a similar behavior is recovered: as shown in Fig. 3.2, the trajectory is initially oscillating, when the amplitude is still small, and acquires a longitudinal part as the field grows. Therefore, already the solution of a simple problem as that of a free electron in a plane wave, gives a feeling of how electrons can be accelerated under the effect of an intense laser pulse. Another interesting feature is the fact that, after the pulse action, the particle is at rest, even after being accelerated at relativistic speeds, so that no energy has been transferred. This however happens only in vacuum, while in a plasma the action of self-consistent fields and collisions makes energy absorption possible.

3.1.1.3 Wave Interaction with Plasma

The interaction of an electro-magnetic wave with a plasma can be studied by coupling Maxwell equations to the statistical equations governing the motion of plasma particles, which are different according to the level of detail required. A first, useful

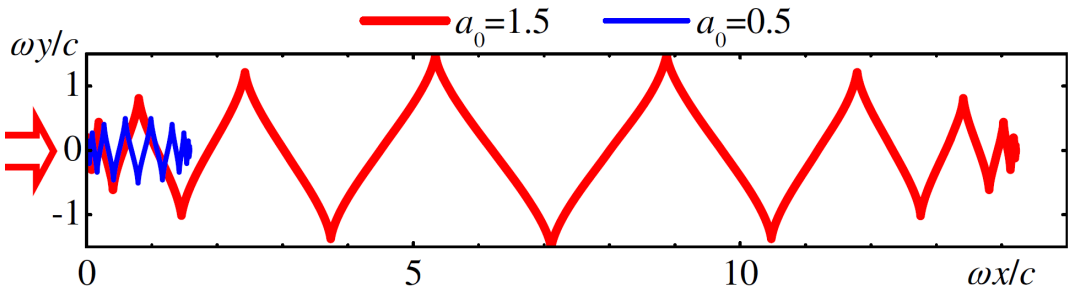

Figure 3.2: - Example trajectories of an electron in vacuum experiencing two different optical fields of ultra-short, linearly polarized, plane electromagnetic waves. The laser is incident from the left and the amplitudes are $a0 = 0.5$ (blue line) and 1.5 (red line) (Figure from Ref. [23]).

approximation, already containing some crucial features of the realistic interaction, is that of cold, fluid and homogeneous plasma. In such a description, the non-relativistic general dispersion relation, which can be retrieved with a perturbative approach, is given by:

$$\epsilon \left(\frac{k^2 c^2}{\omega^2} - \epsilon \right) = 0 \,. \tag{3.11}$$

ϵ is the scalar coefficient of the dielectric tensor, which, in the considered system, is proportional to the identity and provided by the following expression:

$$\epsilon = 1 - \frac{4\pi}{\omega^2} \sum_j \frac{q_j^2 n_{0j}}{m_j} \,, \tag{3.12}$$

in which the subscript j indexes the plasma populations, characterized by charge q_j, density n_{0j} and mass m_j. If the plasma frequency of the j-th component is defined to be:

$$\omega_{\mathrm{p}j} = \sqrt{\frac{4\pi q_j^2 n_{0j}}{m_j}} \,, \tag{3.13}$$

then the general plasma frequency ω_{p}, that is the sum of the single $\omega_{\mathrm{p}j}$'s, can be approximated by the electron frequency ω_{pe}, dominating the others because of the highest charge-to-mass ratio. The dielectric coefficient can thus be approximated by:

$$\epsilon = \left(1 - \frac{\omega_{\mathrm{p}}^2}{\omega^2} \right) \simeq \left(1 - \frac{\omega_{\mathrm{pe}}^2}{\omega^2} \right) \,. \tag{3.14}$$

The dispersion relation (3.11) contains the solutions for the electro-static plasma wave ($\omega = \omega_{\mathrm{pe}}$) and for the transversal electro-magnetic modes that propagate through the plasma:

$$\omega^2 = \omega_{\mathrm{pe}}^2 + k^2 c^2 \,. \tag{3.15}$$

The latter shows that ω_{pe} sets a lower limit to the frequency of an electro-magnetic wave propagating across the plasma. Therefore, a laser pulse of frequency ω can penetrate the plasma until the density reaches a critical value:

$$n_{\mathrm{cr}} = \frac{m_{\mathrm{e}}\omega^2}{4\pi e^2}\,. \tag{3.16}$$

Above this value, named critical density, Eq. (3.15) is solved for an imaginary k and the wave is dumped exponentially over the skin depth $d_{\mathrm{s}} \simeq c/\omega_{\mathrm{pe}}$. This means that laser-plasma interaction takes place either in the "under-dense" region $n_{\mathrm{e}} < n_{\mathrm{cr}}$ or in the region where electron density is close to the critical value $n_{\mathrm{e}} \simeq n_{\mathrm{cr}}$.

Since a relativistic treatment is required, it is necessary to write the dispersion relation for the transversal electro-magnetic modes according to special relativity:

$$\omega^2 = \frac{\omega_{\mathrm{pe}}^2}{\gamma} + k^2c^2\,, \tag{3.17}$$

where γ is the relativistic factor, given by:

$$\gamma = \sqrt{1 + p^2 + a^2}\,, \tag{3.18}$$

in which $p = |\mathbf{p}|/m_{\mathrm{e}}c$ is the normalized magnitude of the electron fluid momentum and $a = e|\mathbf{A}|/m_{\mathrm{e}}c^2$ is the adimensional amplitude of the electro-magnetic vector potential, which reduces to a_0 (Eq. (3.7)) when the peak amplitude A_0 is considered. The definition of critical density is thus modified to obtain:

$$n_{\mathrm{cr}} = \gamma\frac{m_{\mathrm{e}}\omega^2}{4\pi e^2} = \gamma\frac{1.1\times10^{21}}{\lambda^2[\mu\mathrm{m}]}\left[\mathrm{cm}^{-3}\right]\,. \tag{3.19}$$

Eq. (3.19) shows that, for $\gamma > 1$, the wave can propagate in plasma regions which are classically over-critical, in a phenomenon called *relativistic induced transparency*. Starting from these basic notions, it should be underlined that penetration of electro-magnetic waves in a plasma remains a nontrivial physical problem, given that the density of the plasma itself depends self-consistently on the nonlinear effects of radiation pressure. For this reason, in order to understand more in depth the interaction regime in TNSA framework, such nonlinearity has to be considered.

3.1.1.4 Ponderomotive Force

The ponderomotive force appears as a consequence of the nonlinear interaction of electro-magnetic waves with plasma, playing a crucial role in the framework of super-intense laser-matter interaction. A simple form of the ponderomotive force can be already retrieved by means of a perturbative, non-relativistic study of a single charged particle under the effect of a quasi-monochromatic pulse. The latter is modulated by an envelope, slowly dependent on the spatial coordinates according to:

$$\mathbf{E}\,(\mathbf{x},t) = \mathbf{E_0}\,(\mathbf{x})\cos(\psi),\tag{3.20}$$

where $\psi = (\mathbf{x}\cdot\mathbf{k} - \omega t)$ is the field phase. The particle motion is then determined by the Lorentz force:

$$\mathbf{F} = m\ddot{\mathbf{x}} = q\left(\mathbf{E} + \frac{\dot{\mathbf{x}}}{c}\wedge\mathbf{B}\right), \tag{3.21}$$

which is in general analytically unsolvable. Adopting a perturbative approach, the field is expanded around the initial position of the particle $\mathbf{x} = \mathbf{x}_\mathrm{i}$:

$$\mathbf{E}(\mathbf{x}) = \mathbf{E}(\mathbf{x}_\mathrm{i}) + (\delta\mathbf{x}\cdot\nabla)\,\mathbf{E}(\mathbf{x}_\mathrm{i}) + \mathcal{O}\left[\delta\mathbf{x}^2\right], \tag{3.22}$$

In which $\delta\mathbf{x} = \mathbf{x} - \mathbf{x}_\mathrm{i}$. Then the "zero-th" order dynamics is represented by the classical quivering motion, governed by:

$$\ddot{\mathbf{x}}^{(0)} = \frac{q}{m}\left[\mathbf{E}(\mathbf{x}_\mathrm{i})\right]. \tag{3.23}$$

Eq. (3.23) is thus solved by the oscillatory motion:

$$\begin{cases}\mathbf{x}^{(0)} = \mathbf{x}_\mathrm{i} - \frac{\mathbf{v}_{\mathrm{q}0}}{\omega}\cos(\psi)\\ \dot{\mathbf{x}}^{(0)} = -\mathbf{v}_{\mathrm{q}0}\sin(\psi)\end{cases}, \tag{3.24}$$

in which $\mathbf{v}_{\mathrm{q}0} = q\mathbf{E}_0(\mathbf{x}_\mathrm{i})/m\omega$. If the "zero-th" order solution is subtracted from Eq. (3.21) and the result is linearized, the following relation is obtained:

$$\ddot{\mathbf{x}}^{(1)} = \frac{q}{m}\left[\left(\delta\mathbf{x}^{(0)}\cdot\nabla\right)\mathbf{E}(\mathbf{x}_\mathrm{i}) + \frac{\dot{\mathbf{x}}^{(0)}}{c}\wedge\mathbf{B}^{(0)}\right]. \tag{3.25}$$

The right-hand side of Eq. (3.25) contains the coupling of charge oscillation with the B-field, which is relevant at this order of perturbation. Faraday's law,

$$-\frac{1}{c}\frac{\partial\mathbf{B}}{\partial t} = \nabla\wedge\mathbf{E}, \tag{3.26}$$

can be used to explicit $\mathbf{B}$ in term of the electric field:

$$\mathbf{B}^{(0)} = \frac{c}{\omega}(\nabla\wedge\mathbf{E}_0)\sin(\psi) + \frac{c\mathbf{k}}{\omega}\wedge\mathbf{E}_0\cos(\psi). \tag{3.27}$$

Now, if Eqs. (3.24) and (3.27) are substituted into Eq. (3.25) the form of the latter becomes:

$$\ddot{\mathbf{x}}^{(1)} = -\left(\frac{q}{m\omega}\right)^2\left[\mathbf{A}\cos^2(\psi) + \mathbf{B}\sin^2(\psi) + \mathbf{C}\sin(2\psi)\right], \tag{3.28}$$

where $\mathbf{A}$, $\mathbf{B}$ and $\mathbf{C}$ are vectors which combine ∇ and $\mathbf{E}_0(\mathbf{x}_\mathrm{i})$. The cycle average of Eq. (3.28) shows that a secular effect is present:

$$\langle\ddot{\mathbf{x}}^{(1)}\rangle = -\frac{1}{2}\left(\frac{q}{m\omega}\right)^2\left[(\mathbf{E}_0(\mathbf{x}_\mathrm{i})\cdot\nabla)\,\mathbf{E}_0(\mathbf{x}_\mathrm{i}) + \mathbf{E}_0(\mathbf{x}_\mathrm{i})\wedge(\nabla\wedge\mathbf{E}_0(\mathbf{x}_\mathrm{i}))\right], \tag{3.29}$$

an expression that can be simplified by vectorial identities, to get:

$$\langle\ddot{\mathbf{x}}^{(1)}\rangle = -\left(\frac{q}{2m\omega}\right)^2\nabla\left|\mathbf{E}_0(\mathbf{x}_\mathrm{i})\right|^2. \tag{3.30}$$

Such an acceleration term is the effect of the so-called ponderomotive force, given by:

$$\mathbf{f}_{\mathrm{p}}\left(\mathbf{x}\right) = -\nabla U_{\mathrm{p}}\left(\mathbf{x}\right) = -\frac{q^2}{4m\omega^2}\nabla\left|\mathbf{E}_0\left(\mathbf{x}\right)\right|^2 , \tag{3.31}$$

where the $\mathbf{x}_{\mathrm{i}}$ has been substituted by the generic position vector of the particle and the ponderomotive potential U_{p} has been defined. This potential is proportional to the radiation pressure term of Maxwell electro-magnetic stress tensor, and the force is due to the non-homogeneity of the latter [119]. A rigorous relativistic derivation of the ponderomotive force experienced by a particle in an electro-magnetic field can be found in Ref. [28], however, such a heuristic derivation makes some important features of this effect already explicit:

- it is proportional to m^{-1}, so that it acts way more effectively on the electrons,
- it pushes particles towards lower E-field regions independently from the relative charge sign,
- it is a secular effect resulting from cycle averaging,
- it follows from the coupling of the charge oscillation along the E-field with the magnetic field, the so-called "$J \times B$ force".

To obtain the relativistic collective form of the ponderomotive force on a plasma it is necessary to consider a fluid cold plasma model [116, 120]. The equation for the j-th plasma component fluid momentum is:

$$\left(\frac{\partial}{\partial t} + \mathbf{u}_j \cdot \nabla\right)\mathbf{p}_j = q_j\left[-\frac{1}{c}\frac{\partial \mathbf{A}}{\partial t} - \nabla\phi + \frac{\mathbf{u}_j}{c} \wedge \left(\nabla \wedge \mathbf{A}\right)\right] , \tag{3.32}$$

where the radiation is represented by the electro-magnetic potentials $\mathbf{A}$ and ϕ. A choice of dimensionless variable is now convenient, so:

$$\frac{\mathbf{u}_j}{c} \to \mathbf{u}, \qquad \frac{\mathbf{p}_j}{m_j c} \to \mathbf{p}, \qquad \frac{q_j \mathbf{A}}{m_j c^2} \to \mathbf{a}, \qquad \frac{q_j \phi}{m_j c^2} \to \phi\,. \tag{3.33}$$

Now, vector calculus and manipulations lead to:

$$\frac{1}{c}\frac{\partial}{\partial t}\left(\mathbf{p} - \mathbf{a}\right) - \mathbf{u} \wedge \left[\nabla \wedge \left(\mathbf{p} - \mathbf{a}\right)\right] = \nabla\phi - \nabla(\gamma - 1)\,, \tag{3.34}$$

in which a $-(\nabla 1)$ has been formally added to retrieve the non-relativistic ponderomotive force as a limit of this derivation. If the fluid is initially at rest and no electro-magnetic radiation is propagating, then the transversal component of Eq. (3.34) gives $\mathbf{p}_\perp = \mathbf{a}$, and the longitudinal component reads:

$$\frac{1}{c}\frac{\partial}{\partial t}\mathbf{p}_\parallel = \nabla\phi - \nabla(\gamma - 1), \tag{3.35}$$

where $\gamma = \sqrt{1 + |\mathbf{p}_\parallel|^2 + |\mathbf{a}|^2} \simeq \sqrt{1 + |\mathbf{a}|^2}$. The relativistic plasma ponderomotive effect is thus given by the cycle average of last term:

$$f_\mathrm{p} = -m_j c^2 \nabla \left(\sqrt{1 + \langle \mathbf{a}^2 \rangle} - 1 \right) , \tag{3.36}$$

where f_p is now a density force acting on a fluid element. Eq. (3.35) makes it evident that the ponderomotive term $\nabla(\gamma - 1)$ acts as a pressure field, where the potential density $u_\mathrm{p} = m_j c^2 (\gamma - 1)$ plays the role of an effective temperature. If $|\mathbf{p}_\parallel|^2$ is neglected in γ expression, and the only electronic fluid is considered, then the non-relativistic ponderomotive potential density is retrieved:

$$u_\mathrm{p} = \frac{e^2}{2 m_\mathrm{e} \omega^2} \langle \mathbf{E}_0^2 \rangle . \tag{3.37}$$

Which can be brought back to single particle form of Eq. (3.31). This demonstrates that the observations regarding the single-particle derivation are still valid in the laser-plasma framework. The interpretation of ponderomotive effect, as a force arising from radiation pressure of a pulse explains how the laser profile can affect the density of a plasma, pushing and piling up the electrons according to its intensity profile, as required by RPA acceleration schemes. If a plane wave is considered, the pressure is longitudinally directed, and the profile of the plasma can steepen up, hampering wave propagation. Otherwise, taking into account a limited transverse profile, three-dimensional effects are present as well, and electrons are pushed in radial direction, favoring plasma transparency.

This underlines how complex the study of wave propagation through a plasma is, well beyond the simple definition of n_cr. Given this, in the relevant conditions for TNSA, laser interaction with over-critical plasmas is still the key regime of interaction, while the effect of a possible under-dense plasma corona has a minor weight on TNSA acceleration. For such a reason, in the rest of this section, the attention is focused on over-dense plasmas, for a survey on laser interaction with under-dense plasmas the reader can rely for example on Ref. [2] and references therein.

3.1.1.5 Hot Electrons

The profound interest about intense laser interaction with over-dense plasmas, and the key of the multiple phenomenons related to it, lies in the fact that the energy carried by the electro-magnetic pulse can be efficiently absorbed at the critical density surface. Because of the fast timescales involved in the process, this absorbed energy is distributed to the plasma electrons, which gain hundreds of keVs, up to several MeVs of kinetic energy. Actually, the electronic population acquires a particular energetic distribution which can be approximated by a two-temperature Maxwellian, as shown by the numerical results in Fig. 3.3. In this case, a fraction of all the electrons, typically less than the 1%, is heated up to extremely high (keV-MeV) temperatures, while the rest of the plasma maintains a relatively lower mean energy. These super-thermal electrons are usually referred to as *hot electrons* or *fast electrons*.

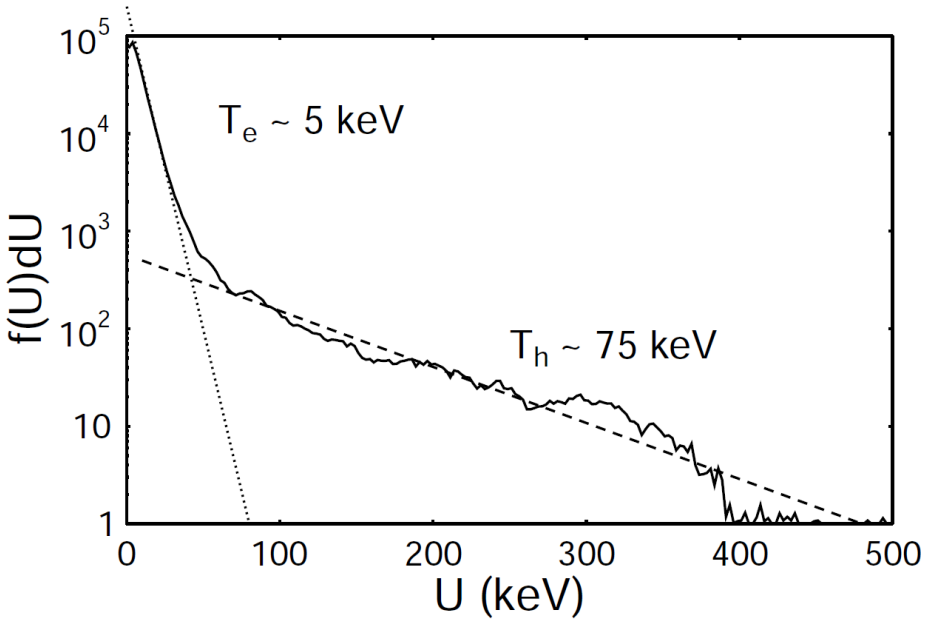

Figure 3.3: - Typical electron energy spectra obtained by numerical simulation. The distribution is approximated by the superimposition of two Maxwellian curves at different temperatures (Figure reprinted from Ref. [27]).

The appearance of an effective temperature in Eq. (3.35) already suggests that one of the consequences of laser interaction with plasma is electron heating. However, the present knowledge of ultra-intense laser-absorption mechanisms, which can determine this kind of electron heating, is still limited by the complexity of the physics involved. While it is not completely understood how the laser energy is absorbed and distributed among the hot electrons, it is certain that this energy repartition results from several different processes, the relative importance of which strongly depends on the laser and plasma properties, as the intensity regime or plasma density scale-length. Moreover, in most of the cases an interplay of these mechanisms takes place, determining a complex behavior which is difficult to read on the basis of simple theoretical assumptions. In the following, the most popular absorption mechanisms are qualitatively introduced, with a particular attention on their consequences on the hot electron population.

3.1.1.6 Collisions

Once the plasma electrons are accelerated by the laser electro-magnetic field, they can undergo Coulomb collisions with other electrons or ions, so that the initial ordered motion acquires stochastic features and part of the radiation energy is transferred to the plasma. While electron-electron collisions contribute only to the thermalization of the distribution function, and ion-ion collisions occur on longer timescales than that of interest, the absorbed energy is almost exclusively due to electron-ion collisions. The

corresponding absorption coefficient can be evaluated from the emissions caused by the electron collisional decelerations by means of Kirchhoff's law [28], which, by the way, explains why such an absorption process is commonly named *Inverse Bremsstrahlung*.

Collisional effects are usually introduced in the plasma description by adding a damping term, proportional to the particle velocity, within Lorentz equation of motion:

$$m_e \frac{\partial \mathbf{v}}{\partial t} = -e\left(\mathbf{E} + \frac{\mathbf{v}}{c} \wedge \mathbf{B}\right) - m_e \nu_{ei} \mathbf{v}\,, \tag{3.38}$$

in which electron-ion collisional frequency ν_{ei} is obtained via classical scattering theory. If the thermal velocity of electrons in plasma is given by $v_{te} = \omega_{pe}\lambda_{De}$, provided that λ_{De} is the electron Debye length (Eq. 3.3). ν_{ei} can be estimated by (see Ref. [121]):

$$\nu_{ei} = \frac{\sqrt{32\pi}}{3} \frac{n_e Z e^4}{m_e^2 v_{te}^3} \ln\Lambda \simeq 2.91 \times 10^{-6} Z n_e \left(T_e\,[\mathrm{eV}]\right)^{-3/2} \ln\Lambda\,. \tag{3.39}$$

Here Z is the degree of ionization and $\ln\Lambda$ is the Coulomb logarithm, which takes into account the range of possible impact parameters:

$$\ln\Lambda = \ln\frac{b_{max}}{b_{min}} = \ln\left(\lambda_{De}\frac{k_B T_e}{Ze^2}\right)\,. \tag{3.40}$$

Eq. (3.39) shows that the importance of collisions decreases as the electron temperature

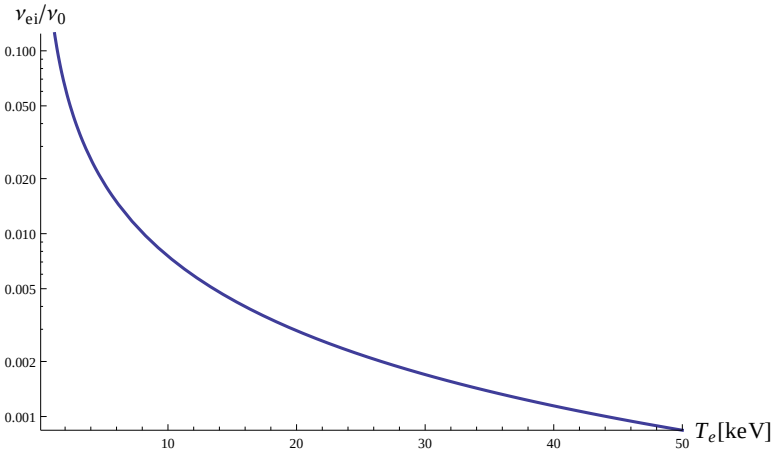

Figure 3.4: - Electron-ion collisional frequency expressed in laser frequency units vs electron temperature. ν_{ei} is evaluated by means of Eq. (3.39) for a solid density ($n_e = 10^{23}\,\mathrm{cm}^{-3}$) plasma with $Z = 1$ and laser wavelength $0.8\,\mu$m.

T_e rises. To give a feeling of the weight of collisional effects in the regime of interest, in Fig. 3.4 ν_{ei} is depicted as a function of the temperature for a solid density plasma. The value decreases below the 1 % of the laser frequency ($\nu_0 = c/\lambda$ for Ti-Sapphire wavelength) at $T_e = 10\,\mathrm{keV}$, which is easily reached during interaction of intense lasers with solids.

The energy absorbed by a plasma, as a result of electron-ion collisions, can be then evaluated by means of Helmoltz equations of wave propagation but, as it is clear from Eq. (3.39), the collisional damping depends self-consistently on the heating itself. A study of the coupling of classical Spitzer heat flow equation with collisional absorption by a sharp density profile is provided in Ref. [122], leading to a plasma surface temperature scaling as:

$$T_{\mathrm{e}} \sim (n_{\mathrm{e}} Z)^{1/12} \, I_{\mathrm{a}}^{1/3} t^{1/6} \,, \tag{3.41}$$

in which I_{a} is the absorbed intensity and t the time coordinate. This behavior justifies the fact that collisional absorption is ruled out before the laser ultra-intense peak reaches the plasma. Moreover, the collision frequency ν_{ei} is also affected by the fact that for high irradiances the electron quiver velocity becomes comparable to the thermal velocity v_{te}.

As a result, TNSA and ultra-intense laser-matter interaction can in general be treated by considering collision-less plasma models, so that laser absorption and hot electron generation have to be mainly attributed to collision-less mechanisms.

3.1.1.7 Collision-less Absorption

The super-thermal component which emerges in the energy distribution of plasma electrons as a result of ultra-intense laser irradiation (see Fig. 3.3) should be interpreted as a hallmark of some collective heating mechanism, alternative to collisional ones, since the latter should in principle broaden the spectra increasing the temperature of the whole electron population. This also supports the belief that collision-less absorption, represented by different mechanisms, should be the main responsible for the generation of the hot electrons.

The most studied collision-less absorption mechanism is the so-called *Resonance Absorption* [123, 124], known and investigated since the 1970's as the cause of detrimental target pre-heating in Inertial Confinement Fusion research. The conditions required to trigger resonant absorption are a longitudinal component of the laser optical field (which, for example, is present in a linearly p-polarized radiation at oblique incidence) and a mild density gradient of the plasma, so that $\mathbf{E} \cdot \nabla n_{\mathrm{e}} \neq 0$. In such a configuration the electro-magnetic wave should be reflected at $n_{\mathrm{e}} = n_{\mathrm{cr}} \cos^2 \theta$, where θ is the incidence angle, but it can be shown that the tunneling of the optical field to the critical surface is allowed. At $n_{\mathrm{e}} = n_{\mathrm{cr}}$ the longitudinal component of the electric field oscillates at the plasma frequency and couples with the electrons exciting a plasma wave. The latter grows resonantly over some laser periods, to be damped, with consequent heating of the plasma, by collisions, Landau damping or, at higher intensities, by wave-breaking. Numerical simulations of laser-matter interaction demonstrated that such resonant absorption leads to a Maxwellian "tail" of hot electrons, the temperature of which grows roughly as $(I\lambda^2)^{1/3}$ [123, 124]. The scheme has been shown to be efficient for long pulses (> ps) and large plasma scale-lengths (> μm), but investigations have confirmed its relevance also for sub-ps pulses and steeper plasma gradients. However, at the TNSA laser intensities, that is above 10^{18} W/cm^2, resonant absorption provides

a minor contribution to electron heating.

In a sharp-edged profile, the longitudinal oscillations of electrons go across a steep density gradient, which hampers the growth and the support of the plasma wave, so that resonant electrons are "not so resonant" anymore. Using these words F. Brunel proposed an alternative collision-less process, characterized by a step-like plasma profile and a strong longitudinal field, see Ref. [125]. In this configuration, the electric field of the incident laser wave can drag electrons from the plasma surface directly into the vacuum, to re-inject them through the plasma boundary after half a laser cycle. Once such electrons, carrying an energy proportional to the square of quiver velocity, overcome the skin depth c/ω_{pe}, they do not experience the laser field anymore, and transport their energy inside the plasma. This results in a pulsed generation of fast electron bunches directed into the target at the same frequency of the laser wave, in a process called *Brunel Mechanism*. To predict the effect of such a process Brunel proposed a one-dimensional "capacitor model", in which the target is represented by a perfect conductor, localized in the $x > 0$ region, while in the vacuum ($x < 0$) an oscillating electric field proportional to laser amplitude can extract electrons from the target and re-inject them back. According to this simple description the temperature (mean kinetic energy) of the accelerated electrons can be estimated by:

$$T_{\mathrm{h}}^{B} = 2m_{\mathrm{e}}v_{\mathrm{q}}^{2}\sin^{2}\theta \simeq 3.7\times10^{-16}\left(I\lambda^{2}\left[\frac{\mathrm{W}\mu\mathrm{m}^{2}}{\mathrm{cm}^{2}}\right]\right), \tag{3.42}$$

evaluated in [keV]. It is easy to see that, for the considered intensity regime, such simple model predicts temperatures of hundreds of keV, up to the MeV scale, as found experimentally. The capacitor model is not self-consistent by the way, since a zero field in the target region would require a surface charge density which is artificial. In Ref. [126], the Brunel mechanism features are studied modeling a cold plasma fluid under the action of an oscillating electric field, providing a self-consistent description.

If the laser impinges normally on the plasma surface (or if it is linearly S-polarized), no longitudinal component of the electric field is available and Brunel mechanism is not activated. However, as introduced before, in intense laser-matter interaction the nonlinear effect which results from the coupling of the wave B-component with the current of electrons oscillating along the transverse E-field, namely the "$J\times B$ force", acquires importance. This coupling provides a longitudinal force which can transfer the radiation energy to the plasma electrons similarly to electric field force in Brunel mechanism, in a process named $J\times B$ *heating* [127]. If a plane, elliptically polarized wave of eccentricity $0<\epsilon<1$, propagating along the x direction is considered, the vector potential may be indicated as:

$$\mathbf{A} = \frac{A(x)}{\sqrt{1+\epsilon^{2}}}\left(\hat{\mathbf{y}}\cos\omega t + \epsilon\hat{\mathbf{z}}\sin\omega t\right), \tag{3.43}$$

where $\hat{\mathbf{y}}$ and $\hat{\mathbf{z}}$ are the transverse direction unit vectors. Then the longitudinal force resulting from the $J\times B$ coupling can be written as:

$$e\frac{\mathbf{v}}{c}\wedge\mathbf{B} = \hat{\mathbf{x}}\frac{e^{2}\partial_{x}A^{2}(x)}{4m_{\mathrm{e}}\gamma c^{2}}\left(1+\frac{1-\epsilon^{2}}{1+\epsilon^{2}}\cos2\omega t\right), \tag{3.44}$$

which exhibits a steady and an oscillating part. The latter can potentially inject bunches of electrons beyond the skin depth, similarly to what happens in Brunel mechanism, but with a doubled frequency. If Eq. (3.44) is cycle averaged the longitudinal ponderomotive force on a single electron is retrieved, consistently with Eq. (3.31). This makes it also evident that circular polarization ($\epsilon = 1$) suppresses the oscillating part of $J \times B$ force, preventing $J \times B$ heating as anticipated in Sec. 2.4, where the progress on RPA mechanism has been discussed.

Further insights on $J \times B$ heating are provided by Eq. (3.35), that is the longitudinal momentum equation retrieved by a cold fluid plasma initially at rest. As mentioned before the relativistic ponderomotive term appearing in such an equation determines a pressure field, so that the potential density u_p plays the role of an effective temperature. In Ref. [77], Wilks has proposed to identify u_p with the hot electron temperature:

$$T_\mathrm{h}^W = \frac{m_\mathrm{e}c^2}{k_\mathrm{B}} \left(\sqrt{1 + a_0^2} - 1 \right) . \tag{3.45}$$

The constraint $T_\mathrm{h} \to u_\mathrm{p}$ leading to Eq. (3.45) actually reduces an intrinsically three dimensional quantity as the electron temperature to a purely longitudinal effect, determined by $J \times B$ coupling. Thus, even if Eq. (3.45) provides a reasonable estimate of T_h, as discussed briefly, it does not represent a rigorous theoretical description of electron heating.

Further collisionless absorption mechanisms are related to laser field penetration through the plasma. If a step-like profile is considered, the optical field can bore into the vacuum-plasma interface, to be damped within the skin length $l_\mathrm{s} = c/\omega_\mathrm{pe}$. In this "penetration" region, the exponentially decaying E-field is still strong enough to accelerate electrons and to force the oscillatory motion. Now, in a collisional regime ν_ei is larger than the laser pulsation ω, so that the electrons immediately cede energy as they bump against the ions, without performing the oscillatory motion. Moreover, the thermal excursion length defined as $\lambda_\mathrm{te} = v_\mathrm{te}/\omega$, is smaller than l_s. Since λ_te indicates the typical distance over which the E-field oscillations are thermalized, this means that the plasma is locally thermalized within the skin depth.

As underlined before, when the temperature is increased ν_ei becomes negligible, as the thermal velocity v_te grows. In this case the electrons can oscillate in the skin layer without occurring in collisions and two regimes of absorption are pointed out. If the $\lambda_\mathrm{te} \gg l_\mathrm{s}$ then the electron population is sufficiently agitated to carry the field energy away from the skin layer before a pulsation of the wave is completed. Thus the laser field influence is transmitted beyond the skin depth and thermalization becomes non-local, in a process named *Anomalous Skin Effect* [128]. In the opposite limit, that is $\lambda_\mathrm{te} \ll l_\mathrm{s}$, the electrons can perform several oscillations in the laser field, within the skin depth. While this motion is active, they can receive a non-adiabatic thrust by the laser ponderomotive potential or by the ambi-polar potential arising via charge separation at the plasma border. This mechanism is named *Sheath Inverse Bremsstrahlung*, since the electron oscillations are affected by "collisions" against a sheath potential, analogous to the Debye sheath in TNSA [129]. In Ref. [130] these two mechanisms, both related

to the vanishing of the wave beyond the critical density, are shown to be different limits of the same absorption process, by means of a theoretical and numerical study.

In a recent work Mulser et al. [131] have looked for a comprehensive picture of the absorption mechanisms just described, proposing that laser absorption in a collision-less plasma is essentially due to electron oscillation across a density gradient. The argument is supported by the idea that the density profile distorts the oscillating potential of the electrons under the field influence, providing anharmonic features. A numerical study of electrons in an anharmonic potential have demonstrated that resonance is not restricted to classical resonant frequency, and that particles can gain energies much higher than the quiver energy, chaotically escaping the potential well. This point of view can then explain why a fraction of electrons overcomes the ponderomotive potential energy, and why absorption shows a generally complex behavior. Anyway, for the moment, such a picture has not provided quantitative predictions.

To conclude this survey on collision-less absorption it is necessary to underline that the structure of laser and plasma fields, governing the motion of the energetic electrons, have been numerically demonstrated to determine a randomization of the heating also in absence of collisional dynamics [132], which explains why the hot electron tail shows a quasi-Maxwellian profile.

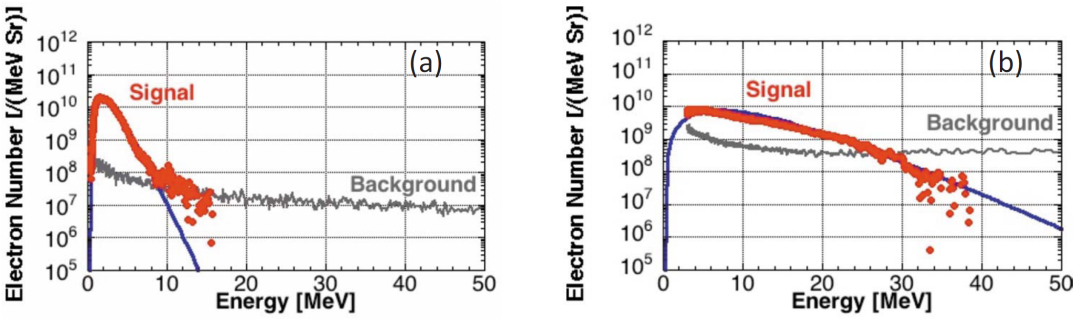

Figure 3.5: - Fast electron energetic spectra detected by means of electron spectrometers. The measured signal is represented by the red dots, the background noise by the gray curves and a relativistic Maxwellian fitting is indicated by the two blue curves (Figure reprinted from Ref. [133]).

3.1.1.8 Measurements and Scalings

In order to reach a deeper comprehension of the relevance of different absorption mechanisms, for the TNSA interaction regime, several absorption measurements have been performed. The energy absorbed in a laser-matter experiment is measured detecting the reflected and scattered laser light, which is not straightforward in TNSA framework, since radiation can be scattered in a 2π solid angle. Besides that, in the contest of laser-driven ion acceleration, it can be also useful to measure the energy amount specifically transferred to the hot electron population or the energy spectrum of the latter, features which are even more complicated to retrieve. In fact, most of the hot electrons

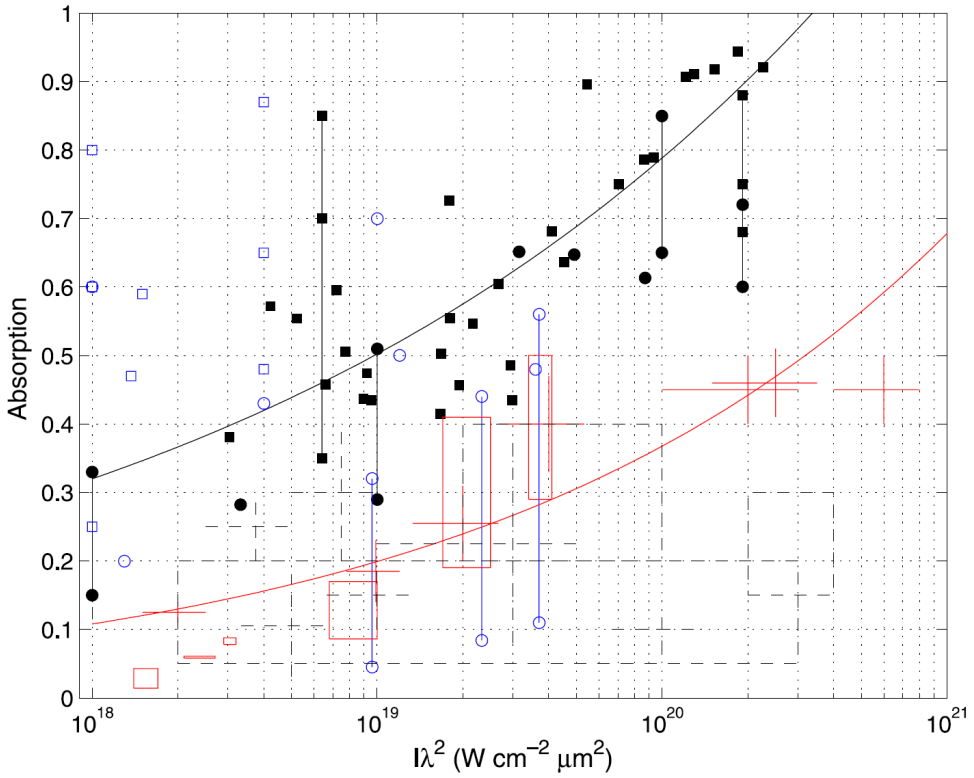

Figure 3.6: - Collection of published experimental and numerical absorption values as a function of laser irradiance. The solid black symbols are the results presented by Ref. [134], the circles represent normal or near normal incidence while the squares indicate oblique incidence. The blue hollow symbols represent numerical results for different models. The vertical lines (black and blue) join the numerical results with same initial setups and different pre-plasma scale lengths, the absorption is always higher for longer pre-plasmas. The solid red and dashed black crosses, display published values of the energy absorbed by hot electrons only, while the boxes group different points localized in a specific region ([135] and references therein). Two curves fit the total absorption (black) and the hot electron absorption (red) experimental values (Figure reprinted from Ref. [135]).

are confined inside the target volume by the strong self-consistent fields generated at the plasma-vacuum interfaces. Thus, the whole spectra have to be detected manly by indirect techniques, exploiting the X-rays or bremsstrahlung emissions resulting from the interaction of fast electrons with the target material. As shown in Fig. 3.5, the direct measurement of energetic distribution by electron spectrometer is possible, provided that the fastest electrons can escape the boundary fields. These spectra anyway, can consider only the most energetic fraction of the real spectrum, and are affected by the action of the self-consistent plasma fields confining the remaining electrons.

In Fig. 3.6 a collection of published experimental absorption measurements is shown together with the results of different numerical simulations, as presented in Ref. [135].

Both total and hot electron absorption are displayed, over the irradiance range of interest in TNSA experiments. Although, empirical fit curves are provided to outline a common trend, the large scattering of data demonstrates that the behavior of absorption physics is almost unpredictable. However, in parametric studies exploiting a single experimental apparatus or numerical simulations at similar conditions, the absorption dependence on parameters as irradiance or incidence angle can be investigated and characteristic trends [136], or transitions among different mechanisms [137], can be retrieved.

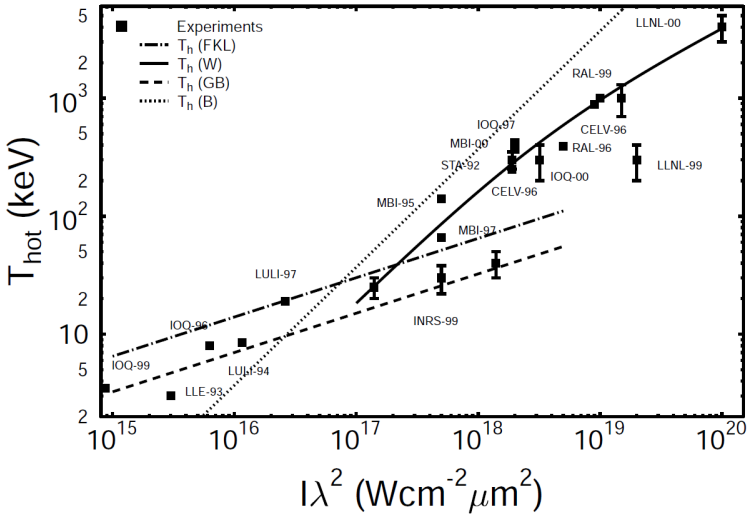

Figure 3.7: - Hot electron temperature measurements as a function of laser irradiance. As showed in the legend, the curves indicate different theoretical scalings. The solid line displays the ponderomotive temperature given by Eq. (3.45), the dotted line refers to Brunel model predictions, Eq. (3.42). The other scalings result from numerical simulations, the dash-dotted line is obtained for ps pulses, and the dashed line for sub-ps durations and finite steep gradient target (Figure reprinted from Ref. [27], where experimental and numerical references are indicated).

With respect to energy absorption, the hot electron temperature exhibits a more systematic behavior, though still affected by large scattering of data, as shown by the collection of the hot electron temperatures measured in a number of different experiments represented in Fig. 3.7 (see Ref. [27] and references therein). Here, a clear dependence on $I\lambda^2$ emerges, while the scalings predicted by numerical and theoretical models show a satisfactory agreement with the data. In particular, a transition in the trend is evident at $I\lambda^2 \simeq 10^{18}\,\mathrm{W}\mu\mathrm{m}^2/\mathrm{cm}^2$. Below such irradiance value a $(I\lambda^2)^{1/3}$ behavior seems to establish, in agreement with the so-called "Beg scaling" based on the experimental results of Ref. [5]. For $I\lambda^2 > 10^{18}\,\mathrm{W}\mu\mathrm{m}^2/\mathrm{cm}^2$ instead, the ponderomotive value given by Eq. (3.45), provides a reliable estimate of the hot electron temperature. Several investigations of the hot electron temperature scaling with laser irradiance have been published in the last years (see for example [138, 139, 140]) and alternative, refined

theoretical schemes have been proposed [141, 142], but the picture outlined by Fig. 3.7 is still reliable and widely accepted.

3.1.2 Hot Electron Transport

Once the hot electron population is generated by laser-matter interaction it expands through the target, approaching relativistic velocities. The hot electron mean velocity for a 3-dimensional relativistic Maxwellian distribution, with temperature T_h, is in fact given by:

$$v_\mathrm{h} = c\left[1 - \left(1 + \frac{\langle K\rangle}{m_\mathrm{e}c^2}\right)^{-2}\right]^{\frac{1}{2}}, \tag{3.46}$$

in which $\langle K\rangle$ is the mean kinetic energy (see Ref. [143]):

$$\langle K\rangle = k_\mathrm{B}T_\mathrm{h}\left[\zeta\left(\frac{\mathcal{K}_3(\zeta)}{\mathcal{K}_2(\zeta)} - 1\right) - 1\right], \tag{3.47}$$

where the $\mathcal{K}_n$ are modified Bessel functions of the second kind. For example at $T_\mathrm{h} \sim 10\,\mathrm{keV}$, a temperature which is easily overtaken by TNSA conditions, Eq. (3.46) gives a relativistic mean velocity of $v_\mathrm{h} \sim c/4$.

The study of relativistic hot electron dynamics through the target bulk have been extensively investigated because of the widespread interest in the exploitation of energetic electrons for the Fast Ignition scheme in Inertial Confinement Fusion [144]. Despite decades of research, hot electron transport physics is still not completely understood and a reliable control of the hot electron beam parameters is far from being achieved. This is mainly due to the development of self-consistent fields related to the electron current traveling inside the plasma, capable to trigger nonlinear and unstable effects, which make the physics extremely involved. Moreover, these difficulties arise already without considering the uncertainties set by the lack of knowledge in the initial hot electron population distribution features, which adds further complications on the study of transport dynamics.

3.1.2.1 Return Current

In an aluminium foil, the range of typical hot electron beam at temperature $T_\mathrm{h} \sim 100\,\mathrm{keV}$, evaluated by means of radiative and collisional stopping powers [145], is of the order of $500\,\mu\mathrm{m}$. At the average speed given by Eq. (3.46), that is $v_\mathrm{h} = 0.6c$, the time of flight over this range is more than 1 ps. Considering the relevant transport space- and time-scales in TNSA physics it is evident that, as a first approximation, collisional effects in hot electron transport can be neglected.

The first obstacle to free hot electron propagation through the target is determined by the huge current density $\mathbf{j}_\mathrm{h}$ that establishes through the material. In Ref. [146] an estimate of the current generated by the free expansion of a typical hot electron beam, produced by a ultra-intense target ($I = 10^{18}\,\mathrm{W/cm^2}$), is performed, resulting in a 24 MA current inside a cylinder of a $30\,\mu\mathrm{m}$ diameter. By means of Ampère's law it

is easy to demonstrate that such kind of current implies a GG static magnetic field, wrapped around the electron beam, which contains more energy than that actually provided by laser absorption. This contradiction means that huge MA currents cannot be maintained by the physical system. Two solutions are possible:

- an inductively or electro-statically generated electric field establishes, which hampers self-consistently the charge flow.
- A cold return current $\mathbf{j}_c$ is supplied by the background material, so that the net charge flow is balanced.

Therefore, to favor the transport of hot electrons, the presence of a background cold electron population is essential. If the target is a conductor, or if preheating processes have ionized the target before the hot electron burst, a solid density substrate of electrons is present and return current is promptly generated. Typically, the fast current is assumed to have a density of the order of $n_{cr} \sim 10^{21}\,\mathrm{cm}^{-3}$, while $\mathbf{j}_c$ is constituted by an almost solid density ($n_c \sim 10^{23}\,\mathrm{cm}^{-3}$) of slower electrons. Collisional effects for the propagation of cold electrons are surely more relevant and Ohmic heating can take place [147].

Otherwise, if the background electron are not dense enough or not available at all, the arising field and the resistive heating can ionize the material, supplying the return current. Of course the energy spent in ionization and heating of the background electrons is subtracted from the hot electron bunch and hampers its propagation. A model of transport inhibition, by means of the electro-static self-consistent field, is proposed in Ref. [146], where Ohm's law and charge continuity equation are used to obtain a non-linear diffusion equation for the hot electron density. This introduces the dependence of electron transport on the material conductivity which, in this case, is determined by Spitzer classical law: $\sigma = n_e e^2/m_e \nu_{ei}$. In a realistic case anyway, the material conductivity is strongly affected by resistive heating, so that a high conductivity channel can establish [148]. For this reason, the nature of fast electron transport has been further studied with Fokker-Planck numerical simulations, underlining the effects of the induced magnetic fields as well [149, 150]. The latter, which are determined by the local imbalance between $\mathbf{j}_h$ and $\mathbf{j}_c$, can be estimated by Faraday's law to be still of MG order. Magnetic fields of such magnitude can perform a pinch of the electron current and favor the collimation of it. Moreover, as already mentioned in Sec. 2.3, the electron propagating in a planar foil are confined inside the target bulk by the self-consistent electro-static sheath field, which arises at the matter-vacuum interfaces. Such sheath field has the effect to reflect the relativistic electrons back so that the fast electron current is inverted. Therefore such electron recirculation can contribute sensibly to the current balance inside the target and should be taken into account.

3.1.2.2 Instabilities

Hot electron transport, and the corresponding generation of electric and magnetic fields, is not just affected by the capability of the substrate to sustain a background balancing

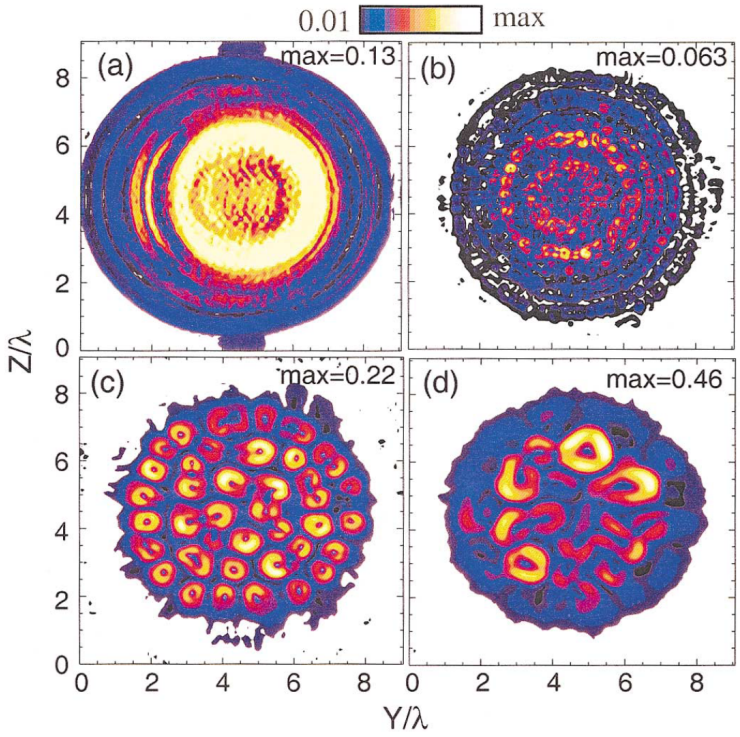

Figure 3.8: - Transverse section of Electric (a) and Magnetic (b,c,d) transverse fields within the target in a three-dimensional simulation of laser-plasma interaction. The magnetic field is represented at three consecutive times, showing the growth of filament diameter (Figure reprinted from Ref. [151]).

current. It has been demonstrated that the configuration of two counter-propagating currents in a plasma is subject to instabilities, which can strongly affect transport dynamics. Such unstable physics is extremely complex and not incline to analytical modeling, demanding for detailed numerical simulations.

A classical unstable behavior which characterizes the a flow of fast particles in a background plasma is the so-called *two-stream instability* [152]. This phenomenon is the inverse of Landau damping, in which a plasma wave looses energy in behalf of the particles traveling at velocities slightly lower than the wave phase velocity. In presence of a faster bunch of particles the energy transfer can be reversed so that the particles provide energy to the wave, determining an instable growth of the latter. Another well-known instability, which is relevant in the regime of electron propagation, is the *Weibel instability* [153]. This phenomenon is determined by an anisotropy in the particle velocity distribution, which is naturally relevant in the case of counter-streaming currents. A small perturbative B-field determines a small-scale repulsion of the opposite currents, which forces the electron stream to break-up in filaments. These, in turn, amplify the magnetic perturbation, repelling or attracting each other according to the current sign. Eventually, filaments of the same sign coalesce, as shown in Fig. 3.8,

growing in the transverse dimension, and causing the establishment of intense quasi-static magnetic fields, which subtract energy and affect electron transport.

Along the years, numerical simulations and theoretical modeling have provided better knowledge about such unstable behavior, outlining in some cases the regions which are safe from it [154, 155]. Nonetheless, the complexity of the physics forces to treat simplified systems, not taking into account the aspects which have an influence on the growth of the instabilities, as three-dimensional effects or collisions [151, 156]. Moreover, experimental evidences of the onset of beam filamentation and quasi-static magnetic fields have been testified in the relevant regime for TNSA [36, 157].

3.1.2.3 Hot Electron Divergence

Another important feature, in the framework of fast electron transport, is the hot electron divergence, that is the angular spread of propagation inside the material. Concerning TNSA, this electron beam property is crucial to establish the transverse dimensions of the ion source, and the electron density which characterizes the Debye sheath. If a collision-less, ballistic transport is assumed, the electron bunch propagates throughout the target according to the diffraction theory, depending on its initial transverse profile. Moreover, the knowledge of this transverse profile is not accessible, because of the uncertainties on the mechanism of hot electron generation, and on the actual beam intensity profile. For this reason, the usual approach is that of considering a Gaussian beam density so that the propagation is characterized by an asymptotic linear spread of the density FWHM, represented by the divergence angle θ.

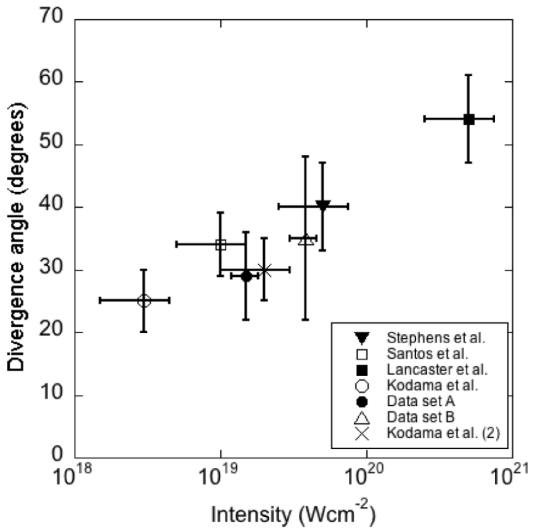

Figure 3.9: - Collection of measured electron beam divergences as a function of the intensity on target (Figure reprinted from Ref. [158], where references to experimental data are provided).

In a recent work published by Debayle et al. [159], a more involved angular depen-

dence modeling has been proposed, introducing the following local angular distribution function at hot electron source:

$$f(\theta, r) = \frac{A}{\lambda} \exp\left[-\frac{(\theta - \theta_r)^2}{\Delta\theta_0^2}\right] . \tag{3.48}$$

Eq. (3.48) describes beam angular spread exploiting two parameters: θ_r, the local electron mean propagation angle, and $\Delta\theta_0$, the local dispersion angle. The former represents the average hot electron direction depending on the initial localization r on the laser focal spot. It takes into account the different angular dispersion determined for example by the radial ponderomotive force variation over the hot electron source. $\Delta\theta_0$, instead, is determined by the hot electron beam transverse temperature and other possible stochastic processes occurring at the beam generation. Still in Ref. [159], by means of numerical simulations, this representation of angular spread is shown to be convenient to resolve the contribution of different physical aspects to electron divergence, as for example the development of Weibel instability with and without a pre-formed plasma in front of the target.

Despite these results, up to now, the problem of electron divergence has been mainly treated with the simple 1-parameter modeling, also due to technical limits in the hot electron distribution measurement. There have been several experimental studies of hot electron divergence in the last years, driven by the interest in electron propagation for Fast Ignition ICF. The typical measurement technique exploits X-ray emission due to fast electron transit through the target, which results in a bright spot indicating the width of the electron burst [160, 161]. The picture outlined by the published measurements attests that the divergence is not an easily predictable parameter, because of the many variables coming into play, both in the framework of laser-matter interaction than in electron transport. Despite such complexity, the different published measurements gathered in Fig. 3.9 demonstrate an almost logarithmic dependence on laser intensity, which is consistent with the diffraction of a Gaussian beam. However, in the interpretation of experimental divergence measurements, one should also take into account the before-mentioned recirculation of hot electrons, which can affect the X-ray emission because of the multiple transits of energetic electrons back and forth.

3.1.3 Ion Acceleration

To conclude this overview on the physical system which is the TNSA mechanism scenario, the attention is now focused on the ion acceleration itself and on those issues strictly related to it.

As already mentioned, the collective motion of ions occurs at longer timescales with respect to the electronic ones. Roughly speaking, if the electron collective reaction to the laser irradiation occurs on fs timescales, due to the smaller charge-to-mass ratio, the ions react on a ps time. In principle, this provides an adiabatic separation between the dynamics of the two plasma populations, which can simplify the modeling of ion acceleration once the electron distribution is known. During the last years, several TNSA models exploiting such feature have been proposed, based on strong assumptions

about the hot electron population, in order to study ion acceleration according to the electro-static or fluid dynamics, triggered by the assumed initial conditions. As shown by these theoretical descriptions, further discussed starting from Sec. 3.2.2, the solution of the ion motion is a simpler physical problem compared to the electron behavior. Of course this statement ignores the fact that, in order to have a reliable model of ion acceleration, the starting description of hot electrons needs to be sufficiently accurate. Despite this, the different timescale of ion motion, suggests the possibility that many subtleties, typical of hot electron dynamics are averaged out from the ion movement so that some simplifications are justified.

Nevertheless, the realistic modeling of ion acceleration phase, even freed from the uncertainties regarding the hot electron distribution features, is still not so trivial and different aspects have to be carefully considered. First of all, as mentioned in Sec. 2.3, the hydrodynamic reaction of the target, due to pre-pulse interaction, can have a strong influence on TNSA. As shown in Fig.2.2 the pre-pulse has different components, which can hit the target from several ns (ASE pre-pulse) down to some tens of ps (the pedestal caused by high order dispersion and cavity imperfections). As shown in Refs. [29, 88], the shock wave launched throughout the matter by the ASE pre-pulse can alter the target surfaces before the ion acceleration dynamics begins, depending on its duration and on the target thickness. Hydrodynamic studies of the ion population have shown that also the ps pedestal demands a careful consideration, since it can determine relevant pre-heating and damage the target ionic structure [23]. Another complex issue in ion acceleration modeling regards the ionization degree of target populations. Ionization physics is of course deeply correlated to laser-matter and hot electron transport, involving itself subtle physical mechanisms of difficult comprehension. At the moment, most of the theoretical studies adopt very rough approaches to take ionization behavior into account, also due to the particular interest on proton acceleration, but in the future TNSA modeling shall not disregard this aspect of the physical system (see Ref. [162] and references therein for a closer glance on ionization problem). In fact, the presence of different ion populations, and also their initial disposition in the target structure has a relevant weight on ion acceleration properties. This aspect have been already underlined in Sec. 2.3, discussing experiments aimed at improving the ion spectra by target structuring [37, 100]. For example, the case of an hydrogen and carbon plasma clearly illustrates this influence: in a first phase, soon after the Debye sheath is established, the carbon ions expansion follows the proton acceleration, because of the different charge-to-mass ratio. Then, due to the evolution of the ion bunches, the carbon front can in some cases reach the slower part of the proton spectra and act as a piston further accelerating less energetic protons. This determines a peak in the spectra, as studied in Refs. [163, 164]. Thus, it should be clear that many issues might arise in the modeling of the ion dynamics as well. Anyway, in the "classic", ideal case of TNSA, with high contrast laser impinging on a planar foil, covered with a thin hydro-carbon layer on the rear surface, these problems can be in principle neglected, while it is not possible to get rid of the intrinsic difficulties in laser-matter interaction and hot electron transport.

3.2 TNSA Theoretical Modeling

In the present section the attention is directed towards theoretical modeling of the previously described system. The research for a TNSA model, capable to predict the ion acceleration features, starting from an initial system configuration has followed, since the discover of the phenomenon, two main paths:

- a rigorous modeling approach, aiming at the description of the physics underlying TNSA on the basis of "first principles"[1] that, in the case of plasma physics, are represented by the Boltzmann kinetic equation and Maxwell's laws.
- An effective modeling approach, based on strong approximations of the system, which can make analytical or semi-analytical solutions available.

The solution of kinetic and Maxwell equations, in the highly nonlinear framework of ultra-intense laser-matter interaction, demands of course the use of numerical calculations. The most popular method in laser-based acceleration study, that is Particle-In-Cell (PIC), is introduced in the next section. However, as anticipated in the introduction, a fully kinetic description of the system demands a huge computational effort in order to reproduce quantitatively reliable results. This stimulated the proposal of different effective models which remarkably simplify the physics involved, trying to provide reliable estimates on some fundamental acceleration aspects. This topic, which is the main interest of present dissertation, is discussed in depth from Sec. 3.2.2 and thereafter.

3.2.1 Particle-In-Cell Method

The study of TNSA as a non-equilibrium statistical mechanics problem, that is via kinetic Boltzmann equation coupled with Maxwell equations, gives a complete description of the phenomenon, which takes into account all its various aspects. However, in order to obtain reliable results with a reasonable computational effort, some simplifications on this theory are mandatory. The most used approximation is that of limiting the kinetic theory to Vlasov equation, neglecting the collisional term of Boltzmann transport equation. According to the considerations of Sec. 3.1.1, collisional effects should indeed have a minor relevance on TNSA, at least on its first stages.

Numerical methods to directly solve Maxwell-Vlasov system are available, but the CPU load required by these so-called Vlasov codes is still extremely large and the simulation of three dimensional systems, with realistic sets of parameters, is not feasible. The most exploited numerical method that computes the solution of such a system is the PIC method [40, 165], in which a statistical approach allows to reduce the computational requests, with the drawback of an artificial noise.

[1] Of course non-equilibrium statistical mechanics does not represent a fundamental theory, so it is not rigorous to speak about "first principles". However, as long as quantum effects are unimportant, kinetic and Maxwell equation represent the theoretical bases of plasma physics, and it is correct to use this definition.

The starting point of PIC method is the Vlasov equation, governing the distribution function relative to a plasma population:

$$(\partial_t + \dot{\mathbf{x}}\partial_{\mathbf{x}} + \dot{\mathbf{p}}\partial_{\mathbf{p}})\, f(\mathbf{x}, \mathbf{p}, t) = 0\,, \tag{3.49}$$

where:

$$\dot{\mathbf{x}} = \frac{\mathbf{p}}{m}\,, \qquad \dot{\mathbf{p}} = \mathbf{F}\,(\mathbf{x}, \mathbf{p}, t)\ . \tag{3.50}$$

Here the force $\mathbf{F}$ is Lorentz force, given by Eq. (3.21). The solution of Eq. (3.49) is then evaluated by means of the "particle" approach, which consists in the discretization of the distribution function f as an ensemble of N_p numerical particles, also named macro-particles, since they correspond to a large number of physical particles. This means that the following discrete representation of f is adopted:

$$f(\mathbf{x}, \mathbf{p}, t) = f_0 \sum_{n=1}^{N_\mathrm{p}} g\left[\mathbf{x} - \mathbf{x}_n(t)\right] \delta^{(3)}\left[\mathbf{p} - \mathbf{p}_n(t)\right]\ , \tag{3.51}$$

where f_0 is a proper normalization constant, δ is the Dirac delta generalized function and g is the density function associated to each single numerical particle, having properties similar to the δ-function:

$$\int \mathrm{d}^3\mathbf{x}\, g(\mathbf{x} - \mathbf{x}_n) = 1\,, \qquad \int \mathrm{d}^3\mathbf{x}\, \partial_x g(\mathbf{x} - \mathbf{x}_n) = 0\,. \tag{3.52}$$

Substituting Eq. (3.51) in Vlasov equation it can be shown that, thanks to δ and g properties, the problem is reduced to $6N_\mathrm{p}$ equations of motion for the numerical particles, that is:

$$\dot{\mathbf{x}}_n = \frac{\mathbf{p}_n}{m}\,, \qquad \dot{\mathbf{p}}_n = \bar{\mathbf{F}}_n\,, \tag{3.53}$$

where $\bar{\mathbf{F}}_n$ is the spatial average of the force, acting on the n-th numerical particle, according to the form of the density g:

$$\bar{\mathbf{F}}_n\,(\mathbf{x}_n, \mathbf{p}_n, t) = \int \mathrm{d}^3\mathbf{x}\, g(\mathbf{x} - \mathbf{x}_n)\mathbf{F}_n\,(\mathbf{x}, \mathbf{p}_n, t)\ . \tag{3.54}$$

This means that the solution of Vlasov equation is approximated by the motion of the N_p macro-particles experiencing the Lorentz force. To determine the latter, the sources of the electro-magnetic fields, namely the charge and current densities, are defined on a numerical space-grid $\{x_i\}_{i=1}^{N_\mathrm{x}}$, where N_x is the number of grid-points:

$$\rho(x_i, t) = f_0 \sum_{j,n} x_j g\,(x_i - \mathbf{x}_n)\ , \tag{3.55}$$

$$\mathbf{J}(x_i, t) = f_0 \sum_{j,n} x_j \mathbf{v}_n g\,(x_i - \mathbf{x}_n)\ , \tag{3.56}$$

in which j labels the particle species, n the macro-particles, and i the grid points. $\mathbf{v}$ is the relativistic velocity of the n-th macro-particle. When the source terms are known,

a numerical solution of discrete Maxwell equations provides the electro-magnetic fields **E** and **B** defined on the grid. This representation makes it eventually possible to set a numerical loop, which is the basic time cycle of PIC simulations:

1. the sources are evaluated on the grid according to the positions and velocities of the macro-particles.

2. By means of discretized Maxwell equations the electro-magnetic fields defined on the grid are computed.

3. The Lorentz force acting on each numerical particle is obtained interpolating the fields.

4. The macro-particles motion is integrated obtaining new positions and velocities.

Reiteration of such a cycle, with the proper time resolution, generates the numerical dynamics of the macro-particles moving through a pattern of electro-magnetic fields defined on a grid. The approach has been named Particle-In-Cell due to such a particle-grid duality in the computational cycle. It is now clear that the particle approach simplifies the coupling of Vlasov and Maxwell equation, with respect to the pure numerical solution of the problem. The price to pay for this advantage is the introduction of an artificial noise, related to the discretization of the distribution function in a limited number of particles.

In more than ten years of research, PIC simulations have imposed as a key instrument for investigation of laser-based ion acceleration, exploited in a large number of published works as a support to theoretical hypothesis and to allow interpretation of experimental results. The TNSA mechanism itself has been tested and confirmed by means of PIC simulations [25, 166].

However, the wide range of time and space-scales involved in TNSA dynamics demand for really high temporal and spatial resolutions, leading to huge computational requirements. Also, the choice of the macro-particle number is constrained by computational resources, introducing numerical artifacts and noise. For this reason, PIC simulations are usually performed both on simplified systems and over a limited temporal window. It is thus common to restrict phase-space dimensionality, as for example using 2 spatial and 3 momentum dimensions, or to simulate the laser interaction with solid by means of a lower-density plasma ($n_e < 100 n_{cr}$), or to stop the simulation time before 1 ps. This approximated numerical modeling of the system can still qualitatively reproduce the features of TNSA physics, but quantitative discrepancies with the realistic case arise. In this sense PIC simulations can be largely exploited to interpret and comprehend the experimental results, but still do not represent a convenient technique to retrieve quantitative predictions for TNSA ion features, given a set of realistic system parameters. Nonetheless the use of PIC simulations for quantitative estimates is widespread, as an example the results of a two-dimensional PIC parametric study is showed in Fig. 3.10, in which the method is exploited to test the dependencies of maximum ion energy on initial parameters.

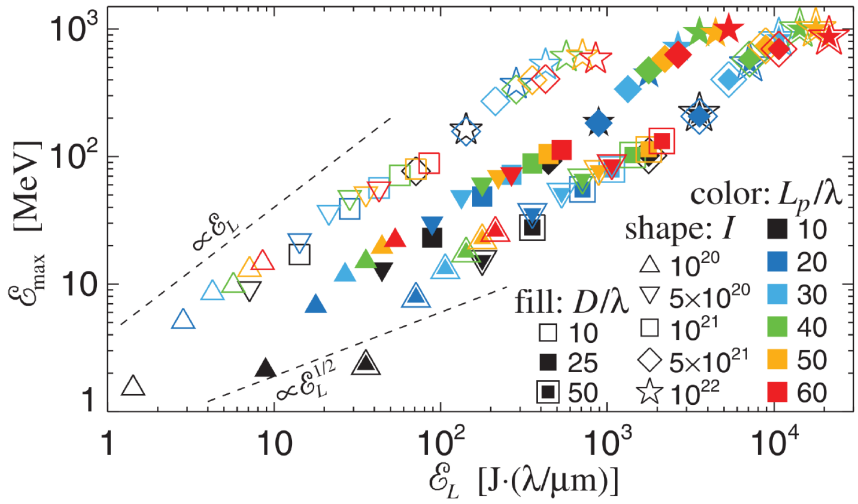

Figure 3.10: - Maximum ion energies vs laser pulse energies resulting from a large set of two-dimensional PIC simulations at different conditions. The target is a 2 layer structure with a fully ionized Al slab of thickness $l = \lambda$ and density $n_e = n_{cr}$. On the backside, a proton layer of $l_2 = 0.06\lambda$, transversally limited to half a focal-spot diameter, provides the particles for acceleration. As indicated in the legend the focal spot diameter D, the intensity I and the FWHM laser length L_p are varied (figure reprinted from Ref. [41]).

3.2.2 Effective Modeling

TNSA effective modeling is an approach complementary to the numerical solution of the Vlasov-Maxwell system, in which strong starting assumptions, mainly based on experimental observations, are exploited to simplify the physical picture. By means of such assumptions, the effective models provide quantitative estimates of TNSA features through analytical or semi-analytical calculations, starting from realistic sets of parameters. The basic purpose of effective modeling is thus the reliable prediction of experimental results, to draw guidelines for future research and, implicitly, to enlighten the relevant TNSA aspects in the framework of potential applications.

A first, quantitative estimate about TNSA is that provided by Eq. (3.2) to evaluate the electro-static field $\mathcal{E}_{sh}$ responsible for the acceleration. As mentioned before, if a typical hot electron temperature of 500 keV and a sheath density of $10^{21}\,\mathrm{cm}^{-3}$ are chosen, Eq. (3.2) gives a field of $3\,\mathrm{MV}/\mu\mathrm{m}$. According to this formula, an elementary estimate of the energy acquired by the ions accelerated in such a field gives $E_{ions} \sim Zk_BT_h$, which exhibits a direct proportionality to the hot electron temperature. Combining this result with the ponderomotive temperature of Eq. (3.45) a $I^{1/2}$ scaling is retrieved, which, going back to Sec. 2.3, is supported by part of the published experimental measurements of ion cut-off energy.

On the one hand, this simple argument suggests that effective modeling can be a convenient path to the prediction of some TNSA features as the ion cut-off energy, on the other hand, it explicits two key assumptions which are commonly exploited by the

main TNSA models which have been proposed, namely:

- the description is focused on the ion dynamics phase, studied in the electro-static approximation, that is governed by Poisson equation:

$$\nabla^2\phi = 4\pi e\left(n_{\mathrm{h}} - \sum_j Z_j n_{\mathrm{i}j}\right), \tag{3.57}$$

  in which j indexes different ionic populations. This means that the physics of laser-matter interaction and electronic transport is reduced to few assumptions about the initial plasma distributions.

- Planar symmetry is assumed, reducing the description to a one-dimensional system. In fact, over a central spot of micro-metric diameter, the sheath field can be considered planar-symmetric with reasonable accuracy.

Having these two features in common, many TNSA effective models have been conceived during this decade of research, resulting in several interesting works [44, 45, 46, 47, 48, 49, 50, 51, 52], capable in some cases to provide reliable predictions, that agree with the experimental trends beyond the expectations. Despite the promising results, these descriptions still present several problems and dark sides, and none of them stands out from the others as the most reliable TNSA effective model, even if some have become popular and established by now. Moreover, due to the complexity of the acceleration mechanism, it is not likely that a single effective model can account for the multiple aspects of TNSA. For example, a specific description can be appropriate to explain the maximum ion energy dependence on the laser features, while another can be precise in predicting the laser-to-ion conversion efficiency. In this sense, it would be useful to point out, among the different modeling approaches, which ones are the most suitable to foresee specific TNSA ion properties, or to describe some particular feature of the process. The whole following chapter is dedicated to such a request, presenting an original, comparative study of some existing TNSA models, focused on the peak ion energy prediction, relying on the data available from published experimental results. A quantitative analysis of the theoretical descriptions, performed while keeping in mind the picture outlined by the experiments, can outline more precisely the issues and limits of TNSA effective modeling, and evidence which paths should be undertook to research a significant advance in this topic.

A careful analysis of TNSA modeling state-of-art indeed reveals that the lack of knowledge in laser-matter interaction and hot electron transport phases implies a necessary indetermination in the description, leading to a lower reliability of the theoretical predictions. This leads to the work presented in Ch. 5, in which an already existing TNSA model is extended, by introducing new physical details about hot electron physics, in order to overcome some common limits of the effective theories, also from the viewpoint of experimental open problems outlined in Sec. 2.5.

4

Comparison of TNSA Theoretical Models

In this chapter a quantitative, critical investigation of six TNSA theoretical models is presented. The work is focused on effective descriptions, capable to provide analytical or semi-analytical solutions for TNSA scaling laws, in particular about the prediction of accelerated ion peak energy $E_{\max}$, which is one of the crucial features for the proof of laser-driven ion acceleration suitability to applications. For this reason the six models have been selected among the available ones, so that the main different approaches to TNSA modeling are represented, with the basic requirement that they can provide a straightforward estimate technique for $E_{\max}$. The aim of the present study is to compare the reliability of the different models and their predicting capability, on the basis of an experimental data collection. In fact, to attain this purpose, an extended analysis of published TNSA experimental results has been performed, and a comprehensive database of $E_{\max}$ measurements, with the corresponding system parameters, has been set up.

The chapter is organized as follows: first, in Sec. 4.1, the six models involved in the comparative study are introduced. The presentation is organized through the definition of three descriptive approaches: fluid (4.1.1), quasi-static (4.1.2) and hybrid (4.1.3). After that, in Sec. 4.2, an insight on the methods used to coherently compare the model results is given, focusing on database parameters, required estimates and uncertainties arising from these issues. The comparison of quantitative energy predictions is then presented in Sec. 4.3, discussing the results in an effort to point out the most convenient paths to TNSA modeling, according to the specific aims and the applicability domains. On the basis of such a discussion some conclusions on the reliability of the TNSA descriptions and on the possible theoretical advances are reported in Sec. 4.4, also introducing in this way the motivations behind the work described in Ch. 5.

4.1 Theoretical Models

The six TNSA descriptions selected for this comparative analysis are:

- the *isothermal plasma expansion* model, following the work by Mora, published in Ref. [44] and based on the classic theoretical results of Refs. [115, 167, 168] ,
- the *adiabatic plasma expansion* model, again according to the treatment proposed by Mora in Ref. [45],
- the *cylindrical electro-static description* of Schreiber et al., published in Ref. [46],
- the *quasi-static model* proposed by Lontano and Passoni [169], in the relativistic version developed in Refs. [50, 170],
- the *layered target model* described by Albright et al., in Ref. [47],
- the *moving sheath model* of Robinson et al., formulated in Ref. [48].

Two main reasons justify the choice of these models: first, they all provide a maximum ion energy estimate $E_{\max}$, accessible with analytical or semi-analytical calculations. Second, they thoroughly represent the different approaches to describe the TNSA system. It is in fact possible to distinguish, among the published models, two main modeling approaches, *fluid* and *quasi-static*, characterized by different key assumptions. Isothermal and Adiabatic plasma expansion models, adopt a fluid approach, while Schreiber's and Passoni-Lontano's descriptions adopt a quasi-static approach. The remaining models, proposed by Albright and Robinson, can be instead classified as *hybrid*, since they attempt to properly combine features of both fluid and quasi-static descriptions.

While being remarkably different in the adopted approach, these six models also share some basic features, according to the general considerations on TNSA effective modeling discussed in Sec. 3.2.2. Hot electron generation and transport dynamics are in fact reduced to initial assumptions defining the system, while the study is mainly focused on ion acceleration, restricted to a one-dimensional treatment (except for Schreiber's model, in which a cylindrical system is initially considered, to restrict to one dimensional solutions in a second stage).

4.1.1 Fluid Models

The interpretation of TNSA by means of a fluid plasma description represents by far the most popular modeling approach, probably because it dates back to the first proposal of the TNSA scheme [25, 58]. Nonetheless, the theoretical bases of such fluid models have even an older origin, related to the pure study of a warm plasma expanding into vacuum, a classic problem of plasma physics [3]. According to a fluid description, the illuminated target behaves as a plasma expanding into vacuum, in which the dynamics of the components is governed by fluid equations. This plasma is composed by at least two populations: the hot, laser-generated electrons and a cold ion fluid. The dynamics of the first ones, expanding due to thermal pressure, drives the ion population motion via an electro-static self-consistent field. The fluid system (see for example Ref. [28]) is thus coupled to Poisson equation (3.57).

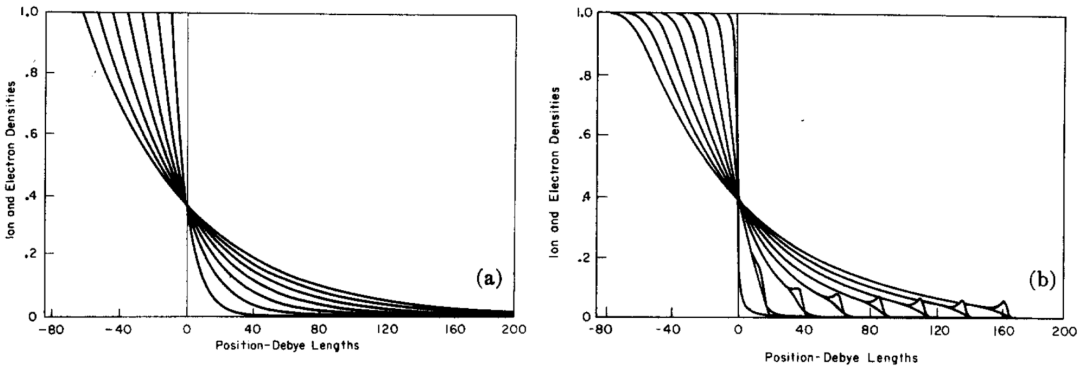

Figure 4.1: - Semi-infinite isothermal plasma solutions. Ion and electron normalized densities $n_{\rm i}(t)$ and $n_{\rm h}(t)$ are depicted at subsequent times according to (a) the quasi-neutral solution and (b) self-consistent numerical evaluation. Higher times correspond to longer plasma scale-length. Ion and electron solutions overlap in (a) while in (b) the ions follow up electronic expansion, creating a density ripple. $n_{\rm i}(t)$ and $n_{\rm h}(t)$ are respectively normalized at $n_{\rm i}(0)$ and $n_{\rm h}(0)$ (Figure from Ref. [115]).

To outline some general aspects of fluid modeling one can consider the simple case of a one-dimensional semi-infinite plasma initially ($t = 0$) localized at in the $x < 0$ region, composed only by hot electrons at fixed temperature $T_{\rm h}$ and cold ions at $T_{\rm i} \sim 0$. The basic approximation which underlies the fluid interpretation is that the timescale of interest is much longer than the electron plasma period, that is $t \gg \omega_{\rm pe}^{-1}$, so that kinetic effects can be neglected and electrons are always in equilibrium with the electrostatic potential. If a single temperature component is considered, this hypothesis leads to the Boltzmann relation that describes the hot electron density $n_{\rm h}$:

$$n_{\rm h} = n_{\rm h0} \exp\left(\frac{e\phi}{k_{\rm B} T_{\rm h}}\right) \tag{4.1}$$

in which $n_{\rm h0}$ is the density of hot electrons where $\phi = 0$. For convention, this point can be located in the region of the plasma where $n_{\rm h} = Z_{\rm i} n_{\rm i}$. In this framework, the assumption that $T_{\rm h}$ is fixed is thus equivalent to that of semi-infinite plasma, since the latter acts as an infinite reservoir of energy, always in thermal equilibrium with each region of the plasma. Since $T_{\rm h} = \text{const}$ this system is called "isothermal".

For $t > 0$, electrons expand into vacuum determining a plane rarefaction wave running through the plasma, as the latter overflows in the $x > 0$ region. As anticipated in Sec. 3.2.2, if the timescale of interest is longer than the ion plasma period $\omega_{\rm pi}^{-1}$, the problem of plasma fluid expansion into vacuum can be studied under the quasi-neutral hypothesis $n_{\rm h} = Z_{\rm i} n_{\rm i}$, which substitutes Poisson equation. Under such an approximation the ion density undergoes the same rarefaction dynamics of the electron fluid, and the plasma expands according to a self-similar solution[1] already known from Ref. [3] (Fig. 4.1a).

[1]The term *self-similar* means that the density solution depends on x and t by means of their ratio x/t, so that, as time runs, the solution maintains the same form, but on a longer space-scale.

In the sub-ps regime, the inertia of ions becomes important and quasi-neutrality condition is broken, so that the Poisson equation is coupled to the system, determining a self-consistent electro-static potential dynamics. The resulting isothermal expansion is depicted in Fig. 4.1b; the ions now expand with a different time-scale with respect to electrons, following these ones into the vacuum with a delayed response. This creates charge separation and an ion density ripple, called "ion front" is driven by the electron expansion, at velocities $\sim T_{\rm h}^{1/2}/m_{\rm i}$.

The dynamics of this system had already been solved in the 70s, but an extremely relevant study of isothermal expansion in the framework of TNSA has appeared in Mora work of 2003 (Ref. [44]). In this paper the problem of semi-infinite sharp plasma isothermal expansion has been solved by means of a Lagrangian hydro-dynamic code, obtaining accurate results concerning the structure of the ion front, the resulting ion energy spectrum, and ion cut-off energy $E_{\rm max}$ as a function of time.

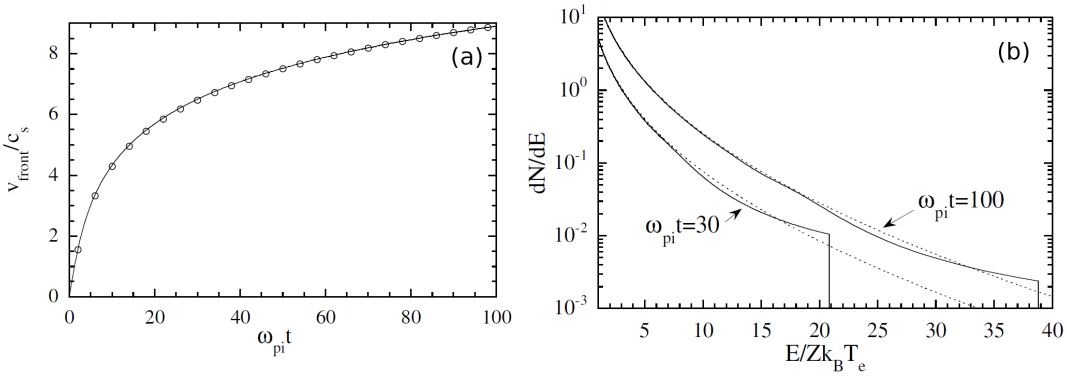

Figure 4.2: - Numerical fluid solutions for (a) ion front velocity and (b) normalized ion energy spectrum as evaluated in Ref. [44]. In (a) the velocity $v_{\rm front}$ is in $c_{\rm s}$ units, the empty circles correspond to numerical results, while the solid line represents the fitted scaling. In (b) two spectra at different times are shown. The solid lines represent the numerical solutions, while the dotted lines are the spectra resulting from the corresponding self-similar solution. The energy on the x-axis is in $Z_{\rm i}k_{\rm B}T_{\rm e}$ units, where $T_{\rm e} \equiv T_{\rm h}$, while the y-axis indicates the number of ions per unit surface and unit energy, normalized to $n_{\rm i0}\lambda_{\rm Dh}/Z_{\rm i}k_{\rm B}T_{\rm h}$, where $\lambda_{\rm Dh}$ is the Debye length relative to the hot electron population (Figure reprinted from Ref. [44]).

In this work it is demonstrated that the velocity evolution of the ion front, obtained through hydro-dynamic calculations, can be fitted with surprisingly good agreement by a logarithmic scaling:

$$v_{\rm front} = 2c_{\rm s} \ln\left(\tau + \sqrt{\tau^2 + 1}\right) , \tag{4.2}$$

in which $c_{\rm s} = (Z_{\rm i}k_{\rm B}T_{\rm h}/m_{\rm i})^{1/2}$ and $\tau = \omega_{\rm pi}t/(2{\rm e_N})^{1/2}$, with ${\rm e_N} \equiv \exp(1)$. The fitting law is compared with hydrodynamic simulations results in Fig. 4.2a, showing a satisfactory agreement at any time. The model provides an ion spectrum as well, which departs

from the self-similar $\sim \exp(-E^{1/2})$ solution, presenting a time dependent energy cut-off, as shown in Fig. (4.2b). Eq. (4.2) leads to an analytical estimate for such a cut-off energy:

$$E_{\max} = 2Z_{\mathrm{i}} k_{\mathrm{B}} T_{\mathrm{h}} \ln^2 \left(\tau + \sqrt{\tau^2 + 1}\right) . \tag{4.3}$$

Eq. (4.3) is the first of the estimates which are considered in the comparative analysis of the present chapter. This formula has been widely used as a prediction for TNSA ion energy in experiments, as for example in Ref. [33]. It is interesting to point out that the obtained $E_{\max}$ scales as $\ln^2(t)$, diverging for $t \to \infty$. This means that a temporal cut-off, that is a value t_{acc} for the duration of the acceleration process, is required to get a finite estimate for ion maximum energy. In the TNSA literature t_{acc} is typically chosen equal to or of the same order of the laser pulse length τ_{p} [33, 45, 46]. From a theoretical viewpoint, the requirement of such a turn-off time suggests that the model lacks in self-consistency, since one has to artificially interrupt the particle dynamics to obtain the observed energy cut-off.

As further discussed in the following, the imposition of an external cut-off is a crucial issue in TNSA modeling. This can be traced back to the thermal equilibrium assumption, coupled with Boltzmann electron density profile (4.1), the form of which ultimately requires a divergent ambi-polar potential ϕ. In fact, in order to have zero electronic density at large distances from the target, that is a realistic physical condition, ϕ must scale to $-\infty$, leading to an unlimited acceleration [147, 171].

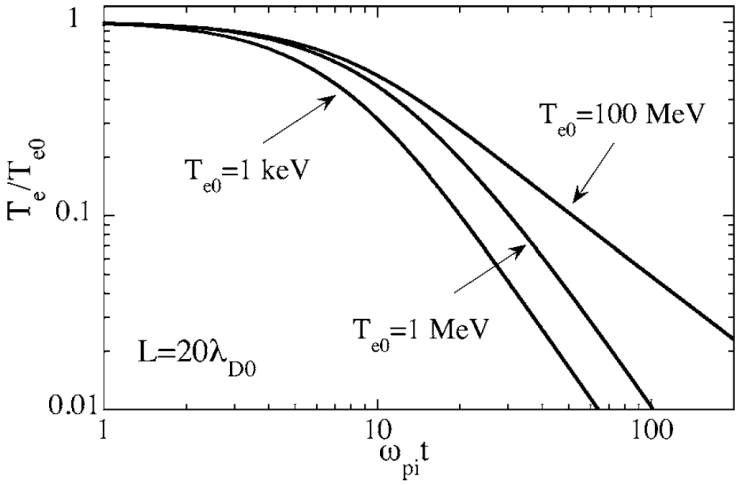

Figure 4.3: - Hot electron temperature $T_{\mathrm{e}} \equiv T_{\mathrm{h}}$ damping for a plasma slab of thickness $L = 20\lambda_{\mathrm{D0}}$ where λ_{D0} and T_{e0} are initial hot electron Debye length and temperature. Three different temperature dynamics are represented, depending on T_{e0} value. The time unit is the ion plasma period $\omega_{\mathrm{pi}}^{-1}$ (Figure reprinted from Ref. [44]).

In a subsequent work, Mora proposed a different model, still based on a fluid plasma classical problem, but including a self-consistent acceleration turn-off feature. The problem is that of a "thin foil expansion into a vacuum" [45], that is the one-dimensional

rarefaction dynamics of a finite plasma slab of thickness D. The key difference with respect to the previous system is not just the finite plasma region since, as mentioned before, the semi-infinite nature of the plasma causes the isothermal behavior and justifies a fixed T_h. In the case of a finite plasma foil the hot electron fluid energy is limited and, as it is transferred to ions by the self-consistent field, T_h must decrease accordingly. In Ref. [45] the problem is solved with the same Lagrangian numerical code as in Ref. [44], with an energy conservation constraint in addition. As shown in Fig. 4.3 the result is that, as the plasma expands, the electron temperature decreases with time, scaling as $\sim t^{-2}$, for the non-relativistic limit, and $\sim t^{-1}$ in the ultra-relativistic case. This dynamics is referred to as "adiabatic expansion" and, as a consequence, the ion front acceleration is damped by energy conservation, leading to an E_max prediction which is self-consistently limited by the amount of energy initially contained in the plasma slab (see also [172] for a different treatment of adiabatic expansion). Also in this case the numerical solution can be well fitted by a logarithmic scaling, depending on both T_h and D:

$$E_\mathrm{max} = 2Z_\mathrm{i}k_\mathrm{B}T_\mathrm{h}\ln^2\left(0.49\frac{D}{\lambda_\mathrm{Dh}} + 5.4\right), \tag{4.4}$$

in which λ_Dh is the hot electron Debye length, T_h is referred to the initial electron temperature and the numerical coefficients slightly depend on it, because of the relativistic corrections contained in the definition of the hot electron mean energy. The values in Eq. (4.4) refer to $T_\mathrm{h} = 1\,\mathrm{MeV}$ and represent a reasonable approximation for typical TNSA temperature ranges. It is clear from Eq. (4.4) that the maximum energy is limited by the plasma slab depth D, which is chosen equal to the foil thickness for real energy estimates. Also, from Fig. 4.3, one can notice that the typical time required by the electron temperature to decrease to the 10% of the initial value is more than ten times ω_pi^{-1}, which is generally a longer timescale with respect to the laser duration τ_p. Since electron cooling is in fact the only physical reason for the acceleration cut-off in the plasma expansion problem, this behavior does not support the choice of $t_\mathrm{acc} = \tau_\mathrm{p}$ which, as previously explained, is usually adopted in the isothermal expansion. Moreover, it has to be underlined that, because of Boltzmann density distribution, the potential is still divergent at large distances also in the adiabatic expansion picture, until the temperature has not evolved to $T_\mathrm{h} \ll e\phi/k_\mathrm{B}$. Theoretically speaking, this is a critical aspect, although the system relaxes self-consistently to a finite acceleration. The adiabatic expansion model is the second fluid description considered in the following analysis of TNSA predicting capability, where Eq. (4.4) is used to estimate E_max.

It should be pointed out that, since in the years fluid approach has become very popular in TNSA modeling, several evolutions of both isothermal and adiabatic expansion have been proposed, introducing further details on plasma description in order to reach a more satisfactory treatment. Relevant examples of this are the introduction of a further, cold electron population described by Boltzmann density relation (Refs. [45, 163]), to describe more realistically the typical electron distribution, or of both heavy and light ion populations ([163]), to mimic the acceleration of the contam-

inant light ions in the presence of a heavy ion substrate. The introduction of such details however requires more involved fluid calculations for which no simple scaling laws for $E_{\max}$ determination have been derived, for this reason, these developments of the fluid approach are not considered in the present analysis.

4.1.2 Quasi-Static Models

In Sec. 3.2.2 a rough $E_{\max}$ estimate has been retrieved according to the electro-static field evaluated in the region of plasma where quasi-neutrality is broken, given by $\mathcal{E}_{\rm sh} = k_{\rm B}T_{\rm h}/e\lambda_{\rm Dh}$ (see Eq. (3.2)). If ions are assumed to be accelerated under the action of such a static field, for few $\lambda_{\rm Dh}$, then they will reach a maximum energy scaling as $\sim Z_{\rm i}T_{\rm h}$, which is consistent with the experimental observations.

Actually, the general approach towards a quasi-static description of TNSA is not that far from such a simple estimate, because the key idea is that of a static field accelerating few ions to the highest energies, before the collective evolution of the ion population. To understand why this simplified picture can be reasonable it is useful to discuss the separation of the most important time-scales for this physical system.

First, it has to be pointed out that, once the hot electrons have been generated and have traveled through the target bulk, it takes a $50 - 100\,\mathrm{fs}$ timescale for electron thermal pressure and ambi-polar potential to relax towards a quasi-equilibrium. The hypothesis of isothermal fluid modeling, which consists in neglecting kinetic effects and considering hot electrons as always in equilibrium, works on a timescale $\Delta\tau_{\rm i} \sim 100\,\mathrm{fs}$, which is detailed enough to resolve ion dynamics but too slow for electron thermalization transient. Quasi-static approach instead describes TNSA by means of a faster timescale $\Delta\tau_{\rm h} \sim 10\,\mathrm{fs}$, so that fluid hypothesis does not hold anymore and electron thermalization process can be resolved.

In such framework, while hot electron pressure and quasi-static potential relax to equilibrium, the heavy bulk ions remain essentially fixed because of their inertia, so that the electro-static field reaches its peak intensity. After this stage the system is settled on a quasi-equilibrium state holding for a few hundreds of fs, during which most of the target ions can be still considered immobile, $T_{\rm h}$ can be assumed approximately fixed, and the field maintains a constant strength. The most energetic ions, which determine the $E_{\max}$ cut-off in the spectra are assumed to be:

- accelerated during this so-called "quasi-static equilibrium", before the collective expansion of bulk ions,

- negligible in number with respect to the hot electrons, that means $N_{\max} \ll N_{\rm h}$, where $N_{\max}$ and $N_{\rm h}$ are respectively the number of accelerated light ions and hot electrons.

Technically speaking, such a picture translates in separating the target ions in two populations: the accelerated light ions, which are studied as test particles running down the electro-static potential slope, and the substrate heavy ions, which are fixed and

guarantee the charge separation[1]. The potential ϕ is then retrieved through solution of Poisson equation, determined by a proper static charge distribution due to the heavy ions and the electrons.

The most simple quasi-static picture of TNSA is given by the $t = 0$ solution of Poisson equation for the semi-infinite sharp plasma problem, with Boltzmann electron distribution, similarly to the problem described in the previous section. This equation, named Poisson-Boltzmann equation, has been treated already in Ref. [167], resulting in a potential ϕ which diverges to $-\infty$ at large distances, as expected from the choice of Boltzmann relation. In Ref. [171], Passoni and Lontano have first attempted a quasi-static description to TNSA, solving the Poisson-Boltzmann equation with the imposition of a spatial cut-off h to the electron cloud extension in vacuum. Such procedure leads to a maximum energy estimate for the ions, namely:

$$E_{\max} = Z_{\mathrm{i}} k_{\mathrm{B}} T_{\mathrm{h}} \ln \left[1 + \tan^2 \left(\frac{h}{\sqrt{2}\lambda_{\mathrm{Dh}}} \right) \right] , \tag{4.5}$$

which still depends on the hot electron temperature but also on h, the external constraint for the sheath field extension, that has to be estimated on physical grounds or used as fitting parameter. This quasi-static model, leading to the energy estimate (4.5), has not been considered in the present comparative analysis, since it has later been developed to a more consistent description, which is named here "Passoni-Lontano" model, published in its latest general formulation in Ref. [170]. Passoni-Lontano model, together with the alternative approach proposed by Schreiber in Ref. [46], have been chosen as representatives of this quasi-static approach in the quantitative study.

In Schreiber's description the planar symmetry is abandoned, assuming that the expanding hot electron population creates a cylindrical quasi-static sheath, at the rear surface of the foil, the radius of which is estimated to be:

$$R_{\mathrm{sh}} = r_{\mathrm{fs}} + D \tan(\theta/2) , \tag{4.6}$$

where r_{fs} is the focal spot radius, D the foil thickness and θ the full divergence angle of the hot electron transported beam[2]. In this picture once again a spatial cut-off is imposed to the source of the field, but in transverse rather than in longitudinal direction. The presence of a cylindrical negatively charged cloud induces a circular positive surface charge on the target rear side, which provides acceleration of test ions by means of Coulomb repulsion. The generated electro-static potential is thus evaluated via Poisson equation, in the vacuum region, restricted to the charge density axis of symmetry. This limitation is due to the interest in $E_{\max}$, since the most energetic ions are likely to be accelerated along the hot electron sheath axis, where the electric field reaches the highest values. The resulting ϕ is limited for large distances, as a

[1] This is actually consistent with the classic TNSA process, in which the protons sitting in the surface impurity layer are efficiently accelerated before the heavier ions.

[2] As explained in Sec. 3.1.2 an estimate as Eq. (4.6) assumes a ballistic transport dynamics for the electrons inside the target.

consequence of the transverse spatial cut-off, providing a maximum energy estimate:

$$E_{\mathrm{i},\infty} = 2Z_{\mathrm{i}} m_{\mathrm{e}} e \sqrt{\frac{\eta P_{\mathrm{p}}}{c}}\,, \tag{4.7}$$

in which $P_{\mathrm{p}} = E_{\mathrm{p}}/\tau_{\mathrm{p}}$ is the laser pulse power, and η is the absorption coefficient. In Ref. [46] the estimate of Eq. (4.7) is interpreted as the energy gained through an infinite time of acceleration. In order to reproduce the experimentally observed energies, the authors assume that acceleration turns off at $t = \tau_p$. Thus, once the potential $\phi(x)$ is known, the ion equation of motion is solved and $E_{\max}$ is evaluated at the temporal cut-off, which is chosen equal to pulse duration τ_p. More in detail, the maximum ion energy is evaluated analytically via the inversion of:

$$\frac{\tau_p}{\tau_0} = X\left(1 + \frac{1}{2}\frac{1}{1-X^2}\right) + \frac{1}{4}\ln\frac{1+X}{1-X}\,, \tag{4.8}$$

in which $X = \sqrt{E_{\max}/E_{\mathrm{i},\infty}}$ and $\tau_0 = R_{\mathrm{sh}}(m_{\mathrm{i}}/2E_{\mathrm{i},\infty})^{1/2}$ is a typical time appearing in the description. This theoretical estimate introduces the feature of an optimal pulse

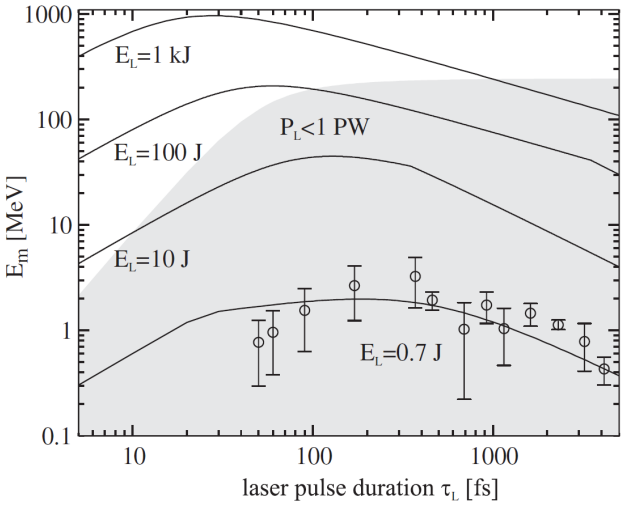

Figure 4.4: - Dependence of maximum proton energies $E_{\mathrm{m}} \equiv E_{\max}$ on laser pulse duration $\tau_{\mathrm{L}} \equiv \tau_{\mathrm{p}}$ evaluated at four constant laser energies E_{L}. The theoretical results are obtained by Eq. (4.8) for $r_{\mathrm{fs}} = 4\,\mu$m, $D = 10\,\mu$m and $\theta = 20°$. The circles represent a set of experimental data published as a support for the model. The gray shaded area denotes the region where the laser pulse power is smaller than 1 PW (Figure from Ref. [46]).

duration at fixed energy, also apparently supported by some experimental measurements [46] (see Fig. 4.4).

The imposition of both spatial and temporal external cut-offs, the latter in particular, represents a serious limit of this model. On the one hand the spatial charge cut-off can be reasonable in an approximate description of charge separation, provided that the field is studied along the central symmetry axis. On the other hand, as seen

in Sec. 4.1.1, there is no physical reason for ion acceleration to be artificially turned off after τ_p, once the electro-static system is defined.

Such a theoretical problem is faced in an alternative way by the second quasi-static description considered, that is the Passoni-Lontano model, first presented in Ref. [169], and later extended to a relativistic formulation in Refs. [50, 170]. Starting from the classic picture of one-dimensional Poisson-Boltzmann equation, the authors assumed that, while the quasi-static equilibrium is reached, some energetic electrons can escape the system and do not affect the electro-static field. This assumption, also supported by experimental evidences of electron emission and positive target charging [173, 174], leads to a description of the hot electron population by means of an energy-truncated 1D Maxwell-Jüttner distribution function:

$$f_{\mathrm{h}}(x,p) = \mathcal{H}\left[e\phi(x) - E_{\mathrm{h}}(p)\right] \frac{\tilde{n}}{2m_{\mathrm{e}}c\mathcal{K}_1(\zeta)} \exp\left[-\zeta\left(\gamma(p) - \frac{e\phi(x)}{m_{\mathrm{e}}c^2}\right)\right], \tag{4.9}$$

where the factor $\tilde{n}$ is a normalization coefficient for the resulting density function, since the momentum part is already normalized. In Eq. (4.9) $\gamma = \sqrt{1 + p^2/m_{\mathrm{e}}^2c^2}$, $\zeta = m_{\mathrm{e}}c^2/k_{\mathrm{B}}T_{\mathrm{h}}$ and $\mathcal{H}$ is the Heaviside function. The latter formalizes a space-dependent cut-off for the hot electron kinetic energy E_{h} at $E_{\mathrm{h}} = e\phi(x)$, which determines an electron density deviating from the Boltzmann function (4.1):

$$n_{\mathrm{h}}(x) = \int_0^\infty f_{\mathrm{h}}(x,p)\,\mathrm{d}p = \tilde{n}\frac{I\left(\varphi(x),\zeta\right)}{\zeta\mathcal{K}_1(\zeta)} \exp\left[\varphi(x)\right], \tag{4.10}$$

where the following definitions are used:

$$\varphi \equiv \frac{e\phi}{k_{\mathrm{B}}T_{\mathrm{h}}}, \qquad \beta(\varphi,\zeta) \equiv \sqrt{(\varphi+\zeta)^2 - \zeta^2}, \qquad I\left(\varphi,\zeta\right) \equiv \int_0^{\beta(\varphi)} \mathrm{e}^{-\sqrt{\zeta^2+p^2}}\mathrm{d}p\,. \tag{4.11}$$

The charge distribution determined by the hot electron density of Eq. (4.10), with the step-like density profiles of target cold electrons and ions, gives rise to a finite self-consistent potential difference $\Delta\phi(x)$. The latter exhibits a maximum corresponding to the highest kinetic energy E_{h}^* allowed by Eq. (4.9), defined as a boundary condition in the quasi-neutral region of the plasma and located well inside the target at $x < 0$. According to this quasi-static approach, $E_{\max}$ is readily evaluated as $Z_{\mathrm{i}}e\Delta\phi(0)$, which is the energy gained by an ion running down the potential slope starting from the matter-vacuum interface. The general relativistic solution, recovered in Ref. [170], reads:

$$E_{\max} = Z_{\mathrm{i}}k_{\mathrm{B}}T_{\mathrm{h}}\left[\varphi^* - 1 + \frac{\beta\left(\varphi^*,\zeta\right)}{I\left(\varphi^*,\zeta\right)\mathrm{e}^{\zeta+\varphi^*}}\right]. \tag{4.12}$$

Besides the ion charge Z_{i}, Eq. (4.12) depends on the hot electron distribution parameters, namely the temperature T_{h} and the normalized energy cut-off $\varphi^* = E_{\mathrm{h}}^*/k_{\mathrm{B}}T_{\mathrm{h}}$.

In this model, though an external cut-off is exploited once again to prevent energy from diverging, the finite $E_{\max}$ is obtained self-consistently according to the system initial conditions, without a posteriori impositions on particle dynamics. Moreover this

picture defines an electro-static potential difference which is always finite, being more attractive from a theoretical point of view, so that the acceleration process neither needs to be turned off artificially nor it requires the long adiabatic cooling times. The relevant question concerns how such a cut-off should be evaluated, a problem which is widely discussed in the following chapter of the present thesis.

4.1.3 Hybrid Models

The quasi-static approach turns out to be a convenient framework to study the very first stage of TNSA but, unlike in fluid models, it rules out any possibility to describe collective motion of ions and its consequences. For this reason few "hybrid models", which try to properly combine features from both fluid and quasi-static descriptions, have been proposed.

Here, two hybrid models are analyzed and compared, the Albright's layered target description, presented in Ref. [47] and the Robinson's moving sheath model, presented in Ref. [48].

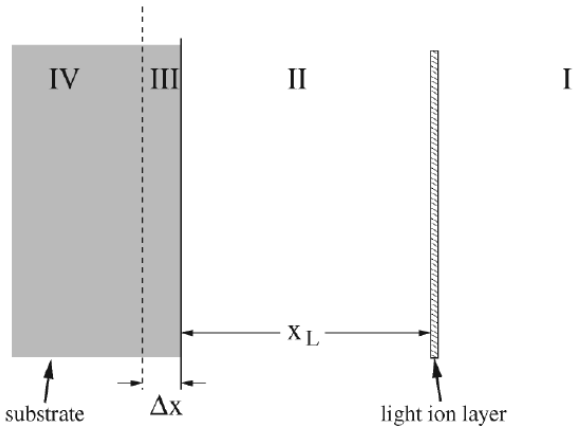

Figure 4.5: - Schematic representation of the planar model of target rear side according to Ref. [47], from which the figure is re-printed. The light ion layer is initially deposited on the heavy ion substrate. The authors define 4 regions: I is the vacuum region outside the light ion bunch, II is the vacuum region delimited by the substrate and the light ion bunch, III is the substrate region in which the electro-static field is gradually shielded up to IV, where the plasma is quasi-neutral and the boundary quantities are defined.

In Ref. [47] a first approximated inclusion of ion dynamics effect on the accelerating field is provided. Here, the bunch of accelerated light ions is treated as a layer of negligible thickness, that carries a defined superficial charge Q_{i} longitudinally distributed as a delta-function, according to the scheme sketched in Fig. 4.5. This picture is meant to take into account the effect of light ion acceleration on the quasi-static field, which is affected as the accelerated charge layer position changes. The electron density is still chosen to be Boltzmann-distributed, and the resulting quasi-static potential is divergent at large distances. Anyway, due to the moving charge layer effect, a finite estimate

of maximum ion energy is achieved. If heavy ions are supposed immobile, Poisson equation provides a solution for the electro-static field as a function of the layer position x_L and of the potential $\phi_\mathrm{L} = \phi(x_\mathrm{L})$. The resulting field changes form discontinuously shifting from region I to II of Fig. 4.5. The median field acting at x_L, obtained by analytical inversion of the self-consistent potential solution, can be then numerically integrated for $x_\mathrm{L} \to \infty$. This integration provides an estimate of the energy transferred from the self-consistent field to the ion layer as $x_\mathrm{L} \to \infty$ (see Ref. [47] for more detailed discussion on calculations), corresponding to the maximum ion energy. As a result of numerical calculations a scaling law for E_max as a function of the normalized surface charge $q = Q_\mathrm{i}/en_\mathrm{h0}\lambda_\mathrm{Dh}$ is obtained:

$$E_\mathrm{max} = Z_\mathrm{i} k_\mathrm{B} T_\mathrm{h} f(q)\,, \tag{4.13}$$

where the function f is defined by:

$$f(q) = 3.40 - 2.66\ln(q) - 0.182\ln^2(q)\,. \tag{4.14}$$

This relation is valid in the range $0.003 \leq q \leq 0.3$, which contains typical TNSA values. In a second stage, a rough approximation of heavy ion dynamics is also considered, as a further development of the description, by treating them as a fluid which expands self-similarly according to the substrate charge density. The present analysis is however limited to the fixed substrate version of Albright's description, since when heavy ion dynamics is added to the system, the evolution gets more complex and only a mean ion energy estimate is directly available by analytical calculations. A similar approach to that proposed by Albright et al. in Ref. [47] has been explored in Ref. [164], studying ion spectra evolution determined by a layered plasma description.

Bulk ions fluid dynamics is also a key-feature in Robinson's model [48], in which light ions are treated as test particles accelerated in the electro-static field, the latter being evaluated by the usual Poisson-Boltzmann equation, according to a simple quasi-static scheme, as that of Ref. [171]. However, in this model the substrate heavy ion dynamics is implemented in the description, resulting in an evolution of the quasi-static field, which affects light ion acceleration. The heavy ions are in fact assumed to behave as in the isothermal expansion model proposed in Ref. [44], that means they follow Eq. (4.2). The substrate front position is given by:

$$x_\mathrm{s} = \sqrt{8\mathrm{e_N}}\left[\tau_\mathrm{s}\log\left(\tau_\mathrm{s} + \sqrt{\tau_\mathrm{s}^2+1}\right) - \sqrt{\tau_\mathrm{s}^2+1} + 1\right]\,, \tag{4.15}$$

where $\tau_\mathrm{s} = \omega_\mathrm{ps} t/(2\mathrm{e_N})^{1/2}$ and ω_ps is the plasma frequency of the substrate ions. Eq. (4.15) is retrieved from Eq. (4.2) as a result of the fitting proposed in Ref. [44]. Then, the electro-static field retrieved from Poisson-Boltzmann integration reads:

$$\mathcal{E}(t) = \frac{\sqrt{2}k_\mathrm{B}T_\mathrm{h}}{e\lambda_\mathrm{Dh}}\exp\left(\frac{e\phi_\mathrm{s}(t)}{2k_\mathrm{B}T_\mathrm{h}}\right)\left[1 + \frac{x - x_\mathrm{s}(t)}{\sqrt{2}\lambda_\mathrm{Dh}}\exp\left(\frac{e\phi_\mathrm{s}(t)}{2k_\mathrm{B}T_\mathrm{h}}\right)\right]^{-1}\,, \tag{4.16}$$

in which ϕ_s is the potential at the substrate front position. In the evaluations of Ref. [48] as well as in those following, the time-dependent function ϕ_s is approximated to a constant[1].

Integration of light-ion motion under the field of Eq. (4.16) provides in principle a maximum energy prediction E_{max}. However, because of the initial hypothesis of Boltzmann density, electro-static potential is again divergent at large distances, determining infinite acceleration. The issue can be solved here by imposing a temporal cut-off as in the isothermal expansion model, so that the equation of motion is integrated up to $t = t_{acc}$. Nonetheless, it has to be underlined that the imposition of t_{acc} as a cut-off cannot be attributed to the authors of Ref. [48], since they do not address the issue of quantitatively predicting E_{max}. In the paper the model results are compared to isothermal expansion or to numerical simulation results at some specific simulation time, focusing the attention on heavy ion population effects, as for example the qualitative structure of multi-species ion spectra, rather than on the maximum energy prediction.

Robinson's model completes the set of descriptions involved in the comparative study discussed in Secs. 4.2 and 4.3; it is worthwhile to point out once again how in each of the considered models an E_{max} estimate technique has been retrieved, involving mostly analytical calculations, except for some straight-forward numerical integration or function inversion. Such kind of energetic predictions are potentially very useful in the experimental framework, because they can in principle enlighten the most convenient paths to E_{max} improvement. However, since the models come to different conclusions, it is useful to have a better understanding of the reliability and domains of applicability of their energy predictions. The analysis presented in the following aims just at this purpose.

4.2 Methods

The prediction capability achieved by the introduced TNSA models can be tested comparing the theoretical E_{max} estimates to actual experimental values. The formulas in Sec. 4.1 show that, to implement the maximum energy calculation, a specific set of system parameters is required by each different model. Some of them are readily available in experimental papers while some others need to be estimated, so that the following distinction is possible:

Parameters - The actual system parameters which are considered known or detected in all the experiments. Examples are the laser pulse properties and the target thickness D.

Estimates - Those quantities which are not directly accessible to measurement or typically not provided in experimental papers. These ones are usually related to hot electron generation and dynamics and have to be coherently estimated from the parameters exploiting empirical scalings or models.

[1] Since the potential carries an arbitrary integration constant, in fact ϕ_s can be set to 0.

In Table 4.1 the required input quantities are organized according to these two categories and summarized for each model; while each of them has been previously defined, the definitions are also gathered for convenience in Table 4.2.

For the present comparative analysis, an extensive set of parameters have been collected, together with the corresponding measured $E_{\max}$, in an experimental database. Then, for each of the experiments included in such a database, estimates have been retrieved according to coherent criteria, so that evaluation and comparison of the different $E_{\max}$ predictions is possible. Eventually, the six energy theoretical estimates are compared to actual measured values and the predicting capability of each model is judged over a wide-range of laser-target conditions.

In the following the methods adopted to retrieve parameters and estimates are described in detail.

4.2.1 Experimental Database

The database of collected measurements contains 34 ion maximum energies detected since the first pioneering works of 2000, in experimental campaigns held on a large number of laser facilities with various purposes. The comprehensive collection of experimental parameters, ion energies and corresponding references is shown in the Appendix. A wide range of laser and target parameters has been correspondingly obtained: overall the laser intensity range is $3 \times 10^{18} - 6 \times 10^{20}$ W/cm^2, the laser energy range is $0.1 - 500$ J and the pulse duration varies from 30 fs to 1 ps. The targets considered are either metal or insulator planar foils of several materials, with thicknesses from the 10 nm of DLC foils of Ref. [109] to the 125 μm Aluminum targets used in the experiment of Ref. [8]. Actually in several experiments different target thicknesses are tested, in order to be optimized because it has experimentally turned out that TNSA is quite sensible to such a parameter. In the database only the optimum D shots are considered, in an attempt to rule out as far as possible the influence of target thickness. Concerning this, it is worthwhile to underline that the optimum thickness ultimately depends on laser contrast, as demonstrated in Refs. [29, 31] (see Sec. 2.3). A typical contrast ratio is about 10^{-7} on a few nanosecond timescale, but in TNSA experimental results conditions can be widely different. In the present database, whenever possi-

Model	Parameters	Estimates
Isothermal Expansion	I, τ_{p}, λ, Z_{i}, m_{i}	t_{acc} n_{h0}, η, T_{h}
Adiabatic Expansion	I, D, λ, Z_{i}, m_{i}	n_{h0}, η, T_{h}
Schreiber	I, P_{p}, D, λ, τ_{p}, r_{fs}, Z_{i}, m_{i}	t_{acc}, θ, η
Passoni-Lontano	I, E_{p}, λ, Z_{i}, m_{i}	φ^*, T_{h}
Albright	I, λ, Z_{i}, m_{i}, Z_{s0}, n_{s}, m_{s}	n_{h0}, Z_{s}, Q_{i}, η, T_{h}
Robinson	I, λ, Z_{i}, m_{i}, Z_{s0}, n_{s}, m_{s}, τ_{p}	n_{h0}, Z_{s}, t_{acc}, η, T_{h}

Table 4.1: Parameters and estimates required by each model for $E_{\max}$ evaluation. The symbol definitions are summarized in Tab. 4.2

Symbol	Definition
I	Laser intensity
λ	Laser wavelength
τ_{p}	Pulse duration
P_{p}	Laser power
E_{p}	Pulse energy
r_{fs}	Focal spot radius
Z_{i}	Accelerated ion charge number
m_{i}	Accelerated ion mass
D	Foil thickness
t_{acc}	Acceleration duration time
n_{h0}	Hot electron density in the quasi-neutral region
n_{s}	Substrate plasma density
Z_{s0}	Substrate material atomic number
Z_{s}	Substrate ion charge state
m_{s}	Substrate ion mass
Q_{i}	Impurity proton layer surface charge density
η	Laser-hot electrons absorption efficiency
T_{h}	Hot-electron temperature
θ	Hot-electron beam full-divergence angle
φ^*	Normalized hot-electron energy cut-off

Table 4.2: Table of definitions for the parameters used in the model implementation.

ble, data obtained in "normal" contrast illumination are chosen. For example, among the results of Ref. [31], which have been recovered with and without DPM device (see Sec. 2.3) to have both ultra-high and normal contrast data, the second ones have been selected. However, to gather a comprehensive database, also those experimental cases where only UHC results are available have been included, as for example the shots on DLC presented in Ref. [109], obtained using a DPM configuration.

Almost all the considered data concern impurity layer proton acceleration, except for the C^{5+} and C^{6+} ion acceleration reported respectively in Refs. [37] and [103, 109]. In Fig. 4.6 all the E_{max} are plotted against laser irradiance; in the case of carbon ion acceleration E_{max} indicates the energy per nucleon, in order to be comparable, at least in principle, with proton results.

From the second column of Tab. 4.1 it is clear that the parameters basically consist in laser and target features. If the latter are usually well known a priori, since target foils are properly manufactured to comply with experimental purposes, laser pulse properties need to be measured, because focusing in general does not provide precisely reproducible pulse features. In this frame it must be said that in different experiments laser configuration parameters are usually diagnosed and controlled using different techniques, and that the published data can lack of some useful information or

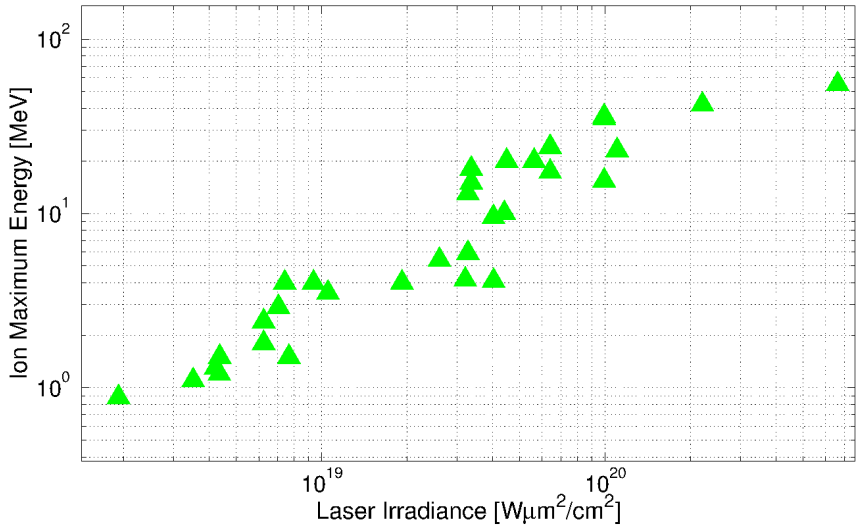

Figure 4.6: - Double logarithmic plot of all experimental $E_{\max}$ measurements included in the database, in function of the laser pulse irradiance. Main experimental parameters and Refs. for each of the results are indicated in the Appendix.

be affected by different kind of uncertainties. For example the laser intensity provided in a paper can refer either to directly measured peak intensity, or to average intensity estimated by laser nominal features using Eq. (2.1). In order to achieve a consistent comparative study, some criteria for the collection of the laser parameters have to be defined, trying to treat the database as much coherently as possible.

The relation among laser pulse intensity, power, energy and duration is of key importance. Usually Eq. (2.1) is considered, since laser spatial and temporal profiles are anything but regular and average quantities can only be controlled. This means that the intensity I is referred to a circular focal spot $A_{\rm fs}$ of radius $r_{\rm fs}$, supposed uniform and uniformly irradiated for a time-lapse $\tau_{\rm p}$. However, several experimental paper provide values of FWHM duration time or focal spot, or otherwise of measured peak intensity. For this reason it is convenient to define the equivalent of Eq. (2.1) for a Gaussian profile, and look for the relationships among different parameters.

The energy density contained in a Gaussian-shaped pulse is given by:

$$I(x,y,t) = I_0 \exp\left[-\log 2\left(\frac{x^2+y^2}{r_{\rm F}^2} + \frac{4t^2}{\tau_{\rm F}^2}\right)\right], \tag{4.17}$$

where I_0 is the peak intensity, x and y are the transversal coordinates, while $r_{\rm F}$ and $\tau_{\rm F}$ are the FWHM radius and duration. If Eq. (4.17) is integrated over the transversal plane, the laser power $P_{\rm p}(t)$, normally distributed over t, is obtained. The peak power $P_{\rm p0}$ is thus related to pulse energy according to:

$$P_{\rm p0} = \sqrt{\frac{4\log 2}{\pi}}\frac{E_{\rm p}}{\tau_{\rm F}} \simeq \frac{E_{\rm p}}{\tau_{\rm F}}. \tag{4.18}$$

In the transverse plane the situation is slightly more involved since, according to Eq. (4.17), only a fraction $\eta_F \simeq 0.58$ of pulse energy is contained within the focal spot delimited by r_F. The mean intensity corresponding to I in Eq. (2.1) can be chosen as the intensity contained in such a spot, obtaining:

$$I = \frac{\eta_F I_0}{\log 2} = \frac{\eta_F P_{p0}}{\pi r_F^2} \simeq \frac{\eta_F E_p}{\tau_F \pi r_F^2} \,. \tag{4.19}$$

Eq. (4.19) is the equivalent of Eq. (2.1) for the Gaussian case, providing the mean intensity I within the FWHM focal spot. Relations (4.17),(4.18) and (4.19) are then used to collect laser parameters coherently, according to those quantities which are provided by each experimental paper and those which are not available.

It is worthwhile to underline that an important parameter as the laser incidence angle θ_{inc}, which plays a key role in the framework of laser-matter interaction, is not included in the present analysis. As explained in Sec. 3.1.1 the influence of incidence angle in laser absorption is non-trivial, and the effects on hot electron generation are hardly predictable with simple calculations. Therefore, though the database contains results coming from different θ_{inc}, incidence angle is set-aside and included among the sources of uncertainties in E_{max} estimate.

4.2.2 Estimates

Quantities which are not directly accessible in experiments, listed in column 3 of Tab. 4.1, need to be retrieved exploiting empirical data and scalings, or by means of simple theoretical models and reasonable assumptions. In Refs. [44, 45, 46, 47, 48, 170], where TNSA effective descriptions are formulated, techniques to obtain such estimates are, in most of the cases, already provided. Therefore, a fair approach to retrieve such missing quantities is to follow authors prescriptions whenever available, or else to use the same estimate evaluation for all the models. Here, the estimate techniques used in the comparative studied are outlined.

From Tab. 4.1 it is evident that hot electron features, resulting from laser-matter interaction and electron-transport phases of TNSA, constitute an important set of the required estimates. As discussed in Sec. 3.1.1, hot electron properties need to be estimated because of the difficulties in properly measuring them and due to the lack of a reliable theoretical model for laser-matter and transport physics. For the hot electron temperature however, few formulas relying on simple theoretical absorption models or comprehensive set of empirical data, are available. For example, the ponderomotive scaling given in Eq. (3.45), has been widely used to predict T_h, showing nice agreement with experimental results at TNSA intensity range (as supported by Fig. 3.7). Moreover, Eq. (3.45) is pointed out as the most reliable temperature prediction by the TNSA model authors and the majority of TNSA theoretical works; for such reasons in the following analysis it is exploited as the main expression to retrieve T_h.

Another hot electron feature which is required by 4 out of 6 models is n_{h0}, namely the hot electron density at the left boundary of the initial electro-static system, that is deep inside the target, where the TNSA field is shielded by the ion bulk. As anticipated

in Sec. 3.1.2 the hot electron density is typically $\sim 1\%$ of the solid density, which means about 10^{21} particles/cm^3. A convenient estimate for n_{h0} can be obtained on the basis of energy conservation:

$$\eta E_{\mathrm{p}} = N_{\mathrm{h}} \langle K \rangle \,, \tag{4.20}$$

where $\langle K \rangle$ is the mean hot electron kinetic energy, which can be modeled by Eq. (3.47), assuming a relativistic Maxwell-Jüttner distribution. If Eq. (4.20) is differentiated in $\mathrm{d}x$, $\mathrm{d}y$ and $\mathrm{d}z = c\mathrm{d}t$, one obtains:

$$\eta I(x, y, t) = c n_{\mathrm{h}}(x, y, z) \langle K \rangle \,. \tag{4.21}$$

n_{h0} can be now estimated by averaging Eq. (4.21) over the focal spot and the time duration:

$$n_{\mathrm{h0}} = \frac{\eta I}{c \langle K \rangle} \,. \tag{4.22}$$

This criterion to retrieve n_{h0} has been used in different theoretical works, as for example in Refs. [46, 47] where a non-relativistic formula is exploited. In other works, as for example those of Refs. [29, 33] a development of Eq. (4.22), taking into account hot electron beam divergence is proposed. The idea is that the density estimated by Eq. (4.22) holds just close to the focal spot where electrons are heated, while at the target back side, n_{h} decreases due to ballistic electron expansion, so that

$$n_{\mathrm{h0}}^{(1)} = n_{\mathrm{h0}} \frac{r_{\mathrm{fs}}^2}{\left(r_{\mathrm{fs}} + D \tan \theta / 2\right)^2} \tag{4.23}$$

is the correct estimate for the hot electron boundary density because acceleration, at least in the TNSA model, takes place in correspondence of the rear surface of the target. Eq. (4.23) requires three more parameters, focal spot radius, target thickness and hot electron divergence, that should be added in column 2 of Tab. 4.1, if this estimate is used. In the comparative analysis n_{h0} is mainly evaluated by means of Eq. (4.22), maintaining the non-relativistic formula for the Albright model, according to the author suggestion. The alternative use of Eq. (4.23) is discussed as well, also in the light of the role it plays in the work presented in Ch. 5.

Eq. (4.22) (and thus also Eq. (4.23)) requires itself a further estimate, that is the fraction η of energy absorbed by the hot electrons. As anticipated in Sec. 3.1.1 this quantity is one of the most difficult to obtain, due to the complexity of hot electron generation dynamics, and to the absence of some general reliable scalings as for example those of T_{h} (see Fig. 3.6). Authors of Ref. [46] propose to use an empirical scaling for η, published as a result of a parametric study (Ref. [136]) and of a collection of measurements (Ref. [175]). The estimate reads:

$$\eta = \min \left[1.2 \times 10^{-15} (I\lambda^2)^{3/4}; \, 0.5 \right] \,, \tag{4.24}$$

Where the irradiance is in units of Wμm^2/cm^2. It should be said that different η scalings for various TNSA intensity ranges have been proposed, as for example in Ref. [135],

where the η measurements represented in Fig. 3.6 have been fitted with the following power law:

$$\eta = \left(2.3 \times 10^{-22} I\lambda^2\right)^{0.2661} , \tag{4.25}$$

where $I\lambda^2$ is still in Wμm^2/cm^2. Eqs. (4.24) and (4.25) set different behaviors; anyway over the TNSA relevant $10^{18} - 10^{21}$ Wμm^2/cm^2 range, the estimates provide similar values.

As for the hot electron divergence, which is required only by Schreiber's model[1], Ref. [46] proposes a phenomenological dependence on laser energy. According to such relation the angular spread for energies smaller than 5 J is $\theta = 20°$ [29], for $5 < E_\mathrm{p} < 50$ J it raises to $\theta = 50°$ [33, 36] while for higher energies $\theta = 90°$ [176]. Of course this criterion is not accurate and leads to uncertainties in the final estimate, but, as discussed in Sec. 3.1.2 there is presently no reliable divergence theory.

The last parameter related to hot electrons which has to be estimated is φ^*, namely the normalized energy cut-off for the hot electron distribution (4.9) adopted in Passoni-Lontano quasi-static description. A model to evaluate φ^* is not available so far, for such a reason in Ref. [50] an empirical scaling law, based on a restricted ion acceleration database, has been proposed:

$$\varphi^* = 4.8 + 0.8 \log(E_\mathrm{p}) , \tag{4.26}$$

where E_p is the laser pulse energy in units of [J]. An interesting challenge in the framework of Passoni-Lontano TNSA theory would then be to give a satisfactory theoretical explanation to this empirical behavior, as discussed more in depth in the next chapter.

Among the other quantities to be estimated, half of the models require a temporal cut-off to the acceleration process, as explained in Sec. 4.1. As previously mentioned, the common approach adopted by several works in the literature is to choose t_acc proportional to laser duration τ_p. In Ref. [33] the scaling of t_acc has been tuned to $1.3\,\tau_\mathrm{p}$, by fitting isothermal expansion model predictions to experimental data. In a subsequent work (Ref. [177]) the fit has been further refined by adding an offset time, to be used when $\tau_p < 150$ fs, in order not to unacceptably underestimate t_acc for ultra-short pulses:

$$t_\mathrm{acc} = 1.3\,\tau_p (+78 \text{ fs}) . \tag{4.27}$$

In the presented comparison Eq. (4.27) is used for Mora isothermal expansion model and for Robinson hybrid description, since no precise suggestion about acceleration duration is made. In Schreiber model, instead, the acceleration duration is explicitly required by the authors to stop at $t_\mathrm{acc} = \tau_\mathrm{p}$, so this prescription is followed.

The remaining estimates are required by the hybrid models and concern the target ion structure. The first is Q_i, namely the surface proton charge density in hydro-carbon impurity layer, once this is completely ionized by the TNSA field. This quantity, which is used by Albright's moving layer description, is not usually controlled in experiments, so that a typical empirical value needs to be considered. The proton density is usually one/two orders of magnitude less than the solid density $\sim 10^{21}$ cm^{-3}, and the impurity

[1] Provided that n_h0 is not estimated by Eq. (4.23).

Quantity	Estimate
T_h	$m_\mathrm{e}c^2/k_\mathrm{B}\left(\sqrt{1+a_0^2}-1\right)$
n_h0	$\eta I/c\langle K\rangle$
η	$\min\left[1.2\times10^{-15}(I\lambda^2)^{3/4};\,0.5\right]$
θ	20° for $E_\mathrm{p}<5\,\mathrm{J}$ 50° for $5<E_\mathrm{p}<50\,\mathrm{J}$ 90° for $E_\mathrm{p}>50\,\mathrm{J}$
φ^*	$4.8+0.8\log(E_\mathrm{p})$
t_acc	$1.3\,\tau_p(+78\text{ fs})$
Q_i	$e\times10^{15}\,\mathrm{C/cm^2}$ for metal targets $5e\times10^{15}\,\mathrm{C/cm^2}$ for plastic targets
Z_s	$Z_\mathrm{s0}/2$ even Z_s0 metal targets $(Z_\mathrm{s0}-1)/2$ odd Z_s0 metal targets 6 for plastic targets

Table 4.3: Table summarizing the estimate techniques used for the quantities in the third column of Tab. 4.1.

layer depth is of $\sim 10\,\mathrm{nm}$, resulting in a surface charge of $10^{15}\,e/\mathrm{cm}^2$. On the basis of such assumptions, if Q_i is not given experimentally paper, it is estimated to be $10^{15}\,e/\mathrm{cm}^2$ for metal targets, and 5 times larger for plastic targets.

The last estimate regards ion substrate charge state Z_s. Since strong ionization occurs, the substrate plasma density n_s can be assumed to be substantially equal to the target material solid density, while Z_s is not trivial to predict. In fact, as introduced in Sec. 3.1.1, ionization physics is an extremely complex topic and reliable theoretical predictions are not straightforward to obtain. As it can be seen from heavy ion acceleration detection, in general different ion species are created, with different, spatially dependent concentrations (see for example Fig. 2.4, or the corresponding reference [61]). Typically, in TNSA modeling, and in the more accurate approach of PIC simulations as well, a single, reasonable value for Z_s is chosen consistently with more frequently detected ions. As a rule of thumb here Z_s is chosen to be 6 for plastic targets, equivalent to fully ionized carbon atoms, or equal to half the atomic number for metal targets[1]. With Z_s the estimate list is completed, for convenience, all the criteria exposed in this

[1] If the atomic number is odd $Z_\mathrm{s}=(Z_\mathrm{s0}-1)/2$

section have been summarized in Tab. 4.3.

The equations of Tab. 4.3, together with the experimental database accounted in the Appendix, provide all the necessary input parameter to perform $E_{\max}$ estimates according to each of the six considered TNSA models. It is however important to underline that the use of such estimates introduces some arbitrariness in the analysis, and this has to be taken into account in the discussion of the obtained results.

4.3 Results and Discussion

In the present section the results of the comparative analysis are presented and discussed. In Fig. 4.7 different theoretical predictions, obtained according to the model implementation previously described, are plotted against the laser irradiance, together with the experimentally detected energies. In order to keep the data representation as clear as possible $E_{\max}$ results are organized in six sub-figures, one for each model predictions. From Fig. 4.7, since data are displayed in double logarithmic scale, it is evident that TNSA models cannot afford a precise agreement with experimental measurements, as it can be foreseen considering the strong approximations adopted by each of them. At the same time, in the light of such approximations, and of the wide variety of laser-target conditions involved, reliability of some theoretical predictions turns out to be remarkable.

In order to give a quantitative support to the evidences in Fig. 4.7 an estimator of average deviation between theoretical predictions and measurements has been evaluated, namely the mean relative difference between experimental and theoretical values:

$$\langle \Delta \rangle \equiv \frac{1}{N_{\text{exp}}} \sum_{i=1}^{N_{\text{exp}}} |\delta_{\text{rel},i}| \,, \tag{4.28}$$

where N_{exp} is the number of experimental database energies, indexed by i, and $\delta_{\text{rel},i}$ is given by:

$$\delta_{\text{rel},i} = \frac{E^{(\text{theo})}_{\text{max},i} - E^{(\text{exp})}_{\text{max},i}}{E^{(\text{exp})}_{\text{max},i}} \,. \tag{4.29}$$

The percentage values of $\langle \Delta \rangle$ corresponding to Fig. 4.7 estimates are:

$\langle \Delta \rangle_{\%} = 106.5\%$ - isothermal plasma expansion model,

$\langle \Delta \rangle_{\%} = 254.0\%$ - the adiabatic plasma expansion model,

$\langle \Delta \rangle_{\%} = 75.1\%$ - Schreiber model,

$\langle \Delta \rangle_{\%} = 25.6\%$ - Passoni-Lontano model,

$\langle \Delta \rangle_{\%} = 123.4\%$ - Albright model,

$\langle \Delta \rangle_{\%} = 51.6\%$ - Robinson model.

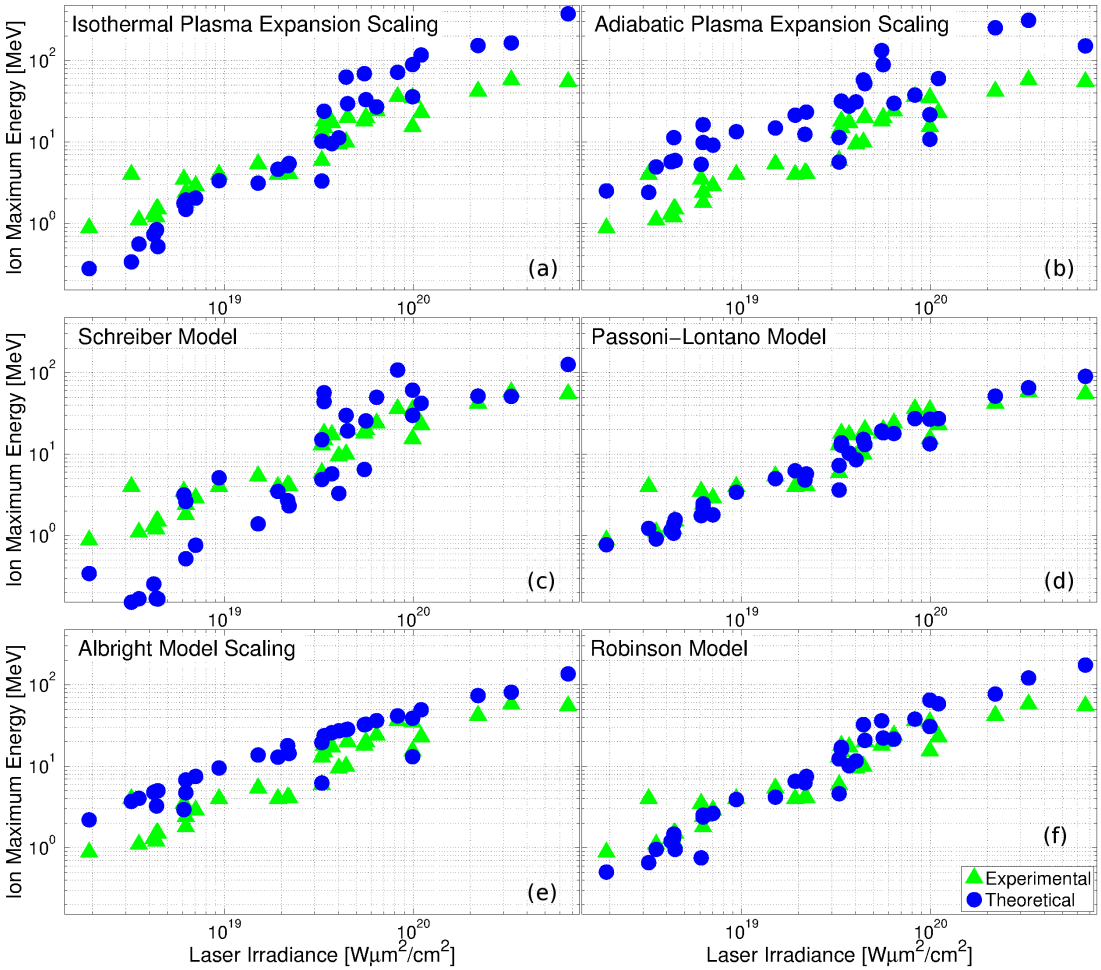

Figure 4.7: - Theoretical predictions of $E_{\max}$ (blue circles) for each of the six models, compared to the experimental measurements (green triangles). The energy is plotted against the laser pulse irradiance in double logarithmic scale.

Such results confirm quantitatively that the Passoni-Lontano energy estimates appear to be the most reliable for the entire set. In fact the values of $\langle\Delta\rangle$ underline that this theory achieves a remarkable agreement with experimental data, compared to other models, resulting in a mean deviation which is half that of Robinson model, the second best description in term of energy prediction. This is already an interesting result by itself, pointing out that quasi-static approach is the most convenient way to estimate $E_{\max}$ in ordinary TNSA experiments. This could be in some sense expected, since this approach is actually "dedicated" to the $E_{\max}$ prediction, while the knowledge of other TNSA aspects as ion conversion efficiency or specific spectra dynamics falls outside its purposes.

Despite this, as anticipated in the previous section, the choice of Table 4.3 estimate criteria, necessarily introduces some arbitrariness in the energy predictions, reducing the generality of the comparison outcomes. Therefore the present analysis can be drawn more in depth, working on the estimates of some quantities, in order to limit somehow this arbitrariness and to reach more robust conclusions.

A first interesting point regards the estimate of the hot electron boundary density n_{h0}, which in Fig. 4.7 is obtained by means of Eq. (4.22). As previously explained, in Ref. [29], and later in Ref. [33], it is proposed that n_{h0} should rather be evaluated using Eq. (4.23), which introduces the effect of hot electron expansion through the target bulk, reducing n_{h0} by a factor $1 + D/r_{\mathrm{fs}} \tan\theta/2$ according to collision-less ballistic transport hypothesis. On the one hand this observation makes sense, since TNSA models describe the physics taking place at the target rear side, but at the same time the use of Eq. (4.23) widens the number of required quantities with three more parameters, the focal spot radius r_{fs}, the target thickness D and the hot electron divergence angle θ. If the first two are readily available from experimental papers, θ is usually not measured and needs to be estimated by the empirical criterion reported in table 4.3. Moreover the ballistic collision-less transport assumption is a rough approximation of actual electron dynamics, so that Eq. (4.23) may introduce further uncertainties in the $E_{\max}$ calculation and may turn out to be not convenient for theoretical predicting capability. For such reasons it can be useful to observe how TNSA theories behave shifting from one n_{h0} estimate to the other. Four out of six models require n_{h0} as input parameter, namely the fluid isothermal and adiabatic expansion models and the hybrid Albright's and Robinson's descriptions. In Fig. 4.8 the ion cut-off energy estimates obtained by means of Eq. (4.23) are compared to those resulting from the use of Eq. (4.22) displayed together with experimental measurements. From the figure an improvement in agreement with experimental $E_{\max}$ is visible, for example observing that the three highest-irradiance energy predictions, strongly over-estimating the measurements if Eq. (4.22) is used, reduce the gap with experimental values in all four cases. On a quantitative basis the improvement translates in a clear reduction of $\langle\Delta\rangle_{\%}$ values. For the isothermal expansion model the estimator reduces from 106.5 % to 67.3 %, while the adiabatic description exhibits a deviation decrease from 254.0 % to 152.1 %. For the Albright model $\langle\Delta\rangle_{\%}$ falls from 123.4 % to 76.6 % and for Robinson description a slight improvement, from 51.6 % to 46.5 % is obtained. On the one hand

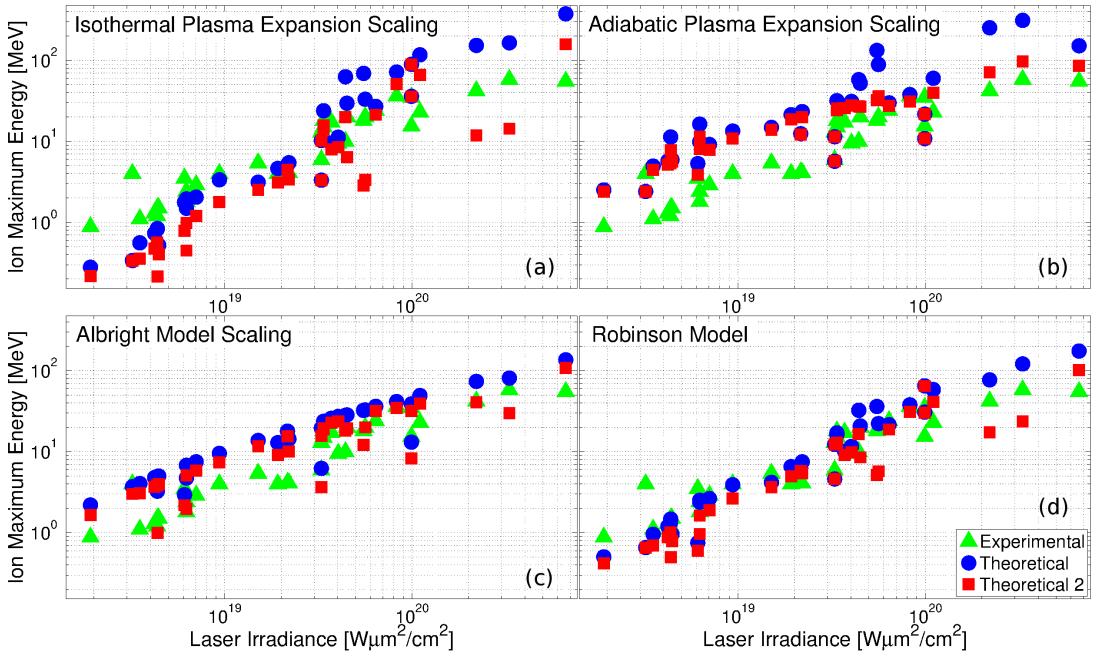

Figure 4.8: - Theoretical predictions of $E_{\max}$ for each model, compared to the experimental results. The energy estimates are retrieved by using both Eq. (4.22) (blue circles) and Eq. (4.23) (red squares) to evaluate n_{h0}.

these results lead to a revaluation of some $E_{\max}$ estimates as that of isothermal fluid expansion model, while on the other hand they support Eq. (4.23) as more suitable formula for hot electron boundary density evaluation. This is in agreement with the results of Refs. [29, 33] which exploit the idea of a ballistic hot electron transport in Eq. (4.23) to introduce foil thickness dependence in TNSA modeling, a concept which is developed more in detail in the next chapter.

The laser energy conversion η plays a role in both Eq. (4.22) and Eq. (4.23) estimates. If the empirical scaling (4.24), used to obtain the energies of Figs. 4.7 and 4.8, is substituted by Eq. (4.25) the general agreement with experimental data is mainly unchanged, with a sensible improvement registered only by Schreiber's description, for which $\langle\Delta\rangle$ reduces to 65 %. This test, while supporting somehow the more recent η estimate of Eq. (4.25), confirms that the incidence of this choice is not crucial for energy prediction as long as efficiency is kept within reasonable values, consistent with empirical observations (η varies from $0.1-0.2$ to $0.5-0.6$ over the considered irradiance range).

The picture gets more intricate if the hot electron temperature T_{h} estimate is considered. As explained in Sec. 3.1.1, while the ponderomotive scaling (Eq. (3.45)) seems to be the more suitable model for the typical TNSA intensity range, T_{h} measurement still remains a challenging physical problem and experimental achievements do not pro-

vide a clear picture. For this reason different T_h scaling laws have been proposed during last years (see e.g. Refs. [141, 142]); a popular alternative to the ponderomotive scaling is the so-called Beg Scaling, proposed in Ref. [5] by experimental data fitting, and given by:

$$T_\mathrm{h} = 0.215 \left(I\lambda^2\right)^{1/3} . \tag{4.30}$$

In the present comparative analysis, also Eq. (4.30) has been tested as temperature estimate, to observe how ion energies change in this case. In Fig. (4.9) the E_max values obtained with Beg scaling are represented as a function of laser irradiance together with the experimental values. The energy predictions are still obtained through the two n_h0 estimates, to underline different behaviors. At first sight it is evident that the scaling of E_max predictions becomes less steep than in Figs. 4.7 and 4.8, as expected because of the milder $I\lambda^2$ dependence of T_h in Eq. (4.30). Estimator $\langle\Delta\rangle_\%$ is once again useful to get a quantitative feeling of the model predictions general behaviors; the resulting values are collected in Tab. 4.4 and compared with those calculated by means of the ponderomotive scaling. The picture outlined by such values is quite complex, since on one side the use of Beg scaling remarkably reduces the mean overestimate of fluid models, while on the other side it spoils the agreement provided by other descriptions, as for example of Passoni-Lontano model. Moreover, as shown in Fig. 4.8, the choice of Eq. (4.23) to estimate n_h0, determines a general improvement of the predictions if T_h is retrieved via ponderomotive scaling. If, on the other hand, T_h is evaluated via Beg Eq. (4.23) a stronger underestimate of experimental values is retrieved.

Although these conflicting results make it difficult to draw some conclusions on T_h evaluation, in the following Eq. (3.45) is preferred to Eq. (4.30), because of two main reasons. First, the ponderomotive formula has exhibited a nice trend agreement with a large set of hot electron temperature measurements (see for example Fig. 3.7), and second, it has been broadly used in TNSA modeling literature, adopted as a proper T_h estimate especially by the authors of the considered models. Nonetheless, hot electron temperature estimate still remains one of the most subtle points in TNSA modeling and the theory requires substantial advances in this field.

From Sec. (4.1) it is evident that a key point in the formulation of different TNSA theories is that of the external cut-off required to prevent ion maximum energy from diverging, therefore it is interesting to discuss this aspect in the light of present analysis quantitative results. Three out of the six considered descriptions (isothermal, Schreiber's and Robinson's), include a temporal cut-off t_acc to stop acceleration.

As discussed in section 4.1, t_acc is often considered proportional to the laser pulse length τ_p, while it is clear that the acceleration process duration is directly related to the TNSA field dynamics, and thus to several other system parameters, including for example laser energy and intensity as well. This lack in the interpretation is implicitly admitted in Ref. [177] where the empirical 78 fs off-set of Eq. (4.27) is introduced to avoid excessive energy under-estimate for ultra-short pulse durations.

The present analysis makes it possible to point out, with quantitative bases, the limits of a temporal acceleration cut-off proportional to laser duration. In Fig. 4.10 the relative deviation $\delta_{\mathrm{rel},i}$ of the energy estimates from the experimental results is plotted

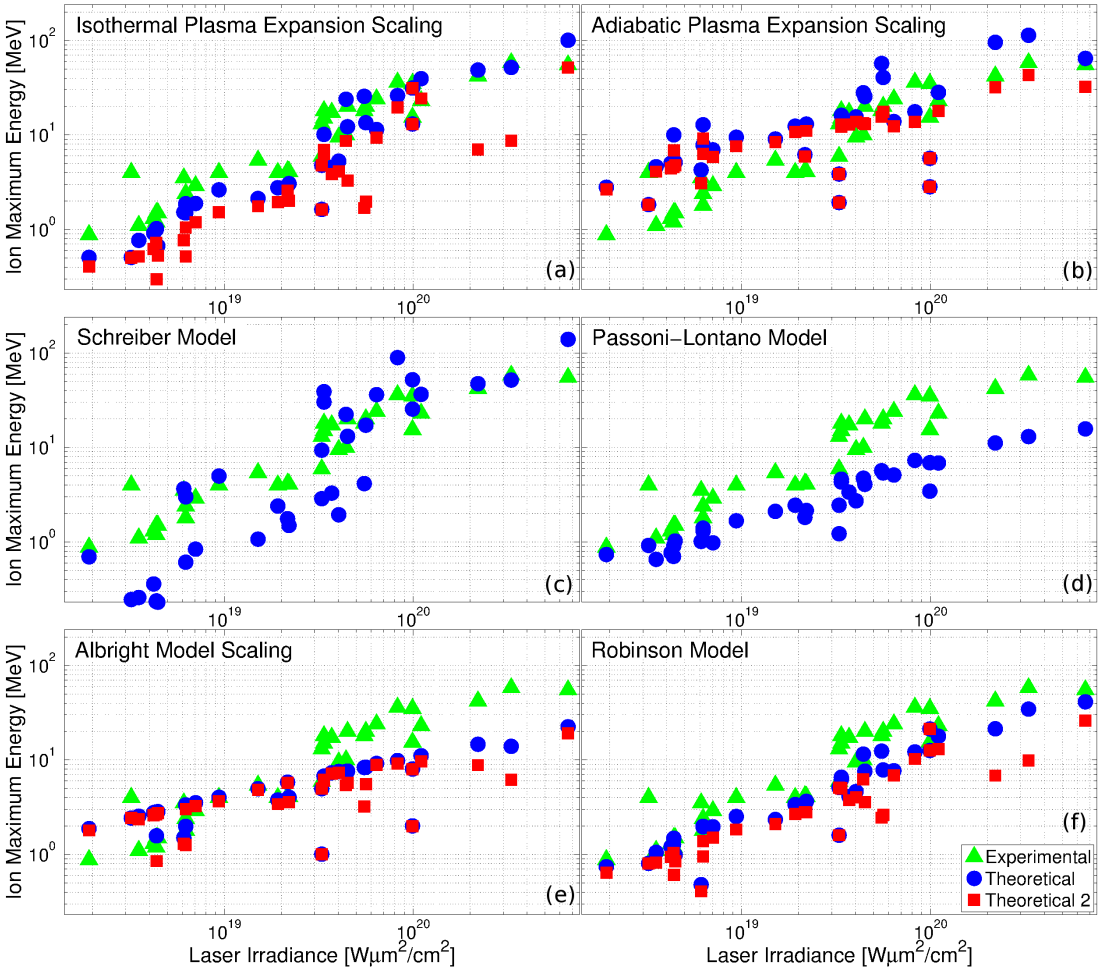

Figure 4.9: - Theoretical $E_{\max}$ predictions obtained using Beg temperature scaling for $T_{\rm h}$ (Eq. (4.30)). Blue circles and red squares are again referred to evaluations exploiting different $n_{\rm h0}$ estimates as in Fig. (4.8).

Model	Eq. n_{h0}	T_h scaling	$\langle\Delta\rangle_{\%}$
Isothermal Expansion	(4.22)	PM	92.6 %
		Beg	43.4 %
	(4.23)	PM	68.0 %
		Beg	57.2 %
Adiabatic Expansion	(4.22)	PM	248.9 %
		Beg	146.5 %
	(4.23)	PM	151.0 %
		Beg	105.3 %
Passoni-Lontano	None	PM	25.6 %
		Beg	61.6 %
Albright	(4.22)	PM	123.5 %
		Beg	59.9 %
	(4.23)	PM	77.1 %
		Beg	102 %
Robinson	(4.22)	PM	47.6 %
		Beg	38.9 %
	(4.23)	PM	42.7 %
		Beg	55.3 %

Table 4.4: - Comparison of $\langle\Delta\rangle_{\%}$ values obtained by means of different T_h estimates. PM stands for ponderomotive scaling of Eq. (3.45) and Beg refers to Eq. (4.30). For the four models requiring boundary hot electron density n_{h0} the estimates of Eq. (4.22) and (4.23) are both tested. Schreiber's model is not included in the table since it does not require T_h as input.

versus laser pulse duration, in order to make any τ_p effect on E_{max} prediction capability evident. As shown in Fig. 4.10a, this temporal representation allows to separate the database in two subsets: long, energetic pulses data and short, low energy pulses data. The first subset considers laser pulse durations from 300 to 1000 ps, and corresponding pulse energies from 6.7 to 500 J, while the second includes data with τ_p ranging from 30 to 80 fs and E_p ranging from 0.1 to 3 J[1]. In Fig. 4.10a, c and f one can notice that energy predictions are generally prone to underestimate short pulse ion energies and to overestimate long pulse ones. These three plots correspond in fact to those models exploiting a temporal cut-off τ_{acc} proportional to τ_p. A proper estimator to verify quantitatively this behavior is the following:

$$\langle\Delta^{\pm}\rangle_l \equiv \frac{1}{N_{sub,l}} \sum_{i=1}^{N_{sub,l}} \delta_{rel,i} \,, \tag{4.31}$$

where l indexes the long and short pulse subsets and the sample number has changed

[1]Three points are not accounted in this distinction because of their "intermediate" nature, namely the results from Ref. [32], obtained at moderate length (100 fs) and energy (14.4 J) and Ref. [29], where $\tau_p = 150$ fs for a low energy pulse (0.51 − 0.85 J).

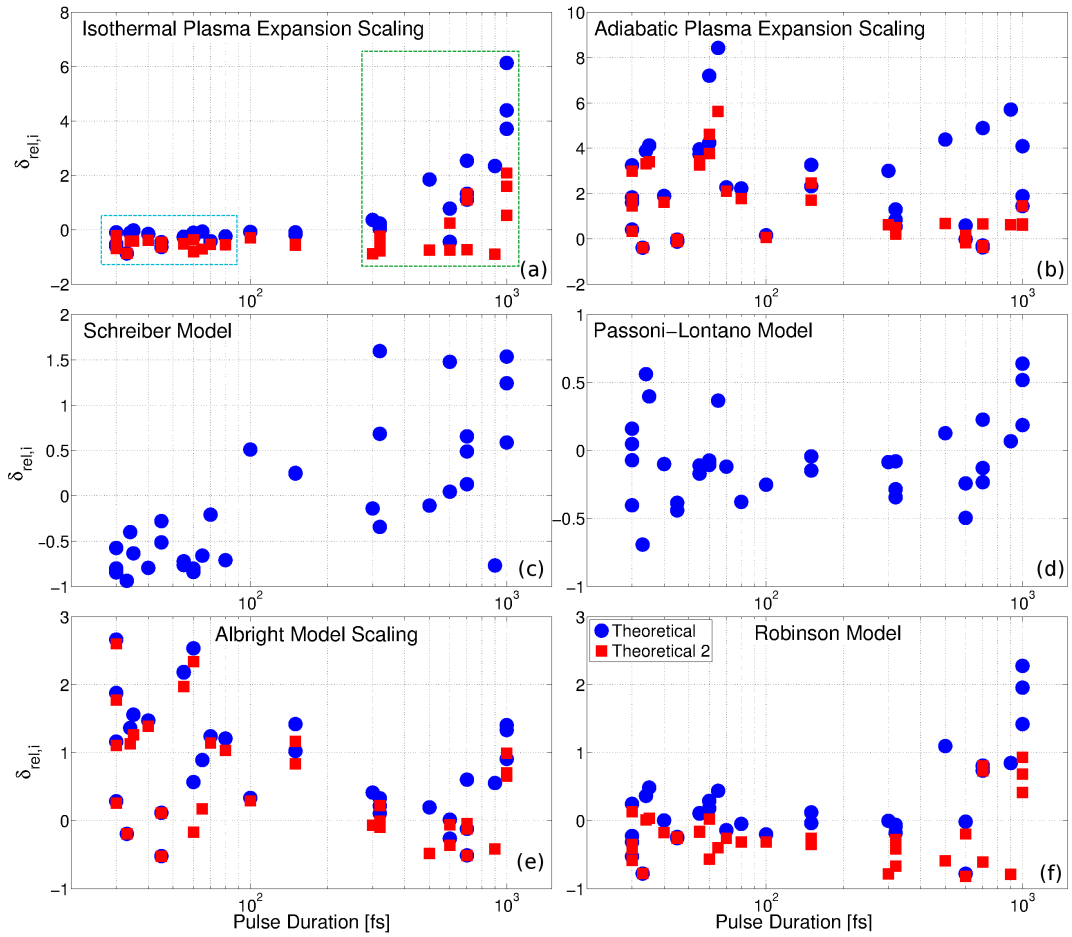

Figure 4.10: - Values of the ion cut-off energy estimate relative difference $\delta_{\mathrm{rel},i}$, as defined by Eq. (4.29), as a function of pulse duration τ_{p}. In a), b), e) and f) "Theoretical 1" and "Theoretical 2" sets correspond respectively to the use of n_{h0} estimates (4.22) and (4.23) for the evaluation of E_{max} prediction. The dark green and light blue dashed rectangles in (a) delimit in order long pulse, high energy subset and short pulse, low energy subset.

from N_{exp} to $N_{\mathrm{sub},l}$ according to the considered subset. Eq. (4.31) is similar to the average deviation defined by Eq. (4.28), but without the modulus, so that the sign of the sum indicates if experimental energies are overestimated ($\langle\Delta^{\pm}\rangle > 0$) or underestimated. The values of $\langle\Delta^{\pm}\rangle$ obtained for each model over the two data subsets are listed in Tab. 4.5, again taking into account both the n_{h0} estimates of Eqs. (4.22) and (4.23). As suggested by Fig. 4.10, Tab. 4.5 shows that in general the use of a temporal cut-off t_{acc} coincides with an overestimate of long pulse energy values and an underestimate of short pulse ones, while the models not requiring t_{acc} behave differently. Schreiber's model provides a nice example for this statement, as the acceleration duration proposed by Ref. [46], namely $t_{\mathrm{acc}} = \tau_{\mathrm{p}}$, contributes to a mean overestimate of 50 % on long pulses and an underestimate of 67 % on short pulses. Isothermal and Robinson's models, exploiting a t_{acc} cut-off given by Eq. (4.27), exhibit a similar behavior despite the use of the temporal offset for short pulses.

As an apparent counter-example, it must be noticed that the values of $\langle\Delta^{\pm}\rangle$ retrieved for Robinson's model with boundary density estimate of Eq. (4.23) testify a relevant underestimate for both short and long pulse data. In fact it is evident that the introduction of Eq. (4.23) substantially reduces the overestimate of long pulse energies, with an improvement of both isothermal and Robinson's model prediction capabilities. However it is also true that the use of such n_{h0} evaluation increases the underestimation for short pulse durations.

From such a study it can be concluded that the imposition of an acceleration temporal cut-off proportional to laser pulse duration does not favor the predicting capability of the models, adding a τ_{p} dependence of E_{max} which is not well supported by experimental data. This confirms that the imposition of a direct dependence of t_{acc} on τ_{p}, as expected, is not justified. Nonetheless it is worth noting that the results achieved by Robinson picture are still encouraging and more reliable than those obtained by Adiabatic or Albright models, which do not require any acceleration time. In fact it is evident that, among those solutions to diverging energy issue which are alternative to temporal cut-off, the only one which guarantees a remarkable predicting capability is that proposed by Passoni-Lontano model, arising from the requirement of a maximum hot electron energy.

However, in order to retrieve the promising predictions of Fig. 4.7d the cut-off parameter φ^*, namely the hot electron maximum kinetic energy at the inner plasma boundary, is evaluated using the empirical scaling of Eq. (4.26), proposed in Ref. [50]. Of course the experimental bases of φ^* quasi-logarithmic dependence on pulse energy contribute to the success of Passoni-Lontano energy predictions in reproducing actual measurements. Therefore, if the idea of a self-consistent energetic cut-off in hot electron distribution turns out to be convenient, the use of Eq. (4.26) requires a theoretical explanation which can rely on satisfactory physical bases, going beyond the empirical agreement.

In this sense, the idea of adiabatic expansion model does not require any cut-off, since the acceleration is self-consistently limited by the finite amount of energy contained in the plasma slab cooling down. From a theoretical point of view this approach

Model	Eq. n_{h0}	Subset	$\langle\Delta^{\pm}\rangle_{\%}$
Isothermal Expansion	(4.22)	Long	175 %
		Short	−33.5 %
	(4.23)	Long	9.9 %
		Short	−55.2 %
Adiabatic Expansion	(4.22)	Long	200 %
		Short	285 %
	(4.23)	Long	39.1 %
		Short	228 %
Schreiber	None	Long	50.6 %
		Short	−66.5 %
Passoni-Lontano	None	Long	−0.94 %
		Short	−8.94 %
Albright	(4.22)	Long	56.9 %
		Short	173 %
	(4.23)	Long	2.95 %
		Short	102 %
Robinson	(4.22)	Long	63.1 %
		Short	−1.74 %
	(4.23)	Long	−11.23 %
		Short	−26.2 %

Table 4.5: $\langle\Delta^{\pm}\rangle_{\%}$ values for the two database subsets "long" and "short" indicated in Fig. 4.10. For the four models requiring boundary hot electron density n_{h0} the estimates of Eq. (4.22) and (4.23) are both tested.

can be attractive, because the adiabatic decrease of T_h is physically reasonable as acceleration turn-off process. Anyway, on the one hand the thickness dependent scaling provided in Eq. (4.4) does not agree with experimental evidences (see e. g. Refs. [29, 76]), and on the other hand all the energy predictions retrieved with this theory strongly overestimate experimental measurements. In fact one should not forget that this approach still considers a divergent electro-static potential, making use of the Boltzmann distribution for the hot electron density. As shown by isothermal expansion results, in order to obtain reliable ion energies, such infinite potential needs to be turned-off after a time t_{acc} which is shorter than the typical hot electron cooling timescale. To perform a further test of the adiabatic expansion description, the concept of plasma length, which previously has been chosen equal to target thickness D, can be considered in a different perspective. The choice of D for the plasma extension is consistent with original Ref. [45] but, if densities estimates of Eqs. (4.22) or (4.23) are assumed, the thickness in Eq. (4.4) can acquire a different meaning. In fact, going back to energy conservation of Eq. (4.20), it is clear that the plasma depth leading to the considered hot electron density is the laser pulse spatial length. For this reason $D_{eff} = c\tau_p$ can in principle substitute target thickness D in adiabatic expansion E_{max} prediction. However D_{eff} is

greater than D for almost all the database experiments except in two cases, so that the model general behavior is necessarily worsened by this alternative interpretation. Therefore, the results of adiabatic expansion model suggest once again that the choice of a divergent potential, besides being theoretically unacceptable, is not convenient to get the maximum energy cut-off. Given this, also the tendency of Albright's model to typically overestimate experimental data can be similarly interpreted as a consequence of adopting a divergent potential. However, to conclude this a deeper analysis of Albright's theory, which falls beyond the purposes of present work, is needed.

4.4 Summary

It is now useful to summarize the conclusions which can be drawn according to the results of the performed analysis of TNSA models. First of all, it turns out that, according to the calculations performed, Passoni-Lontano description clearly represents the most convenient approach to evaluate the ion energy cut-off $E_{\max}$, providing reliable energy estimates over a wide range of laser-target system parameters, as that considered in the comparative analysis. The validity of this comparison is affected by the arbitrariness introduced by choosing the estimate criteria indicated in Tab. 4.3, which are required to implement the $E_{\max}$ calculation for each of the TNSA theories. In order to perform a more detailed comparative analysis, and to reduce this arbitrariness, some alternative criteria have been explored and the resulting model outcomes have been observed.

As a first example, the hot electron boundary density $n_{\mathrm{h}0}$ have been evaluated both by Eqs. (4.22) and (4.23), considering the consequent energy prediction variations. As explained in Sec. 4.2, Eq. (4.23) is more reasonable from a theoretical point of view since it includes, by means of a very simple ballistic picture, some features of hot electron transport through the matter. This means that more physics can be included within the TNSA theory as for example the possible effect of target thickness D, not included in Eq. (4.22). However, at the same time, this estimate introduces an input parameter as the hot electron divergence angle, which can represent a significant source of uncertainty in the calculations. The results of the comparative analysis, shown in Fig. 4.8, attest that the use of Eq. (4.23) determines generally a higher reliability of TNSA models than that achieved estimating $n_{\mathrm{h}0}$ via Eq. (4.22), supporting the ballistic electron transport hypothesis proposed by the former equation. The idea of extending TNSA theoretical description by introducing further details on hot electron physics is a central topic in the next chapter, where also the ballistic transport assumption is reconsidered.

Similarly to the procedure adopted for $n_{\mathrm{h}0}$ calculation, alternative estimates for hot electron absorption fraction η and temperature T_{h} have been investigated as well. In the case of η the choice of Eq. (4.24) or (4.25) does not exhibit a crucial influence on the final results because of the quantitative similarity between the two estimates. On the contrary the choice among T_{h} ponderomotive and Beg scalings, provides deeply different energy estimates. In the present dissertation no definitive answer is proposed about T_{h} evaluation, which is considered as an open problem in TNSA modeling. However,

due to its success in hot electron investigation experiments (see Fig. 3.7), over TNSA typical parameter range, and due to the promising results achieved by Passoni-Lontano model, the ponderomotive formula is adopted in the following as preferred hot electron temperature estimate.

A further conclusion which can be stated from the present comparative analysis is related to the divergence of electro-static potential at large distances, determined by the use of a Boltzmann density relation for the hot electrons. As said, the six model propose different strategies to face this problem and to avoid the subsequent divergent $E_{\max}$ prediction. The first one is the imposition of a temporal cut-off $t_{\rm acc}$ to the acceleration process, chosen proportional to the laser pulse duration, exploited by isothermal expansion model and, as a result, by Robinson's as well. Also Schreiber's description introduces the acceleration time, even if in this case the potential divergence is actually removed by a transversal spatial cut-off. Besides the fact that such a cut-off strategy is theoretically questionable, the comparison of different energy predictions demonstrates that if $t_{\rm acc} \propto \tau_{\rm p}$, an artificial time dependence is introduced, leading to an overestimate for long pulse systems and an underestimate for short pulses (see results in Fig. 4.10 and Tab. 4.5). However, it should be underlined that Robinson model still provides quite reliable predictions and that alternative interpretations of the acceleration time $t_{\rm acc}$ as for example that proposed in Ref. [49] can reduce such an effect.

A self-consistent acceleration turn-off dynamics is proposed by the adiabatic expansion model, which assumes energy conservation to determine hot electron adiabatic cooling and thus electro-static field damping. While this approach is theoretically more attractive, the resulting quantitative predictions largely overestimate experimental energies. This is easily understood considering that the hot electron cooling time is typically much longer than the $t_{\rm acc}$ values used in the isothermal expansion model. Since in both fluid descriptions the potential is determined by Boltzmann-like hot electron density, the longer adiabatic expansion timescales lead to higher peak energies, even if the acceleration is mitigated by electron cooling. As a consequence one can state that the main problem of these descriptions is the divergent electro-static potential determined by Poisson-Boltzmann equation, which does not reproduce the actual TNSA acceleration dynamics. In the light of such a statement Passoni-Lontano model approach, based on a limited accelerating potential, suggests a more convenient solution to describe TNSA. An interesting alternative to this path can be the description of Ref. [51], in which a power law profile for the hot electron density is assumed, resulting in a limited potential solution.

To conclude the present chapter, Passoni-Lontano model has turned out to be the most convenient and reliable approach for ion maximum energy prediction in "ordinary" TNSA, that is with planar, optimum thickness targets and normal contrast conditions. However, still remaining in the restricted framework of $E_{\max}$ evaluation, this model exhibits two main drawbacks that demand further development of the description. First of all, the ion cut-off energy estimate requires the value of the normalized potential φ^*, which has to be retrieved by the empirical law (4.26), since no theoretical model is

currently available. Eq. (4.26) has been formulated via the fitting of the experimental $E_{\max}$ over a restricted number of published results (see Ref. [50]). The validity of such an empirical quasi-logarithmic scaling is further supported, in the current analysis, by the reliability of Passoni-Lontano model over an extended set of experimental data. Anyway, a theoretical explanation of φ^* behavior is necessary to give a solid support to this TNSA description. Moreover, one can notice that Eq. (4.12), together with estimates of Eqs. (3.45) and (4.26), provides an $E_{\max}$ estimate depending only on the laser irradiance $I\lambda_{\mathrm{p}}^2$, energy E_{p} and on the accelerated ion charge Z_i. This means that several TNSA aspects are not taken into account in such a calculation, as for example laser contrast conditions, pulse duration or target geometrical features like the thickness. Since, as discussed in Sec. 2.3, the tuning of foil thickness is one of the most explored paths to $E_{\max}$ optimization in TNSA experiments, leading to efficient increase of peak energy if associated with contrast enhancement (see for example Refs. [29, 31] or Fig. 2.10), a reliable technique to predict TNSA maximum ion energy should be able to describe this feature. Passoni-Lontano theory estimates are instead restricted to normal contrast and optimum thickness conditions, as the majority of the database energies refer to this situation, so that an advance in this direction is required.

Based on the above considerations, in the remaining part of present dissertation, the work is focused on the Passoni-Lontano model, with the goal of extending it, in order to overcome its main drawbacks. First, Eq. (4.26) is discussed more in depth and a theoretical interpretation is proposed, second, introducing further TNSA aspects about hot electron physics within the model, the predicting capability of the latter is extended over a broader parameter range.

5

Extension of the TNSA Model

In Sec. 4.4 the major limits of the quasi-static model, proposed by Passoni and Lontano in Refs. [169, 170] as an instrument for reliable estimates of TNSA ion cut-off energies in experiments, have been discussed. They can be schematically summarized as follows:

- the need for a theoretical explanation of the empirical scaling formula (4.26), used to obtain the normalized potential φ^*, which is convenient to report here:

$$\varphi^* = 4.8 + 0.8 \log(E_p) \,. \tag{5.1}$$

- The resulting E_{max} estimate does not depend on crucial system parameters, which have experimentally demonstrated to affect the ion cut-off energy value, as for example the target thickness.

In this chapter such issues are faced, proposing an extension of the model which is obtained by introducing new features of the hot electron physics not previously considered in the description. This leads to a development of the existing model which, on the one hand, allows to provide a stronger theoretical interpretation to the resulting scalings of TNSA ion energy with the system parameters and, on the other hand, broadens the predicting capability of the E_{max} estimate to a wider set of experimental data. In fact, while the original description introduced in Ch. 4 can predict E_{max} only for optimum thickness targets, the extended version can reproduce the experimental ion energy behavior for different foil depths. The same approach is then applied to the case of mass limited targets (MLTs, see Sec. 2.3) as well, in an attempt to model the optimization of TNSA energies testified by recent experiments, as published e.g. in Ref. [35].

The chapter is structured as follows: in Sec. 5.1 the extension of Passoni-Lontano model is presented, first of all by recalling the experimental results of target thickness tuning (Sec. 5.1.1), then by describing the implementation of new physical details (Sec. 5.1.2), and deriving the consequences on the TNSA description, eventually discussing the theoretical meaning of the resulting expressions (Sec. 5.1.3).

After that, a validation of the extended model is provided, based on comparisons with numerical and experimental results. In particular, in Sec. 5.2, the dependence of

ion cut-off energy on laser pulse energy is tested by means of PIC simulations, while in Sec. 5.3 some published experimental measurements, obtained in relevant TNSA campaigns, are exploited to test the model capability in reproducing target thickness dependence.

As a further test, the effects of considering a more detailed hot electron distribution description, which can introduce some dynamical features in the original static picture, are investigated in Sec. 5.4 by using a Monte-Carlo numerical code.

Finally, in Sec. 5.5 another development is proposed, by addressing the issue of MLT case, adapting the results of previous sections to formulate a description which is capable to reproduce the effects retrieved in recent TNSA experiments exploiting MLTs.

5.1 Theoretical Development

5.1.1 Role of Target Thickness in TNSA

In Sec. 2.3 it has been shown how experimental results indicate that the reduction of target thickness D, if accompanied with proper pre-pulse cleaning, is a convenient way to increase TNSA ion maximum energy. Several published works have in fact adopted thickness tuning to increase the energy reached by the produced beams (see e.g. [7, 29, 32, 33, 76, 89, 90]), providing a clear experimental picture on this issue, characterized by the existence of an optimum thickness $\tilde{D}$, the position of which mainly depends on laser contrast ratio and pre-pulse duration. Moving away from $\tilde{D}$ towards both larger and smaller thicknesses the ion cut-off energy strongly decreases. If, on one side, the reduction occurring for sub-optimum thicknesses depends on pre-pulse interaction, the behavior exhibited in above-optimum thickness foils is related to hot electron dynamics. In fact, as already mentioned in Secs. 2.3 and 3.1.2, the generated hot electrons, which are responsible for ion acceleration, are "confined" inside the target bulk by the huge electro-static fields arising at the matter-vacuum interfaces. It is easily understood that the same potential gradients which push ions in the outward directions have an opposite effect on hot electron expansion dynamics, rejecting the majority of them back inside the foil bulk. This possibly establishes a recirculation process [32, 42, 91], which can significantly affect ion acceleration, in a way strongly dependent on the target thickness D. In fact, for fixed laser conditions, an increase of D corresponds to a larger longitudinal volume in which hot electrons are confined, leading to a decrease of the mean hot electron density and to a subsequent reduction of self-consistent accelerating fields.

Introduction of target thickness dependence in TNSA theories has been proposed in Ref. [29], in which the $n_{\mathrm{h}0}$ density estimate of Eq. (4.23) is introduced, but here it is the hot electron beam lateral expansion that determines the target thickness influence on $n_{\mathrm{h}0}$. The same assumption introduces D as a parameter in Schreiber's model as well, while in Mora's adiabatic expansion description, D sets the longitudinal extension of the hot electron cloud, at least as initial condition. However, the results of the latter

are not able to reproduce target thickness effects, predicting higher energies for larger D, in contradiction with experimental evidences. It should be underlined that such a behavior, which is determined by the higher energetic content of a larger hot electron cloud, presumes a fixed density for different target depths, being inconsistent with the interpretation of experimental thickness scalings as a result of hot electron confinement within the target volume. Moreover, the adiabatic model describes the expansion of a single ion component plasma in vacuum, which is not meant to reproduce TNSA dependence on target thickness.

5.1.2 Extension of the Quasi-Static TNSA Model

As mentioned before, Passoni-Lontano model does not include target thickness effects within the $E_{\max}$ estimate, since it is devoted to optimal target thickness conditions, through the use of empirical scaling (5.1) for φ^*. To introduce hot electron confinement within the description it is necessary to enter information about hot electron transport, which is directly affected by foil thickness variations. Eq. (4.12), that is the potential energy difference between $x = 0$ and $x = +\infty$, depends only on three parameters: $T_{\rm h}$, φ^* and Z. According to the quasi-static picture and to the typical hot electron cooling timescales it is evident that the temperature does not significantly depend on electron transport, at least as a first approximation, being mainly related to the only laser interaction phase. This means that, in Passoni-Lontano model, the parameter φ^* must contain the hot electron density dependence and thus target thickness information. In fact, the relationship between φ^* and $n_{\rm h}$ is readily available considering the hot electron density profile defined by the Maxwell-Jüttner distribution (4.9), given by Eq. (4.10). In fact, let $x = -x_{\rm w}$ be the left boundary of the electro-static problem, namely well inside the target, where the TNSA field is shielded by the ion bulk and, by definition, $\varphi(x) = \varphi^*$. At this position, Eq. (4.10) provides a relation between φ^* and $n_{\rm h0}$, the boundary hot electron density at $x = -x_{\rm w}$:

$$n_{\rm h}(-x_{\rm w}) = \tilde{n}\frac{I\left(\varphi^*, T_{\rm h}\right)}{\zeta \mathcal{K}_1(\zeta)} \mathrm{e}^{\varphi^*} = n_{\rm h0}\,. \tag{5.2}$$

As said in Sec. 4.1 $\tilde{n}$ is a normalization constant for hot electron density, discussed later on. If hot electron generation and transport physics is described with enough detail to independently provide an expression for $n_{\rm h0}$, as a function of the laser and target parameters, Eq. (5.2) transfers such dependences on φ^* and therefore on the maximum energy estimate.

The question now is how to model $n_{\rm h0}$, also taking into account the idea of electron confinement and recirculation inside the foil volume. As already pointed out in Secs. 3.1.1 and 3.1.2, present knowledge on hot electron generation and transport dynamics is still defective and, to obtain realistic theoretical predictions, extremely demanding numerical calculations are required. On the other hand, in order to keep the spirit of a TNSA effective modeling, it is highly desirable that calculations do not become too expensive, to require the use of numerical descriptions as PIC codes. Moreover, in the present theoretical frame, $n_{\rm h0}$ needs to be a boundary condition for an ion

acceleration model which is static, so that hot electron dynamics needs to be studied through its averaged behavior, over the timescale characterizing the quasi-static equilibrium condition, as defined in Sec. 4.1. Therefore, the use of analytical or empirical laws as for example Eqs. (3.45) for T_h and (4.24) for η, and of an approximated hot electron physics picture, appear to be the right strategy to extend the model towards the outlined purposes.

According to such considerations, the development of Passoni-Lontano picture is formulated by the following assumptions:

1. laser-target interaction is described by assigning the ponderomotive temperature T_h (Eq. 3.45) to a fraction of the electron population, determined by energy balance condition (4.20) and proper assumptions about the mean electron kinetic energy. To evaluate the latter Eq. (3.47), namely the expression relevant for a three-dimensional relativistic Maxwellian distribution, is considered (see Ref. [143] for further details). While introducing energy conservation within the original model, interaction features as ASE pre-pulse properties are still neglected. The absence of laser pre-pulse information suggests that the resulting description will be suitable to describe TNSA for above-optimum thickness targets, which is actually the region of main interest for predictions on E_max optimization via laser contrast enhancement [31].

2. In order to obtain the hot electron density relevant for the quasi-static equilibrium phase, transport dynamics is described over a timescale of the order of 100 fs, assumed to be representative of the time required for this equilibrium to establish. According to Sec. 3.1.2, radiative and collisional effects influence relativistic electron dynamics on longer timescales, therefore a collision-less ballistic electron transport is adopted, a solution which has already been used in different works addressing the hot electron expansion issue in TNSA (see Refs. [29, 33, 43, 178]).

3. Hot electron confinement is modeled by considering the target boundaries as perfectly reflecting walls, forcing the particles to move within the foil volume and set the recirculation dynamics.

4. Ballistic transport is described as a three-dimensional expansion but, to maintain the simplicity and effectiveness of a 1-dimensional description, the relevant density estimate n_h0 is evaluated along the electro-static sheath axis, where Passoni-Lontano original model and Eq. (4.12) are valid, and where the most energetic ions are likely to be accelerated.

Starting from these hypotheses, an effective value for n_h0, which can quantitatively describe longitudinal confinement of hot electrons in the target bulk, can be retrieved via simple calculations and estimates. Before deriving it, it should be stressed once again that such a n_h0 estimate is referred to the left boundary of electro-static problem $x = -x_\mathrm{w}$. In the overall description, for $x > -x_\mathrm{w}$, Poisson equation solution holds, providing a more realistic density profile, not considered in the approximated picture exploited to retrieve n_h0.

First of all, according to energy conservation (Eq. (4.20)), laser-matter interaction generates N_h hot electrons given by:

$$N_\mathrm{h} = \frac{\eta E_\mathrm{p}}{\langle K \rangle}\,, \tag{5.3}$$

where the same notations of Ch. 4 are adopted, so that η is the fraction of absorbed pulse energy and $\langle K \rangle$ is the hot electron mean kinetic energy. If these two quantities are known, Eq. (5.3) can be exploited as a starting point for the density estimate, setting a direct relation between the total number of hot electrons and the laser energy E_p. As said, $\langle K \rangle$ is given by Eq. (3.47), while for η calculation one can refer to Eqs. (4.24) or (4.25), as extensively explained in Sec. 4.2.

The hypothesis of ballistic collision-less transport, together with an effective description of recirculation effects, leads to an expression for the hot electron spatial distribution, so that the density n_h0 can be easily retrieved. To clearly explain how recirculation dynamics is taken into account, the issue is treated in two steps: first, a "semi-infinite thickness" target is considered, in which recirculation does not occur since no solid-vacuum interface limits the path of the transported electrons; second, the finite thickness target case is studied. As long as the foil thickness is infinite, the expanding hot electron cloud ballistically distributes over a truncated spherical cone volume V_∞ (represented in Fig. 5.1), with a constant opening angle θ, corresponding to the hot-electron divergence, given by:

$$V_\infty = \frac{\pi}{3}\left[2\left(1-\cos(\theta/2)\right)\left(\frac{r_\mathrm{fs}}{\tan(\theta/2)} + D_\mathrm{h}\right)^3 - \frac{r_\mathrm{fs}^3}{\tan(\theta/2)}\right]\,, \tag{5.4}$$

where r_fs is the focal spot radius and D_h is the hot electron cloud average longitudinal extension at the time-scale of interest. As a further, strong approximation the density is assumed to be uniformly distributed over V_∞, leading to a mean electron density $n_\mathrm{h0}^\infty = N_\mathrm{h}/V_\infty$. Of course the assumption of uniform distribution is anything but precise, anyway, as long as the purpose is to describe the average effect of hot electron expansion on the boundary condition of the electro-static problem, it can be adopted as a first useful approximation. Once D_h, the mean path of hot electrons at the time of quasi-static equilibrium establishment, is properly evaluated, n_h0^∞ represents a suitable estimate for "ordinary", forward TNSA in sufficiently thick targets, in which recirculation does not take place soon enough to affect the acceleration of the most energetic ions, or for backward TNSA with thick targets and UHC pulses (see Ref. [179]).

On the other hand, if the foil is thin enough ($D < D_\mathrm{h}$, see Fig. 5.1), the electro-static fields at the matter-vacuum interfaces longitudinally confine the hot electron cloud inside the target depth, and electrons can reflux back and forth several times before the quasi-static equilibrium is reached, strongly influencing the TNSA field. To take such a recirculation dynamics into account, the electron volume V_∞ is here longitudinally "shrunk" within the domain of a target of finite thickness $D < D_\mathrm{h}$, according to the assumption that the foil interfaces act as totally reflective walls on the electron motion (see Fig. 5.1). In this framework, a straightforward way to evaluate recirculation effects

along the electro-static sheath axis is to multiply V_∞ by a "shrinking factor" $\kappa = D/D_\mathrm{h}$, that determines a corresponding increase of the on-axis hot electron density n_h0 with respect to the semi-infinite target case. $1/\kappa$ then represents the "amplification" of n_h0 which takes place along the spherical cone axis, due to overlapping and confinement of electron trajectories. This gives:

$$n_\mathrm{h0} = \frac{N_\mathrm{h}}{\kappa V_\infty} = \frac{D_\mathrm{h}}{D}\frac{N_\mathrm{h}}{V_\infty}\,, \tag{5.5}$$

which is assumed to be valid only in the central part of hot electron cloud, where density is affected by longitudinal shrinking, unlike the lateral regions, where electrons arrive after several target round-trips and no significant overlapping occurs (as pictorially indicated in Fig. 5.1 by the different colors within the target). In Eqs. (5.4) and (5.5)

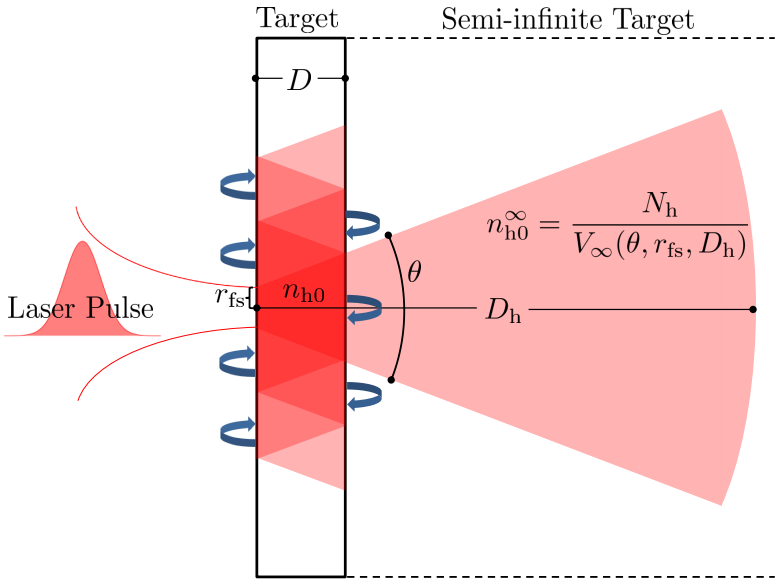

Figure 5.1: - Pictorial representation of the hot electron expansion volume at the quasi-static equilibrium for both a semi-infinite and a finite target thickness. In the latter, the on-axis hot electron density n_h0 is increased by recirculation.

the hot electron cloud longitudinal extension D_h, corresponding to "free" expansion in a semi-infinite target, is required. As said, such an extension has to be evaluated at $t = \tau_\mathrm{E}$, defined as the time needed for quasi-static equilibrium to set up. Therefore τ_E can be estimated as the sum of the hot electron mean flight time through the target, to be added to a "zero-thickness" relaxation time τ_E0, which is assumed to be approximately independent from the target geometrical features. The longitudinal extension D_h is then given by:

$$D_\mathrm{h} = v_\mathrm{h}\tau_\mathrm{E} = D + v_\mathrm{h}\tau_\mathrm{E0}\,, \tag{5.6}$$

where $v_h = c(1-\gamma_h^{-2})^{1/2}$ is the hot electron mean expansion velocity and $\gamma_h = 1 + \langle K\rangle/mc^2$, depending on the mean kinetic energy (3.47). Since $v_h \simeq c$ and τ_{E0} is of the order of $50-100$ fs, D_h can easily exceed the target thickness D by tens of μm, making recirculation relevant for μm and sub-μm targets. Combining Eqs. (5.5), (5.6) and (4.20), the average hot electron density on the hot electron beam axis can be expressed as:

$$n_{h0} = \left(1 + \frac{v_h \tau_{E0}}{D}\right) \frac{\eta E_p}{\langle K\rangle V_\infty}, \tag{5.7}$$

which is an effective expression for the boundary hot electron density, depending on several parameters, as target thickness D, hot electron beam divergence θ and laser pulse parameters (energy, irradiance, focal-spot). Eq. (5.7) describes a density which increases for decreasing D, consistently with the interpretation of the E_{max} behavior, obtained in experiments for over-optimum targets, as a result of hot electron confinement. Therefore, n_{h0} can be substituted in Eq. (5.2) to include thickness effects in ion energy predictions from the quasi-static model.

5.1.3 Theoretical Results and Significance

Using Eq. (5.7) and Eq. (5.2), the following relation is obtained:

$$\varphi^* + \log\left[\frac{I(\varphi^*, T_h)}{\zeta \mathcal{K}_1(\zeta)}\right] = \log\left[\frac{\eta E_p}{\tilde{n}\kappa\langle K\rangle V_\infty}\right]. \tag{5.8}$$

Eq. (5.8) reflects on φ^* the different dependences of n_{h0} on the system parameters, as for example the target thickness, thus influencing the E_{max} estimate. In this way, the developed description is able to shed light on a number of additional crucial issues of TNSA.

First of all, Eq. (5.8) provides a theoretical interpretation to the empirical scaling law (5.1), previously used to determine φ^*. In fact, the second logarithm at the left hand side of Eq. (5.8) is usually negligible for experimentally relevant parameters, differing from zero only for low pulse energies, of 0.1 J order. Neglecting such a term leads to:

$$\varphi^* = \log\left[\frac{\eta}{\tilde{n}\kappa\langle K\rangle V_\infty}\right] + \log(E_p), \tag{5.9}$$

where the E_p dependence has been separated from the others, to show that the quasi-logarithmic behavior of Eq. (5.1), supported by the agreement with experiments (see Sec. 4.3) presented in the previous chapter, has a theoretical foundation in the physics introduced to obtain Eq. (5.8). The logarithmic growth of φ^* with laser energy, exhibited by Eq. (5.9), comes directly from the Maxwellian features of the hot electron distribution (4.9), which imply a quasi-exponential density profile (Eq. (4.10)), and from the energy balance (4.20), that determines the linear dependence of n_{h0} on E_p. Actually, the empirical scaling is quasi-logarithmic, with a 0.8 coefficient which slightly reduces the growth rate of φ^*. The dependence on E_p of the first logarithm in Eq. (5.9) right hand side, should then "compensate" in some way the fully logarithmic dependence of the second term. Accordingly, in Fig. 5.2 a comparison among the trends of

Eqs. (5.9), (5.1) and a simple logarithmic scaling $A + \log(E_p)$ is displayed over a wide range of pulse energies. The only parameters of Eq. (5.9) allowed to change in the figure are E_p and, according to Eq. (4.19), laser intensity I, while other quantities are fixed to typical values (see figure caption). Here, the normalization constant $\tilde{n}$ has been tuned to provide the best absolute agreement between Eqs. (5.9) and (5.1) (see also the discussion below and Sec. 5.2). The figure confirms that Eq. (5.9) predicts a φ^* scaling which is extremely close to that of Eq. (5.1), showing the importance of this theoretical result to partially explain the origin of the empirical scaling in the framework of Passoni-Lontano model. On the other hand, it should be pointed out that the present results do not completely explain why such an empirical scaling can be applied on so widely different parameter sets, as those discussed in chapter 4. This feature is in fact difficult to explore through Eq. (5.8), mainly because of the normalization parameter $\tilde{n}$, which is discussed below.

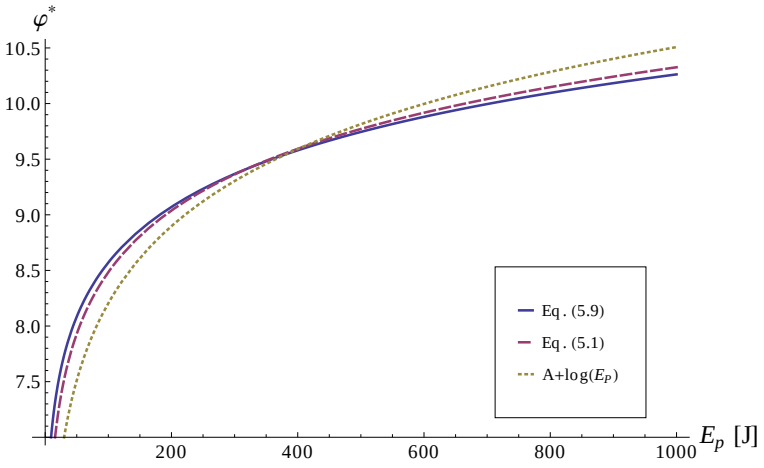

Figure 5.2: - Comparison of different φ^* scalings. The evaluation of Eq. (5.9) is performed by keeping the system parameters $\tau_p = 100\,\text{fs}$, $r_{fs} = 3\,\mu\text{m}$, $D = 10\,\mu\text{m}$, $\tau_{E0} = 50\,\text{fs}$ and by letting the intensity change with energy variation (see Eq. (4.19)). The normalization $\tilde{n}$ in Eq. (5.9) curve and the coefficient A in $\log(E_p)$ scaling are tuned to find the best agreement with Eq. (5.1).

In this framework Eq. (5.1), as supported by phenomenological evidences, can be considered as a particular case of Eq. (5.8), reliable only for experimental setups adopting "normal" laser contrast conditions and the corresponding optimal target thickness $\tilde{D}$. In this sense Eq. (5.8) extends the original model predicting capabilities, making possible to explore a larger region of the input (laser/target) parameter space. As a relevant example, Eq. (5.8) clears the way towards energy predictions at variable thicknesses, also differing from the contrast-dependent optimum $\tilde{D}$, which is indeed one of the main purposes of the present work, both because of its practical interest in energy optimization with available UHC lasers and because of the presence of several published parametric studies, which can be useful for validation of the theoretical results

(see Sec. 5.3).

To achieve the estimate of maximum ion energy as a function of target thickness, φ^* should be determined by means of Eq. (5.8), so that the D dependence of n_{h0} is reflected on E_{max}. However, once all the parameters to evaluate n_{h0} by Eq. (5.7) are available, the problem is not completely determined yet, since the normalization density $\tilde{n}$ still has to be specified. A possible relation to fix $\tilde{n}$ is the boundary condition (5.2), but this would indeed require the independent knowledge of φ^*. The difficulty here is due to the intrinsic link of $\tilde{n}$ to the self-consistent potential profile, which can be determined only once φ^* is known. For this reason, the evaluation of $\tilde{n}$ is non-trivial and a further, independent physical information is required. At the present knowledge of TNSA physics, no theoretical model is available to fulfill such a request, so that a criterion based on the empirical relation (5.1) is here developed.

The basic idea is that, if a system setup corresponding to a given optimum thickness $\tilde{D}$ is considered, then Eq. (5.1) can be adopted to calculate φ^* with good reliability. The result can be then substituted in Eq. (5.8), with $D = \tilde{D}$, to retrieve $\tilde{n}$, so that a complete analytical description of the specific experimental arrangement is obtained. In fact, once $\tilde{n}$ is fixed through Eqs. (5.8) and (5.1), the considered electro-static problem is completely determined, allowing the evaluation of Poisson equation dimensioned solution. This is a possibility opened by the proposed model extension since, in the original formulation of Passoni-Lontano model, Poisson equation is solved using the dimensionless variable $\xi = x/\tilde{\lambda}_h$, where $\tilde{\lambda}_h = \sqrt{\zeta \mathcal{K}_1(\zeta) k_B T_h / 4\pi \tilde{n} e^2}$ is a typical scale-length of the hot-electron density distribution. On one side the use of ξ removes the normalization $\tilde{n}$ from the problem, as shown explicitly in Ref. [170], but on the other side it leads to the dimensionless solution $\varphi(\xi)$, which makes it possible to estimate E_{max}, but not to determine the physical spatial profiles. If instead $\tilde{n}$ is known, the dimensioned potential, field and density can be evaluated, as shown for example in Figs. 5.3 and 5.4. The capability to retrieve such spatial profiles can be useful for comparisons with more detailed models, as for example with PIC simulation results, or with possible spatial measurements, in order to reach a better comprehension of Passoni-Lontano model limits and applicability. Anyway, this goes beyond the purpose of present thesis, which is rather focused on ion cut-off energy prediction, more than on spatial profile details.

Since the main interest of Eq. (5.8) lies in the possibility to extend the knowledge of φ^* outside the region of validity of Eq. (5.1), according to the dependencies of n_{h0}, it is mandatory to prescribe how the factor $\tilde{n}$, evaluated for this region by means of Eqs. (5.1) and (5.8), changes as the system parameters are varied. To clarify this, it is convenient to focus first on the relevant case of thickness variation, and to subsequently generalize the discussion to the other dependencies. If a thickness D higher than the experimental optimum $\tilde{D}$ is chosen, φ^* should experience a variation due to an expected decrease of the hot electron boundary density n_{h0}. However, according to Eq. (5.8) such a variation could in principle be absorbed by artificially changing $\tilde{n}$, thus leaving φ^* constant. A first, useful step is therefore to comprehend how an artificial variation of $\tilde{n}$ influences the dimensioned solution of Poisson equation, that is the electro-static sheath

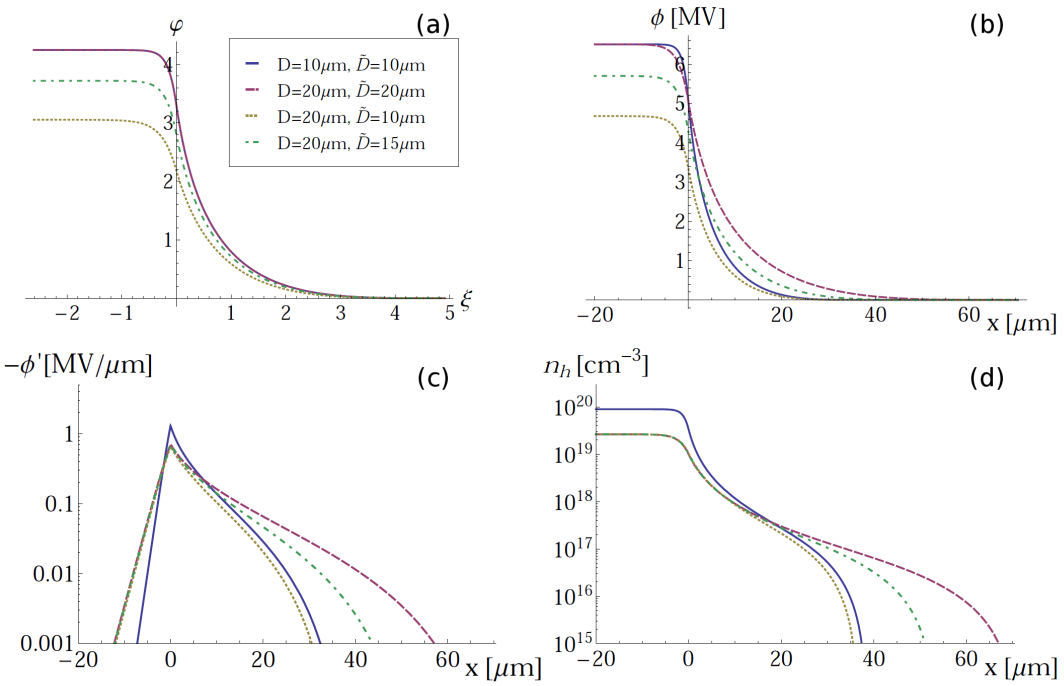

Figure 5.3: - Spatial profiles obtained by the solution of Poisson equation according to Passoni-Lontano model and Eq. (5.8). Subfig. (a) represents the normalized potential φ, Subfig. (b) the dimensioned potential ϕ, Subfig. (c) the electric field $-\phi'$ and Subfig. (d) the hot electron density $n_{\rm h}$. As shown by the legend different curves correspond to different cases described in the text, where parameters can be found as well.

profile, and to critically interpret the result on physical grounds. The calculation of spatial profiles is useful in this sense, because it helps to establish the role of $\tilde{n}$ in the determination of electro-static system properties as the thickness changes. The case of a D increase is represented in Fig.5.3, where the spatial profiles of normalized potential φ (Fig.5.3a), potential ϕ (Fig.5.3b), electric field $\mathcal{E} = -\phi'$ (Fig.5.3c) and hot electron density $n_{\rm h}$ (Fig.5.3d) are plotted for four different cases:

Case 0 - Blue solid curves. The reference solution, obtained assuming $\tilde{D} = 10\,\mu$m, $D_0 = \tilde{D}$, $E_{\rm p} = 0.5\,$J, $r_{\rm fs} = 3\,\mu$m and $\tau_{\rm p} = 30\,$fs. (Except for $\tilde{D}$ and D the latter parameters are the same for each case).

Case 1 - Beige short-dashed curves. Obtained for a thicker target, $D_1 = 20\,\mu$m, keeping the same $\tilde{D}$ and, correspondingly, $\tilde{n}$ of Case 0, so that φ^* "absorbs" the whole $n_{\rm h0}$ decrease.

Case 2 - Purple long-dashed curves. Obtained for $D_2 = 20\,\mu$m, with higher optimum thickness $\tilde{D}_2 = 20\,\mu$m, so that $\tilde{n}$ "absorbs" the variation of $n_{\rm h0}$.

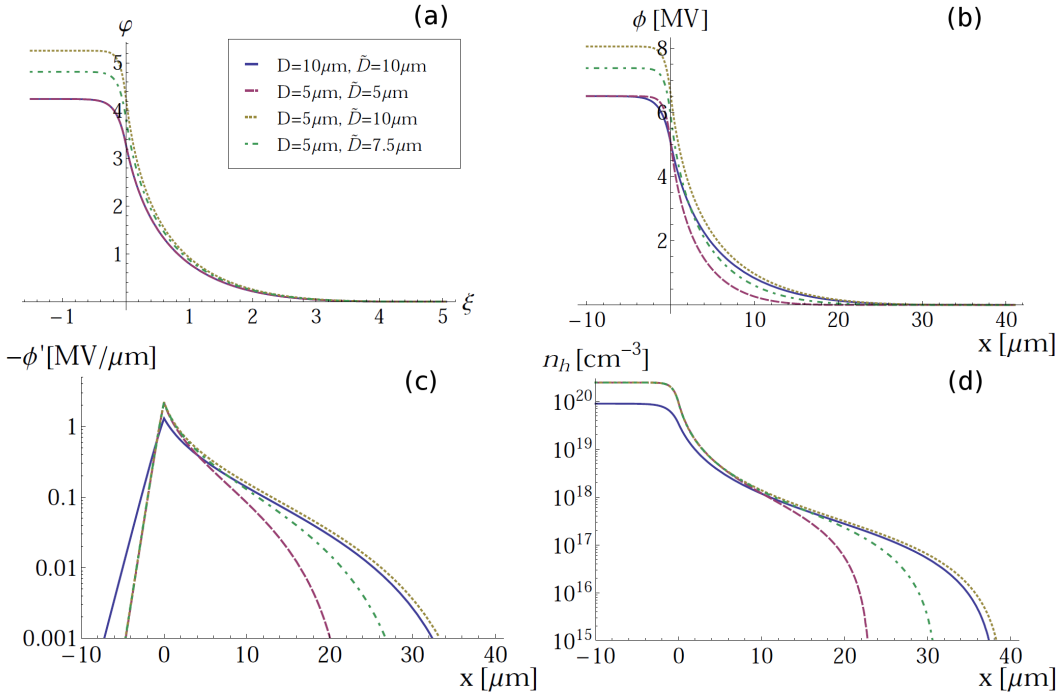

Figure 5.4: - Spatial profiles obtained by the solution of Poisson equation according to Passoni-Lontano model and Eq. (5.8), the subfigures are organized as in Fig. 5.3. As shown in the legend the target thickness is decreased to 5 μm for a comparison with the reference $D = 10\,\mu$m.

Case 3 - Green dash-dotted curves. Obtained for $D_3 = 20\,\mu$m and $\tilde{D}_3 = 15\,\mu$m to describe an intermediate case between 1 and 2.

From Fig. 5.3a it is evident that $\varphi(\xi)$ depends just on φ^* as expected, so that Case 2 overlaps Case 0, despite the different n_{h0} predicted. As a result, the $E_{\max}$ estimate for the 2 cases is the same, since it is assumed that the variation in n_{h0} determined by the thicker target is "absorbed" by $\tilde{n}$, which has no influence on the ion cut-off energy (see Eq. (4.12)). Differently, in Case 1, the n_{h0} decrease is reflected on φ^*, resulting in a lower potential profile, which implies a smaller maximum ion energy, as expected and experimentally confirmed (considering TNSA with the same laser pulse properties but different target thicknesses one obtains: $D_a > D_b \Rightarrow E_{\max,a} < E_{\max,b}$). Shifting from $\varphi(\xi)$ to $\phi(x)$ (Fig. 5.3b), it turns out that a reduction of $\tilde{n}$ which, as in Case 1, compensates the variation of n_{h0}, results in a less steep potential slope, which extends farther in space. In fact the profile scale-length $\tilde{\lambda}_{\mathrm{h}}$ is inversely dependent on $\tilde{n}$. This is confirmed by the trends represented in Fig. 5.3c which testifies that cases 1 and 2 reach the same peak electric field, but in the latter the spatial decay is slower, determining a longer acceleration length and leading to a higher energy. Accordingly, hot electron density profiles in Fig. 5.3d show that the solution of Case 2 corresponds

to a less dense but longer cloud of electrons with respect to Case 0, while Case 1 is less dense but maintains the same scale-length. As expected, Case 3 profiles show that the solutions with an "intermediate" normalization setting are contained between the two limiting cases (1 e 2), further highlighting the system dependences.

In Fig. 5.4 an analogous study is represented, starting from the same reference solution as before (Case 0, blue solid curves), this time focusing on a reduction of the target thickness to $D = 5\,\mu$m. The other profiles reported follow a scheme similar to that of Fig. 5.3:

Case 1 - Beige short-dashed curves. $D_1 = 5\,\mu$m, same $\tilde{D}$ of Case 0, so that φ^* increases with n_{h0}.

Case 2 - Purple long-dashed curves. $D_2 = \tilde{D}_2 = 5\,\mu$m, so that $\tilde{n}$ absorbs the increase of n_{h0}.

Case 3 - Green dash-dotted curves. Intermediate case between Case 1 and 2 ($D_3 = 5\,\mu$m, $\tilde{D}_3 = 7.5\,\mu$m).

The figure confirms the influence of $\tilde{n}$ on the spatial profiles scale-length, this time determining a shorter hot electron cloud extension in Case 2, which results in a weaker acceleration with respect to Case 1.

Therefore, even if the imposition of Eq. (5.1) can completely determine the system at $D = \tilde{D}$, in order to extend the model predictions at thicknesses differing from the optimum $\tilde{D}$, it is necessary that a prescription for $\tilde{n}$ is chosen, since it can affect the φ^* behavior predicted by Eq. (5.8), implying a different charge distribution and E_{max} prediction. The phenomenological dependence of TNSA ion cut-off energy on target thickness suggests that φ^* is indeed affected by a variation of the boundary density n_{h0}, ruling out the possibility of "Case 2", in which the normalization changes artificially suppress the thickness dependence.

The criterion proposed here is therefore to assume that a variation of n_{h0} influences only φ^*, while $\tilde{n}$ remains fixed to the value obtained at $D = \tilde{D}$. Such a prescription allows to eventually extrapolate the E_{max} prediction dependence on target thickness.

As pointed out, formula (5.7) introduces, in Eq. (5.8), dependences on further parameters, which have to be discussed similarly to the target thickness. Therefore, generalizing the discussion about D, let a generic parameter a be considered. If the imposition of Eq. (5.1) to retrieve $\tilde{n}$ is operated each time a changes, the dependence of n_{h0} on a would be artificially balanced by a variation of the normalization. If, otherwise, $\tilde{n}$ is obtained for a fixed value $\tilde{a}$ and kept constant as a varies (as discussed for a D variation), then φ^* is directly affected by $n_{\mathrm{h0}}(a)$, thus determining an influence on E_{max}. The parameters to be considered are the laser features E_{p}, $I\lambda^2$ and r_{fs}, the hot electron divergence θ and the "offset" time τ_{E0}. For what concerns the laser parameters, it is reasonable to set $\tilde{n}$ after any coherent variation of them, since the validity of the empirical scaling (5.1) includes variations of them, unlike in target thickness variations. The same approach can be followed for the offset time τ_{E0}, which, in general, according to the simplifications of the adopted hot electron transport model,

has the same value for any laser-target system (see Sec. 5.1). Concerning the hot electron divergence angle θ, a different approach seems to be more reasonable. Since this quantity is not directly accessible for measurements or predictable with some model, its value cannot be retrieved in a reliable way. To have a better characterization of this uncertainty a wide range between 30 and 90 degrees [158] is taken into account, fixing $\tilde{n}$ for an average value $\tilde{\theta} = 60°$. As said, in this way the normalization does not absorb the θ-dependence, reflecting it on the $E_{\max}$ prediction. In this sense, θ here is treated as the target thickness, assuming that the scaling law Eq.(5.1) holds just for the typical value $\tilde{\theta}$, used to normalize the problem. However, while D is a well-controlled parameter of the system, which is precisely known in experimental conditions, θ is not available. Therefore, in this case, the choice of this normalization prescription is made to introduce a confidence interval for the resulting $E_{\max}$, in order to study the sensitivity of the latter on the uncertain parameter θ.

The normalization prescriptions just established make thus possible to perform predictions of the TNSA maximum energy to be compared with experiments or simulations, and a test of the extended model predicting capability is available. According to this scheme $\tilde{D}$ or $\tilde{\theta}$ values can also be considered as fitting parameters, in order to tune the energy prediction to some known value. In the next sections such possibilities are explored, by presenting comparisons of theoretical estimates with numerical and experimental results.

5.1.4 Operating Summary: Evaluation of $E_{\max}$

It is now convenient to provide an operating summary describing, step-by-step, the procedure used in the following sections to retrieve $E_{\max}$ estimates, according to the presented theoretical model:

1. The system parameters have to be defined:
   - the laser features λ, I, E_{p}, τ_{p} and r_{fs}.
   - The "zero-thickness" relaxation time to quasi-static equilibrium τ_{E0}.
   - The specific target thickness D.
   - The hot electron divergence angle θ.
2. T_{h} and η are evaluated from $I\lambda^2$, according to Eqs. (3.45) and (4.25) respectively.
3. The normalization parameters $\tilde{D}$ and $\tilde{\theta}$, are fixed.
4. $n_{\mathrm{h0}}(\tilde{D}, \tilde{\theta})$ is evaluated by means of Eq. (5.7).
5. Eq. (5.8), for $D = \tilde{D}$, $\theta = \tilde{\theta}$ and with φ^* value given by Eq. 5.1, is inverted to obtain $\tilde{n}$.
6. $n_{\mathrm{h0}}(D, \theta)$, referred to the specific thickness and divergence angle of the considered system, is evaluated using Eq. (5.7).

7. $\varphi^*(D,\theta)$ is calculated through Eq. (5.8) using the fixed $\tilde{n}$.

8. Eq. (4.12) is used to obtain $E_{\max}$ from T_{h} and $\varphi^*(D,\theta)$.

In this computation process, there are three parameters that are not available from the system, τ_{E0}, $\tilde{D}$ and $\tilde{\theta}$. In the following, the criteria and values adopted to choose them are indicated:

- τ_{E0} is set equal to 50 fs for any studied system, consistently with its meaning of relaxation timescale to quasi-static equilibrium, considered independent from the system settings by the proposed description.
- $\tilde{D}$ is selected equal to the experimental optimum thickness at "normal" contrast conditions or, if this is not available, it is tuned to provide agreement in absolute value with the data.
- $\tilde{\theta}$ is selected equal to a typical value of 60°.

Following these few evaluation steps it is therefore possible to extend Passoni-Lontano $E_{\max}$ predictions in the parameter space, as shown in the following sections.

5.2 Laser Energy Dependence

In this section the issue of TNSA dependence on laser energy E_{p} is faced. As introduced in Sec. 2.3, TNSA peak ion energy dependence on laser irradiance $I\lambda^2$ is one of the most evident features from experimental literature and even a common, rough trend among the various measured energies can be retrieved. However, the complete understanding of $E_{\max}$ dependence on laser parameters is difficult, since it is not possible to change one of them independently from the others. For this reason it is important to clarify also the role of the other parameters as pulse energy, duration or focal spot, in order to reach a deeper comprehension of the possible $E_{\max}$ optimization paths. Different TNSA models lead to different $E_{\max}$ scalings with these parameters. In particular Passoni-Lontano model introduces a quasi-logarithmic growth with laser energy, for fixed $I\lambda^2$, which has phenomenological bases. Such an energy dependence is a fundamental trait also in the extended model formulation here presented, through which a theoretical explanation for the empirical trend can be found as well (see Sec. 5.1.3). For this reason it is interesting to test predictions resulting from Eqs. (4.12) and (5.8) with parametric studies on E_{p}. In experiments the pulse energy can usually be tuned, but energetic scans are performed with fixed pulse duration and focal spot, so that intensity changes accordingly. Since $E_{\max}$ is strongly affected by I, this partially hides the pulse energy dependence, so that the investigation of different directions in the parametric space, namely by keeping I fixed, turns out to be very interesting. In experiments, the variation of τ_{p} or r_{fs} is indeed possible, but it is not easily controlled, since it heavily affects the laser pulse profile. In numerical PIC simulations instead, there is full pulse-shape control, so that these parameters can be systematically modified.

This is exploited here, where a set of simulations[1] is performed at constant I and τ_p, in which E_p is increased by changing the focal spot size. The calculations have been carried out using ALaDyn PIC code [180], restricting to a two-dimensional space and considering an overcritical plasma density $n_e = 40 n_{cr}$. As mentioned in Sec. 3.2 such approximations are mandatory in order to limit computational requirements to a reasonable CPU time, as a consequence, the discussion of the results has to take into account such simplifications of the actual physical system. The laser is represented by a linearly polarized pulse with Gaussian transverse profile and $\sin^2$ temporal profile, normally impinging on a pre-ionized plasma foil of thickness $D = 0.5\,\mu$m. The pulse FWHM temporal length is $\tau_p = 25$ fs, focused at variable waists, in a FWHM radius range from $r_{fs} = 1.18\,\mu$m up to $4.71\,\mu$m. The normalized pulse amplitude is $a_0 = 10$, which corresponds to a peak irradiance of $1.37 \times 10^{20}\,\mathrm{W}\mu\mathrm{m}^2/\mathrm{cm}^2$, and a peak intensity of $2.14 \times 10^{20}\,\mathrm{W/cm}^2$. In Fig. (5.5) the electron energy spectra, for each simulation of the set, are displayed, as they appear 100 fs after the interaction time. The most evident feature of this comparison is that, while the number of electrons is clearly related to r_{fs}, and thus to laser energy, the spectra slope, which is representative of the electron population temperature, is remarkably similar among the entire set. This, on the one hand, supports the idea that T_h is mainly dependent on $I\lambda^2$ and so on a_0, which is kept constant in these calculations. On the other hand it also confirms that the hot electron number is proportional to laser energy, as described by Eq. (5.3)

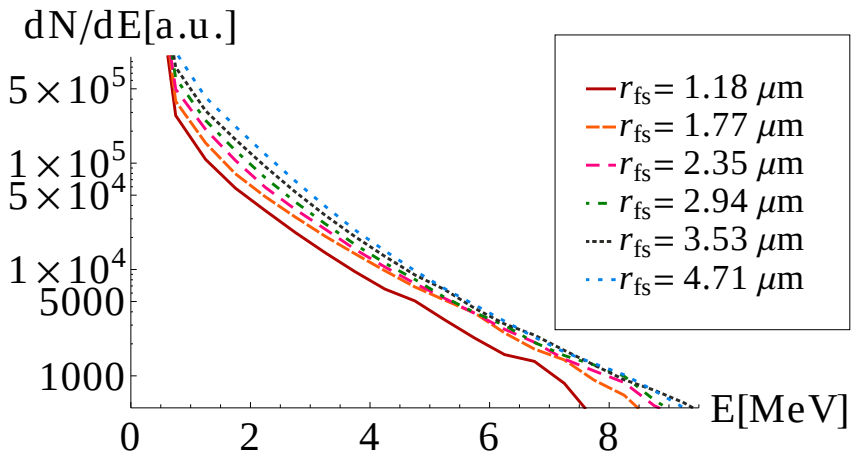

Figure 5.5: - Simulated electron energetic spectra at $t = 100$ fs after the interaction time, for different beam radii as indicated in the legend. The y-axis range is set in order to display the hot electron region. Electrons below 1 MeV are not included, as well as the sub-sampled (< 500 macroparticles per bin) high-energy tails.

[1] The simulation work has been performed by A. Sgattoni on the SP6 machine of CINECA (Bologna, Italy).

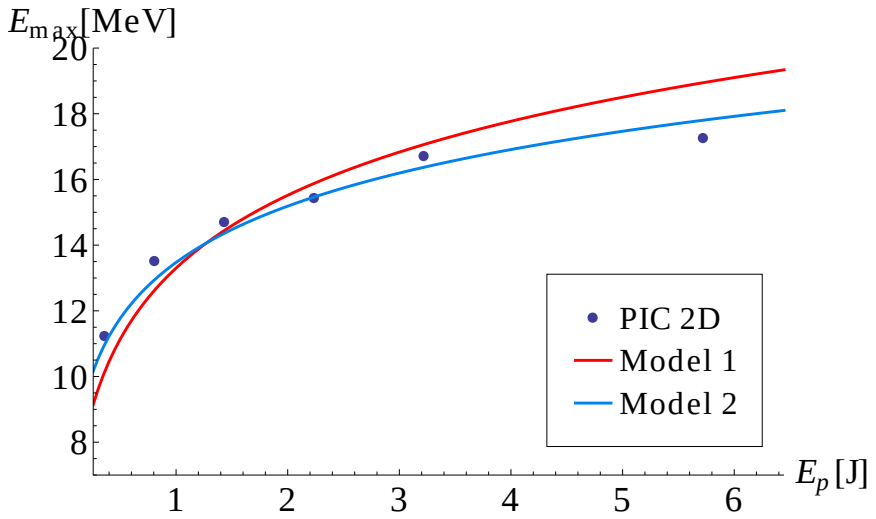

Figure 5.6: - Proton maximum energy at variable laser pulse energy E_p. The blue circles indicate 2D PIC results, obtained using the parameters indicated in the text, the red and light blue curves are theoretical model predictions obtained with different temperature estimates, as explained in the text.

In Fig. 5.6 the proton cut-off energies resulting from such simulations are represented as a function of E_p, together with two analytical scalings obtained by the developed TNSA model. The red curve, indicated in the legend as "Model 1", has been retrieved applying the methods described in Sec. 5.1.4, for laser and target parameters corresponding to the simulation settings, and adopting $\tilde{D} = 0.25\,\mu$m, $\tau_{E0} = 50\,$fs, $\theta = 60°$. Consistently with the calculations of previous chapter, the intensity used to evaluate T_h is not the peak value, but rather the average over the FWHM focal spot, obtained by Eq. (4.19) to be $I = 1.8 \times 10^{20}\,$W/cm^2, leading to a temperature of 4.19 MeV. According to the normalization procedure previously described $\tilde{D}$ should correspond to an experimental optimum thickness at "normal" contrast. Of course, in a comparison with PIC results there is no experimental optimum. In this frame, as far as comparison with PIC results is concerned, $\tilde{D}$ is a degree of freedom that can be exploited to reach the best agreement between numerical and analytical E_{max}, which is why the value $\tilde{D} = 0.25\,\mu$m, not consistent with the typical micro-metric experimental values, has been chosen. However, it should be said that the real aim of this study is that of comparing qualitative trends rather than to reach an absolute quantitative agreement. The latter is indeed dependent on a number of factors, like dimensionality of the simulation, incidence angle or coupling efficiency. In particular, comparisons among 3D and 2D PIC simulations have shown that the latter usually fail in providing correct quantitative predictions, e.g. over-estimating E_{max} with respect to 3D and experimental energies. At the same time, they are effective in reproducing functional trends, provided that the 2D parameters are suitably "translated" to the proper 3D equivalents, as it is done

in Fig. 5.6 to retrieve the pulse energy [39].

In the specific case, the trend of the simulated $E_{\max}$, indicated by the blue dots in Fig. 5.6, shows an evident logarithmic dependence on the laser energy, being in qualitative agreement with the model predictions. More in detail, the scaling obtained (red curve in Fig. 5.6), exhibits a growth with E_{p} which is clearly steeper than that retrieved by the set of simulations, even if the energy predictions are pretty close in the E_{p} range from 0.36 to 5.4 J. The light blue curve referred as "Model 2" is instead obtained at $\tilde{D} = 0.8\,\mu$m, retrieving the temperature still by ponderomotive scaling, but this time according to:

$$k_{\mathrm{B}} T_{\mathrm{h}} = m_{\mathrm{e}} c^2 \left(\sqrt{1 + \frac{a_0^2}{2}} - 1 \right) , \tag{5.10}$$

which basically means that half of the peak intensity value is considered as effective intensity, rather than the FWHM average. In this case the temperature becomes $T_{\mathrm{h}} = 3.14\,\mathrm{MeV}$ and a remarkable agreement with numerical results is observed. In fact, from Eq. (4.12), it is evident that the steepness of $E_{\max}$ as a function of laser energy depends noticeably on hot electron temperature, so that the reliability of the predicted scalings is heavily affected by the temperature estimate. The choice of Eq. (5.10) to evaluate T_{h} can be explained in some sense considering that in two dimensions, because of the restricted spatial dispersion, hot electrons in the peripheral part of focal spot can play a more important role in determining the temperature with respect to three-dimensional case, so that the effective intensity is averaged over a larger area. Of course this result cannot be considered conclusive, since T_{h} has been adjusted to reach the agreement of "Model 2" curve in Fig. 5.6, but it is also clear that a logarithmic scaling with laser energy is exhibited by the numerical results. As said, this behavior is a fundamental trait of present model, descending from the key theoretical hypothesis of Maxwellian hot electron distribution, so that the results of Fig. 5.6, besides the discussed uncertainties, turn out to be quite significant.

5.3 Target Thickness Dependence

In the present section, the $E_{\max}$ estimates obtained with the analytical TNSA model are directly compared with some published experimental measurements of TNSA at variable D targets. For each comparison, the input parameters used to evaluate $E_{\max}$ are chosen consistently with the data provided by the corresponding experimental references, following the prescriptions introduced in Sec. 4.2 and 5.1.4. As discussed in Sec. 5.1.3 the theoretical predictions are calculated for a θ-range from 30 to 90 degrees, to take into account the uncertainty on this critical parameter.

The first comparison involves results from Ref. [29], in which Al foils of different thicknesses have been illuminated at the ATLAS 10 TW laser facility in Garching Max-Planck-Institut. In such a work the ion peak energy dependence on target thickness is studied for variable laser intensity and pre-pulse duration. In Fig. 5.7a-b-c theoretical predictions are compared with three experimental thickness scans, performed at

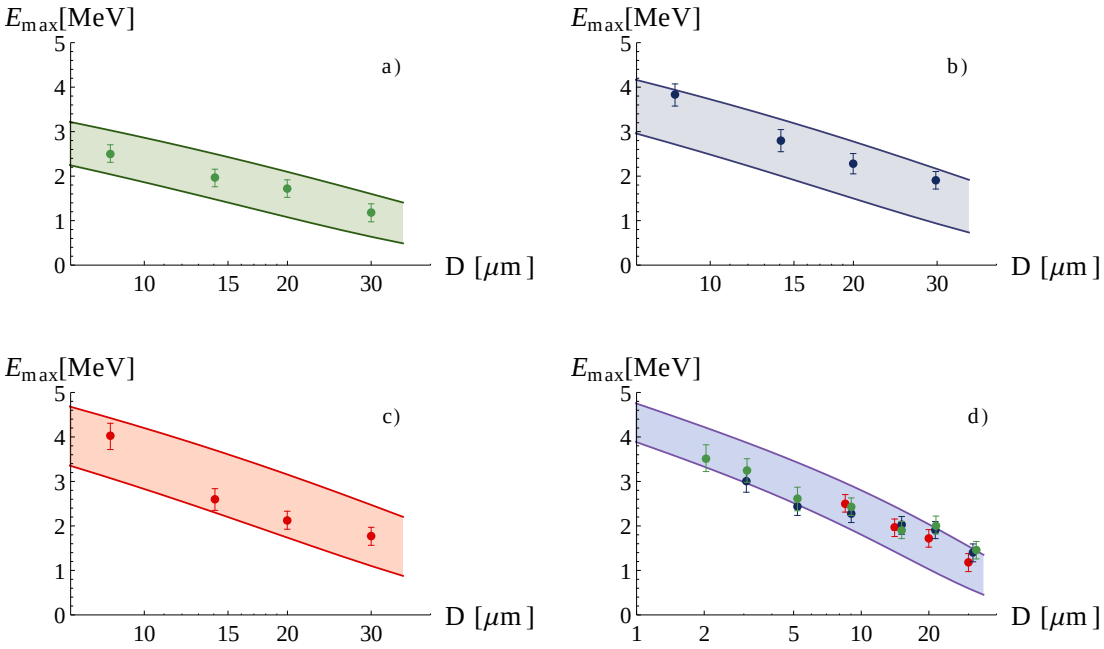

Figure 5.7: - Comparison of the results in Ref. [29] with predicted thickness scalings for the ion maximum energy E_{max} at $\tilde{D} = 9\,\mu$m. Subplot a) and d) correspond to a laser intensity of $10^{19}\,\mathrm{W/cm^2}$, subplot b) to $1.3 \times 10^{19}\,\mathrm{W/cm^2}$ and subplot c) to $1.5 \times 10^{19}\,\mathrm{W/cm^2}$. In subplot d) the experimental results are obtained at different pre-pulse durations, 2.5 ns for the red dots, 0.7 ns for the blue dots and 0.5 ns for the green dots. Theoretical predictions are displayed over a range of divergence angles from 30 to 90 degrees.

fixed pulse duration and focal-spot, but different intensities. The theoretical trend is in agreement with experimental evidences, reproducing the measured intensity dependence in a satisfactory way, although the experimental variation of I is rather small and few thicknesses are available. The calculations are performed considering a normalization thickness $\tilde{D}$ equal to $9\,\mu$m, corresponding to the experimental optimum thickness, which is the same for each of the three sets, as demonstrated by the measurements. As already shown in Fig. 2.10, Ref. [29] provides also two further scans at fixed intensity but different ASE pre-pulse durations, obtained by a Pockel cell tuning. Fig.5.7d displays how the theoretical predictions obtained for $\tilde{D} = 9\,\mu$m provide a nice agreement also with the energies measured for shorter pre-pulses. As mentioned before, $\tilde{D}$ is consistent with the optimum thickness for a "normal" laser contrast, therefore it preserves its meaning and value also when the contrast is enhanced. The agreement obtained here makes it evident how this description is suitable to scale above-optimum experimental results through the sub-optimum region. The use of such target depths, for which TNSA is not efficient under "normal" contrast conditions, is promising in term of energy optimization thanks to the recent developments of Ultra-High-Contrast

(UHC) techniques. In particular, with the present model, it is possible to trace the $E_{\max}(D)$ curve for "ideal" contrast conditions, evaluating the maximum ion energy gain determined by contrast enhancement at some given experimental setting. However, it is important to keep in mind that such a result is referred to a "pure" TNSA behavior, while in a realistic situation, the illumination of ultra-thin targets under UHC conditions can give rise to relativistic induced transparency or hole boring, triggering alternative acceleration mechanisms (see Sec. 2.4).

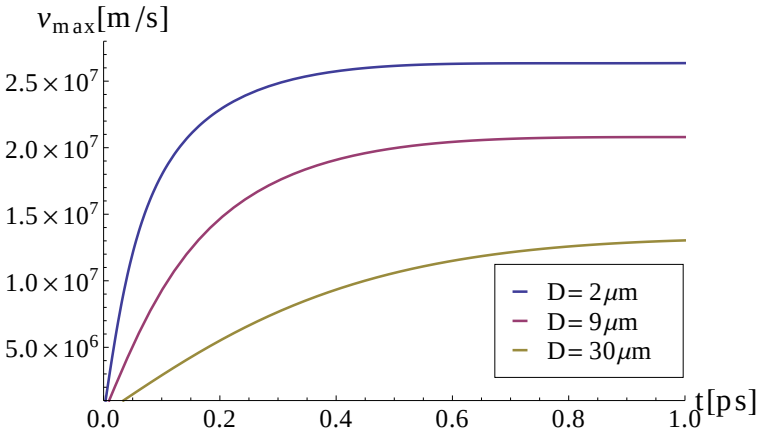

Figure 5.8: - Time evolution of fastest proton velocity for the system parameters of the experiment in Ref. [29], with laser intensity $I = 10^{19}\,\mathrm{W/cm^2}$. The three curves refer to three different target thicknesses.

In Sec. 5.1.3, it has been discussed how the extension of the model makes it possible to evaluate the dimensioned solution of the electro-static problem, so that the accelerating field profile $\mathcal{E}(x)$ is available. This allows also to retrieve the acceleration time of the fastest ions, by solving the equation of motion:

$$\ddot{x}(t) = \frac{Z_{\mathrm{i}} e}{m_{\mathrm{i}}} \mathcal{E}(x(t))\,, \tag{5.11}$$

to get $x(t)$ and $v(t)$. Once these are known, numerical integration can provide an estimate of t_{acc}, for example by inversion of the integral equation:

$$\int_0^{t_{\mathrm{acc}}} v(t)\,\mathrm{d}t = x_{\mathrm{sheath}} \tag{5.12}$$

where x_{sheath} is the extension of the electro-static field in vacuum. Otherwise it is useful to evaluate acceleration time exploiting the following equation:

$$\int_0^{t_{\mathrm{acc}}} \frac{m_{\mathrm{i}} v^2(t)}{2}\,\mathrm{d}t = k E_{\max}\,, \tag{5.13}$$

where k gives the fraction of final energy at which the time is evaluated. Since the electric field decays very steeply, relevant acceleration takes place in an interval of

time which can be significantly shorter than that required to completely travel along the sheath. As an example, maximum velocity evolution for the system parameters of Fig. 5.7d, for three values of D, is represented in Fig. 5.8. The plot shows that acceleration is more intense and brief for the thin target, in this case Eq. (5.13) gives $t_{\rm acc} = 0.53\,\mathrm{ps}$ for $k = 0.99$ and $t_{\rm acc} = 0.73\,\mathrm{ps}$ for $k = 0.9999$, while Eq. (5.12) gives $t_{\rm acc} = 0.81\,\mathrm{ps}$. Increasing the thicknesses the acceleration time becomes longer, $t_{\rm acc} = 0.72\,\mathrm{ps}$ ($k = 0.99$) for $D = 9\,\mu\mathrm{m}$ and $t_{\rm acc} = 1.11\,\mathrm{ps}$ ($k = 0.99$) for $D = 30\,\mu\mathrm{m}$. These timescales of acceleration, being of the ps order, are also consistent with, and support a posteriori, the discussion about quasi-static assumption of Sec. 4.1.

In Fig. 5.9 another comparison is presented, based on the results obtained using the 100 TW laser facility at LULI, published in Ref. [33]. In this case a more energetic laser pulse, reaching an intensity of $4 \times 10^{19}\,\mathrm{W/cm^2}$, with a 320 fs duration, is involved, and the thickness range investigated is extended up to $250\,\mu\mathrm{m}$. Theoretical results are represented in figure by the red and blue bands, respectively calculated for $\tilde{D} = 20\,\mu\mathrm{m}$ and $\tilde{D} = 30\,\mu\mathrm{m}$. In both cases a nice agreement is achieved, with energies slightly underestimated for $\tilde{D} = 20\,\mu\mathrm{m}$, which corresponds to the actual experimental optimum thickness detected by the authors. The results obtained at $\tilde{D} = 20\,\mu\mathrm{m}$ are those which follow correctly the normalization prescriptions expressed in Sec. 5.1.3, so the underestimate somewhat points out the limitations of this normalization criterion. However, at the same time, it is evident that the choice of $\tilde{D}$ affects $E_{\rm max}$ predictions mainly by changing the offset, with little influence on the trend, supporting the capability of the model in reproducing the $E_{\rm max}$ behavior, independently from the arbitrariness introduced by the choice of $\tilde{D}$. It can be also noticed that the highest ion energy reached experimentally, that is 20 MeV at $D = 20\,\mu\mathrm{m}$, is the most underestimated point by the theoretical scaling, although the measurement uncertainty makes it compatible with the predictions. This might be caused by further laser heating of those recirculating electrons which come back to the interaction domain while the laser field is still there, an effect which gets more probable for thinner targets and longer pulses. Considering that the hot electron bunch travels at c, the weight of such an effect can be approximately estimated by evaluating:

$$P_{\rm r}(D) = \int_{-\infty}^{\infty} f(t + 2D/c) f_D(t)\,\mathrm{d}t\,, \tag{5.14}$$

which is the convolution between the laser temporal intensity profile f and f_D, the latter representing the density of electrons close to the focal spot after one longitudinal round-trip through the foil. This is assumed proportional to the intensity profile but decreased by a factor $r_{\rm fs}^2/(r_{\rm fs} + D/\tan\theta/2)^2$ (see Eq. (4.23)). Therefore $P_{\rm r}(D)$ measures the over-imposition of laser temporal profile to the recirculating electron bunch, defining a sort of "re-heating probability", which for example is 3.3 times greater for $D = 20\,\mu\mathrm{m}$ than for $D = 30\,\mu\mathrm{m}$. This effect seems to be present also in Fig. 5.7c, for which $P_{\rm r}(D)$ at the optimum thickness is 3.8 times higher than at $D = 14\,\mu\mathrm{m}$. Of course Eq. 5.14 cannot provide a precise quantitative information on the influence of re-heating on $E_{\rm max}$, but it is useful to enlighten a possible role of laser pulse duration $\tau_{\rm p}$ which is excluded from the proposed theoretical model.

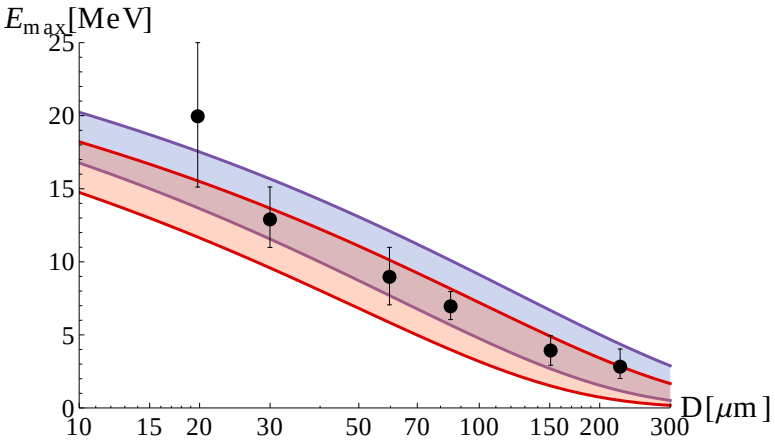

Figure 5.9: - Comparison of the predicted ion maximum energies with the results of Ref. [33]. The predictions obtained for $\tilde{D} = 20\,\mu$m are contained by the red curves, while those obtained for $\tilde{D} = 30\,\mu$m are contained by the blue curves. The considered range of divergence angles is $[30° - 90°]$.

To test the model predictions, an important aspect to put under consideration is the theoretical results sensitivity to the input parameters, whose measurement or estimate can be only partially reliable. As already seen in the previous section, the hot electron temperature T_h, estimated by means of ponderomotive scaling (3.45), is an essential parameter for the determination of peak ion energy trend. Therefore the reliability of such an estimate, but also of the declared I value on which it is based, play a crucial role for the agreement between experimental measurements and theoretical predictions. From this viewpoint an interesting set of experimental measurements is provided by Ref. [89] where the multi-TW system at Lund Laser Centre, coupled with a plasma mirror, irradiates Al foils of thicknesses variable from 12 μm down to tens of nm, with ultra-short (33 fs), high contrast (10^8) pulses. All the measurements are obtained with such enhanced contrast, meaning that the experimental value of the optimum thickness at "normal" contrast is not available. For this reason $\tilde{D}$ is tuned looking for the best agreement with the experimental energies. The comparison with theoretical predictions is displayed in Fig. 5.10, where the blue band contains the energies computed for the declared peak intensity of $I_0 = 10^{19}\,\mathrm{W/cm^2}$, at $\tilde{D} = 5\,\mu$m, while the energies within the red band are evaluated assuming a slightly larger focal spot, so that the peak intensity is reduced to $6.7\times10^{18}\,\mathrm{W/cm^2}$. $\tilde{D}$, in this second calculation, is set equal to 18 μm. In the first case the theoretical trend is steeper than the experimental one, while in the second case it provides a better agreement with the data. The intensity difference between the two cases is not remarkable according to the usual accuracy of the provided I values, but results in a relevant temperature decrease, from 640 keV to 460 keV. This aspect is a crucial limit of TNSA effective modeling in general, more than of the particular theoretical description, and it can be solved only by building a solid phenomenological background of experimental parameters, or a reliable laser-matter interaction theory

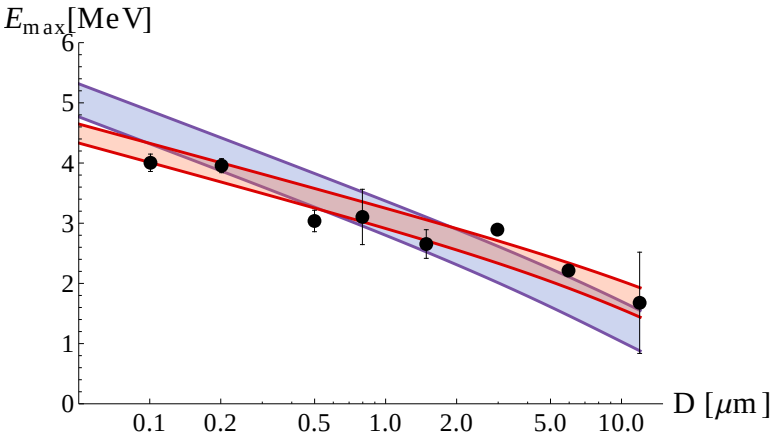

Figure 5.10: - Comparison of the predicted ion maximum energies with the results of Ref. [89]. The blue band shows the predictions evaluated for $I_0 = 10^{19}\,\mathrm{W/cm^2}$ and $\tilde{D} = 3\,\mu\mathrm{m}$ while the red band displays the $I_0 = 6.7 \times 10^{18}\,\mathrm{W/cm^2}$, $\tilde{D} = 20\,\mu\mathrm{m}$ case. The considered range of divergence angles is $[30° - 90°]$.

to predict T_h.

The last comparison presented is based on the results of Ref. [31], obtained on the 10 TW UHI10 laser system at Saclay Laser Interaction Center Facility. During such an experiment an ultrashort (65 fs) pulse is focused on mylar targets of variable thicknesses from 0.1 to 100 μm. In Fig. 5.11 the values of E_max detected in the forward direction for ultra-high contrast (10^{10}) and low contrast (10^6) conditions, together with theoretical estimates, are reported. In the first case a double plasma mirror system is coupled to the laser in order to remove the pre-pulse. Theoretical predictions are evaluated assuming $\tilde{D} = 24\,\mu\mathrm{m}$ which corresponds to experimental optimum thickness for the low contrast configuration. From the figure it is evident that a remarkable agreement between theoretical predictions and measurements is achieved, over a wide thickness range extending from 100 down to 0.1 μm, and based on stable and controlled experimental conditions. Fig. 5.11 represents a sound support and the most promising result for the present TNSA description, which is definitely demonstrated to be reliable in predicting the effect of combined contrast enhancement and thickness reduction, over a D-range of about 3 orders of magnitude.

The presence of ultra-thin targets suggests that in this case, as well as in the preceding (Fig. 5.10), electron re-heating should have a non-negligible role. According to the estimate of Eq. (5.14) such an effect is reduced by 100 times between 0.1 and 10 μm but no appreciable deviations of trend with model predictions are present. Because of the shorter pulse duration, P_D decreases even faster for the data of Fig. 5.10, where already at 6 μm the effect is 100 times attenuated, while no difference of E_max behavior is recorded. On the contrary, the fact that the lower intensity predictions (red region in Fig. 5.10) are in better agreement with the energy measurements, suggests that the actual T_h in this experiment is rather lower than the ponderomotive estimate, while the

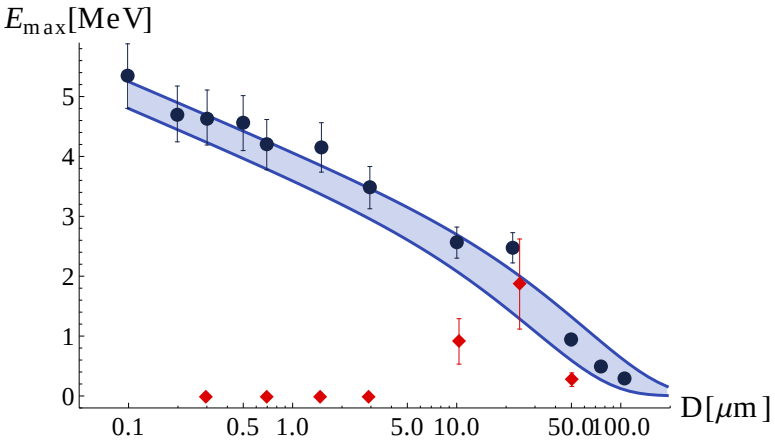

Figure 5.11: - Comparison of the predicted ion maximum energies with the results of Ref. [31]. The blue dots represent the energies measured for the ultra-high contrast pulse (with double plasma mirror), while the red dots represent the energies measured for the low contrast pulse. The model predictions are obtained with $\tilde{D} = 24\,\mu$m which corresponds to the optimum thickness in the low contrast measurements. The considered range of divergence angles is $[30° - 90°]$.

presence of reheating would suggest a higher T_h. Moreover, for ultra-thin targets, the probability that electrons are re-heated multiple times can in principle become relevant. This complex behavior makes it evident that the interpretation of subtleties in the experimental E_{max} measurements is extremely difficult, due to the limited reliability of the considered scaling laws and to the multiple factors that intervene in laser-matter interaction and hot electron physics.

In fact, the attempt to include re-heating within the present TNSA description clashes with the absence of dynamical aspects, which is an advantage in order to reach analytical solutions, but at the same time one of the main limits of the model. At the lowest approximation, the first consequence of lack in dynamics is an energy prediction which is independent from laser pulse duration τ_p, except for the important, indirect dependence through the other laser parameters. This is of course a drawback, since experiments have demonstrated (see Sec. 2.3) that laser duration might play a role in determination of E_{max} although with non-conclusive and somewhat controversial information. An analysis of the dynamical aspects of ballistic, collision-less hot electron transport is provided in Sec. 5.4, by means of a further TNSA modeling development.

Anyway, the overall agreement attained by present description for four widely different experimental results is promising and represents a strong validation of the model assumptions. In particular, it can be concluded that a ballistic, collision-less interpretation of the hot electron transport, combined with a quasi-static picture of TNSA fields, can model to a good level of reliability the hot electron physics relevant for the determination of E_{max}, both for absolute values predictions and for the evaluation of correct scalings. The arbitrariness implied by the normalization process still represents a modeling limit, as far as absolute energy estimate is concerned. On the other hand

the introduction of a phenomenological information by means of scaling (5.1) can be practically convenient, mostly to overcome a number of uncertainties deriving from the rough estimate of key parameters, as for example T_h or θ, and from the intricate connection between laser and target features (e.g. the role of pulse contrast in TNSA physics).

5.4 Study of the Dynamical Aspects

Up to this point, the study of hot electron transport under the assumption of ballistic, collision-less motion, and the description of recirculation process by means of totally reflecting target walls, have shown to be remarkably reliable despite the significant approximations adopted. In addition, the electro-static picture imposes temporal constraints on the described system, forcing to consider a time-averaged, effective hot electron density $n_{\mathrm{h}0}$, and to neglect all the possible effects implied by the electron cloud temporal evolution.

In this section, this lack of dynamical information in $n_{\mathrm{h}0}$ description is addressed, in an effort to investigate the role of electron transport dynamical effects on ion acceleration, still remaining in the framework of quasi-static approach to TNSA description. The basic idea is that of exploiting once again the useful assumptions of collision-less, ballistic transport and of totally reflecting target walls, but from a more rigorous point of view, that is by including more details on the hot electron initial distribution. This is achieved by introducing $f_{\mathrm{hs}}(\mathbf{x}, \mathbf{p}, t)$, namely the hot electron distribution function at the source of the electron beam, that is at the laser focal spot. The spatial and temporal features of this f_{hs} will determine a dynamical behavior of hot electron density inside the target which can influence the acceleration of fastest ions.

The technical approach exploited to study the dynamics of ballistic, collision-less transport, determined by a detailed hot electron initial distribution f_{hs}, is that of Monte Carlo (MC) sampling [181]. A number N_p ($\sim 10^8 - 10^9$) of sample particles, much smaller than the physical number N_h, is generated using pseudo-random number generation and importance sampling common techniques[1]. Then, the motion of the sample particles is studied according to the assumptions on transport and recirculation modeling, and the resulting hot electron density at the source is investigated. This leads to a time-dependent $n_{\mathrm{h}0}$, which can be exploited as a variable boundary parameter in the Poisson equation, providing an evolving accelerating field. The latter can be exploited for a numerical solution of the equation of motion for the light ions. This way, the fastest ions can experience the field evolution determined by the dynamical description of hot electron boundary density, and a more rigorous TNSA model is obtained, still restricted to quasi-static equilibrium timescales and once again neglecting the collective response of bulk ions.

[1] A huge literature about Monte-Carlo methods and pseudo-random number generation is available, in this work the introduction provided in Ref. [182] has been used, and the RANLUX random number generation algorithm, presented in Ref. [183], is exploited.

5.4.1 A Monte-Carlo Approach to Transport Modeling

As just described, new elements have to be introduced within the analytical model of Sec. 5.1, in order to reach the detail being looked for. In fact, the generated hot electron distribution at the source f_{hs}, needs to be chosen realistically, according to the available information about laser-matter interaction.

The information on interaction phase which has been implemented in the model up to now consists in:

- the generated electrons distribute according to a Relativistic Maxwellian distribution of temperature T_{h}.
- The temperature of hot electrons can be estimated by the ponderomotive scaling (3.45).
- The number of heated electrons N_{h} can be retrieved through energy balance considerations, according to Eq. (4.20).
- The fraction of laser energy absorbed by hot electrons can be estimated by Eq. (4.25).

The idea is then to choose a hot electron distribution f_{hs} at the source which complies with these few constraints. The most natural way to achieve this is to assume that f_{hs} is distributed in energy as a relativistic Maxwell-Jüttner function, with temperature T_{h} given by Eq. (3.45), and to impose that the distribution normalization satisfies energy balance (4.20), where η is given by Eq. (4.25). Therefore the relativistic energy γ_{h} of hot electrons is distributed according to:

$$f_{\mathrm{hs}}\left(\gamma,\zeta\right)=\frac{\gamma^{2}\beta_{\mathrm{h}}(\gamma)\zeta}{\mathcal{K}_{2}\left(\zeta\right)}\exp\left(-\zeta\gamma\right), \tag{5.15}$$

where $\zeta=m_{\mathrm{e}}c^{2}/k_{\mathrm{B}}T_{\mathrm{h}}$, consistently with Defs. (4.11), while $\beta_{\mathrm{h}}=(1-\gamma^{-2})^{1/2}$ is the hot electron velocity in units of c. The choice of spatial, temporal and angular distributions is then arbitrary, as long as the number is fixed to N_{h} by energy balance. For what concerns spatial and temporal coordinates, the solution adopted here is that of considering the hot electron generation proportional to laser intensity profile. This means that, being the laser pulse approximated to a Gaussian distribution, both in temporal and in transverse spatial profiles, hot electron density at the source follows the same distribution. Therefore, an electron is generated at a time t (where $t=0$ when the intensity peak hits the target) with probability proportional to:

$$f_{\mathrm{hs}}(t)=\frac{1}{\sqrt{2\pi\sigma_{t}^{2}}}\exp\left(-\frac{t^{2}}{2\sigma_{t}^{2}}\right), \tag{5.16}$$

in which $\sigma_{t}=\tau_{\mathrm{p}}(8\log 2)^{-1/2}$ is the standard deviation. Moreover, assuming an axially symmetric Bi-normal transverse profile, the hot electron radial coordinate follows a

Rayleigh distribution, namely:

$$f_{\mathrm{hs}}(r) = \frac{r}{\sigma_r^2} \exp\left(-\frac{r^2}{2\sigma_r^2}\right), \tag{5.17}$$

in which $\sigma_r = r_{\mathrm{fs}}(2\log 2)^{-1/2}$ is the beam waist. Assuming that hot electron source density is proportional to laser intensity profile actually presumes a loss of generality, but it is reasonable, considering the required level of precision and the limited knowledge in laser-matter interaction. For what concerns angular distribution, the results published in Ref. [159], and briefly introduced in Sec. 3.1.2 can be exploited, by using the following distribution:

$$f_{\mathrm{hs}}\left(\theta, \sigma_\theta, \theta_r\right) = C \exp\left[-\frac{(\theta - \theta_r)^2}{2\sigma_\theta^2}\right], \tag{5.18}$$

where C is a normalization factor and the local mean angular deviation depends on r according to:

$$\theta_r = \tan^{-1}\left(\frac{\lambda r}{2\sigma_r^2}\right), \tag{5.19}$$

which accounts for the ponderomotive force determined by the transverse Gaussian profile (see Ref. [159]), and σ_θ is a further parameter that can be chosen afterwards, representing the θ dispersion from θ_r. The modeling for hot electron distribution at the source, namely Eqs. (5.15), (5.16), (5.17) and (5.18), introduces plenty of new details in transport dynamics, by relying on reasonable arguments and observations. Different choices for f_{hs} dependencies are anyway possible and should be investigated, a work which goes beyond the purposes of present thesis.

As mentioned before, the approach adopted to translate these assumptions into practical evaluations, and thus to study the hot electron transport resulting from the defined f_{hs}, is the Monte-Carlo approach. $N_{\mathrm{p}} \ll N_{\mathrm{h}}$ sample particles are numerically generated, and then the trajectory of each of these particles is computed according to the assumptions of collision-less transport and perfectly reflecting walls. This means that each electron undergoes a uniform, rectilinear motion which is folded within the target volume at each reflection from the foil boundaries. To simplify and speed up the evaluation a cylindrical target box is considered. As a consequence, after the N_{p} electrons have been generated, their position inside the target volume at the time of interest $\bar{t}$ can be computed and the hot electron density distribution $n_{\mathrm{h}}(\mathbf{x}, \bar{t})$ is evaluated, obtaining an axially symmetric function, depending on radial and longitudinal coordinates (r, z), as that represented in Fig. 5.12.

It should be underlined that the code developed for the results presented here is a preliminary version, which correctly performs the demanded operations, but still the computational efficiency can be substantially improved. The main issue concerns the inclusion of electron motion within the MC iteration, so that the output of the latter is already a density distribution $n_{\mathrm{h}}(\mathbf{x}, \bar{t})$. It would be in fact more efficient to generate first the actual distribution at the source, and make it evolve in time and expand through

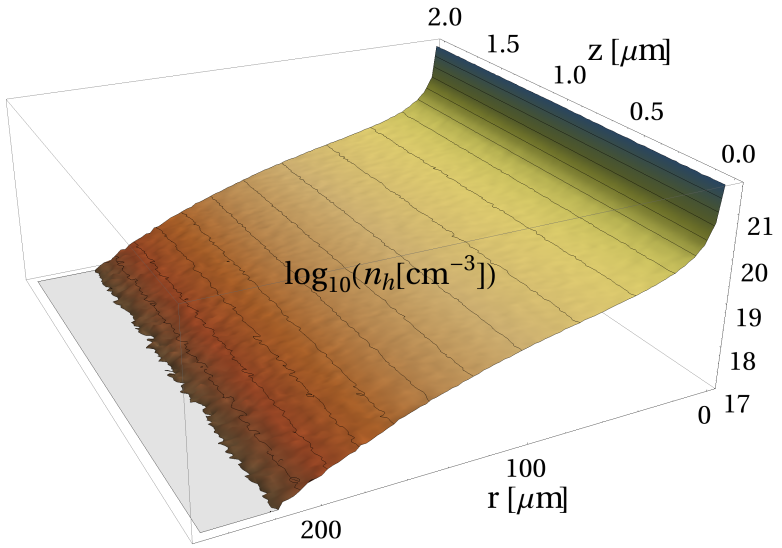

Figure 5.12: - Plot of hot electron density as a function of radial (r) and longitudinal (z) coordinate. The density is indicated by $\log_{10}\left(n_{\mathrm{h}}\left[\mathrm{cm}^{-3}\right]\right)$ and the plot is delimited by the target boundaries. The parameters of numerical calculations are chosen consistently with the experiment of Ref. [35] and the density is evaluated at $t = 350\,\mathrm{fs}$.

the target volume only in a second phase. This way the transport dynamics would be separated from the MC generation phase and could be studied more in detail, since several temporal snapshots would be possible after a single MC computation. Instead, the present numerical algorithm allows the electron dynamics study only if an entire MC loop is performed for each required temporal snapshot, which is a very inefficient approach. Nonetheless, for future perspectives, this scheme can be convenient because of its simplicity, since more physics can be implemented in the single particle trajectories with straightforward and rapid computation. Of course, the collective transport effects cannot be reproduced in this framework, and simple "one-particle" terms should be considered, but the study of probability density function evolution would be way more complex and computationally demanding.

5.4.2 Connection to the Electro-Static Problem

As in the fully analytical model presented in Sec. 5.1, hot electron transport information is required to evaluate the effective density n_{h0} at the left boundary of the Poisson equation characterizing Passoni-Lontano model. The inclusion of spatial and temporal dynamics of the hot electron distribution determines a detailed description of hot electron density inside the target, generating in output a space-time function $n_{\mathrm{h}}(\mathbf{x}, \bar{t})$. The value n_{h0} thus corresponds to the average of n_{h} over a micro-metric spot, localized along the rotational axis of the system ($r \sim 0$), and close to the foil rear surface ($z \sim D$). The calculation results have verified that, over μm space-scales, n_{h} varies slowly enough that the specific average domain choice is not essential, as long as

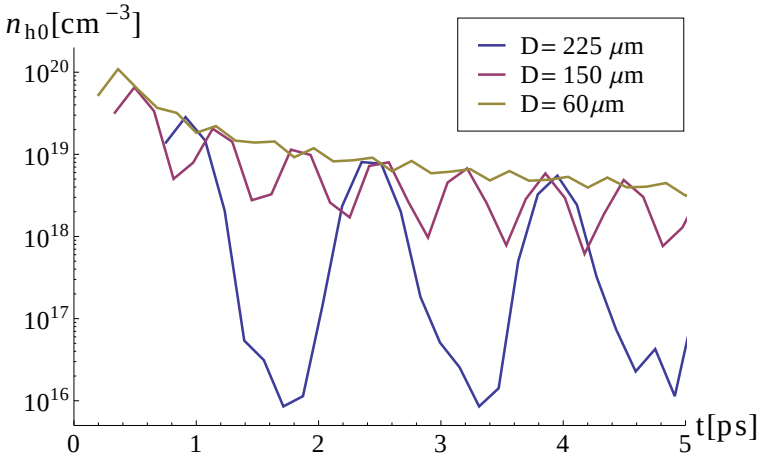

Figure 5.13: - Time evolution of boundary effective density n_{h0}, for the system parameters of the experiment in Ref. [33]. The rather low time resolution $\Delta t = \tau_p/2 = 160\,fs$, explains the haltingly behavior. The three curves correspond to different target thicknesses and $t = 0$ when the irradiating intensity reaches the half maximum value. n_{h0} curves start at $t = D/v_h$, that is when mean velocity (v_h) electrons, generated by the laser half-peak, reach the back surface.

it does not exceed few μms of extension.

As shown by Fig. 5.13 the resulting boundary value is now a time-dependent density $n_{h0}(t)$ so that the electro-static accelerating field should follow this dependence, as hot electron transport dynamics takes place. For this reason an analytical solution for E_{max} is not available anymore, but numerical integration of Eq. (5.11) for light ions motion, with a time-dependent electric field, is required. Once MC evaluations have provided $n_{h0}(t)$ with a time resolution Δt for an overall time range of some ps, a numerical approach to evaluate E_{max} is the following:

1. The initial value $\varphi^*(t = 0)$ is obtained via Eq. (5.8), according to the methods introduced in Sec. 5.1.

2. The initial electro-static field at $x = 0$ is analytically recovered by means of the known Poisson equation solution from Ref. [170].

3. Poisson equation is numerically solved to obtain the electric field $\mathcal{E}(x)$ in the region $(0, \Delta x)$, where Δx has been chosen according to the initial $\mathcal{E}$ value at $x = 0$, by a criterion which is clarified at the next step.

4. Ion motion is integrated over Δt time-step and new position x_i and velocity v_i are retrieved. Therefore Δx has to be chosen large enough that this motion integration does not lead the ion in the region where $\mathcal{E}(x)$ is unknown (that is $x > \Delta x$).

5. The evaluation is iterated for the subsequent values of $n_{\mathrm{h0}}(t_i)$ and therefore for $\varphi^*(t_i)$. One should take into account that Poisson equation integration is now extended to the domain $(0, x_{\mathrm{i}} + \Delta x)$, while motion integration is performed over the next time-step $(t_{\mathrm{i}}, t_{\mathrm{i}} + \Delta t)$.

This process makes it possible to reconstruct an approximated fastest ion trajectory under the action of the variable field, and to evaluate its energy when it leaves the electro-static sheath. Because of the time-dependent φ^* the velocity dynamics is of course different from that of the static description (see e.g. Fig. 5.8), as it is evident in the example represented in Fig. 5.14, where energy is transferred to the ion with an oscillating rate until it is far enough from $x = 0$. In some sense, this approach overcomes the quasi-static picture, introducing some elements of TNSA field dynamics, but still describing the system over ps order timescales, that means still neglecting the collective contribution of ion motion.

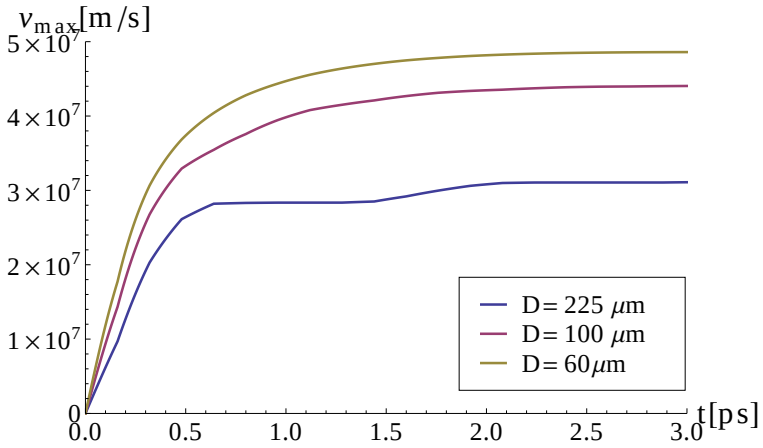

Figure 5.14: - Time evolution of fastest proton velocity for the system parameters of the experiment in Ref. [33]. The three curves refer to three different target thicknesses and $t = 0$ when mean velocity (v_{h}) electrons, generated by the half-peak of the pulse, reach the back surface.

5.4.3 Results

It is now evident that, with such a numerical structure, the weight of n_{h0} dynamics on E_{max} can be investigated and further conclusions about TNSA modeling can be drawn.

For example, it is interesting to test this model E_{max} prediction capability on target thickness dependence, comparing the results with published energies and analytical estimates of Sec. 5.3. This allows to check if, in these cases, the introduction of dynamical effects has a consistent weight on the energy predictions. The two experiments of Refs. [33] and [31] (measurements and analytic predictions are already displayed in Figs. 5.9 and 5.11) have been selected for a comparison, since they cover a wide range

of thicknesses. In fact $n_{h0}(t)$ dynamics is supposed to substantially differ between the measurements obtained either with thin and thick targets, as one can see from the MC results plotted in Fig. 5.13. Here the boundary density evolutions for $D = 60\,\mu$m and $D = 225\,\mu$m show totally different behaviors, decaying almost smoothly in the first case and heavily oscillating in the second.

Starting from the experimental system parameters of Ref. [33], the MC code have been applied to a set of different target thicknesses, retrieving n_{h0} for t up to 5 ps (three examples of the resulting dynamics are represented in Fig. 5.13). In Fig. 5.15 the E_{max} predictions obtained from $n_{h0}(t)$ with the proceeding described in Sec. 5.4.2 are displayed together with the experimental results of Ref. [33] and the analytical predictions already shown in Fig. 5.9. The laser parameters used for the two sets of estimates correspond, with the exception of electron divergence information. In fact, while in the analytical model a single angular parameter θ is chosen (in figure the range $[30° - 90°]$ is represented) in the MC code the electrons are generated following the angular distribution of Eq. (5.18), where θ_r is given by Eq. 5.19 and the dispersion σ_θ is chosen to be 90°. The energies obtained with the dynamical model (red open circles) are in substantial agreement with the analytical model and with experimental energies, considering the possible error sources of the methods. More precisely, some overestimate with respect to experimental energies is exhibited for larger thicknesses, demonstrating that analytical predictions are more reliable in this case, despite the higher approximation level. This is possibly due to the explicit choice of f_{hs}, which might introduce some hot electron density artificial features, not showing in the simple analytical calculations.

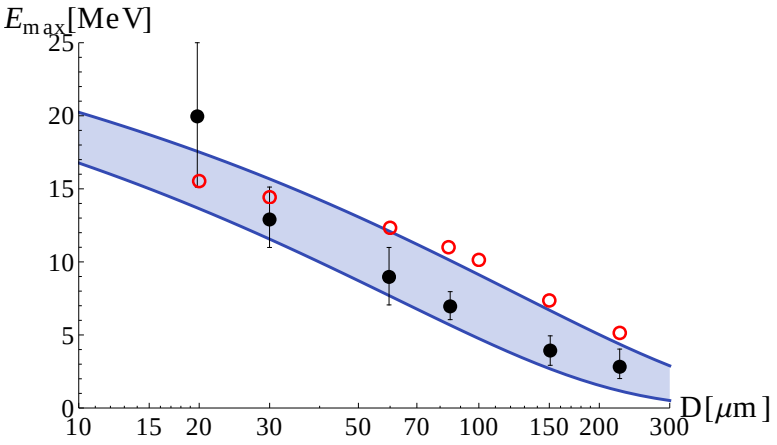

Figure 5.15: - Comparison of the predicted ion maximum energies obtained with the analytical model (blue stripe, same evaluation of Fig. 5.9), with the dynamical estimates (red open circles) and the measurements of Ref. [33]. The normalization is obtained for $\tilde{D} = 30\,\mu$m in both theoretical estimates. The system parameters correspond, except for the electron divergence information, as explained in the text. $\sigma_\theta = 90°$ for the MC generated distribution while the analytical results are displayed for a $[30° - 90°]$ range of divergence angles.

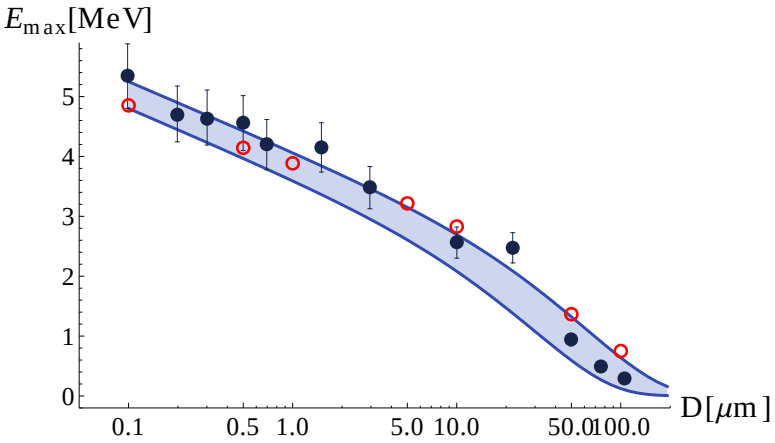

Figure 5.16: - Comparison of the predicted ion maximum energies obtained with the analytical model (blue stripe, same evaluation of Fig. 5.11), with the dynamical estimates (red open circles) and the measurements of Ref. [33]. The normalization is obtained for $\tilde{D} = 24\,\mu$m in both theoretical estimates. $\sigma_\theta = 90°$ for the MC generated distribution and the analytical results are displayed for a $[30° - 90°]$ range of divergence angles.

Fig. 5.16 represents an analogous comparison of dynamic model E_{max} predictions with analytical and experimental results relative to Ref. [31], already shown in Fig. 5.11. Also in this case the modeling parameters are chosen equal to those of Sec. 5.3 analytical calculations, except for the divergence settings, which are chosen as in the previous calculation. The E_{max} estimates obtained by means of the dynamical transport model show once again a substantial agreement with analytical predictions and measurements. In this case the energies are reproduced with higher accuracy, nonetheless, an analogous bias as in Fig. 5.15 is noticeable, with the introduction of a slight overestimate for thicker targets. Therefore, also in this comparison, the dynamical model predictions happen to be less reliable than the simpler analytical ones, supporting the idea that higher detail in hot electron distribution can introduce artificial features with respect to the realistic case. Moreover, one can interpret these results by considering that the averaged approach presented in Sec. 5.1 probably hides some of the issues resulting from the starting assumptions of totally reflecting target walls and collision-less, ballistic transport. Therefore, the results shown in Figs. 5.15 and 5.16 support the idea that dynamical effects do not have a relevant influence on E_{max} determination and strengthen the belief that a static, averaged approach, as that applied in the analytical model presented in Sec. 5.1, is generally valid and reliable for TNSA fastest ions description.

In Fig. 5.17 the cut-off energy temporal evolution for all the different target thickness cases is displayed, so that the reader can appreciate the dynamics of acceleration resulting from n_{h0} oscillations (thicker targets). The figure also shows that the acceleration time for $D > 50\,\mu$m targets is of the order of 2 ps, so that collisions might have a relevant influence in the determination of E_{max}. In this sense it would be extremely

interesting to introduce new physical effects as the electron stopping power or as a more precise modeling of electron boundary reflection in the motion of MC generated particles, to determine their weight on final E_{max} predictions. As already mentioned, also the test of present method with different distribution f_{hs} can be useful to reach a better understanding of hot electron transport effects on ion acceleration. These possibilities however are beyond the purposes of present dissertation, and qualify as potential perspectives of this modeling work for the immediate future.

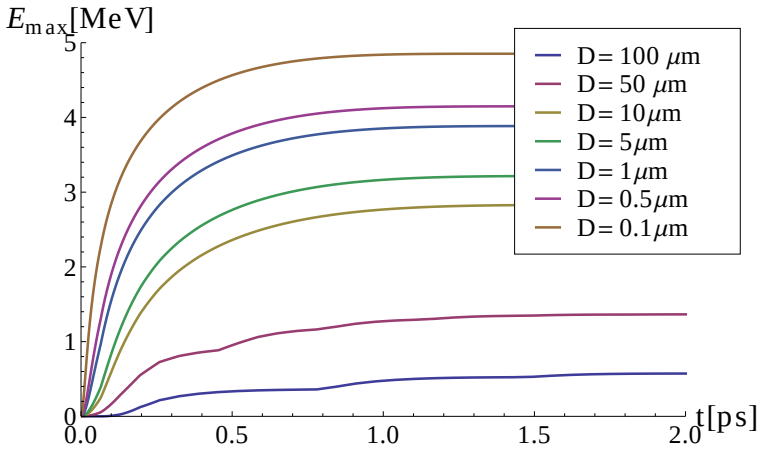

Figure 5.17: - Time evolution of E_{max} for the set of MC calculations performed referring to the experiment in Ref. [31]. Each curve refers to a different target thicknesses (see the legend values) and $t = 0$ when mean velocity v_h electrons generated by the half-peak of the pulse reach the target. The time-step of these calculations is $\Delta t = \tau_p = 65\,fs$.

5.5 Mass Limited Targets and Transverse Recirculation

In Sec. 2.3 an alternative way to optimize TNSA, still exploiting the hot electron confinement by the electro-static fields at the target boundaries, has been discussed. It consists in reducing the transversal dimensions of the irradiated foils, using the so-called Mass Limited Targets. This is possible because the hot electrons expand along the transversal direction as well, as demonstrated by ion source area measurements [64] or by the detection of TNSA ion bunches emitted from the lateral edges of the target [92]. Therefore, a reduced transverse size can contribute to TNSA enhancement by raising the hot electron density at the ion source region, thanks to the lateral confinement of hot electron expansion, in an analogous way as target thickness longitudinally confines the hot electron cloud.

In various theoretical works this approach has been tested with PIC simulations, confirming the TNSA efficiency improvement with promising results [93, 94, 95, 96, 97]. However, the application of this principle in experiments has required some time, because the illumination of MLTs has turned out to be more challenging with respect to

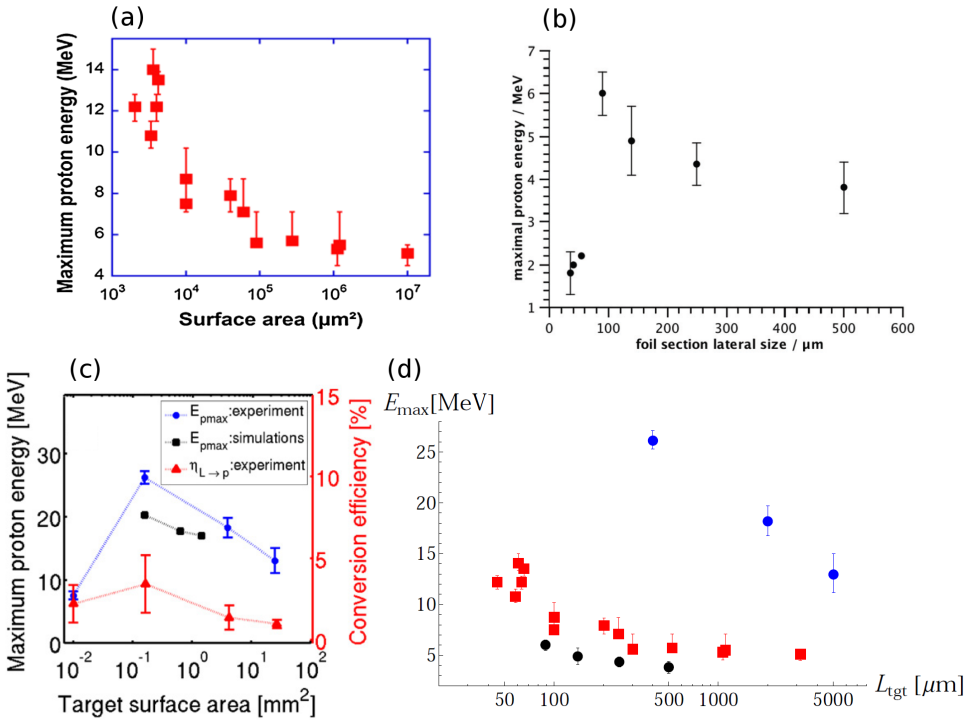

Figure 5.18: - Proton cut-off energies measured at constant laser conditions for fixed thickness but variable transverse size targets, in three different MLT experiments: (a) at LULI 100 TW facility, with 400 fs pulse and 2 μm thick gold foils (reprinted from [35], same as Fig. 2.11a). (b) At Düsseldorf Arcturus 100 TW laser, with 80 fs pulse and 3 μm thick gold foils (reprinted from [98]). (c) At GSI Phelix laser, with 1 ps pulse and 20 μm thick copper foils (reprinted from [99]). Here the laser-to-proton conversion efficiency $\eta_{\mathrm{L}\to\mathrm{p}}$ is displayed as well. In (d) the above-optimum measurements are shown all together as a function of target transverse size L_{tgt}. The same notation of other figures is kept, that is red rectangles for (a) set, black circles for (b) set and blue circles for (c) set.

extended planar foils, and only recently few proof-of-principle measurements have been published. Experimental results, that are ascribable to TNSA enhancement by hot electron lateral confinement with MLTs, have been published in Refs. [35, 98, 99] and are reproduced here in Fig. 5.18. In each of the three experiments the decrease of target transverse size, at fixed irradiation conditions, has provided an enhancement of E_{max}, as well as an increase of ion number and energy conversion efficiency. The supporting numerical simulations and the theoretical work accompanying the measurements suggest that such an efficiency increase is indeed due to lateral hot electron confinement. In this context it can be interesting to note that a first demonstration of peak ion energy increase with MLTs has already been published in Ref. [34], exploiting 20 μm sized, spherical plastic targets, but that can be interpreted as a result of a different acceleration process, in which a converging shock front is created, accelerating highly

collimated ions with low reproducibility.

The present MLT experimental picture is still constituted by few results, which do not outline a clearly reproducible behavior, nonetheless the use of reduced mass targets is an extremely promising path to TNSA conversion efficiency and ion energy optimization, and several experimental groups are beginning to involve themselves in the exploration of this field. Since the theoretical treatment presented in Sec. 5.1 has given satisfactory results in predicting the effects of electron recirculation for variable thickness targets, an analogous approach can be exploited to attempt a modeling of transversal recirculation, which appears to be among the main causes of the $E_{\max}$ optimization detected in MLT experiments. This is the basic idea motivating the work presented in this section.

5.5.1 MLT Timescales

At the intensity range relevant for TNSA, hot electrons expand with an average velocity v_{h} which is close to c. Therefore, according to the approximation of collision-less, ballistic transport, the electron cloud spreads in the transverse direction with constant velocity $v_{\mathrm{ht}} = v_{\mathrm{h}} \sin(\theta/2) \sim c \sin(\theta/2)$. The effect of transversal recirculation on TNSA is related to the target size by τ_{trt}, namely the average hot electron round-trip time along the transverse direction. The expanding electrons are indeed required to come back to the central region of the target, where they can contribute to the peak accelerating field. Considering a cylindrical foil of height D (which corresponds to the target thickness, assuming that the cylinder axis lies along the longitudinal direction) and radius R, representing the transverse scale of the target[1], τ_{trt} is given by:

$$\tau_{\mathrm{trt}} = \frac{2R}{v_{\mathrm{ht}}} \,. \tag{5.20}$$

Following the quasi-static picture of TNSA, if the reduced transverse dimension of the target has to affect maximum ion energy, τ_{trt} has to be small enough that hot electrons can come back in the ion source region and influence the acceleration field before the most energetic ions have left. Another possibility is that, if transverse recirculation is too slow to affect the first accelerated ions, which are the fastest in ordinary planar foils, then the effect is strong enough to push slower ions to the highest energies in a second stage of the acceleration process.

A first, useful insight is the evaluation of τ_{trt} for the experimental results shown in Fig. 5.18, in particular for the critical target size L_{MLT} (or surface A_{MLT}) at which the MLT effect starts to play a role on $E_{\max}$. This value, used in Eq. (5.20), can give a feeling on the typical timescales required for lateral recirculation to affect peak ion energy. In the case of Fig. 5.18a, referring to Ref. [35] experimental results, a detailed size scan is provided, from which it turns out that $A_{\mathrm{MLT}} \simeq 6 \times 10^4\,\mu\mathrm{m}^2$ ($L_{\mathrm{MLT}} \simeq 250\,\mu\mathrm{m}$), where $E_{\max}$ shifts from 5.6 MeV to 7.1 MeV. It should be underlined

[1] In a square target of side L (as in Fig. 5.18 experiments), R can be substituted by $(1+\sqrt{2})L/4$, which is the median between half-side and half-diagonal, in order to take the shape difference somehow into account.

that the result of Eq. (5.20) depends on θ, so that, in order to establish the influence of this parameter, it is again useful to consider a divergence confidence range, as in Sec. 5.3. The resulting τ_{trt} goes from 1.46 ps for $\theta = 90°$, to 4 ps for $\theta = 30°$, being consistent with the ps timescale of quasi-static equilibrium duration. More specifically, 4 ps is actually too large, since the ion acceleration time t_{acc} is of the order of $0.5 - 2$ ps, so that a quasi-static picture is consistent with $\theta > 60°$ ($\tau_{\mathrm{trt}} \lesssim 2$ ps). On the basis of Eq. (5.20), the results displayed in Fig. 5.18b are in good agreement with those of Fig. 5.18a, since L_{MLT} seems to be localized at a similar value, around 250 μm, consistently with $\tau_{\mathrm{trt}} \lesssim 2$ ps. In this case the detected energies are smaller, and the E_{max} optimum occurs for larger foils (see Fig. 5.18d), probably due to the lower laser energy and contrast ratio[1]. The coincidence of L_{MLT} values for such different laser conditions confirms the validity of the estimate (5.20), which is independent from the laser features[2], as the temporal scale governing the appearance of MLT effects on E_{max}.

This picture is however not supported by the energies displayed in Fig. 5.18c. First of all it is difficult to point out A_{MLT} value, since no E_{max} trend deviation has been detected. Moreover, according to the few E_{max} measurements, A_{MLT} should be at least 4×10^6 μm^2, corresponding to the second highest energy detected. This target extension is larger than in the other two experiments, leading to a longer transverse round-trip time $\tau_{\mathrm{trt}} = 11.5$ ps, already for $\theta = 90°$. This duration is surely larger than the timescale of quasi-static picture validity, suggesting that, in this case, fastest ions should be accelerated in a second stage, in order to take advantage of lateral recirculation. In fact, in this experiment, the involved laser pulse is quite different from the pulses usually exploited for "ordinary" TNSA experiments, since it is rather long ($\tau_{\mathrm{p}} = 1$ ps) and, while a large amount of energy ($E_{\mathrm{p}} = 63$ J) is delivered, the intensity is kept on moderate levels ($I \sim 10^{19}$ μm). Therefore, in this specific case, an acceleration regime involving longer timescales with respect to the quasi-static picture might have occurred.

The experimental background outlined by the available published data is definitely less uniform and established than for the experiments looking at the target thickness dependence of TNSA, and further experimental insights on MLT behavior are necessary to guide theoretical development. Nonetheless, in the next pages, an attempt to model MLT effects on E_{max}, based on the main key hypotheses about hot electron physics introduced in present chapter, is described.

5.5.2 Energy Estimates for the MLT Effect

The analytical description of hot electron physics presented in Sec. 5.1 already contains the information of lateral transport, which depends on divergence angle θ, so that, in principle, it is possible to apply the same approach to model the E_{max} dependence on target transverse size, given that lateral recirculation is the relevant cause of the

[1] To obtain the results of Ref. [35] Nd:Glass radiation is converted to second-harmonic, resulting in a cleaner pulse.

[2] Actually τ_{trt} depends very weakly on T_{h} through v_{ht}, the latter being approximately equal to c along the intensity range of interest.

$E_{\max}$ increment in MLTs. The basic idea is thus to maintain ballistic, collision-less transport hypotheses, leading to the expansion within the volume V_∞ (Eq. (5.4)) for a semi-infinite target, and then to model longitudinal and lateral re-circulation with a similar static, averaged approach as described in Sec. 5.1.2. Namely Eq. (5.7) for n_{h0} should be modified with a factor taking into account the effective density amplification related to the transverse hot electron confinement. A possible, straightforward estimate for such an amplification is:

$$\alpha_{\mathrm{ml}}(t) = \max\left[1,\ \frac{A_{\mathrm{hc}}(t) - A_{\mathrm{fs}}}{A_{\mathrm{tgt}} - A_{\mathrm{fs}}}\right], \tag{5.21}$$

where A_{fs} is the focal spot area, A_{tgt} is the foil surface area and A_{hc} is the transverse section of the hot electron cloud at the time t. Consistently with ballistic expansion, A_{hc} can be estimated by:

$$A_{\mathrm{hc}}(t) = \pi\left[v_{\mathrm{ht}} t \sin(\theta/2)\right]^2 . \tag{5.22}$$

α_{ml} is larger than 1 only if transverse hot electron confinement is relevant, that is if hot electron cloud exceeds the lateral size of the target[1]. In this sense the time at which $\alpha_{\mathrm{ml}}(t)$ has to be evaluated, $t = \tau_{\mathrm{ml}}$ from now on, represents a further parameter to be carefully chosen. The acceleration time of most energetic ions ($\sim 1 - 2\,\mathrm{ps}$) gives a reasonable scale for τ_{ml}, considering that the transverse hot electron confinement influences $E_{\max}$ as long as it can modify the density while the fastest ions are being accelerated and before they leave the electro-static sheath.

The discussion of Sec. 5.5.1 makes it evident that longitudinal and transverse recirculation affect $E_{\max}$ according to different timescales, because of the typical difference in longitudinal and transverse target dimensions. In other words, if hot electrons undergo several longitudinal round-trips before most energetic ions are accelerated, they can perform just few transversal recirculations that can influence $E_{\max}$. For this reason longitudinal density amplification κ^{-1} (see Eq. (5.5)) is evaluated at a different, and usually earlier time τ_{E} with respect to α_{ml}, which is instead calculated at τ_{ml}. From such considerations a formula for the boundary effective density n_{h0}, under the influence of transverse hot electron recirculation, is now proposed:

$$n_{\mathrm{h0}} = n_{\mathrm{h0,ext}}(\tau_{\mathrm{E}})\alpha_{\mathrm{ml}}(\tau_{\mathrm{ml}}) = \left(1 + \frac{v_{\mathrm{h}}\tau_{\mathrm{E0}}}{D}\right)\frac{\eta E_{\mathrm{p}}}{\langle K\rangle V_\infty}\alpha_{\mathrm{ml}}(\tau_{\mathrm{ml}}), \tag{5.23}$$

where $n_{\mathrm{h0,ext}}$ is the effective density estimate used for extended planar targets, that is Eq. (5.7). A key aspect of Eq. (5.23) is that it relates two elements $n_{\mathrm{h0,ext}}$ and α_{ml} which are evaluated at different times, respectively $t = \tau_{\mathrm{E}}$ and $t = \tau_{\mathrm{ml}}$ according to the above considerations. A related logical objection to this formula regards the fact that $\alpha_{\mathrm{ml}}(\tau_{\mathrm{ml}})$ in fact amplifies the hot electron density at $t = \tau_{\mathrm{E}}$, while at first sight it would

[1] The focal spot area is subtracted to take into account its influence on lateral recirculation. For example a larger focal spot means that hot electrons are generated closer to the target edges. However, for the target size range considered by experiments, this effect is mainly negligible.

be more reasonable if transverse confinement term would involve the density evaluated at $t = \tau_{\mathrm{ml}}$. This choice is motivated by the fact that lateral recirculation somehow cancels out the dilution of hot electrons towards the transverse direction, re-focusing them close to the beam axis.

Of course the hot electron dynamics, in the MLT case, becomes more complex, and formula (5.23) is the attempt to model its effect on E_{max} by a static viewpoint; for this reason, some theoretical inconsistencies are to be expected following this approach. Anyway, it is interesting to look at the results of this simple model and to compare them to experimental measurements, in order to understand if the given interpretation of MLT behavior is correct and to what extent the dynamics of hot electrons can be reduced to a static, averaged effect. Therefore the E_{max} predictions obtained with Passoni-Lontano quasi-static model using Eq. (5.23) have been tested on the experimental parameters and energies of Ref. [35], already presented in Fig. 5.18a. As mentioned, the measurements of such an experiment represent a useful test for theoretical predictions, since several foil sizes have been used and a detailed scan is retrieved, also exploiting the enhanced contrast guaranteed by the conversion to second harmonic. This second aspect is in fact very important since it means that target thickness ($D = 2\,\mu$m) is possibly in the above optimum region, so that the present theoretical description can be used (see Sec. 5.1.2).

In Ref. [35] the declared laser parameters are: peak intensity $I_0 = 2 \times 10^{19}\,\mathrm{W/cm^2}$, pulse duration (FWHM) $\tau_{\mathrm{p}} = 400\,$fs and a FWHM focal spot of radius $r_{\mathrm{fs}} = 3\,\mu$m containing 2.1 J of laser energy[1]. In Fig. 5.19 the green scaling corresponds to theo-

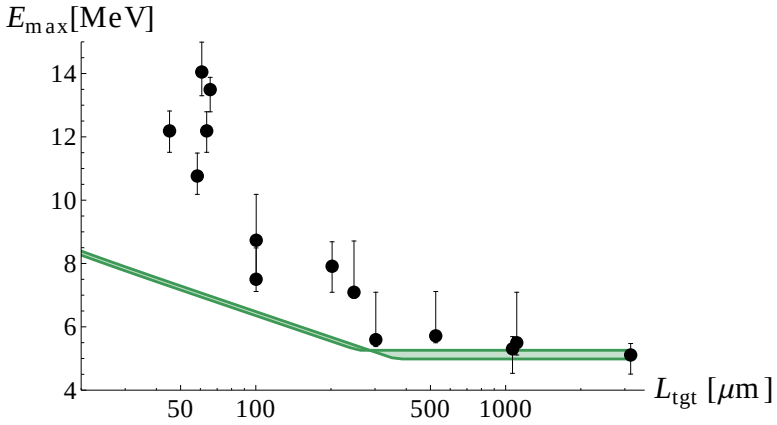

Figure 5.19: - Comparison of the predicted ion maximum energies with the results of Ref. [35]. The model predictions are obtained considering $\tau_{\mathrm{ml}} = 1\,$ps, $\tau_{\mathrm{E}} = 56\,$fs (corresponding to longitudinal time-of-flight through the target plus $\tau_{\mathrm{E0}} = 50\,$fs) and the system parameters of the experiment, indicated in the text. The considered range of divergence angles is $[60° - 90°]$, consistently with the estimates of Sec. 5.5.1 about lateral round-trip time.

[1]The amount of energy in the focal spot is specified in Ref. [184] rather than in the related publication [35], where there is an inconsistency in the declared laser parameters.

retical estimates obtained using this parameter set, with $\tau_{\mathrm{ml}} = 1\,\mathrm{ps}$ and normalization evaluated at $\tilde{D} = 30\,\mu\mathrm{m}$, in order to reach energy agreement for transversally extended targets ($L > 300\,\mu\mathrm{m}$). It is clear that, in these conditions, the analytical evaluation cannot satisfactorily reproduce the experimental energy trend, suggesting that this static approach is not suitable to effectively account for MLT effects.

A first explanation to the limits of present static picture in explaining the MLT effect on E_{max}, is related to the timescale τ_{ml} involved in the process. As mentioned before the transverse extension of considered targets allows only for few lateral recirculations of hot electrons during the acceleration time of fastest ions. Therefore one can intuitively understand how the hot electrons, getting back to the longitudinal axis after a transverse round-trip, determine a time-dependent effect on ion acceleration, rather than an average increase of the electric field. For this reason, the dynamical aspects become surely relevant in this framework and can heavily affect E_{max} predictions. In this sense, as far as MLTs are concerned, the total lack of dynamics in the model can be overcome by a more detailed dynamical transport description, capable to introduce further information within the system. Therefore, as in Sec. 5.4, the developed MC method can be exploited to study the MLT case as well.

Indeed, the MC code implemented to simulate collision-less, ballistic hot electron transport, allows to consider in a straightforward way also the lateral electron recirculation, provided that a cylindrically symmetric target of limited radius R is simulated and that hot electrons are reflected also by the lateral wall. A set of MC simulations for initial laser and target parameters chosen consistently with the previous analytical evaluations, represented in Fig 5.19, have thus been performed. The laser features and the target thickness ($D = 2\,\mu\mathrm{m}$) are the same used for the analytical estimates displayed in figure, while for hot electron divergence an analogous solution as that adopted in Sec. 5.4.3, considering $\sigma_\theta = 90°$ is chosen. Since the numerical code considers a cylindrically symmetric target, the transverse dimension correspondence with experimental values (that involve square foils) can be set, as anticipated in Sec. 5.5.1, by means of the following relation:

$$R = (1 + \sqrt{2})\frac{L}{2}\,, \tag{5.24}$$

in which the median between half-side and half-diagonal is elected as the square equivalent of the radius of cylindrical targets. This rough approximation is considered to compare theoretical and experimental results despite the target shape difference.

Fig. 5.20 displays the time evolution of boundary on axis density n_{h0} obtained, as in Sec. 5.4, from the hot electron density $n_{\mathrm{h}}(r, z)$ produced by the considered set of calculations, with an average over a micro-metric spot, localized along the rotational axis of the system ($r \sim 0$), and close to the foil rear surface ($z \sim D$). The figure shows the different behavior obtained for several target radius R. For the largest target, $R = 1\,\mathrm{mm}$, the density is not affected by transverse recirculation within the considered time interval, while longitudinal recirculation determines an averaged effect, because of the relatively small target thickness ($D = 2\,\mu\mathrm{m}$). This case can be considered as the "extended target" case, corresponding to the region of Fig. 5.19 where experimental results are not affected by MLT effects ($L \sim 1.7\,\mathrm{mm}$ according to Eq. (5.24)). For

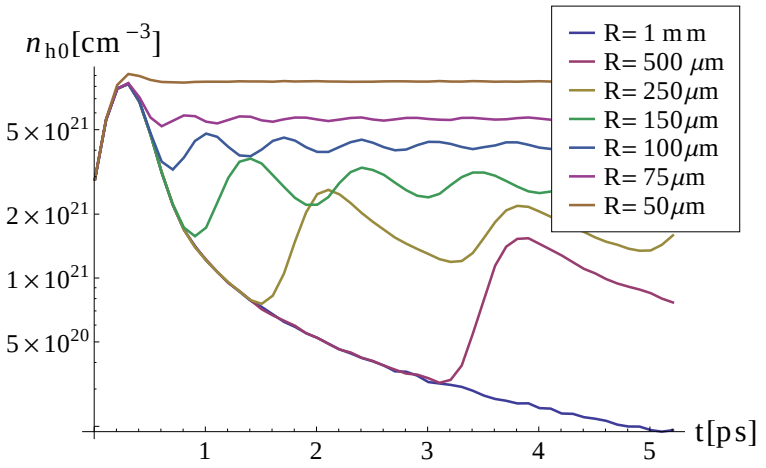

Figure 5.20: - Time evolution of boundary effective density n_{h0}, for the system parameters of MLT experiment in Ref. [35]. Each curve refers to different target transverse radius R (see the legend values) and time origin is set as in Fig. 5.13. The time resolution is $\Delta t = \tau_p/2 = 100\,\text{fs}$.

$R = 500\,\mu\text{m}$ lateral reflux comes into play and boosts n_{h0} value at $t \sim 3.2\,\text{ps}$ with considerable difference from the extended target case. For this target, however, the comeback of hot electron beam takes place too late to affect E_{max}. In fact, the radius corresponds to $L = 830\,\mu\text{m}$ in the experiment, which is still in the region of Fig. 5.19 where no MLT effects have been measured. As the target radius gets smaller, the lateral recirculation becomes effective on n_{h0} at earlier times, for example at $R = 150\,\mu\text{m}$ (which corresponds to $L = 250\,\mu\text{m}$) the density ripple takes place from 1 to 2 ps, which is soon enough for fastest ion motion to be influenced. This is consistent with the experimental results of Ref. [35] and with the discussion of Sec. 5.5.1, supporting the interpretation of the E_{max} increase as a result of lateral recirculation. At later times, further n_{h0} oscillations indicate successive recirculations, which influence E_{max} only for the target sizes smaller than $100\,\mu\text{m}$.

Therefore, the MC calculations generate a n_{h0} temporal dynamics which is in promising agreement with the experimental energy trend. However, when the procedure introduced in Sec. 5.4.2 is applied to retrieve E_{max} estimates from the time-dependent densities plotted in Fig. 5.20, the resulting values reveal that no appreciable energy increase is detected among the different target radii. More precisely, the ion cut-off energy computed with the technique defined in Sec. 5.4.2, barely raises as R changes from 1 mm to $50\,\mu\text{m}$, in strong contradiction with the MLT effect interpretation provided in Sec. 5.5.

The energy calculation is indeed affected by the electro-static sheath structure obtained through Poisson equation solution. In this case, the evaluated electro-static field happens to be too steep, so that ions are pushed far from the influence of the hot-electron sheath in a short time, and the comeback of recirculating electrons does

not occur soon enough to affect ion acceleration. This might be due to a wrong estimate of some key system parameters, as for example the hot electron temperature. In the proposed evaluation T_h is in fact retrieved as usual by ponderomotive scaling, but the declared laser intensity ($I_0 = 2 \times 10^{19}\,\mathrm{W/cm^2}$) and the shorter wavelength ($\lambda = 0.529\,\mu\mathrm{m}$) result in a relatively low temperature value of 0.58 MeV if compared with the measured ion energies of Fig. 5.19, ranging from 5 to 14 MeV. Moreover, in Ref. [35], T_h is experimentally found to increase with the reduction of target transverse size, a feature which is likely to influence ion energy trend. This temperature increase can be for example attributed to a multiple heating of recirculating hot electrons, which gets more probable as the target size decreases, resulting in an higher effective T_h for less extended foils (as explained in Sec. 5.3 relatively to longitudinal recirculation). Therefore, the purpose to attain a satisfactory ion energy cut-off predicting capability for MLTs still requires further theoretical work and refining of the proposed model, so that the evolution of hot electron density can be properly linked to the electro-static accelerating field and MLT effects on T_h are introduced. Nonetheless, the agreement between n_{h0} temporal dynamics and the experimental behavior still remains as a relevant support to the idea of lateral recirculation.

5.6 Summary

As for Ch. 4, the main results of present chapter are now summarized. In the presented work, an extension to the quasi-static TNSA theoretical description proposed by Passoni and Lontano (see Sec. 4.1) has been provided. This was obtained by including further information about hot electron physics within the original model, exploiting the key hypotheses of collision-less, ballistic electron transport and a simple approximation of re-circulation process.

The analytical development derived from such assumptions, presented in Sec. 5.1, has attained two main achievements. First, it provides a theoretical support to the phenomenological relation (5.1), necessary for the evaluation of E_{max} according to the quasi-static model, partially explaining the empirically retrieved behavior. Second, it has extended the predicting capability of Passoni-Lontano model, introducing new, crucial dependences in the calculated value of maximum ion energy, thus allowing to estimate E_{max} on a broader set of laser-target parameters. The resulting model predictions have been tested, exploiting 2D PIC simulations and published experimental measurements, which have provided solid confirmations on its reliability, in particular in reproducing the E_{max} dependence on the target thickness. It has to be mentioned that the agreement with numerical and experimental data is affected by the choice of a normalization coefficient, which in fact represents a further degree of freedom that needs to be fixed, either relying on the empirical scaling (5.1) or on a known E_{max} value, measured or simulated. Anyway, the normalization has shown a relevant influence mainly on the offset of E_{max} predictions, not influencing the resulting scaling trends with parameters.

A further development of the initial assumptions on hot electron dynamics have

also been proposed in Sec. 5.4, this time exploiting a numerical MC code, in order to include electron spatial and temporal dynamics details within the description. This numerical instrument has allowed to observe the effect of hot electron density evolution in time on fastest ion acceleration, by comparing the resulting $E_{\max}$ estimate with the analytical and experimental values. In the cases which have been tested, the computed energies have demonstrated to be compatible with the retrieved analytical estimates, confirming that the averaged, static approach adopted for the latter ones is a reasonable and convenient approximation for the described system.

In Sec. 5.5, the same analytical and numerical approaches have also been applied in the framework of MLTs, in order to describe the effect of hot electron transverse recirculation on maximum ion energy. In this case, the obtained $E_{\max}$ predictions are not in agreement with the published experimental results, suggesting that more physical details are required to reproduce the realistic scalings. However, apart from the ion energy estimates, the time evolution of hot electron boundary density $n_{\mathrm{h}0}$, retrieved by means of MC calculations, has confirmed the idea that transverse recirculation is a crucial factor in the TNSA enhancement resulting from MLT illumination.

Moreover, the proposed Monte-Carlo method has turned out to be a useful instrument to study hot electron dynamics in the collision-less ballistic approximation, opening the possibility to explore different initial distribution functions and to refine the reflux modeling without heavy computational requirements. As already mentioned, the introduction of averaged, single particle, collisional and radiative effects or of a more detailed recirculation model can indeed be implemented within the electron trajectories evaluation, so that the influence on the resulting hot electron effective density can be investigated.

6

Conclusions and Perspectives

In this chapter an outline of the main achievements, and of the possible future developments for the work described in the present dissertation is provided.

This PhD thesis work has been entirely dedicated to the study and advancement of TNSA theoretical understanding, motivated by the crucial role that such a mechanism plays in the field of laser-based ion acceleration.

Indeed, as already stressed in Ch. 1 and 2, nowadays TNSA represents the most experimentally accessible scheme to laser-driven ion acceleration, being "naturally consequential" to the irradiation of planar solid foils with ultra-intense laser pulses. On the contrary, alternative mechanisms as RPA, BOA or CSA, still require a sensible development of the available technology, in order to establish as feasible ion generation processes in ultra-intense laser-matter experiments. Moreover, a deeper knowledge of TNSA can also stimulate the progress of these alternative schemes, since it presumes a more robust control of relativistic laser-plasma physics, which governs collective particle acceleration.

As extensively described in Ch. 2, the numerous experiments, performed in more than ten years since the first appearance of TNSA in 2000, have outlined a complex phenomenology; on the one hand, they identified this mechanism as the dominant ion acceleration scheme but, on the other hand, they also revealed a multi-faceted physical behavior, which makes it extremely challenging to reach control and optimization of the ion features. In particular, a few relevant open problems have emerged from the TNSA experimental state-of-the-art, mainly related to the understanding of the accelerated ion properties dependencies on the laser and target parameters. The control of these dependencies is indeed extremely important for directing future experiments exploiting the next developments in high-power laser technology.

The solution of these problems demands for a satisfactory theoretical knowledge of TNSA mechanism, and for models that can provide reliable predictions on the accelerated ion features. The purpose of the present dissertation is indeed the research of a reliable TNSA effective description, capable to predict the ion maximum cut-off energy, reproducing the behavior outlined by the experimental literature, without the huge computational efforts that "first principle", numerical approaches as PIC require

to simulate a realistic TNSA system.

The achievement of such aims is hampered by the intrinsic complexity of TNSA physics, lying mainly in the fundamental aspects of relativistic laser-over-dense plasma physics, a field which is still not completely understood and in which theoretical modeling happens to be anything but straightforward. In the overview provided in Ch. 3, the theoretical background of TNSA process has been presented in order to outline the starting point for the formulation of a description capable to catch the fundamental features of TNSA.

After the introduction and discussion of the main TNSA theoretical modeling approaches available in the literature, a first step towards the purpose of present dissertation is made through an extensive quantitative analysis of six (among the most known) published descriptions, based on the experimental achievements resulting from 12 years of research. This work, illustrated in Ch. 4, consists in the comparison of the maximum ion energy predictions, obtained by means of each different model, with the actual energies measured and reported in the experimental articles. Such a comparative study, despite the technical issues to be faced in order to reduce the arbitrariness of the results, has allowed to draw some interesting conclusions about the effectiveness of the six models considered and about TNSA modeling in general. First of all the Passoni-Lontano quasi-static description has turned out as the most reliable for predicting capability, providing energetic estimates in remarkable agreement with the experimental measurements over a wide range of laser-target conditions. Moreover, the use of different techniques to estimate relevant system parameters, as hot electron source density or temperature, have been tested to check which ones can guarantee the best energetic predictions according to the different models; the detailed results of this analytical work on the estimates are summarized in Sec. 4.4. Another important conclusion regards the problem of the diverging electro-static potential, which is generated by the Boltzmann-like charge distribution considered in some of the TNSA theoretical models. The different solutions proposed by the models to overcome this issue have been discussed in the light of the quantitative analysis and it have been possible to conclude that the self-consistent limitation of the potential well, proposed by Passoni-Lontano model, is the most convenient approach in this sense.

Therefore, the quasi-static description of Passoni-Lontano has turned out to be the most reliable in predicting the ion cut-off energy, at the same time achieving such estimates through a self-consistent treatment of the accelerating potential. However, from the study of Ch. 4, important limitations in the estimate capability and in the theoretical foundations of Passoni-Lontano model have emerged, motivating the work of Ch. 5. First, the ion cut-off energy calculation requires as input parameter the value of φ^*, that is the normalized potential at the inner boundary of the electro-static problem which defines the adopted TNSA model. φ^* needs to be estimated by means of an empirical scaling law (Eq. (4.26)), because of the lack of a suitable theoretical model. Therefore a theoretical explanation of φ^* phenomenological behavior is required, in order to strengthen the foundations of the description and to justify the use of Eq. (4.26). Second, the energy estimate obtained through Passoni-Lontano description

depends only on laser pulse irradiance, energy and on the accelerated ion charge. Thus it is not presently capable to take into account some fundamental factors of TNSA, as for example laser contrast conditions, pulse duration and target thickness. These issues are the consequence of a lack in physical information related to hot electron generation and transport phases, which is common in TNSA effective modeling, due to the complexity of the physics involved.

As said, such considerations lead to the work presented in Ch. 5, where an extension of original Passoni-Lontano description, intended to overcome such drawbacks, is proposed. The basic idea is that of implementing further information about hot electron physics within the model, still remaining in the domain of a quasi-static picture. Therefore, by considering a ballistic, collision-less electron dynamics, able to approximately reproduce the recirculating motion experienced by the electrons inside the target, an analytical estimate for the effective hot electron density at the inner boundary of the electro-static problem is retrieved. Such a result links the potential φ^* to some key parameters of the system, as for example the target thickness, introducing further crucial dependences in the $E_{\max}$ predictions. As a first result, the implementation of electron transport physics within the model, has given a theoretical support to Eq. (4.26), explaining the scaling of φ^* with the laser energy as a consequence of energy conservation during the laser-matter interaction and of the Maxwellian distribution assumed for the hot electrons. Furthermore, the new dependencies introduced in the behavior of φ^* have significantly extended the $E_{\max}$ predicting capability of the original Passoni-Lontano model. In particular, the scaling of $E_{\max}$ with the target thickness, for "ideal" contrast conditions, has been evaluated for different setups, showing a remarkable agreement with the published experimental results, and demonstrating that the proposed theoretical picture is capable to take into account some crucial aspects of the TNSA physics. A normalization issue is still present in the overall model, since a factor has to be fixed in order to completely define the electro-static system. This requires once again the use of Eq. (4.26), but does not affect in a relevant way the predicted trends, keeping intact the physical meaning of the obtained results.

As a further confirmation and development of the proposed theoretical model, a more detailed, numerical description of collision-less, ballistic electron transport has been presented, based on a Monte-Carlo method. The resulting calculations allow to study the effects of hot electron temporal dynamics, during the quasi-static equilibrium phase, thus going beyond the averaged, static approach used for the analytical estimates. Despite the inclusion of these details about hot electron dynamics, the $E_{\max}$ predicted with the numerical method have turned out to be consistent with the estimates obtained from the analytical model, thus confirming the reliability of the latter.

Therefore, two different methods to estimate $E_{\max}$, based on the same assumptions about hot electron transport and recirculation, have been formulated: the first reaching an analytical solution by means of a static, averaged approach and the second exploiting numerical techniques to obtain a more detailed representation of the physics. These methods have eventually been exploited in an attempt to model the ion energy gain which have been experimentally obtained by performing TNSA experiments on Mass

Limited Targets. In the literature, this TNSA enhancement has been interpreted as an effect of transverse hot electron confinement and recirculation, a mechanism which can be described by the hot electron transport model presented in the chapter. Despite this, in the MLT case both the analytical and numerical approaches have revealed to be unsuitable in reproducing the experimental achievements, although the numerical computations have qualitatively supported the picture of transverse hot electron recirculation. This suggests that further factors, not considered in the provided description, are possibly involved in TNSA experiments with MLTs, thus requiring further physical ingredients to achieve a reliable effective model.

Such a discussion leads to one of the main potential perspectives of the present work, which is the development of an MLT model, addressed to attain a reliable description, capable to predict the experimental results obtained in this field. As mentioned in 5.5.2, the use of reduced mass target seems to have a remarkable effect also on the hot electron temperature T_{h}, which can sensibly affect the predicted $E_{\max}$ values and trend. Therefore, a first step towards a refined MLT description is that of providing an estimate of the temperature which, possibly starting from the ponderomotive formula (3.45), can include this insight, leading to a more realistic prediction. In this sense a proper model of electron re-heating process (see Sec. 5.3) can be an important advancement, since the multiple interactions of hot electrons with the laser field are more likely to take place in MLTs, provided that the laser pulse is long enough, or that the target transverse dimensions are small enough. Anyway, it should be underlined once again that the picture outlined by the available experimental data is not uniform and that several more results would be necessary to efficiently direct the theoretical work.

A further possible development on TNSA modeling, which directly follows the results of present thesis, concerns the improvement of the MC hot electron transport model, which, as described in Sec. 5.4, can be enriched by means of one-particle terms, acting on the single electrons in order to mimic collisional or radiative effects. Also the re-circulation dynamics can be refined in this framework, overcoming the rough approximation of reflective target walls. Moreover, the presented MC method can be applied to generate different kind of hot electron distributions, in order to investigate their approximated behavior in term of recirculation and TNSA dynamics and to search the functional form which reproduces, in the most reliable way, the available experimental results.

Other aspects which can be included within the transport and recirculation description, both in the analytical and in the numerical implementations, are the expansion of bulk ions, which has a minor effect on fastest ion acceleration, but can still be relevant in case the timescale of the process is long enough, or the presence of a “cold” electron population, for a more realistic description of the electron distribution function. In fact, the introduction of a second, cold electronic component has already been discussed in Ref. [147] for a quasi-static description (or in Ref. [45] for the fluid approach), but it still needs to be implemented within the Passoni-Lontano model.

These latter features, namely bulk ion motion and “cold” electron population, do not involve the only transport and recirculation model, but they require a re-definition

of the electro-static problem. This introduces another possible path in the improvement of the proposed theoretical description, which concerns the formulation of the electro-static problem as well. As extensively discussed in Sec. 5.1.3 the determination of the normalization coefficient for the hot electron density represents an important theoretical issue. This requires a further physical relation involving φ^*, which is the reason why, in this work, a normalization strategy relying on the empirical scaling of Eq. (4.26) has been set. Nonetheless, in order to remove the arbitrariness introduced by these normalization prescriptions, it would be useful to obtain, on theoretical bases, an independent relation, which would allow to fix the normalization factor. A purely theoretical work in this direction can be undertook, focusing on the formal definition of the electro-static problem and on the statistical bases of the quasi-static description.

Another possibility, which can be useful to retrieve further physical ingredients that could complete the electro-static problem definition, is that of extending the description to three dimensions. This might for example provide a link with the transverse extension of the charge separation, which could lead to another independent boundary condition and to a consistent closure of the system. A three-dimensional definition of the electro-static sheath can be also useful in the MLT case, provided that the target transverse extension is small enough that the lateral boundaries themselves directly affect the on-axis accelerating field. However, the three-dimensional electro-static problem, also in the cylindrical symmetry, requires expensive numerical calculations involving a differential equation which is mathematically similar to the well-known biophysical problem of Poisson-Boltzmann equation (see Ref. [185]). Therefore, in a possible path towards three-dimensional formulation of the model, it should be kept in mind that an effective TNSA description cannot require too expensive numerical calculations.

The possibilities described in these latter lines highlight the various perspectives of the presented work, efficaciously underlining the wide range of open problems in the specific topic of the thesis. Nonetheless, it is important to remark that this potential theoretical work always needs to be combined with intensive numerical and experimental parametric studies, in order to reach important and conclusive results.

Appendix

Experimental Database

In the present appendix the most relevant parameters of the experimental database exploited for the analysis of Chapter 4 are gathered in a table. The unity I_{18} used to indicate the laser intensity corresponds to $10^{18}\,\mathrm{W/cm^2}$.

Ref.	I [I_{18}]	λ [μm]	E_p [J]	τ_p [fs]	r_fs [μm]	D [μm]	Target	Particle	E_max [MeV/u]
[8]	50	1.06	50	900	6.0	125	Al	p^+	18
[9]	300	1.06	500	500	9.0	100	CH	p^+	58
[31]	10	0.79	0.69	65	4.0	20	CH	p^+	1.8
[186]	200	1.05	400	700	7.0	100	Cu	p^+	42
[32]	100	0.8	14.4	100	5.0	3.0	Al	p^+	24
[14]	60	0.8	0.84	40	4.0	6.0	Al	p^+	9.5
[29]	10	0.79	0.51	150	2.65	8.5	Al	p^+	2.4
”	15	0.79	0.85	150	2.65	8.5	Al	p^+	4.0
[187]	3.0	0.8	0.25	70	3.5	3.0	Ta	p^+	0.9
[188]	6.8	0.8	0.09	60	3.5	5.0	Cu	p^+	1.2
[76]	7.0	0.79	0.2	60	3.0	20	CH	p^+	1.5
[70]	30	0.8	1.7	34	4.1	7.5	CH	p^+	4.0
[54]	30	1.06	35	320	7.8	10	Au	p^+	15
[53]	30	1.06	20	320	6.0	10	Al	p^+	18
[75]	5.5	0.8	0.09	55	3.0	5.0	Cu	p^+	1.1
”	6.6	0.8	0.12	55	3.0	5.0	Cu	p^+	1.3
[176]	100	1.05	35	1000	3.0	10	Al	p^+	23
[63]	50	1.06	30	300	4.0	4.8	Au	p^+	20
[72]	58	0.8	3.0	30	5.6	5.0	Ti	p^+	17.3
”	24	0.8	1.2	30	5.6	5.0	Ti	p^+	5.4
”	6.9	0.8	0.3	30	5.6	5.0	Ti	p^+	1.5
[189]	11	0.8	0.15	80	2.5	6.0	Ti	p^+	2.9
[37]	5.5	1.05	20	600	10	20	Pd	C^{5+}	3.5
[49]	40	1.05	20.8	1000	3.0	25	Al	p^+	10
”	600	1.05	312	1000	3.0	10	Al	p^+	55

Ref.	I [I_{18}]	λ [μm]	E_{p} [J]	τ_{p} [fs]	r_{fs} [μm]	D [μm]	Target	Particle	E_{max} [MeV/u]
[103]	90	1.05	50	700	5.0	0.03	DLC	p^+	35
"	90	1.05	50	700	5.0	0.03	DLC	C^{6+}	15.4
[109]	50	0.81	0.7	45	1.8	0.01	DLC	C^{6+}	13
"	50	0.81	0.7	45	1.8	0.01	DLC	C^{6+}	5.9
[90]	34	0.8	0.36	30	2.48	1.5	Al	p^+	4.2
[89]	5.0	0.8	0.3	33	5.6	0.1	Al	p^+	4.0
[190]	33	0.82	0.72	35	3.3	7.5	CH	p^+	4.1
[33]	40	1.06	6.7	320	3.0	20	Al	p^+	20
[191]	75	1.05	150	600	7.6	5.0	Au	p^+	36

List of Figures

References

[1] V. I. Veksler. **The Principle of Coherent Acceleration of Charged Particles**. *At. Energ.*, **2**:525–528, 1957. 10.1007/BF01491001. 1

[2] E. Esarey, C. B. Schroeder, and W. P. Leemans. **Physics of laser-driven plasma-based electron accelerators**. *Rev. Mod. Phys.*, **81**:1229–1285, 2009. 1, 35

[3] Gurevich A. V., L. V. Pariiskaya, and L. P. Pitaevskii. **Self-similar motion of rarefied plasma**. *J. Exp. Theor. Phys.*, **49**:647, 1965. in Russian. 1, 27, 56, 57

[4] D. Strickland and G. Mourou. **Compression of amplified chirped optical pulses**. *Opt. Commun.*, **55**(6):447 – 449, 1985. 1

[5] F. N. Beg, A. R. Bell, A. E. Dangor, C. N. Danson, A. P. Fews, M. E. Glinsky, B. A. Hammel, P. Lee, P. A. Norreys, and M. Tatarakis. **A study of picosecond laser–solid interactions up to 10[sup 19] W cm[sup - 2]**. *Phys. Plasmas*, **4**(2):447–457, 1997. 1, 43, 79

[6] K. Krushelnick, E. L. Clark, Z. Najmudin, M. Salvati, M. I. K. Santala, M. Tatarakis, A. E. Dangor, V. Malka, D. Neely, R. Allott, and C. Danson. **Multi-MeV Ion Production from High-Intensity Laser Interactions with Underdense Plasmas**. *Phys. Rev. Lett.*, **83**:737–740, 1999. 1

[7] A. Maksimchuk, S. Gu, K. Flippo, D. Umstadter, and V. Yu. Bychenkov. **Forward Ion Acceleration in Thin Films Driven by a High-Intensity Laser**. *Phys. Rev. Lett.*, **84**(18):4108–4111, 2000. 2, 18, 90

[8] E. L. Clark, K. Krushelnick, J. R. Davies, M. Zepf, M. Tatarakis, F. N. Beg, A. Machacek, P. A. Norreys, M. I. K. Santala, I. Watts, and A. E. Dangor. **Measurements of Energetic Proton Transport through Magnetized Plasma from Intense Laser Interactions with Solids**. *Phys. Rev. Lett.*, **84**(4):670–673, 2000. 2, 68, 137

[9] R. A. Snavely, M. H. Key, S. P. Hatchett, T. E. Cowan, M. Roth, T. W. Phillips, M. A. Stoyer, E. A. Henry, T. C. Sangster, M. S. Singh, S. C. Wilks, A. MacKinnon, A. Offenberger, D. M. Pennington, K. Yasuike, A. B. Langdon, B. F. Lasinski, J. Johnson, M. D. Perry, and E. M. Campbell. **Intense High-Energy Proton Beams from Petawatt-Laser Irradiation of Solids**. *Phys. Rev. Lett.*, **85**(14):2945–2948, 2000. 2, 10, 26, 137

[10] S.V. Bulanov, T.Zh. Esirkepov, V.S Khoroshkov, A.V. Kuznetsov, and F. Pegoraro. **Oncological hadrontherapy with laser ion accelerators**. *Phys. Lett. A*, **299**(2–3):240 – 247, 2002. 2

[11] E. Fourkal, B. Shahine, M. Ding, J. S. Li, T. Tajima, and C.-M. Ma. **Particle in cell simulation of laser-accelerated proton beams for radiation therapy**. *Med. Phys.*, **29**(12):2788–2798, 2002. 2

[12] V. Malka, S. Fritzler, E. Lefebvre, E. d'Humières, R. Ferrand, G. Grillon, C. A., S. Meyroneinc, J.-P. Chambaret, A. Antonetti, and D. Hulin. **Practicability of protontherapy using compact laser systems**. *Med. Phys.*, **31**(6):1587–1592, 2004. 2

[13] M. I. K. Santala, M. Zepf, F. N. Beg, E. L. Clark, A. E. Dangor, K. Krushelnick, M. Tatarakis, I. Watts, K. W. D. Ledingham, T. McCanny, I. Spencer, A. C. Machacek, R. Allott, R. J. Clarke, and P. A. Norreys. **Production of radioactive nuclides by energetic protons generated from intense laser-plasma interactions**. *Appl. Phys. Lett.*, **78**(1):19–21, 2001. 2

[14] S. Fritzler, V. Malka, G. Grillon, J. P. Rousseau, F. Burgy, E. Lefebvre, E. d'Humières, P. McKenna, and K. W. D. Ledingham. **Proton beams generated with high-intensity lasers: Applications to medical isotope production**. *Appl. Phys. Lett.*, **83**(15):3039–3041, 2003. 2, 137

[15] M. Roth, T. E. Cowan, M. H. Key, S. P. Hatchett, C. Brown, W. Fountain, J. Johnson, D. M. Pennington, R. A. Snavely, S. C. Wilks, K. Yasuike, H. Ruhl, F. Pegoraro, S. V. Bulanov, E. M. Campbell, M. D. Perry, and H. Powell. **Fast Ignition by Intense Laser-Accelerated Proton Beams**. *Phys. Rev. Lett.*, **86**:436–439, 2001. 2

[16] V. Bychenkov, W. Rozmus, A. Maksimchuk, D. Umstadter, and C. Capjack. **Fast ignitor concept with light ions**. *Plasma Phys.*

Rep., **27**:1017–1020, 2001. 10.1134/1.1426135. 2

[17] M. Temporal, J. J. Honrubia, and S. Atzeni. **Numerical study of fast ignition of ablatively imploded deuterium–tritium fusion capsules by ultra-intense proton beams**. *Phys. Plasmas*, **9**(7):3098–3107, 2002. 2

[18] M. Borghesi, D. H. Campbell, A. Schiavi, M. G. Haines, O. Willi, A. J. MacKinnon, P. Patel, L. A. Gizzi, M. Galimberti, R. J. Clarke, F. Pegoraro, H. Ruhl, and S. Bulanov. **Electric field detection in laser-plasma interaction experiments via the proton imaging technique**. *Phys. Plasmas*, **9**(5):2214–2220, 2002. 2

[19] L. Romagnani, J. Fuchs, M. Borghesi, P. Antici, P. Audebert, F. Ceccherini, T. Cowan, T. Grismayer, S. Kar, A. Macchi, P. Mora, G. Pretzler, A. Schiavi, T. Toncian, and O. Willi. **Dynamics of Electric Fields Driving the Laser Acceleration of Multi-MeV Protons**. *Phys. Rev. Lett.*, **95**:195001, 2005. 2, 12

[20] S. Bulanov and V. Khoroshkov. **Feasibility of using laser ion accelerators in proton therapy**. *Plasma Phys. Rep.*, **28**:453–456, 2002. 10.1134/1.1478534. 2

[21] A. Brahme, R. Lewensohn, U. Ringborg, U. Amaldi, F. Gerardi, and S. Rossi. **Design of a centre for biologically optimised light ion therapy in Stockholm**. *Nucl. Instrum. Methods Phys. Res., Sect. A*, **184**(4):569 – 588, 2001. 2

[22] M. Borghesi, J. Fuchs, S. V. Bulanov, A. J. Mackinnon, P. K. Patel, and M. Roth. **Fast ion generation by high-intensity laser irradiation of solid targets and applications**. *Fusion Sci. Technol.*, **49**:412 – 439, 2006. 2, 7, 16

[23] H. Daido, M. Nishiuchi, and A. S. Pirozhkov. **Review of laser-driven ion sources and their applications**. *Rep. Prog. Phys.*, **75**(5):056401, 2012. 2, 3, 7, 9, 16, 17, 20, 31, 49

[24] A. Macchi, M. Borghesi, and M. Passoni. **Ion acceleration by superintense laser pulses**. *Rev. Mod. Phys.*, **To be published**. 2, 3, 7, 20

[25] S. C. Wilks, A. B. Langdon, T. E. Cowan, M. Roth, M. Singh, S. Hatchett, M. H. Key, D. Pennington, A. MacKinnon, and R. A. Snavely. **Energetic proton generation in ultra-intense laser–solid interactions**. *Phys. Plasmas*, **8**(2):542–549, 2001. 2, 26, 27, 52, 56

[26] S. D. Kraft, C. Richter, K. Zeil, M. Baumann, E. Beyreuther, S. Bock, M. Bussmann, T. E. Cowan, Y. Dammene, W. Enghardt, U. Helbig, L. Karsch, T. Kluge, L. Laschinsky, E. Lessmann, J. Metzkes, D. Naumburger, R. Sauerbrey, M. Schürer, M. Sobiella, J. Woithe, U. Schramm, and J. Pawelke. **Dose-dependent biological damage of tumour cells by laser-accelerated proton beams**. *New J. Phys.*, **12**(8):085003, 2010. 3

[27] P. Gibbon. **Short Pulse Laser Interactions With Matter: An Introduction**. Imperial College Press, 2005. 3, 21, 28, 30, 36, 43

[28] P. Mulser and D. Bauer. **High Power Laser-Matter Interaction**. Springer, Springer, Berlin Heidelberg, 2010. 3, 16, 21, 28, 34, 37, 56

[29] M. Kaluza, J. Schreiber, M. I. K. Santala, G. D. Tsakiris, K. Eidmann, J. Meyer-ter Vehn, and K. J. Witte. **Influence of the Laser Prepulse on Proton Acceleration in Thin-Foil Experiments**. *Phys. Rev. Lett.*, **93**(4):045003, 2004. 3, 18, 49, 68, 72, 73, 77, 78, 81, 84, 87, 90, 92, 105, 106, 107, 137, 139, 140

[30] P. McKenna, F. Lindau, O. Lundh, D. Neely, A. Persson, and Wahlström C-G. **High-intensity laser-driven proton acceleration: influence of pulse contrast**. *Philos. Trans. R. Soc. London, Ser. A*, **364**(1840):711–723, 2006. 3

[31] T. Ceccotti, A. Lévy, H. Popescu, F. Réau, P. D'Oliveira, P. Monot, J. P. Geindre, E. Lefebvre, and Ph. Martin. **Proton Acceleration with High-Intensity Ultrahigh-Contrast Laser Pulses**. *Phys. Rev. Lett.*, **99**(18):185002, 2007. 3, 17, 19, 68, 69, 87, 92, 110, 111, 117, 119, 120, 137, 140

[32] A. J. Mackinnon, Y. Sentoku, P. K. Patel, D. W. Price, S. Hatchett, M. H. Key, C. Andersen, R. Snavely, and R. R. Freeman. **Enhancement of Proton Acceleration by Hot-Electron Recirculation in Thin Foils Irradiated by Ultraintense Laser Pulses**. *Phys. Rev. Lett.*, **88**(21):215006, 2002. 3, 18, 19, 81, 90, 137

[33] J. Fuchs, P. Antici, E. d'Humieres, E. Lefebvre, M. Borghesi, E. Brambrink, C. A. Cecchetti, M. Kaluza, V. Malka, M. Manclossi, S. Meyroneinc, P. Mora,

J. Schreiber, T. Toncian, H. Pepin, and P. Audebert. **Laser-driven proton scaling laws and new paths towards energy increase**. *Nat. Phys.*, **2**:48–54, 2006. 3, 13, 14, 15, 17, 18, 59, 72, 73, 77, 78, 90, 92, 108, 109, 116, 117, 118, 119, 138, 139, 140

[34] A. Henig, D. Kiefer, M. Geissler, S. G. Rykovanov, R. Ramis, R. Hörlein, J. Osterhoff, Zs. Major, L. Veisz, S. Karsch, F. Krausz, D. Habs, and J. Schreiber. **Laser-Driven Shock Acceleration of Ion Beams from Spherical Mass-Limited Targets**. *Phys. Rev. Lett.*, **102**:095002, 2009. 3, 19, 121

[35] S. Buffechoux, J. Pšikal, M. Nakatsutsumi, L. Romagnani, A. Andreev, K. Zeil, M. Amin, P. Antici, T. Burris-Mog, A. Compant-La-Fontaine, E. d'Humières, S. Fourmaux, S. Gaillard, F. Gobet, F. Hannachi, S. Kraft, A. Mancic, C. Plaisir, G. Sarri, M. Tarisien, T. Toncian, U. Schramm, M. Tampo, P. Audebert, O. Willi, T. E. Cowan, H. Pépin, V. Tikhonchuk, M. Borghesi, and J. Fuchs. **Hot Electrons Transverse Refluxing in Ultraintense Laser-Solid Interactions**. *Phys. Rev. Lett.*, **105**:015005, 2010. 3, 19, 89, 115, 121, 122, 123, 125, 127, 128, 140

[36] J. Fuchs, T. E. Cowan, P. Audebert, H. Ruhl, L. Gremillet, A. Kemp, M. Allen, A. Blazevic, J.-C. Gauthier, M. Geissel, M. Hegelich, S. Karsch, P. Parks, M. Roth, Y. Sentoku, R. Stephens, and E. M. Campbell. **Spatial Uniformity of Laser-Accelerated Ultrahigh-Current MeV Electron Propagation in Metals and Insulators**. *Phys. Rev. Lett.*, **91**:255002, 2003. 3, 12, 47, 73

[37] B. M. Hegelich, B. J. Albright, J. Cobble, K. Flippo, S. Letzring, M. Paffett, H. Ruhl, J. Schreiber, R. K. Schulze, and J. C. Fernández. **Laser acceleration of quasi-monoenergetic MeV ion beams**. *Nature*, **439**:441–444, 2006. 3, 49, 69, 137

[38] P. McKenna, A. P. L. Robinson, D. Neely, M. P. Desjarlais, D. C. Carroll, M. N. Quinn, X. H. Yuan, C. M. Brenner, M. Burza, M. Coury, P. Gallegos, R. J. Gray, K. L. Lancaster, Y. T. Li, X. X. Lin, O. Tresca, and C.-G. Wahlström. **Effect of Lattice Structure on Energetic Electron Transport in Solids Irradiated by Ultraintense Laser Pulses**. *Phys. Rev. Lett.*, **106**:185004, 2011. 3

[39] A. Sgattoni, P. Londrillo, A. Macchi, and M. Passoni. **Laser ion acceleration using a solid target coupled with a low-density layer**. *Phys. Rev. E*, **85**:036405, 2012. 3, 17, 105

[40] John M. Dawson. **Particle simulation of plasmas**. *Rev. Mod. Phys.*, **55**:403–447, 1983. 4, 50

[41] T. Esirkepov, M. Yamagiwa, and T. Tajima. **Laser Ion-Acceleration Scaling Laws Seen in Multiparametric Particle-in-Cell Simulations**. *Phys. Rev. Lett.*, **96**:105001, 2006. 4, 22, 53

[42] Y. Sentoku, T. E. Cowan, A. Kemp, and H. Ruhl. **High energy proton acceleration in interaction of short laser pulse with dense plasma target**. *Phys. Plasmas*, **10**(5):2009–2015, 2003. 4, 19, 90

[43] E. d'Humières, E. Lefebvre, L. Gremillet, and V. Malka. **Proton acceleration mechanisms in high-intensity laser interaction with thin foils**. *Phys. Plasmas*, **12**(6):062704, 2005. 4, 92

[44] P. Mora. **Plasma Expansion into a Vacuum**. *Phys. Rev. Lett.*, **90**(18):185002, 2003. 4, 14, 54, 56, 58, 59, 60, 66, 71, 139

[45] P. Mora. **Thin-foil expansion into a vacuum**. *Phys. Rev. E*, **72**(5):056401, 2005. 4, 54, 56, 59, 60, 71, 84, 134, 139

[46] J. Schreiber, F. Bell, F. Grüner, U. Schramm, M. Geissler, M. Schnürer, S. Ter-Avetisyan, B. M. Hegelich, J. Cobble, E. Brambrink, J. Fuchs, P. Audebert, and D. Habs. **Analytical Model for Ion Acceleration by High-Intensity Laser Pulses**. *Phys. Rev. Lett.*, **97**(4):045005, 2006. 4, 15, 54, 56, 59, 62, 63, 71, 72, 73, 83, 139

[47] B. J. Albright, L. Yin, B. M. Hegelich, Kevin J. Bowers, T. J. T. Kwan, and J. C. Fernández. **Theory of Laser Acceleration of Light-Ion Beams from Interaction of Ultrahigh-Intensity Lasers with Layered Targets**. *Phys. Rev. Lett.*, **97**(11):115002, 2006. 4, 54, 56, 65, 66, 71, 72, 139

[48] A. P. L Robinson, A. R. Bell, and R. J. Kingham. **Effect of Target Composition on Proton Energy Spectra in Ultraintense Laser-Solid Interactions**. *Phys. Rev. Lett.*, **96**(3):035005, 2006. 4, 54, 56, 65, 66, 67, 71

[49] L. Robson, P. T. Simpson, R. J. Clarke, K. W. D. Ledingham, F. Lindau, O. Lundh, T. McCanny, P. Mora, D. Neely, C. G. Wahlstrom, M. Zepf, and P. McKenna. **Scaling of proton acceleration driven by**

petawatt-laser-plasma interactions. *Nat. Phys.*, **3**:58–62, 2007. 4, 14, 15, 54, 86, 137

[50] M. Passoni and M. Lontano. **Theory of Light-Ion Acceleration Driven by a Strong Charge Separation**. *Phys. Rev. Lett.*, **101**(11):115001, 2008. 4, 5, 54, 56, 64, 73, 83, 87

[51] A. Andreev, A. Lévy, T. Ceccotti, C. Thaury, K. Platonov, R. A. Loch, and Ph. Martin. **Fast-Ion Energy-Flux Enhancement from Ultrathin Foils Irradiated by Intense and High-Contrast Short Laser Pulses**. *Phys. Rev. Lett.*, **101**:155002, 2008. 4, 54, 86

[52] P. Mora and T. Grismayer. **Rarefaction Acceleration and Kinetic Effects in Thin-Foil Expansion into a Vacuum**. *Phys. Rev. Lett.*, **102**(14):145001, 2009. 4, 54

[53] J. Fuchs, P. Audebert, M. Borghesi, H. Pépin, and O. Willi. **Laser acceleration of low emittance, high energy ions and applications**. *C.R. Phys.*, **10**(2-3):176 – 187, 2009. Laser acceleration of particles in plasma. 7, 137

[54] M. Borghesi, T. Toncian, J. Fuchs, C. A. Cecchetti, L. Romagnani, S. Kar, K. Quinn, B. Ramakrishna, P. A. Wilson, P. Antici, P. Audebert, E. Brambrink, A. Pipahl, R. Jung, M. Amin, O. Willi, R. J. Clarke, M. Notley, P. Mora, T. Grismayer, E. D'Humiéres, and Y. Sentoku. **Laser-driven proton acceleration and applications: Recent results**. *Eur. Phys. J. Spec. Top.*, **175**:105–110, 2009. 7, 137

[55] C. A. J. Palmer, N. P. Dover, I. Pogorelsky, M. Babzien, G. I. Dudnikova, M. Ispiriyan, M. N. Polyanskiy, J. Schreiber, P. Shkolnikov, V. Yakimenko, and Z. Najmudin. **Monoenergetic Proton Beams Accelerated by a Radiation Pressure Driven Shock**. *Phys. Rev. Lett.*, **106**:014801, 2011. 8, 21

[56] D. Haberberger, S. Tochitsky, F. Fiuza, C. Gong, R. A. Fonseca, L. O. Silva, W. B. Mori, and C. Joshi. **Collisionless shocks in laser-produced plasma generate monoenergetic high-energy proton beams**. *Nat. Phys.*, **8**:95–99, 2012. 8, 22

[57] A. Lévy, T. Ceccotti, P. D'Oliveira, F. Réau, M. Perdrix, F. Quéré, P. Monot, M. Bougeard, H. Lagadec, P. Martin, J.-P. Geindre, and P. Audebert. **Double plasma mirror for ultrahigh temporal contrast ultraintense laser pulses**. *Opt. Lett.*, **32**(3):310–312, 2007. 9, 19

[58] S. P. Hatchett, C. G. Brown, T. E. Cowan, E. A. Henry, J. S. Johnson, M. H. Key, J. A. Koch, A. B. Langdon, B. F. Lasinski, R. W. Lee, A. J. Mackinnon, D. M. Pennington, M. D. Perry, T. W. Phillips, M. Roth, T. C. Sangster, M. S. Singh, R. A. Snavely, Stoyer M. A., S. C. Wilks, and K. Yasuike. **Electron, photon, and ion beams from the relativistic interaction of Petawatt laser pulses with solid targets**. *Phys. Plasmas*, **7**(5):2076–2082, 2000. 10, 11, 27, 56

[59] A. J. Mackinnon, M. Borghesi, S. Hatchett, M. H. Key, P. K. Patel, H. Campbell, A. Schiavi, R. Snavely, S. C. Wilks, and O. Willi. **Effect of Plasma Scale Length on Multi-MeV Proton Production by Intense Laser Pulses**. *Phys. Rev. Lett.*, **86**:1769–1772, 2001. 10

[60] J. Fuchs, C. A. Cecchetti, M. Borghesi, T. Grismayer, E. d'Humières, P. Antici, S. Atzeni, P. Mora, A. Pipahl, L. Romagnani, A. Schiavi, Y. Sentoku, T. Toncian, P. Audebert, and O. Willi. **Laser-Foil Acceleration of High-Energy Protons in Small-Scale Plasma Gradients**. *Phys. Rev. Lett.*, **99**:015002, 2007. 11

[61] M. Hegelich, S. Karsch, G. Pretzler, D. Habs, K. Witte, W. Guenther, M. Allen, A. Blazevic, J. Fuchs, J. C. Gauthier, M. Geissel, P. Audebert, T. Cowan, and M. Roth. **MeV Ion Jets from Short-Pulse-Laser Interaction with Thin Foils**. *Phys. Rev. Lett.*, **89**:085002, 2002. 11, 20, 74

[62] M. Allen, P. K. Patel, A. Mackinnon, D. Price, S. Wilks, and E. Morse. **Direct Experimental Evidence of Back-Surface Ion Acceleration from Laser-Irradiated Gold Foils**. *Phys. Rev. Lett.*, **93**:265004, 2004. 11

[63] M. Roth, A. Blazevic, M. Geissel, T. Schlegel, T. E. Cowan, M. Allen, J.-C. Gauthier, P. Audebert, J. Fuchs, J. Meyer-ter Vehn, M. Hegelich, S. Karsch, and A. Pukhov. **Energetic ions generated by laser pulses: A detailed study on target properties**. *Phys. Rev. ST Accel. Beams*, **5**(6):061301, 2002. 11, 137

[64] M. Roth, M. Allen, P. Audebert, A. Blazevic, E. Brambrink, T. E. Cowan, J. Fuchs, J. C. Gauthier, M. Geissel, M. Hegelich, S. Karsch, J. Meyer ter Vehn, H. Ruhl, T. Schlegel, and R. B. Stephens. **The generation of high-quality, intense ion beams**

by ultra-intense lasers. *Plasma Phys. Controlled Fusion*, **44**(12B):B99, 2002. 11, 12, 19, 120

[65] M. Borghesi, A. Schiavi, D. H. Campbell, M. G. Haines, O. Willi, A. J. MacKinnon, L. A. Gizzi, M. Galimberti, R. J. Clarke, and H. Ruhl. **Proton imaging: a diagnostic for inertial confinement fusion/fast ignitor studies**. *Plasma Phys. Controlled Fusion*, **43**(12A):A267, 2001. 12

[66] T. E. Cowan, J. Fuchs, H. Ruhl, A. Kemp, P. Audebert, M. Roth, R. Stephens, I. Barton, A. Blazevic, E. Brambrink, J. Cobble, J. Fernández, J.-C. Gauthier, M. Geissel, M. Hegelich, J. Kaae, S. Karsch, G. P. Le Sage, S. Letzring, M. Manclossi, S. Meyroneinc, A. Newkirk, H. Pépin, and N. Renard-LeGalloudec. **Ultralow Emittance, Multi-MeV Proton Beams from a Laser Virtual-Cathode Plasma Accelerator**. *Phys. Rev. Lett.*, **92**:204801, 2004. 12, 13

[67] M. Borghesi, A. J. Mackinnon, D. H. Campbell, D. G. Hicks, S. Kar, P. K. Patel, D. Price, L. Romagnani, A. Schiavi, and O. Willi. **Multi-MeV Proton Source Investigations in Ultraintense Laser-Foil Interactions**. *Phys. Rev. Lett.*, **92**:055003, 2004. 12

[68] M. Roth, E. Brambrink, P. Audebert, M. Basko, A. Blazevic, R. Clarke, J. Cobble, T. E. Cowan, J. Fernandez, J. Fuchs, M. Hegelich, K. Ledingham, B. G. Logan, D. Neely, H. Ruhl, and M. Schollmeier. **Laser accelerated ions in ICF research prospects and experiments**. *Plasma Phys. Controlled Fusion*, **47**(12B):B841, 2005. 12

[69] M. Nishiuchi, H. Daido, A. Sagisaka, K. Ogura, S. Orimo, M. Kado, A. Yogo, M. Mori, Y. Hayashi, S. Bulanov, A. Fukumi, Z. Li, A. Noda, and S. Nakamura. **Repetitive highly collimated intense proton beam with sub-MeV energy range driven by a compact few terawatt femtosecond laser**. *Appl. Phys. B*, **87**:615–621, 2007. 12

[70] M. Nishiuchi, H. Daido, A. Yogo, S. Orimo, K. Ogura, J. Ma, A. Sagisaka, M. Mori, A. S. Pirozhkov, H. Kiriyama, S. V. Bulanov, T. Zh. Esirkepov, I. W. Choi, C. M. Kim, T. M. Jeong, T. J. Yu, J. H. Sung, S. K. Lee, N. Hafz, K. H. Pae, Y.-C. Noh, D.-K. Ko, J. Lee, Y. Oishi, K. Nemoto, H. Nagatomo, K. Nagai, and H. Azuma. **Efficient production of a collimated MeV proton beam from a polyimide target driven by an intense femtosecond laser pulse**. *Phys. Plasmas*, **15**(5):053104, 2008. 12, 137

[71] F. Nurnberg, M. Schollmeier, E. Brambrink, A. Blazevic, D. C. Carroll, K. Flippo, D. C. Gautier, M. Geissel, K. Harres, B. M. Hegelich, O. Lundh, K. Markey, P. McKenna, D. Neely, J. Schreiber, and M. Roth. **Radiochromic film imaging spectroscopy of laser-accelerated proton beams**. *Rev. Sci. Instrum.*, **80**(3):033301, 2009. 12

[72] K. Zeil, S. D. Kraft, S. Bock, M. Bussmann, T. E. Cowan, T. Kluge, J. Metzkes, T. Richter, R. Sauerbrey, and U. Schramm. **The scaling of proton energies in ultrashort pulse laser plasma acceleration**. *New J. Phys.*, **12**(4):045015, 2010. 14, 15, 137

[73] E. L. Clark, K. Krushelnick, M. Zepf, F. N. Beg, M. Tatarakis, A. Machacek, M. I. K. Santala, I. Watts, P. A. Norreys, and A. E. Dangor. **Energetic Heavy-Ion and Proton Generation from Ultraintense Laser-Plasma Interactions with Solids**. *Phys. Rev. Lett.*, **85**:1654–1657, 2000. 14, 16

[74] M. Allen, Y. Sentoku, P. Audebert, A. Blazevic, T. Cowan, J. Fuchs, J. C. Gauthier, M. Geissel, M. Hegelich, S. Karsch, E. Morse, P. K. Patel, and M. Roth. **Proton spectra from ultraintense laser–plasma interaction with thin foils: Experiments, theory, and simulation**. *Phys. Plasmas*, **10**(8):3283–3289, 2003. 14

[75] Y. Oishi, T. Nayuki, T. Fujii, Y. Takizawa, X. Wang, T. Yamazaki, K. Nemoto, T. Kayoiji, T. Sekiya, K. Horioka, Y. Okano, Y. Hironaka, K. G. Nakamura, K. Kondo, and A. A. Andreev. **Dependence on laser intensity and pulse duration in proton acceleration by irradiation of ultrashort laser pulses on a Cu foil target**. *Phys. Plasmas*, **12**(7):073102, 2005. 14, 15, 137

[76] I. Spencer, K. W. D. Ledingham, P. McKenna, T. McCanny, R. P. Singhal, P. S. Foster, D. Neely, A. J. Langley, E. J. Divall, C. J. Hooker, R. J. Clarke, P. A. Norreys, E. L. Clark, K. Krushelnick, and J. R. Davies. **Experimental study of proton emission from 60-fs, 200-mJ high-repetition-rate tabletop-laser pulses interacting with solid targets**. *Phys. Rev. E*, **67**(4):046402, 2003. 14, 18, 84, 90, 137

[77] S. C. Wilks, W. L. Kruer, M. Tabak, and A. B. Langdon. **Absorption of ultra-intense laser pulses**. *Phys. Rev. Lett.*, **69**(9):1383–1386, 1992. 16, 21, 40

[78] M. Borghesi, A. Bigongiari, S. Kar, A. Macchi, L. Romagnani, P. Audebert, J. Fuchs, T. Toncian, O. Willi, S. V. Bulanov, A. J. Mackinnon, and J. C. Gauthier. **Laser-driven proton acceleration: source optimization and radiographic applications**. *Plasma Phys. Controlled Fusion*, **50**(12):124040, 2008. 16

[79] J. S. Green, D. C. Carroll, C. Brenner, B. Dromey, P. S. Foster, S. Kar, Y. T. Li, K. Markey, P. McKenna, D. Neely, A. P. L. Robinson, M. J. V. Streeter, M. Tolley, C-G. Wahlström, M. H. Xu, and M. Zepf. **Enhanced proton flux in the MeV range by defocused laser irradiation**. *New J. Phys.*, **12**(8):085012, 2010. 16

[80] A. Fukumi, M. Nishiuchi, H. Daido, Z. Li, A. Sagisaka, K. Ogura, S. Orimo, M. Kado, Y. Hayashi, M. Mori, S. V. Bulanov, T. Esirkepov, K. Nemoto, Y. Oishi, T. Nayuki, T. Fujii, A. Noda, and S. Nakamura. **Laser polarization dependence of proton emission from a thin foil target irradiated by a 70 fs, intense laser pulse**. *Phys. Plasmas*, **12**(10):100701, 2005. 17

[81] D. C. Carroll, O. Tresca, R. Prasad, L. Romagnani, P. S. Foster, P. Gallegos, S. Ter-Avetisyan, J. S. Green, M. J. V. Streeter, N. Dover, C. A. J. Palmer, C. M. Brenner, F. H. Cameron, K. E. Quinn, J. Schreiber, A. P. L. Robinson, T. Baeva, M. N. Quinn, X. H. Yuan, Z. Najmudin, M. Zepf, D. Neely, M. Borghesi, and P. McKenna. **Carbon ion acceleration from thin foil targets irradiated by ultrahigh-contrast, ultraintense laser pulses**. *New J. Phys.*, **12**(4):045020, 2010. 17

[82] K. A. Flippo, E. d'Humières, S. A. Gaillard, J. Rassuchine, D. C. Gautier, M. Schollmeier, F. Nurnberg, J. L. Kline, J. Adams, B. Albright, M. Bakeman, K. Harres, R. P. Johnson, G. Korgan, S. Letzring, S. Malekos, N. Renard-LeGalloudec, Y. Sentoku, T. Shimada, M. Roth, T. E. Cowan, J. C. Fernandez, and B. M. Hegelich. **Increased efficiency of short-pulse laser-generated proton beams from novel flat-top cone targets**. *Phys. Plasmas*, **15**(5):056709, 2008. 17

[83] S. A. Gaillard, T. Kluge, K. A. Flippo, M. Bussmann, B. Gall, T. Lockard, M. Geissel, D. T. Offermann, M. Schollmeier, Y. Sentoku, and T. E. Cowan. **Increased laser-accelerated proton energies via direct laser-light-pressure acceleration of electrons in microcone targets**. *Phys. Plasmas*, **18**(5):056710, 2011. 17

[84] A. Yogo, H. Daido, A. Fukumi, Z. Li, K. Ogura, A. Sagisaka, A. S. Pirozhkov, S. Nakamura, Y. Iwashita, T. Shirai, A. Noda, Y. Oishi, T. Nayuki, T. Fujii, K. Nemoto, I. W. Choi, J. H. Sung, D-K. Ko, J. Lee, M. Kaneda, and A. Itoh. **Laser prepulse dependency of proton-energy distributions in ultraintense laser-foil interactions with an online time-of-flight technique**. *Phys. Plasmas*, **14**(4):043104, 2007. 17

[85] A. Flacco, A. Guemnie-Tafo, R. Nuter, M. Veltcheva, D. Batani, E. Lefebvre, and V. Malka. **Characterization of a controlled plasma expansion in vacuum for laser driven ion acceleration**. *J. Appl. Phys.*, **104**(10):103304, 2008. 17

[86] P. McKenna, D.C. Carroll, O. Lundh, F. Nürnberg, K. Markey, S. Bandyopadhyay, D. Batani, R.G. Evans, R. Jafer, S. Kar, D. Neely, D. Pepler, M.N. Quinn, R. Redaelli, M. Roth, C.-G. Wahlström, X.H. Yuan, and M. Zepf. **Effects of front surface plasma expansion on proton acceleration in ultraintense laser irradiation of foil targets**. *Laser Part. Beams*, **26**(04):591–596, 2008. 17

[87] D. Batani, R. Jafer, M. Veltcheva, R. Dezulian, O. Lundh, F. Lindau, A. Persson, K. Osvay, C-G. Wahlström, D. C. Carroll, P. McKenna, A. Flacco, and V. Malka. **Effects of laser prepulses on laser-induced proton generation**. *New J. Phys.*, **12**(4):045018, 2010. 17

[88] F. Lindau, O. Lundh, A. Persson, P. McKenna, K. Osvay, D. Batani, and C.-G. Wahlström. **Laser-Accelerated Protons with Energy-Dependent Beam Direction**. *Phys. Rev. Lett.*, **95**:175002, 2005. 18, 49

[89] D. Neely, P. Foster, A. Robinson, F. Lindau, O. Lundh, A. Persson, C.-G. Wahlström, and P. McKenna. **Enhanced proton beams from ultrathin targets driven by high contrast laser pulses**. *Appl. Phys. Lett.*, **89**(2):021502, 2006. 18, 90, 109, 110, 138, 140

[90] A. Flacco, F. Sylla, M. Veltcheva, M. Carrié, R. Nuter, E. Lefebvre, D. Batani, and V. Malka. **Dependence on pulse duration and foil thickness in high-contrast-laser proton acceleration**. *Phys. Rev. E*, **81**:036405, 2010. 18, 90, 138

[91] J. Myatt, W. Theobald, J. A. Delettrez, C. Stoeckl, M. Storm, T. C. Sangster, A. V. Maximov, and R. W. Short. **High-intensity laser interactions with mass-limited solid targets and implications**

for fast-ignition experiments on OMEGA EP. *Phys. Plasmas*, **14**(5):056301, 2007. 19, 90

[92] P. McKenna, D. C. Carroll, R. J. Clarke, R. G. Evans, K. W. D. Ledingham, F. Lindau, O. Lundh, T. McCanny, D. Neely, P.Ľ. Robinson, A. L. Robson, P. T. Simpson, C.-G. Wahlström, and M. Zepf. **Lateral Electron Transport in High-Intensity Laser-Irradiated Foils Diagnosed by Ion Emission**. *Phys. Rev. Lett.*, **98**:145001, 2007. 19, 120

[93] J. Pšikal, J. Limpouch, S. Kawata, and A. Andreev. **Pic simulations of femtosecond interactions with mass-limited targets**. *Czech. J. Phys.*, **56**:B515–B521, 2006. 10.1007/s10582-006-0246-8. 19, 120

[94] J. Limpouch, J. Pšikal, A.A. Andreev, K. YU. Platonov, and S. Kawata. **Enhanced laser ion acceleration from mass-limited targets**. *Laser Part. Beams*, **26**(02):225–234, 2008. 19, 120

[95] J. Pšikal, V. T. Tikhonchuk, J. Limpouch, A. A. Andreev, and A. V. Brantov. **Ion acceleration by femtosecond laser pulses in small multispecies targets**. *Phys. Plasmas*, **15**(5):053102, 2008. 19, 120

[96] A. A. Andreev, J. Limpouch, J. Pšikal, K. Yu. Platonov, and V. T. Tikhonchuk. **Laser ion acceleration in a mass limited targets**. *Eur. Phys. J. Spec. Top.*, **175**:123–126, 2009. 10.1140/epjst/e2009-01128-1. 19, 120

[97] T. Kluge, W. Enghardt, S. D. Kraft, U. Schramm, K. Zeil, T. E. Cowan, and M. Bussmann. **Enhanced laser ion acceleration from mass-limited foils**. *Phys. Plasmas*, **17**(12):123103, 2010. 19, 120

[98] T. Toncian, M. Swantusch, M. Toncian, O. Willi, A. A. Andreev, and K. Y. Platonov. **Optimal proton acceleration from lateral limited foil sections and different laser pulse durations at relativistic intensity**. *Phys. Plasmas*, **18**(4):043105, 2011. 19, 121

[99] O. Tresca, D. C. Carroll, X. H. Yuan, B. Aurand, V. Bagnoud, C. M. Brenner, M. Coury, J. Fils, R. J. Gray, T. Kühl, C. Li, Y. T. Li, X. X. Lin, M. N. Quinn, R. G. Evans, B. Zielbauer, M. Roth, D. Neely, and P. McKenna. **Controlling the properties of ultraintense laser–proton sources using transverse refluxing of hot electrons in shaped mass-limited targets**. *Plasma Phys. Controlled Fusion*, **53**(10):105008, 2011. 19, 121

[100] H. Schwoerer, S. Pfotenhauer, O. Jackel, K.-U. Amthor, B. Liesfeld, W. Ziegler, R. Sauerbrey, K. W. D. Ledingham, and T. Esirkepov. **Laser-plasma acceleration of quasi-monoenergetic protons from microstructured targets**. *Nature*, **439**:445–448, 2006. 20, 49

[101] L. Yin, B. J. Albright, B. M. Hegelich, and J. C. Fernandez. **GeV laser ion acceleration from ultrathin targets: The laser break-out afterburner**. *Laser Part. Beams*, **24**(02):291–298, 2006. 20

[102] L. Yin, B. J. Albright, B. M. Hegelich, K. J. Bowers, K. A. Flippo, T. J. T. Kwan, and J. C. Fernandez. **Monoenergetic and GeV ion acceleration from the laser breakout afterburner using ultrathin targets**. *Phys. Plasmas*, **14**(5):056706, 2007. 20

[103] A. Henig, D. Kiefer, K. Markey, D. C. Gautier, K. A. Flippo, S. Letzring, R. P. Johnson, T. Shimada, L. Yin, B. J. Albright, K. J. Bowers, J. C. Fernández, S. G. Rykovanov, H.-C. Wu, M. Zepf, D. Jung, V. Kh. Liechtenstein, J. Schreiber, D. Habs, and B. M. Hegelich. **Enhanced Laser-Driven Ion Acceleration in the Relativistic Transparency Regime**. *Phys. Rev. Lett.*, **103**:045002, 2009. 21, 69, 138

[104] J. Denavit. **Absorption of high-intensity subpicosecond lasers on solid density targets**. *Phys. Rev. Lett.*, **69**:3052–3055, 1992. 21, 22

[105] A. Macchi, F. Cattani, T. V. Liseykina, and F. Cornolti. **Laser Acceleration of Ion Bunches at the Front Surface of Overdense Plasmas**. *Phys. Rev. Lett.*, **94**:165003, 2005. 21

[106] T. Schlegel, N. Naumova, V. T. Tikhonchuk, C. Labaune, I. V. Sokolov, and G. Mourou. **Relativistic laser piston model: Ponderomotive ion acceleration in dense plasmas using ultraintense laser pulses**. *Phys. Plasmas*, **16**(8):083103, 2009. 21

[107] J. F. L. Simmons and C. R. McInnes. **Was Marx right? or How efficient are laser driven interstellar spacecraft?** *Am. J. Phys.*, **61**(3):205–207, 1993. 21

[108] T. Esirkepov, M. Borghesi, S. V. Bulanov, G. Mourou, and T. Tajima. **Highly Efficient Relativistic-Ion Generation in the Laser-Piston Regime**. *Phys. Rev. Lett.*, **92**:175003, 2004. 21, 22

[109] A. Henig, S. Steinke, M. Schnürer, T. Sokollik, R. Hörlein, D. Kiefer, D. Jung, J. Schreiber, B. M. Hegelich, X. Q. Yan, J. Meyer-ter Vehn, T. Tajima, P. V. Nickles, W. Sandner, and D. Habs. **Radiation-Pressure Acceleration of Ion Beams Driven by Circularly Polarized Laser Pulses**. *Phys. Rev. Lett.*, **103**:245003, 2009. 21, 68, 69, 138

[110] L. O. Silva, M. Marti, J. R. Davies, R. A. Fonseca, C. Ren, F. S. Tsung, and W. B. Mori. **Proton Shock Acceleration in Laser-Plasma Interactions**. *Phys. Rev. Lett.*, **92**:015002, 2004. 22

[111] S. Bulanov, D. Dylov, T. Esirkepov, F. Kamenets, and D. Sokolov. **Ion acceleration in a dipole vortex in a laser plasma corona**. *Plasma Phys. Rep.*, **31**:369–381, 2005. 10.1134/1.1925787. 22

[112] S. V. Bulanov and T. Zh. Esirkepov. **Comment on "Collimated Multi-MeV Ion Beams from High-Intensity Laser Interactions with Underdense Plasma"**. *Phys. Rev. Lett.*, **98**:049503, 2007. 22

[113] L. Willingale, S. R. Nagel, A. G. R. Thomas, C. Bellei, R. J. Clarke, A. E. Dangor, R. Heathcote, M. C. Kaluza, C. Kamperidis, S. Kneip, K. Krushelnick, N. Lopes, S. P. D. Mangles, W. Nazarov, P. M. Nilson, and Z. Najmudin. **Characterization of High-Intensity Laser Propagation in the Relativistic Transparent Regime through Measurements of Energetic Proton Beams**. *Phys. Rev. Lett.*, **102**:125002, 2009. 22

[114] L. Willingale, P. M. Nilson, A. G. R. Thomas, S. S. Bulanov, A. Maksimchuk, W. Nazarov, T. C. Sangster, C. Stoeckl, and K. Krushelnick. **High-power, kilojoule laser interactions with near-critical density plasma**. *Phys. Plasmas*, **18**(5):056706, 2011. 22

[115] M. Widner, I. Alexeff, and W. D. Jones. **Plasma Expansion into a Vacuum**. *Phys. Fluids*, **14**(4):795–796, 1971. 27, 56, 57

[116] S.C. Wilks and W.L. Kruer. **Absorption of ultrashort, ultra-intense laser light by solids and overdense plasmas**. *IEEE J. Quantum Electron.*, **33**(11):1954 –1968, 1997. 28, 34

[117] G.S. Voronov and N.B. Delone. **Ionization of the xenon atom by the electric field of ruby laser emission**. *J. Exp. Theor. Phys.*, **1**:66, 1965. 29

[118] L.V. Keldysh. **Ionization In The Field Of A Strong Electromagnetic Wave**. *J. Exp. Theor. Phys.*, **20**:13107, 1964. 29

[119] L. D. Landau and E. M. Lifshitz. **The Classical Theory of Fields, Fourth Edition: Volume 2 (Course of Theoretical Physics Series)**. Pergamon Press Ltd, 1951. 34

[120] D. Bauer, P. Mulser, and W. H. Steeb. **Relativistic Ponderomotive Force, Uphill Acceleration, and Transition to Chaos**. *Phys. Rev. Lett.*, **75**:4622–4625, 1995. 34

[121] R. J. Goldston and P. H. Rutherford. ***I*ntroduction to Plasma Physics**. Taylor & Francis, New York, NY 10016, 1995. 37

[122] W. Rozmus and V. T. Tikhonchuk. **Skin effect and interaction of short laser pulses with dense plasmas**. *Phys. Rev. A*, **42**:7401–7412, 1990. 38

[123] D. W. Forslund, J. M. Kindel, and K. Lee. **Theory of Hot-Electron Spectra at High Laser Intensity**. *Phys. Rev. Lett.*, **39**:284–288, 1977. 38

[124] K. Estabrook and W. L. Kruer. **Properties of Resonantly Heated Electron Distributions**. *Phys. Rev. Lett.*, **40**:42–45, 1978. 38

[125] F. Brunel. **Not-so-resonant, resonant absorption**. *Phys. Rev. Lett.*, **59**:52–55, 1987. 39

[126] P. Mulser, H. Ruhl, and J. Steinmetz. **Routes to irreversibility in collective laser–matter interaction**. *Laser Part. Beams*, **19**(01):23–28, 2001. 39

[127] W. L. Kruer and K. Estabrook. **J x B heating by very intense laser light**. *Phys. Fluids*, **28**(1):430–432, 1985. 39

[128] E.S. Weibel. **Anomalous Skin Effect in a Plasma**. *Phys. Fluids*, **10**(4):741–748, 1967. 40

[129] P. J. Catto and R. M. More. **Sheath inverse bremsstrahlung in laser produced plasmas**. *Phys. Fluids*, **20**(4):704–705, 1977. 40

[130] T.-Y. B. Yang, W. L. Kruer, R. M. More, and A. B. Langdon. **Absorption of laser light in overdense plasmas by sheath inverse bremsstrahlung**. *Phys. Plasmas*, **2**(8):3146–3154, 1995. 40

[131] P. Mulser, D. Bauer, and H. Ruhl. **Collisionless Laser-Energy Conversion by Anharmonic Resonance**. *Phys. Rev. Lett.*, **101**:225002, 2008. 41

[132] B. Bezzerides, S. J. Gitomer, and D. W. Forslund. **Randomness, Maxwellian Distributions, and Resonance Absorption**. *Phys. Rev. Lett.*, **44**:651–654, 1980. 41

[133] T. Tanimoto, H. Habara, R. Kodama, M. Nakatsutsumi, Kazuo A. Tanaka, K. L. Lancaster, J. S. Green, R. H. H. Scott, M. Sherlock, P. A. Norreys, R. G. Evans, M. G. Haines, S. Kar, M. Zepf, J. King, T. Ma, M. S. Wei, T. Yabuuchi, F. N. Beg, M. H. Key, P. Nilson, R. B. Stephens, H. Azechi, K. Nagai, T. Norimatsu, K. Takeda, J. Valente, and J. R. Davies. **Measurements of fast electron scaling generated by petawatt laser systems**. *Phys. Plasmas*, **16**(6):062703, 2009. 41, 139

[134] Y. Ping, R. Shepherd, B. F. Lasinski, M. Tabak, H. Chen, H. K. Chung, K. B. Fournier, S. B. Hansen, A. Kemp, D. A. Liedahl, K. Widmann, S. C. Wilks, W. Rozmus, and M. Sherlock. **Absorption of Short Laser Pulses on Solid Targets in the Ultrarelativistic Regime**. *Phys. Rev. Lett.*, **100**:085004, 2008. 42

[135] J. R. Davies. **Laser absorption by overdense plasmas in the relativistic regime**. *Plasma Phys. Controlled Fusion*, **51**(1):014006, 2009. 42, 72

[136] J. Yu, Z. Jiang, J. C. Kieffer, and A. Krol. **Hard x-ray emission in high intensity femtosecond laser–target interaction**. *Phys. Plasmas*, **6**(4):1318–1322, 1999. 43, 72

[137] P. Gibbon and A. R. Bell. **Collisionless absorption in sharp-edged plasmas**. *Phys. Rev. Lett.*, **68**:1535–1538, 1992. 43

[138] H. Chen, S. C. Wilks, W. L. Kruer, P. K. Patel, and R. Shepherd. **Hot electron energy distributions from ultraintense laser solid interactions**. *Phys. Plasmas*, **16**(2):020705, 2009. 43

[139] P. M. Nilson, A. A. Solodov, J. F. Myatt, W. Theobald, P. A. Jaanimagi, L. Gao, C. Stoeckl, R. S. Craxton, J. A. Delettrez, B. Yaakobi, J. D. Zuegel, B. E. Kruschwitz, C. Dorrer, J. H. Kelly, K. U. Akli, P. K. Patel, A. J. Mackinnon, R. Betti, T. C. Sangster, and D. D. Meyerhofer. **Scaling Hot-Electron Generation to High-Power, Kilojoule-Class Laser-Solid Interactions**. *Phys. Rev. Lett.*, **105**:235001, 2010. 43

[140] A. G. Mordovanakis, P.-E. Masson-Laborde, J. Easter, K. Popov, B. Hou, G. Mourou, W. Rozmus, M. G. Haines, J. Nees, and K. Krushelnick. **Temperature scaling of hot electrons produced by a tightly focused relativistic-intensity laser at 0.5 kHz repetition rate**. *Appl. Phys. Lett.*, **96**(7):071109 –071109–3, 2010. 43

[141] M. G. Haines, M. S. Wei, F. N. Beg, and R. B. Stephens. **Hot-Electron Temperature and Laser-Light Absorption in Fast Ignition**. *Phys. Rev. Lett.*, **102**:045008, 2009. 44, 79

[142] T. Kluge, T. Cowan, A. Debus, U. Schramm, K. Zeil, and M. Bussmann. **Electron Temperature Scaling in Laser Interaction with Solids**. *Phys. Rev. Lett.*, **107**:205003, 2011. 44, 79

[143] D.I. Dzhavakhishvili and N.L. Tsintsadze. **Transport phenomena in a completely ionized ultrarelativistic plasma**. *J. Exp. Theor. Phys.*, **64**(4):1314–1325, 1973. 44, 92

[144] R. R. Freeman, D. Batani, S. Baton, M. Key, and R. Stephens. **The Generation and Transport of Large Currents in Dense Materials: The Physics of Electron Transport Relative to Fast Ignition**. *Fus. Sci. Techn.*, **49**(3):297, 2006. 44

[145] M.J. Berger, J.S. Coursey, M.A. Zucker, and J. Chang. **Stopping-Power and Range Tables for Electrons, Protons, and Helium Ions**, 2009. 44

[146] A. R. Bell, J. R. Davies, S. Guerin, and H. Ruhl. **Fast-electron transport in high-intensity short-pulse laser - solid experiments**. *Plasma Phys. Controlled Fusion*, **39**(5):653, 1997. 44, 45

[147] M. Passoni, V. T. Tikhonchuk, M. Lontano, and V. Yu. Bychenkov. **Charge separation effects in solid targets and ion acceleration with a two-temperature electron distribution**. *Phys. Rev. E*, **69**(2):026411, 2004. 45, 59, 134

[148] J. R. Davies, A. R. Bell, M. G. Haines, and S. M. Guérin. **Short-pulse high-intensity laser-generated fast electron transport into thick solid targets**. *Phys. Rev. E*, **56**:7193–7203, 1997. 45

[149] J. R. Davies, A. R. Bell, and M. Tatarakis. **Magnetic focusing and trapping of high-intensity laser-generated fast electrons at the rear of solid targets**. *Phys. Rev. E*, **59**:6032–6036, 1999. 45

[150] A. R. Bell and R. J. Kingham. **Resistive Collimation of Electron Beams in Laser-Produced Plasmas**. *Phys. Rev. Lett.*, **91**:035003, 2003. 45

[151] Y. Sentoku, K. Mima, P. Kaw, and K. Nishikawa. **Anomalous Resistivity Resulting from MeV-Electron Transport in Overdense Plasma**. *Phys. Rev. Lett.*, **90**:155001, 2003. 46, 47

[152] L. E. Thode and R. N. Sudan. **Two-Stream Instability Heating of Plasmas by Relativistic Electron Beams**. *Phys. Rev. Lett.*, **30**:732–735, 1973. 46

[153] E. S. Weibel. **Spontaneously Growing Transverse Waves in a Plasma Due to an Anisotropic Velocity Distribution**. *Phys. Rev. Lett.*, **2**:83–84, 1959. 46

[154] F. Pegoraro, S. V. Bulanov, F. Califano, and M. Lontano. **Nonlinear development of the weibel instability and magnetic field generation in collisionless plasmas**. *Phys. Scr.*, **1996**(T63):262, 1996. 47

[155] L. O. Silva, R. A. Fonseca, J. W. Tonge, W. B. Mori, and J. M. Dawson. **On the role of the purely transverse Weibel instability in fast ignitor scenarios**. *Phys. Plasmas*, **9**(6):2458–2461, 2002. 47

[156] A. Karmakar, N. Kumar, G. Shvets, O. Polomarov, and A. Pukhov. **Collision-Driven Negative-Energy Waves and the Weibel Instability of a Relativistic Electron Beam in a Quasineutral Plasma**. *Phys. Rev. Lett.*, **101**:255001, 2008. 47

[157] M. Tatarakis, F. N. Beg, E. L. Clark, A. E. Dangor, R. D. Edwards, R. G. Evans, T. J. Goldsack, K. W. D. Ledingham, P. A. Norreys, M. A. Sinclair, M-S. Wei, M. Zepf, and K. Krushelnick. **Propagation Instabilities of High-Intensity Laser-Produced Electron Beams**. *Phys. Rev. Lett.*, **90**:175001, 2003. 47

[158] J. S. Green, V. M. Ovchinnikov, R. G. Evans, K. U. Akli, H. Azechi, F. N. Beg, C. Bellei, R. R. Freeman, H. Habara, R. Heathcote, M. H. Key, J. A. King, K. L. Lancaster, N. C. Lopes, T. Ma, A. J. MacKinnon, K. Markey, A. McPhee, Z. Najmudin, P. Nilson, R. Onofrei, R. Stephens, K. Takeda, K. A. Tanaka, W. Theobald, T. Tanimoto, J. Waugh, L. Van Woerkom, N. C. Woolsey, M. Zepf, J. R. Davies, and P. A. Norreys. **Effect of Laser Intensity on Fast-Electron-Beam Divergence in Solid-Density Plasmas**. *Phys. Rev. Lett.*, **100**(1):015003, 2008. 47, 101

[159] A. Debayle, J. J. Honrubia, E. d'Humières, and V. T. Tikhonchuk. **Divergence of laser-driven relativistic electron beams**. *Phys. Rev. E*, **82**:036405, 2010. 47, 48, 114

[160] J. J. Santos, F. Amiranoff, S. D. Baton, L. Gremillet, M. Koenig, E. Martinolli, M. Rabec Le Gloahec, C. Rousseaux, D. Batani, A. Bernardinello, G. Greison, and T. Hall. **Fast Electron Transport in Ultraintense Laser Pulse Interaction with Solid Targets by Rear-Side Self-Radiation Diagnostics**. *Phys. Rev. Lett.*, **89**:025001, 2002. 48

[161] J. J. Santos, A. Debayle, Ph. Nicolai, V. Tikhonchuk, M. Manclossi, D. Batani, A. Guemnie-Tafo, J. Faure, V. Malka, and J. J. Honrubia. **Fast-electron transport and induced heating in aluminum foils**. *Phys. Plasmas*, **14**(10):103107, 2007. 48

[162] G. M. Petrov, J. Davis, and Tz. Petrova. **Ionization dynamics of high-intensity laser–target interactions**. *Plasma Phys. Controlled Fusion*, **51**(9):095005, 2009. 49

[163] V. T. Tikhonchuk, A. A. Andreev, S. G. Bochkarev, and V. Yu Bychenkov. **Ion acceleration in short-laser-pulse interaction with solid foils**. *Plasma Phys. Controlled Fusion*, **47**(12B):B869, 2005. 49, 60

[164] A. V. Brantov, V. T. Tikhonchuk, V. Yu. Bychenkov, and S. G. Bochkarev. **Laser-triggered ion acceleration from a double-layer foil**. *Phys. Plasmas*, **16**(4):043107, 2009. 49, 66

[165] C. K. Birdsall and A. B. Langdon. **Plasma Physics Via Computer Simulation**. IOP Publishing, Bristol, Philadelphia, New York, 1991. 50

[166] A. Pukhov. **Three-Dimensional Simulations of Ion Acceleration from a Foil Irradiated by a Short-Pulse Laser**. *Phys. Rev. Lett.*, **86**:3562–3565, 2001. 52

[167] J. E. Crow, P. L. Auer, and J. E. Allen. **The expansion of a plasma into a vacuum**. *J. Plasma Phys.*, **14**(01):65–76, 1975. 56, 62

[168] J. Denavit. **Collisionless plasma expansion into a vacuum**. *Phys. Fluids*, **22**(7):1384–1392, 1979. 56

[169] M. Lontano and M. Passoni. **Electrostatic field distribution at the sharp interface between high density matter and vacuum**. *Phys. Plasmas*, **13**(4):042102, 2006. 56, 64, 89

[170] M. Passoni, L. Bertagna, and A. Zani. **Target normal sheath acceleration: theory, comparison with experiments and future perspectives**. *New J. Phys.*, **12**(4):045012, 2010. 56, 62, 64, 71, 89, 97, 116

[171] M. Passoni and M. Lontano. **One-dimensional model of the electrostatic ion acceleration in the ultraintense laser–solid interaction**. *Laser Part. Beams*, **22**(02):163–169, 2004. 59, 62, 66

[172] S. Betti, F. Ceccherini, F. Cornolti, and F. Pegoraro. **Expansion of a finite-size plasma in vacuum**. *Plasma Phys. Controlled Fusion*, **47**(3):521, 2005. 60

[173] S. Kar, K. Markey, P. T. Simpson, C. Bellei, J. S. Green, S. R. Nagel, S. Kneip, D. C. Carroll, B. Dromey, L. Willingale, E. L. Clark, P. McKenna, Z. Najmudin, K. Krushelnick, P. Norreys, R. J. Clarke, D. Neely, M. Borghesi, and M. Zepf. **Dynamic Control of Laser-Produced Proton Beams**. *Phys. Rev. Lett.*, **100**:105004, 2008. 64

[174] K. Quinn, P. A. Wilson, C. A. Cecchetti, B. Ramakrishna, L. Romagnani, G. Sarri, L. Lancia, J. Fuchs, A. Pipahl, T. Toncian, O. Willi, R. J. Clarke, D. Neely, M. Notley, P. Gallegos, D. C. Carroll, M. N. Quinn, X. H. Yuan, P. McKenna, T. V. Liseykina, A. Macchi, and M. Borghesi. **Laser-Driven Ultrafast Field Propagation on Solid Surfaces**. *Phys. Rev. Lett.*, **102**:194801, 2009. 64

[175] M. H. Key, M. D. Cable, T. E. Cowan, K. G. Estabrook, B. A. Hammel, S. P. Hatchett, E. A. Henry, D. E. Hinkel, J. D. Kilkenny, J. A. Koch, W. L. Kruer, A. B. Langdon, B. F. Lasinski, R. W. Lee, B. J. MacGowan, A. MacKinnon, J. D. Moody, M. J. Moran, A. A. Offenberger, D. M. Pennington, M. D. Perry, T. J. Phillips, T. C. Sangster, M. S. Singh, M. A. Stoyer, M. Tabak, G. L. Tietbohl, M. Tsukamoto, K. Wharton, and S. C. Wilks. **Hot electron production and heating by hot electrons in fast ignitor research**. *Phys. Plasmas*, **5**(5):1966–1972, 1998. 72

[176] M. Zepf, E. L. Clark, K. Krushelnick, F. N. Beg, C. Escoda, A. E. Dangor, M. I. K. Santala, M. Tatarakis, I. F. Watts, P. A. Norreys, R. J. Clarke, J. R. Davies, M. A. Sinclair, R. D. Edwards, T. J. Goldsack, I. Spencer, and K. W. D. Ledingham. **Fast particle generation and energy transport in laser-solid interactions**. *Phys. Plasmas*, **8**(5):2323–2330, 2001. 73, 137

[177] J. Fuchs, Y. Sentoku, E. d'Humières, T. E. Cowan, J. Cobble, P. Audebert, A. Kemp, A. Nikroo, P. Antici, E. Brambrink, A. Blazevic, E. M. Campbell, J. C. Fernandez, J.-C. Gauthier, M. Geissel, M. Hegelich, S. Karsch, H. Popescu, N. Renard-LeGalloudec, M. Roth, J. Schreiber, R. Stephens, and H. Pepin. **Comparative spectra and efficiencies of ions laser-accelerated forward from the front and rear surfaces of thin solid foils**. *Phys. Plasmas*, **14**(5):053105, 2007. 73, 79

[178] M. Coury, D. C. Carroll, A. P. L. Robinson, X. H. Yuan, C. M. Brenner, M. Burza, R. J. Gray, M. N. Quinn, K. L. Lancaster, Y. T. Li, X. X. Lin, O. Tresca, C.-G. Wahlstrom, D. Neely, and P. McKenna. **Influence of laser irradiated spot size on energetic electron injection and proton acceleration in foil targets**. *Appl. Phys. Lett.*, **100**(7):074105, 2012. 92

[179] M. Passoni, L. Bertagna, T. Ceccotti, and P. Martin. **Proton Maximum Energy Cutoff Scaling Laws For Bulk Targets**. *AIP Conf. Proc.*, **1153**(1):159–163, 2009. 93

[180] C. Benedetti, A. Sgattoni, G. Turchetti, and P. Londrillo. **ALaDyn: A High-Accuracy PIC Code for the Maxwell-Vlasov Equations**. *IEEE Trans. Plasma Sci.*, **36**(4):1790 –1798, 2008. 103

[181] N. Metropolis, A. W. Rosenbluth, M. N. Rosenbluth, A. H. Teller, and E. Teller. **Equation of State Calculations by Fast Computing Machines**. *J. Chem. Phys.*, **21**(6):1087–1092, 1953. 112

[182] S. Weinzierl. **Introduction to Monte Carlo methods**. *ArXiv e-prints*, **arXiv:hep-ph/0006269**, 2000. 112

[183] F. James. **RANLUX: A Fortran implementation of the high-quality pseudorandom number generator of Lüscher**. *Comput. Phys. Commun.*, **79**(1):111 – 114, 1994. 112

[184] S. Buffechoux. **Augmentation de l'énergie des faisceaux de protons accélérés par laser ultra-intense et étude des caractéristiques des faisceaux accélérés par laser ultra-court.** PhD thesis, École Polytechnique de Paris, 2011. 125

[185] F. Fogolari, A. Brigo, and H. Molinari. **The Poisson–Boltzmann equation for biomolecular electrostatics: a tool for structural biology**. *J. Mol. Recognit.*, **15**(6):377–392, 2002. 135

[186] P. McKenna, K. W. D. Ledingham, J. M. Yang, L. Robson, T. McCanny, S. Shimizu, R. J. Clarke, D. Neely, K. Spohr, R. Chapman, R. P. Singhal, K. Krushelnick, M. S. Wei, and P. A. Norreys. **Characterization of proton and heavier ion acceleration in ultrahigh-intensity laser interactions with heated target foils**. *Phys. Rev. E*, **70**(3):036405, 2004. 137

[187] M. Nishiuchi, A. Fukumi, H. Daido, Z. Li, A. Sagisaka, K. Ogura, S. Orimo, M. Kado, Y. Hayashi, M. Mori, S.V. Bulanov, T. Esirkepov, K. Nemoto, Y. Oishi, T. Nayuki, T. Fujii, A. Noda, Y. Iwashita, T. Shirai, and S. Nakamura. **The laser proton acceleration in the strong charge separation regime**. *Physics Letters A*, **357**(4-5):339 – 344, 2006. 137

[188] T. Fujii, Y. Oishi, T. Nayuki, Y. Takizawa, K. Nemoto, T. Kayoiji, K. Horioka, Y. Okano, Y. Hironaka, K. G. Nakamura, and K. Kondo. **MeV-order proton and carbon ion acceleration by irradiation of 60 fs TW laser pulses on thin copper tape**. *Appl. Phys. Lett.*, **83**(8):1524–1526, 2003. 137

[189] O. Jäckel, J. Polz, S. M. Pfotenhauer, H.-P. Schlenvoigt, H. Schwoerer, and M. C. Kaluza. **All-optical measurement of the hot electron sheath driving laser ion acceleration from thin foils**. *New J. Phys.*, **12**(10):103027, 2010. 137

[190] A. S. Pirozhkov, M. Mori, A. Yogo, H. Kiriyama, K. Ogura, A. Sagisaka, J.-L. Ma, S. Orimo, M. Nishiuchi, H. Sugiyama, T. Zh. Esirkepov, S. V. Bulanov, H. Okada, S. Kondo, S. Kanazawa, Y. Nakai, A. Akutsu, T. Motomura, M. Tanoue, T. Shimomura, M. Ikegami, T. Shirai, Y. Iwashita, A. Noda, I. W. Choi, S. K. Lee, J. Lee, Y. Oishi, T. Kimura, T. Tajima, and H. Daido. **Laser-driven proton acceleration and plasma diagnostics with J-KAREN laser**. *Proc. SPIE*, pages 735414–735414–10, 2009. 138

[191] D. S. Hey, M. E. Foord, M. H. Key, S. L. LePape, A. J. Mackinnon, P. K. Patel, Y. Ping, K. U. Akli, R. B. Stephens, T. Bartal, F. N. Beg, R. Fedosejevs, H. Friesen, H. F. Tiedje, and Y. Y. Tsui. **Laser-accelerated proton conversion efficiency thickness scaling**. *Phys. Plasmas*, **16**(12):123108, 2009. 138

Declaration

I herewith declare that I have produced this paper without the prohibited assistance of third parties and without making use of aids other than those specified; notions taken over directly or indirectly from other sources have been identified as such. This paper has not previously been presented in identical or similar form to any other Italian or foreign examination board.

The thesis work was conducted from January 2010 to December 2012 under the supervision of Dr. Matteo Passoni and Prof. Dimitri Batani at Milano-Bicocca University.

Milan, 21st December, 2012